Repository-Scale Performance Assessment Incorporating Postclosure Criticality

Spent Fuel and Waste Disposition

Prepared for
US Department of Energy
Spent Fuel and Waste Science and Technology
L.L. Price, A. Salazar, E. Basurto, A.A. Alsaed, J. Cardoni, M. Nole, J. Prouty, C. Sanders
Sandia National Laboratories

G. Davidson, M. Swinney, S. Bhatt
Oak Ridge National Laboratory

E. Gonzalez, B. Kiedrowski
University of Michigan

September 30, 2021
M2SF-21SN010305061
SAND2022-7932 R

DISCLAIMER

This is a technical report that does not take into account contractual limitations or obligations under the Standard Contract for Disposal of Spent Nuclear Fuel and/or High-Level Radioactive Waste (Standard Contract) (10 CFR Part 961). For example, under the provisions of the Standard Contract, spent nuclear fuel in multi-assembly canisters is not an acceptable waste form, absent a mutually agreed to contract amendment.

To the extent discussions or recommendations in this report conflict with the provisions of the Standard Contract, the Standard Contract governs the obligations of the parties, and this report in no manner supersedes, overrides, or amends the Standard Contract.

This report reflects technical work which could support future decision making by DOE. No inferences should be drawn from this report regarding future actions by DOE, which are limited both by the terms of the Standard Contract and Congressional appropriations for the Department to fulfill its obligations under the Nuclear Waste Policy Act including licensing and construction of a spent nuclear fuel repository.

Prepared by
Sandia National Laboratories
Albuquerque, New Mexico 87185

Sandia National Laboratories is a multimission laboratory managed and operated by National Technology & Engineering Solutions of Sandia, LLC, a wholly owned subsidiary of Honeywell International Inc., for the U.S. Department of Energy's National Nuclear Security Administration under contract DE-NA0003525. SAND2022-7932 R.

Revision 6
10/7/2019

APPENDIX E

NFCSC DOCUMENT COVER SHEET[1]

Name/Title of Deliverable/Milestone/Revision No.: Repository-Scale Performance Assessment Incorporating Postclosure Criticality

Work Package Title and Number: Probabilistic Postclosure DPC Criticality Consequence Analyses

Work Package WBS Number: SF-21SN01030506

Responsible Work Package Manager: Laura Price Laura Pri
(Name/Signature)

Date Submitted: September 30, 2021

Quality Rigor Level for Deliverable/Milestone[2]	☐ QRL-1 ☐ Nuclear Data	☐ QRL-2	☒ QRL-3	☐ QRL-4 Lab QA Program[3]

This deliverable was prepared in accordance with Sandia National Laboratories
(Participant/National Laboratory Name)

QA program which meets the requirements of

☒ DOE Order 414.1 ☐ NQA-1 ☐ Other

This Deliverable was subjected to:

☒ Technical Review	☐ Peer Review
Technical Review (TR)	**Peer Review (PR)**
Review Documentation Provided	**Review Documentation Provided**
☐ Signed TR Report or,	☐ Signed PR Report or,
☐ Signed TR Concurrence Sheet or,	☐ Signed PR Concurrence Sheet or,
☒ Signature of TR Reviewer(s) below	☐ Signature of PR Reviewer(s) below

Name and Signature of Reviewers

Heeho Park	Heeho Park
Matthew Paul	Matthew Paul
Philip Jones	PGJ

NOTE 1: *Appendix E should be filled out and submitted with the deliverable. Or, if the PICS:NE system permits, completely enter all applicable information in the PICS:NE Deliverable Form. The requirement is to ensure that all applicable information is entered either in the PICS:NE system or by using the NFCSC Document Cover Sheet.*

- *In some cases there may be a milestone where an item is being fabricated, maintenance is being performed on a facility, or a document is being issued through a formal document control process where it specifically calls out a formal review of the document. In these cases, documentation (e.g., inspection report, maintenance request, work planning package documentation or the documented review of the issued document through the document control process) of the completion of the activity, along with the Document Cover Sheet, is sufficient to demonstrate achieving the milestone.*

NOTE 2: *If QRL 1, 2, or 3 is not assigned, then the QRL 4 box must be checked, and the work is understood to be performed using laboratory QA requirements. This includes any deliverable developed in conformance with the respective National Laboratory / Participant, DOE or NNSA-approved QA Program.*

NOTE 3: *If the lab has an NQA-1 program and the work to be conducted requires an NQA-1 program, then the QRL-1 box must be checked in the work Package and on the Appendix E cover sheet and the work must be performed in accordance with the Lab's NQA-1 program. The QRL-4 box should not be checked.*

This page is intentionally left blank.

SUMMARY

A key objective of the United States Department of Energy's (DOE) Office of Nuclear Energy's Spent Fuel and Waste Science and Technology Campaign is to better understand the technical basis, risks, and uncertainty associated with the safe and secure disposition of spent nuclear fuel (SNF) and high-level radioactive waste. Commercial nuclear power generation in the United States has resulted in thousands of metric tons of SNF, the disposal of which is the responsibility of the DOE (Nuclear Waste Policy Act of 1982, as amended). Any repository licensed to dispose of SNF must meet requirements regarding the long-term performance of that repository. For an evaluation of the long-term performance of the repository, one of the events that may need to be considered is the SNF achieving a critical configuration during the postclosure period. Of particular interest is the potential behavior of SNF in dual-purpose canisters (DPCs), which are currently licensed and being used to store and transport SNF but were not designed for permanent geologic disposal.

A study has been initiated to examine the potential consequences, with respect to long-term repository performance, of criticality events that might occur during the postclosure period in a hypothetical repository containing DPCs. The first phase (a scoping phase) consisted of developing an approach to creating the modeling tools and techniques that may eventually be needed to either include or exclude criticality from a performance assessment (PA) as appropriate; this scoping phase is documented in Price et al. (2019a). In the second phase, that modeling approach was implemented and future work was identified, as documented in Price et al. (2019b). This report gives the results of a repository-scale PA examining the potential consequences of postclosure criticality, as well as the information, modeling tools, and techniques needed to incorporate the effects of postclosure criticality in the PA.

This page is intentionally left blank.

ACKNOWLEDGEMENTS

This work was supported by the DOE Office of Nuclear Energy, through the Office of Spent Fuel and Waste Science and Technology.

The authors would like to thank Philip Jones, Heeho Park, and Matthew Paul of Sandia National Laboratories for their technical review, David Ames of Sandia National Laboratories for his review, and Tim Gunter and Bob Clark from the DOE for their suggestions and guidance.

This page is intentionally left blank.

CONTENTS

LIST OF FIGURES

LIST OF TABLES

This page is intentionally left blank.

ACRONYMS

1D, 2D, 3D	one-dimensional, two-dimensional, three-dimensional
ACRR	Annular Core Research Reactor
BOL	beginning-of-life
BWR	boiling water reactor
CFD	computational fluid dynamics
CFR	Code of Federal Regulations
CRDM	control rod drive mechanism
DOE	US Department of Energy
DPC	dual-purpose canister
DRZ	disturbed rock zone
EBS	engineered barrier system
ENDF/B-VII.1	Evaluated Nuclear Data File/Version B – Rev. 7.1
EOC	end-of-cycle
EOL	end-of-life
EPKE	Exact Point Kinetics Equations
ERB	Example Reference Biosphere
FEP	feature, event, and/or process
FTC	fuel temperature coefficient
H/X	hydrogen-to-fissile (atomic ratio)
IAPWS	International Association for the Properties of Water and Steam
IF97	Industrial Formulation 1997
LEU	low-enriched uranium
MCNP	Monte-Carlo N-Particle
MOX	mixed oxide
MTC	moderator temperature coefficient
MTU	Metric Tons of Uranium
n.d.	no date (an abbreviation used when a reference has no date)
NRC	US Nuclear Regulatory Commission
ORNL	Oak Ridge National Laboratory
OTFDB	on-the-fly Doppler broadening
PA	performance assessment
PCQM	predictor-corrector quasi-static method

PWR	pressurized water reactor
REA	rod ejection accident
S–I	smectite-to-illite
S3K	SIMULATE-3K
SNF	spent nuclear fuel
SNL	Sandia National Laboratories
TAD	transportation, aging, and disposal
TCC	thermal characteristic curve
TH	thermal-hydrologic
UFD	Used Fuel Disposition
UNF-ST&DARDS	Used Nuclear Fuel – Storage, Transportation & Disposal Analysis Resource and Data Systems
US	United States
WF	waste form
WIPP	Waste Isolation Pilot Plant

SPENT FUEL AND WASTE SCIENCE AND TECHNOLOGY

REPOSITORY-SCALE PERFORMANCE ASSESSMENT INCORPORATING POSTCLOSURE CRITICALITY

1. INTRODUCTION

One of the objectives of the United States (US) Department of Energy's (DOE) Office of Nuclear Energy's Spent Fuel and Waste Science and Technology Campaign is to better understand the technical basis, risks, and uncertainty associated with the safe and secure disposition of spent nuclear fuel (SNF) and high-level radioactive waste. Commercial nuclear power generation in the US has resulted in thousands of metric tons of SNF, the disposal of which is the responsibility of the DOE (Nuclear Waste Policy Act 1982, as amended [42 U.S.C. 10101 et seq.]). Any repository licensed to dispose the SNF must meet requirements regarding the long-term performance of that repository. For an evaluation of the long-term performance of the repository, one of the events that may need to be considered is the SNF achieving a critical configuration. Of particular interest is the potential behavior of SNF in dual-purpose canisters (DPCs), which are currently being used to store and transport SNF but were not designed for permanent geologic disposal.

A study has been initiated to examine the potential consequences of criticality events with respect to long-term repository performance. These events are postulated to occur during the postclosure period in a hypothetical repository containing DPCs. In the first phase (a scoping phase), the study team developed an approach to creating the modeling tools and techniques that may eventually be required to either exclude criticality from or include criticality in a performance assessment (PA) as appropriate; this effort is documented in Price et al. (2019a). In the second phase, the study team implemented this modeling approach and identified future work, as documented in Price et al. (2019b). The next step was a repository-scale PA examining the potential consequences of postclosure steady-state criticality, an effort that includes the information, modeling tools, and techniques developed as a part of this study. This report documents the results of that repository-scale PA research.

This report fulfills the Spent Fuel and Waste Science and Technology Campaign milestone M2SF-21SN010305061.

1.1 Background

The DOE submitted the *Yucca Mountain Repository License Application* (DOE 2008a) to the US Nuclear Regulatory Commission (NRC) in 2008. An update to the license application was completed later in the same year (DOE 2008b) and submitted to the NRC in 2009. The license application included a PA analyzing the long-term performance of the repository consistent with applicable requirements given in the Code of Federal Regulations (CFR): 10 CFR Part 63 and 40 CFR Part 197. In that PA, SNF was assumed to be placed in transportation, aging, and disposal (TAD) canisters specifically designed to transport fuel from its current storage location to Yucca Mountain, store it for aging purposes (if needed), and dispose it in Yucca Mountain. These TAD canisters were designed such that the probability of an in-package criticality event during the repository postclosure period was sufficiently low to exclude it from consideration in the PA (DOE 2008b, Section 2.1.2.2). That is, the probability of a criticality event was less than one chance in 10,000 of occurring within 10,000 years after disposal.

However, the license application process was suspended in 2010, TADs were never built, and thus were not available to be loaded with SNF by utilities. Rather, utilities have continued the practice of storing SNF in DPCs designed to meet relevant NRC requirements for the storage and transportation of SNF (10 CFR Part 72 and 10 CFR Part 71, respectively). While DPCs were designed, licensed, and loaded to preclude the possibility of a criticality event during storage and transport of SNF, they were not designed or loaded to preclude the possibility of a criticality event during the regulated postclosure period following disposal, which can be up to 1,000,000 years (see Assumption 3 in Section 1.4.3).

A key requirement for assessing the long-term performance of a repository is that all features, events, or processes (FEPs) must be included in the PA unless the probability of occurrence of the FEP is below a specified limit or the consequences of its occurrence "…(however probable) can be demonstrated not to be significant" (73 FR 61256). As noted above, for the Yucca Mountain PA, the probability of in-package criticality in TAD canisters during the postclosure period was, by design, less than one chance in 10,000 in 10,000 years after disposal. Thus, postclosure criticality in TAD canisters was excluded from the Yucca Mountain PA based on probability. Based on studies investigating the probability of occurrence of in-package criticality in DPCs during the postclosure performance period, it is not clear that in-package criticality in DPCs can be excluded from a PA based on probability for all geologies (Hardin et al. 2015).

Therefore, if direct disposal of SNF in DPCs in a geologic repository is to be considered, the associated PA for the repository may have to include in-package criticality. The DOE has developed a methodology for addressing the consequences of in-package criticality during the postclosure period (YMP 2003). If the DOE pursues a disposal licensing strategy that excludes in-package criticality in DPCs from the PA based on low consequence rather than low probability, the DOE will have to demonstrate that the consequences of in-package criticality events are not significant in terms of repository performance. Alternatively, if the consequences of in-package criticality events are included in the PA, then the DOE must demonstrate that the regulatory performance standards can still be met. Regardless of the approach, the DOE will need the ability to model the consequences of postclosure in-package criticality events in terms of repository performance.

1.2 Purpose

One objective of this report is to identify those FEPs that affect or are affected by postclosure criticality and to develop the capability to include these FEPs in PA calculations. Another objective is twofold: (1) provide the results of repository-scale PA calculations that include the occurrence of criticality, including as many FEPs as possible in the model, and (2) compare those results with those obtained from repository-scale PA calculations in which criticality did not occur. The eventual goal is to develop modeling capabilities that can be used to either exclude criticality from a PA based on consequence or can be implemented in a PA if criticality is to be included. The approach used in this report is consistent with that developed in the past (YMP 2003). The work discussed in this report focuses solely on the consequences of criticality during the postclosure period, not the probability of occurrence of criticality. The probability of occurrence of postclosure criticality will be researched in the future. Further limitations on the scope of work are described in Section 1.3.

1.3 Scope

The approach implemented in the first two phases (Price et al. 2019a,b) and continued here is consistent with relevant regulations and requirements and uses existing generic models (Mariner et al. 2017; 2018) as much as possible. The study team investigated in-package criticality in DPCs only; that is, criticality events external to the waste package, either in the near field or far field, were not examined. For this report, the only type of waste form considered is commercial SNF in DPCs, and the DPCs are represented by a single DPC using its as-loaded radionuclide inventory and configuration.

The approach identifies conceptual models (Section 1.5) featuring two different hypothetical repositories and the occurrence of both steady-state criticality events (low power and long duration) and transient criticality events (high power and short duration). As previously stated, the approach considers only the consequences of criticality, not the probability of occurrence of criticality. Consistent with DOE's methodology (YMP 2003), the primary consequence of a steady-state criticality event is a change in the radionuclide inventory, which could affect repository performance; however, other effects of a steady-state criticality event such as thermal and chemical effects are considered as well. The same effects can also occur because of a transient criticality event. However, for a transient criticality event the primary consequence is a sudden power pulse, which might damage neighboring waste packages or damage the engineered barrier system (EBS) in the vicinity of the critical waste package.

1.4 Assumptions

The broad, overarching assumptions used in the analyses in Price et al. (2019b) were adapted for use in the current work. These assumptions are simplifying or bounding in nature as they were developed originally to support an initial scoping analysis. In Price et al. (2019b), the associated analyses involved a single waste package. While the transient criticality work discussed in Section 6 still involves a single waste package, the work on steady-state criticality has been expanded to consider a repository scale with multiple waste packages, which is reflected in the assumptions in this subsection. As noted below, some of these assumptions are being studied, and the research progress made thus far is discussed herein.

1.4.1 Assumption 1—Waste packages fail and criticality occurs.

To facilitate criticality calculations, the study team assumed that the waste packages fail, water enters the waste packages, and the configuration of water and SNF in the waste packages has an effective neutron multiplication factor (k_{eff}) greater than or equal to 1.0. This combination of circumstances formed a conservative assumption for the purposes of the study described in Price et al. (2019b). The probability that these conditions occur is not calculated. Assuming that all waste packages experience a criticality event at the same time (for the simulations in which steady-state criticality occurs) is computationally expedient; it does not represent an expectation that such a situation will occur. Future studies will examine the effects of varying the onset of in-package postclosure criticality events spatially and temporally.

The analyses consider the timing of any criticality event in a manner that is consistent with 10 CFR 63.114, which limits the time period over which FEPs must be evaluated to 10,000 years. Therefore, the steady-state criticality event in each waste package is assumed to begin 9,000 years after the repository closes. Previous analyses used the assumption that the steady-state criticality event continues for 10,000 years; that is, until 19,000 years after closure (Price et al. 2019b); the analyses described in Section 5 are also based on this assumption.

1.4.2 Assumption 2—Fuel assembly configurations remain intact, but cladding permits radionuclide transport.

Conservative, yet seemingly paradoxical, fuel conditions are assumed for performing criticality analyses and repository performance analyses.

For the criticality analyses, the study team assumed that the fuel pins and cladding in each DPC remain intact such that the fuel pins are retained in their original assembly lattice configurations. This assumption is conservative because it represents the most reactive credible fuel configuration under disposal conditions. Low enriched fuel (i.e., less than 5 wt% ^{235}U) is more reactive in a lumped lattice configuration (i.e., in fuel assemblies) compared to a homogeneous configuration. Additionally, commercial fuel assemblies are designed to be undermoderated (i.e., hydrogen-to-fissile [H/X] atomic ratio less than optimum). Configurations involving reduction in fuel pin pitch (i.e., damage to grid spacers) or degraded fuel (i.e., damaged cladding) are typically of lower reactivity than intact fuel assemblies because they result in a system that is further undermoderated. Mechanisms that could result in configurations with optimum moderation (e.g., relatively uniform pin pitch expansion) or preferentially separate fissile isotopes from neutron absorbers in the fuel are not postulated.

To examine criticality consequences relative to repository performance, the study team assumed that the cladding has failed, thereby permitting radionuclides to be released into a breached waste package and to be transported into the EBS and beyond.

1.4.3 Assumption 3—Postclosure performance requirements are similar to those for Yucca Mountain.

To examine the consequences of criticality in a DPC on postclosure repository performance, the study team needed to define the metric against which this performance is to be measured. It was assumed for the purposes of the analyses described in Price et al. (2019b) that the postclosure performance requirements that will apply to a repository in which DPCs are disposed are similar to those for disposal of SNF and high-level waste in Yucca Mountain. In particular, it was assumed that the following performance metrics are the same as those for Yucca Mountain: the dose to a member of the public, the period of postclosure performance (i.e., 1,000,000 years), and the limits on inclusion of FEPs in the postclosure PA. More details on repository performance requirements and the FEPs screening process are discussed in Price et al. (2019a).

1.4.4 Assumption 4—Basket neutron absorbers have degraded prior to the initiation of a criticality.

Because of the relatively high corrosion rate of aluminum-based materials, it was assumed that borated aluminum-based neutron absorbers in each DPC degrade within tens or hundreds of years once water enters the DPC. Although borated aluminum corrosion products (e.g., B_4C) may remain in the DPCs, the presence of neutron absorber material conservatively was not credited in the k_{eff} calculations for the analyses described in Price et al. (2019b). The location of neutron absorber material inside the basket is paramount for criticality control, and it is difficult to justify whether the absorber material would maintain its original location after corrosion over tens or hundreds of years in an aqueous environment.

1.4.5 Assumption 5—The steady-state criticality events do not oscillate between being supercritical and subcritical.

In the uncontrolled environment of a DPC disposed of in a repository, a criticality event in a DPC is likely to oscillate between supercritical and subcritical as fission heat changes the environmental conditions (e.g., Doppler broadening of ^{238}U neutron capture resonances in the spent fuel; water expands and boils, reducing moderator density; buildup of fission product neutron poisons such as ^{135}X). Modeling this cyclic reactivity in a waste package in a repository-scale model was beyond current modeling capabilities. Therefore, in the repository-scale model of a hypothetical saturated shale repository discussed in Section 5, it was assumed that the heat generated by the steady-state criticality event in each DPC is exactly balanced by heat loss through convection, conduction, radiation, and evaporation, such that there is no cyclic behavior. In contrast, this assumption was not made in the studies described in Section 4.3.1.

1.5 Approach

Two different hypothetical repositories are considered as geologic reference cases in the criticality analyses discussed in this report: a saturated repository in shale and an unsaturated repository in alluvium. The approach to estimating the consequences of steady-state criticality events on the performance of each hypothetical repository involves calculating and comparing the doses to a member of the public (1) with the occurrence of steady-state criticality events and (2) without the occurrence of any criticality event (Section 5). For convenience, the discussions of steady-state criticality events in this report refer to the modeling case in which all waste packages remain subcritical (i.e., no criticality event occurs) as the base case. The modeling case in which steady-state criticality events occur is referred to as the steady-state criticality case.

In addition to steady-state criticality events, the study team also investigated transient criticality events. The strategy for estimating the consequences of transient criticality events on the performance of each hypothetical repository involves calculating the range of predicted power over time produced by the transient criticality event and determining whether the pulse of energy could cause mechanical damage to the engineered or natural barrier. As discussed in Section 6, this report gives a range of predicted power that might be generated by a transient postclosure criticality event; the approach to determining the extent of mechanical damage to barriers is still being developed.

The geologic reference case for a hypothetical repository in saturated shale, or argillite, is illustrated in Figure 1-1. For this reference case, the repository is placed at a depth of 500 m, the emplacement drifts are backfilled with bentonite as a buffer (Mariner et al. 2017), and the waste package center-to-center spacing is 20 m (Hardin and Kalinina 2016). It is assumed that the hydrostatic pressure at repository depth is 50 bar. At this pressure, water boils at approximately 264°C (Weast and Astle 1979); therefore, during the steady-state criticality event, the maximum temperature in the waste package is 264°C. Other characteristics of the host rock are given in relevant subsections of this report and in Section 4.2.2 of Mariner et al. (2017). The results of estimating dose to a member of the public both with and without the occurrence of in-package, steady-state criticality events are presented in Section 5.

Figure 1-2 depicts the hypothetical reference case for a repository in unsaturated alluvium. The repository depth is 250 m, and waste drifts are backfilled with crushed alluvium (based on Mariner et al. 2018). The drift diameter is 4.5 m, and the maximum percolation rate, corresponding to very wet conditions, is 10 mm/yr. Hydrologic and thermal parameters are given below in relevant subsections and in Table 5-1 of Mariner et al. (2018). Analyses of the hypothetical unsaturated repository in alluvium did not result in dose calculations; this situation is discussed further in Section 4.3.1.

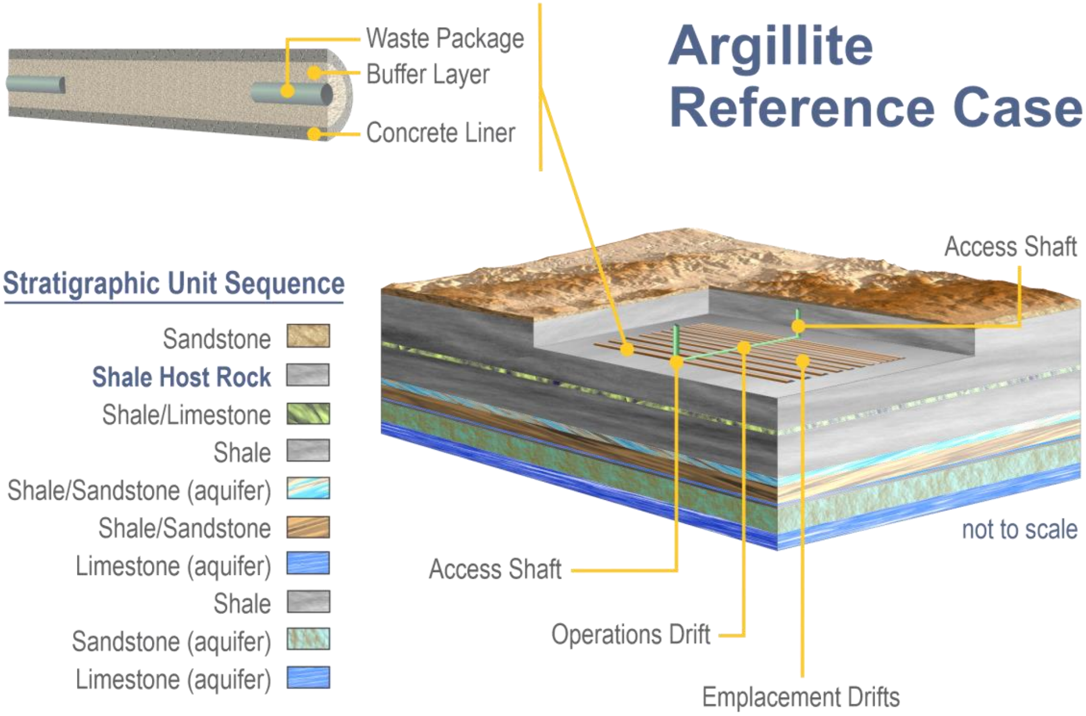

Figure 1-1. Conceptual Drawing of Hypothetical Reference Case for Saturated Shale/Argillite

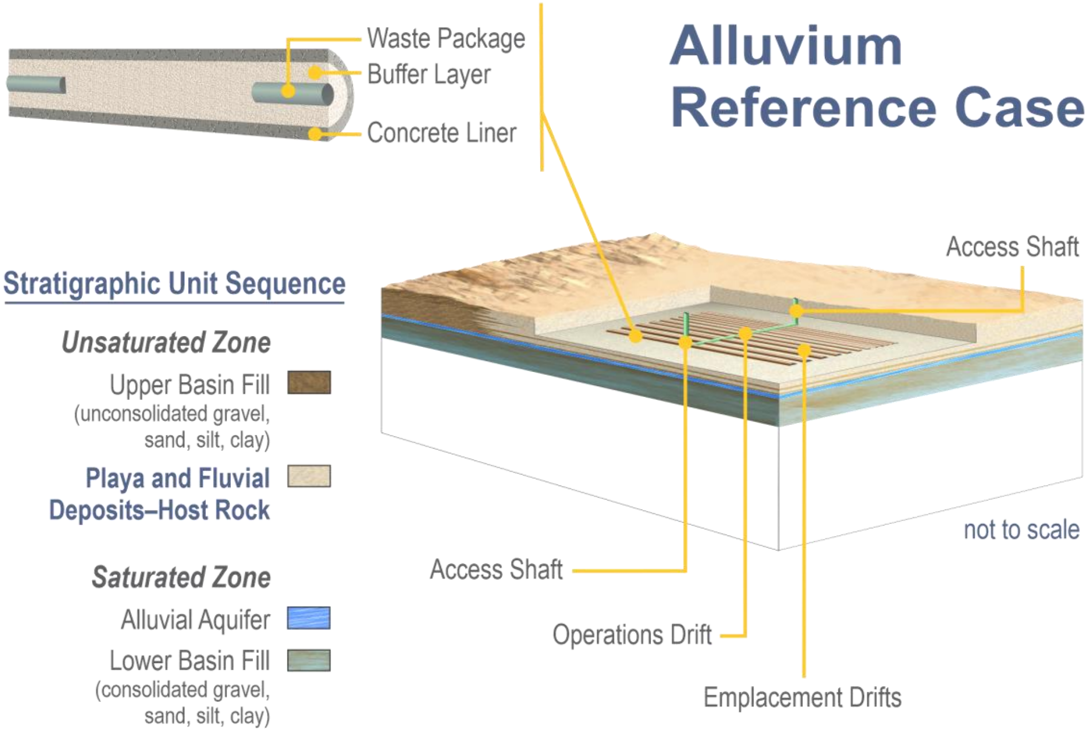

Figure 1-2. Conceptual Drawing of Hypothetical Reference Case for Unsaturated Alluvium

2. SUMMARY OF FEPS CONSIDERED

With respect to estimating the effects of both steady-state and transient criticality events on repository performance, many FEPs could affect the potential for reactivity or the extent of a criticality event (e.g., peak power, steady-state power, duration). Additionally, a criticality event could affect other FEPs, for example due to heat generation or inventory changes. A study was conducted to identify such FEPs (Alsaed and Price 2020) so that consideration might be given to including them in models of postclosure criticality. This study used the FEPs developed for the Yucca Mountain Repository PA (DOE 2008c) and additional FEPs developed as part of a FEPs analysis (Freeze et al. 2011) as a starting point to evaluate the FEPs that could affect or be affected by an in-package criticality event. In addition, this study identified FEPs not previously considered that warrant further development.

Section 2 considers the FEPs that could affect postclosure reactivity, could be affected by a postclosure criticality event, or both. The discussion is organized by whether the criticality event is steady-state (Section 2.1) or transient (Section 2.2). It should be noted that only some of the FEPs discussed below are included in the models discussed in Section 4 or results discussed in Section 5.

2.1 Steady-State Criticality

For the steady-state criticality case, the study team used an approach consistent with the DOE’s disposal criticality analysis methodology (DOE 2003). The team focused on the effects of the relatively low heat (on the order of a few kilowatts or less) generated over long periods of time (tens of thousands of years) and on the resulting changes in the radionuclide inventory. At the relatively low temperatures expected to be present in a critical DPC, changes in radionuclide inventory vary with the power generated by the fission reactions in an approximately linear relationship. A steady-state criticality event that produces 1,000 W of power will result in an inventory change that is about 10 times greater than a steady-state criticality event that produces 100 W of power for the same period of time. Disruptive scenarios, such as seismic activity, volcanism, glaciation, a rise in the water table, and human intrusion, are not considered explicitly here although their occurrence could affect the probability of occurrence of criticality or could affect the evaluation of criticality consequences. For example, seismic activity or other disruptive events could lead to waste package failure, allowing water into the failed waste package and the initiation of corrosion of waste package internals, including neutron absorbers.

2.1.1 Undisturbed Repository Conditions

Processes and features within an undisturbed repository that can affect criticality include the geometry and materials of waste package components, the neutronic characteristics of the SNF in the waste package, the degradation rate of the SNF and other DPC internals, the degradation rate of engineered barriers from both chemical and mechanical processes, the presence of corrosion products in the waste package, the orientation of the waste package, the distance between waste packages, the chemical characteristics of the groundwater, the permeability of any backfill, the presence of fractures or other water-conducting features, and the hydrologic characteristics of the repository. For a saturated repository, the depth of the repository and its depth below the water table determine the hydrostatic pressure of the water that can enter the waste package, which sets the saturation temperature (i.e., the boiling point of water), which in turn can set an upper limit on the power that can be generated by a steady-state criticality event in the waste package. For an unsaturated repository, the infiltration rate can set an upper limit on the power that can be generated by a steady-state criticality event and, if oscillatory behavior is considered, can affect the length of time between criticality events. The undisturbed repository is described further in Section 3.

2.1.2 Nuclear Criticality in a Waste Package

For nuclear criticality to occur in a waste package disposed in a repository, the following events must occur: (1) the waste package outer shell must first fail, (2) the DPC must also fail, (3) water must enter the DPC, and (4) the neutron absorbers in the DPC must dissolve, corrode, or otherwise degrade such that they are no longer capable of keeping the flooded DPC subcritical. These events must occur before an in-package postclosure criticality event can occur, but their occurrence will not necessarily result in a postclosure criticality event. Clarity et al. (2017) evaluated the as-loaded configuration of 554 DPCs and found that 77% of the DPCs would remain subcritical if the neutron absorber material was lost and 68% of the DPCs would remain subcritical if the neutron absorber material was lost *and* the carbon-steel basket structures maintaining the fuel configuration failed.

Once a postclosure criticality event begins, the temperature of the contents of the waste package, the waste package itself, and the surrounding environment will begin to increase. The neutronics of the critical system inside the DPC would be coupled with the thermal-hydrologic (TH) properties of the repository, such as the flow rate of water into and out of the DPC and the rate at which heat could be removed from the system. This coupling is discussed further in Section 4.1.

2.1.3 Thermal Effects on Flow

The heat generated by a steady-state criticality event would affect groundwater flow in the backfill and in the host rock. In an unsaturated repository, the heat would evaporate the water in the waste package and in the surrounding backfill and rock, causing them to dry out. This situation would result in terminating the criticality event (due to the loss of water) and in diverting water around the heated area. As the temperature decreased, water would return to the surrounding backfill and rock and would once again enter the waste package. Once sufficient water entered the waste package, the criticality event would restart and the cycle would repeat itself. This cyclic drying and rewetting behavior is discussed further in Section 4.3.

In a saturated repository, the heat could set up a convection cell, cause thermally enhanced flow through the backfill, change the flow properties (e.g., permeability and porosity) of the backfill or other engineered barriers, or cause thermal pressurization of the backfill and host rock. Some of these responses of the flow system to the heat generated by the criticality event are included in the analyses as discussed in Section 4.2.

2.1.4 Thermal Effects on Radionuclide Transport

The heat generated by a steady-state criticality event would affect transport of radionuclides from the waste package, through the backfill (if it exists), and into the host rock. Some of these effects could include changing the transport properties of the backfill and host rock (e.g., sorption coefficients, porosity), changing radionuclide solubilities, affecting the formation and stability of colloids, changing the chemical and geochemical conditions in and around the waste package, and temporarily precluding radionuclide transport altogether by evaporating water such that there is no continuous path for radionuclide transport. Thermal effects on radionuclide transport that are included in these analyses are discussed in Section 4.3.

2.1.5 Thermal and Radiolytic Effects on DPC Components

The heat and radiolysis generated by a steady-state criticality event would affect the various components associated with the DPC, including the SNF. These effects would include increasing the rate of various temperature-dependent corrosion processes acting on the grid spacers, the baskets, the fuel cladding, the fuel itself, the DPC shell, the waste package overpack, and any other hardware in the DPC. In addition, temperature-sensitive properties of the materials in those components would change during the thermal period, such as the yield strength or the creep rate. Corrosion of the components listed above would create corrosion products, which could fill the waste package and affect the neutronic characteristics in the waste package. Of the processes listed above, grid spacer corrosion is the only one for which a model has been developed, although it was not included in the PA calculations discussed further in Section 4.4 and Section 5.1. The intention is to include the grid spacer corrosion model in future repository-scale PAs incorporating postclosure criticality events.

The heat and radiolysis generated by a steady-state criticality event would also affect the chemistry of the water inside the waste package, which could also affect the corrosion rates of the various components listed above and the reaction kinetics of other chemical reactions occurring in the waste package. Radiolysis is accounted for in the model of grid spacer corrosion, as discussed further in Section 4.4.

2.1.6 Thermal Effects on Near-Field Conditions

The heat generated by a steady-state criticality event would affect the region around the waste package, including the backfill, the liner, and regions of the host rock close enough to experience a significant increase in temperature. Aside from thermal effects on flow and transport discussed in Section 2.1.3 and Section 2.1.4, other possible effects could include altering the chemical characteristics of the groundwater and backfill; changing the mineralogy of the backfill or host rock material; damaging the liner by increasing the degradation rate of metal components (e.g., rebar) in the liner; and damaging the backfill, liner, or host rock as a result of thermal pressurization of the backfill. The heat generated by a criticality event could also cause the temperature near an adjacent waste package to rise. Of the processes listed above, changing the mineralogy of the backfill (i.e., illitization) is included in the PA calculations, as discussed further in Section 4.2.2.

2.1.7 Inventory Effects

The steady-state criticality event, which represents self-sustaining fission of radionuclides (e.g., ^{233}U, ^{235}U, and ^{239}Pu), changes the inventory of radionuclides inside the spent fuel rods. The inventory changes include generation of fission products (both long-lived and short-lived), generation of higher actinides (which are relevant to dose), depletion and generation of fissile material, and depletion and generation of neutron absorbers. This inventory effect is discussed further in Section 4.5.

2.1.8 Radiological Toxicity and Effects

The criticality event would generate relatively short-lived radionuclides that might need to be considered in dose calculations, i.e., radionuclides that otherwise would not be included in dose calculations because the radionuclides would have decayed to insignificant levels at the time the criticality event begins. This effect is discussed further in Section 4.5.

2.2 Transient Criticality

For the transient criticality case, consistent with the DOE’s disposal criticality analysis methodology (DOE 2003), the study team focused on the mechanical effects of the transient criticality on engineered and natural barriers. The mechanical effects would be caused by an exponential increase in power that continues until the negative feedback mechanisms cause the system to become subcritical again, on the order of milliseconds to seconds. Occurrence of a transient criticality is based on the premise that there is a relatively rapid (e.g., seconds to hours) shift in the internal geometry of the SNF and/or neutron absorbers resulting in a supercritical configuration. The mechanical consequences can result from the pressure pulse generated by rapid volatilization of water with power production and from rapid heating or thermal cycling of the waste package internals, including water.

2.2.1 Causes of Rapid Reactivity Insertion

Some of the processes or events that could occur and that could cause rapid reactivity insertion include seismicity, corrosion of neutron absorber plates, sudden flooding of the waste package accompanied by loss of neutron moderator, and floor buckling. While none of these processes or events is explicitly modeled here, the reactivity insertion rates used in the calculations in Section 6 are consistent with the rate at which a neutron absorber plate could fall through a water-filled DPC once the weld holding it in place had corroded.

2.2.2 Damage to Fuel, Engineered Barriers, and Natural Barriers

The possible consequences of the thermal or pressure pulse generated by a transient criticality event include damage to the fuel (e.g., melting of the fuel or cladding, cracking of the fuel or cladding), damage to the backfill surrounding the waste package or to other engineered barriers (e.g., fracturing of the backfill, damage to the drift liner, damage to the waste package, damage to an adjacent waste package), and damage to the host rock (e.g., fracturing of the host rock). Note that some of these consequences would have little effect on repository performance because the criticality event cannot occur unless some of these components have already failed. For example, the waste package overpack and the DPC must have breached such that the waste package has filled with water, and the neutron moderators must have corroded or otherwise degraded such that they no longer maintain the SNF assemblies in a subcritical configuration prior to initiation of any kind of criticality event. Therefore, if the waste package is modeled as having already failed, further damage to the waste package from a transient criticality event would not affect modeled repository performance.

3. MODELING THE UNDISTURBED REPOSITORY

As noted in Section 1.5, for this report, the study team estimated the consequences of a steady-state criticality event on the performance of each hypothetical repository by calculating and then comparing the doses to a member of the public with and without the occurrence of the steady-state criticality event (i.e., the steady-state criticality case versus the base case). This approach was successful for the hypothetical saturated shale repository, but it was not successful for the hypothetical unsaturated alluvial repository because improvements to the simulation software (PFLOTRAN) necessary for modeling unsaturated media were only recently completed. The results obtained to date are discussed in Section 4.3.1.

The subsections below describe how the undisturbed (i.e., without the occurrence of a postclosure criticality event) repository is modeled. Section 3.1 provides a general description of PFLOTRAN and Section 3.2 summarizes how the repositories are represented in PFLOTRAN. Section 3.3 explains how anisotropic temperature-dependent thermal conductivity was incorporated into PFLOTRAN. Finally, the biosphere model used to calculate dose to a member of the public is summarized in Section 3.4.

3.1 PFLOTRAN Description

PFLOTRAN (Hammond et al. 2014; Lichtner et al. 2020a,b; Nole et al. 2021) is an open source, state-of-the-art, massively parallel, subsurface flow and reactive transport code used to simulate subsurface earth system processes. The code is written in object-oriented Fortran 2003/2008 and solves nonlinear partial differential equations describing nonisothermal multiphase flow, reactive transport, and geomechanics in porous media. The latest PFLOTRAN capabilities, documentation, and installation instructions are available at https://www.pflotran.org/ (Lichtner et al. 2020a,b).

3.2 Description of PFLOTRAN Models

The following subsections describe the model of the hypothetical saturated shale repository as implemented in PFLOTRAN (Section 3.2.1) and the model of the hypothetical unsaturated alluvial system as implemented in PFLOTRAN (Section 3.2.2). Note that the saturated shale model domain is a repository containing 4,200 waste packages, while the unsaturated alluvial domain is a single waste package.

3.2.1 Description of Hypothetical Saturated Shale Model

The model domain used for this study is the same as that used in Mariner et al. (2017). Figure 3-1 is a transparent view of the model domain colored by material. The repository (tan) is 500 m from the west (left) face of the domain and 515 m below the top face of the domain. The x-axis is in the east/west direction, the y-axis is in the north/south direction, and the z-axis is vertical. The domain is long enough to place a well 5 km down gradient of the repository as shown in the figure and represented by teal box. The half-symmetry model domain is 6,855 × 1,575 × 1,200 m. Most of each domain is discretized into cells as large as 15 m on a side and as small as 1.67 m (5/3 m) on a side, the latter being within the emplacement drifts. Transition zones of cells 5 m on a side exist between the finely discretized emplacement zones and the rest of the domain. The mesh of the model consists of 6,925,936 cells, of which about 3,000,000 are smaller cells in the repository area.

The model as described by Mariner et al. (2017) has several distinct geologic strata; the ones of interest are (1) the upper sandstone aquifer, which is the release pathway to the biosphere; (2) the shale host rock; and (3) a lower limestone aquifer, which does not release radionuclides directly to the biosphere. Material properties for these strata and regions are given in Table 3-1.

Table 3-1. Parameter Values for Material Properties

Model Region	Permeability (m^2)	Porosity	Tortuosity	Saturated Thermal Conductivity (W/[m·K])	Heat Capacity (J/[kg·K])	Grain Density (kg/m^3)
Overburden	1×10^{-15}	0.20	0.11	1.7	830	2,700
Upper Sandstone	1×10^{-13}	0.20	0.59	3.1	830	2,700
Host rock Shale	1×10^{-19}	0.20	0.11	1.2	830	2,700
Silty Shale	1×10^{-17}	0.20	0.11	1.4	830	2,700
Limestone	1×10^{-14}	0.10	0.04	2.6	830	2,700
Lower Shale	1×10^{-20}	0.10	0.04	1.2	830	2,700
Lower Sandstone	1×10^{-13}	0.20	0.59	3.1	830	2,700
Buffer	1×10^{-20}	0.35	0.23	1.5	830	2,700
Waste Package	1×10^{-16}	0.50	1	16.7	466	5,000

Source: Mariner et al. 2017.

Figure 3-2 shows an *x*–*y* (horizontal) slice through the repository colored by material: shale host rock (blue), disturbed rock zone (DRZ; tan), buffer/backfill (orange), and waste package (red). The south face of the model domain shown in this figure represents the reflection boundary. Two vertical shafts, one at either end of the southern-most hall, are gridded; they are about 1,280 m long. The half-symmetry model consists of 42 drifts and 50 waste packages per drift (2,100 waste packages).

In simulations both with and without an in-package criticality event, waste package breach occurs at 9,000 years simulation time, at which point the waste form is exposed to water in the drift. Radionuclide inventories in the solid waste form as a function of time are read in externally through the PFLOTRAN criticality submodule (see below), and these inventories differ depending on whether a criticality event occurred. In the steady-state criticality case, the criticality event for each waste package is concurrent with when it is breached.

Aqueous radionuclide concentration is tracked after waste package breach with consideration for solubility limits, adsorption, and decay/ingrowth. Adsorption is modeled in PFLOTRAN using a linear isotherm; the sorption distribution coefficient (K_d) characterizes the distribution of the solute between the adsorbed phase and the aqueous dissolved phase. Decay and ingrowth in the aqueous phase are calculated using a three-generation analytical solution (Mariner et al. 2016) through the Used Fuel Disposition (UFD) Decay process model in PFLOTRAN. Parameters are listed in Table 3-2; parameter selection and model implementation are consistent with the shale reference case outlined in Mariner et al. (2017). One of the material properties included in the PFLOTRAN input is SOIL COMPRESSIBILITY, which calculates porosity as a function of the compressibility of the soil matrix, pressure, and reference porosity.

Implementation of the criticality submodule within the PFLOTRAN simulations also included the capability to specify a steady-state heat from a criticality event for a specified period of time, and the capability to change the radionuclide inventory at a specified time. Setting up the simulation input deck required the use of several keywords such as CRITICALITY_MECH, which specifies the use of the submodule within the WASTE_FORM_GENERAL block. This CRITICALITY_MECH submodule requires the specification of several cards such as the NAME associated with the mechanism; CRIT_START, which specifies the start of the criticality event; CRIT_END, which specifies the end of the criticality event; HEAT_OF_CRITICALITY card with CONSTANT_POWER option that specifies the 0.4d-3 MW (0.4 kW) criticality source term used for the simulation; DECAY_HEAT TOTAL card used along with the DATASET option to read an existing dataset for the decay heat; and an INVENTORY card used along with the DATASET option to read in the an existing file. Other modifications occurred within the WASTE_FORM submodule and included the addition of keyword CANISTER_BREACH_TIME, which is set to 9,000 years for all waste forms both in the simulation with and without the occurrence of steady-state criticality events. The simulation was set up to run in PFLOTRAN's GENERAL mode, which involves two-phase liquid water and gas flow coupled to the reactive transport mode.

The original Mariner et al. (2017) simulation used DPCs containing 12 pressurized water reactor (PWR) assemblies; the simulation set up for this study used DPCs containing 37 PWR assemblies as in Price et al. (2019a,b). The radionuclide inventory for both the simulations including steady-state criticality and those not including criticality is the same as that reported in Price et al. (2019b).

An illitization model of the buffer (Section 4.2.2 and Section 4.3.2) was included within the PFLOTRAN input deck for all simulations. With the use of this model, smectite is transformed into illite, resulting in an increase in buffer permeability. In addition, a model of anisotropic temperature-dependent thermal conductivity, as described in Section 3.3, was implemented in all simulations.

The study team used PFLOTRAN to run various preliminary simulations with differing levels of complexity. The two final simulations consisted of the base case and the steady-state criticality case. Simulations were run using 1,024 cores on high performance computers. The steady-state criticality case took 10.8 hours to complete while the base case took 8.9 hours. Results of these simulations are presented in Section 5.

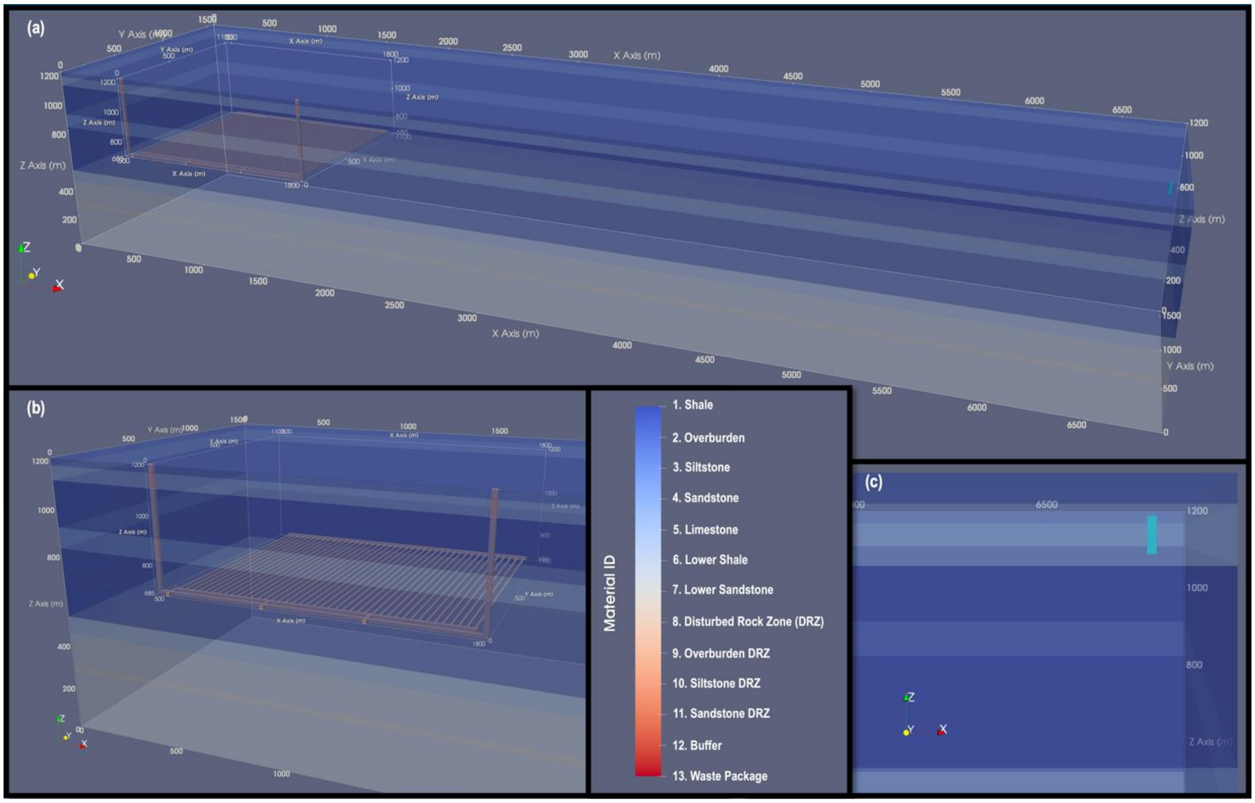

NOTE: The well is represented by the teal box on the right in (a) and (c).

Figure 3-1. Transparent Views of the Model Domain Colored by Material for (a) Full Model Domain, (b) Zoom in on Repository, and (c) Zoom in at the Well

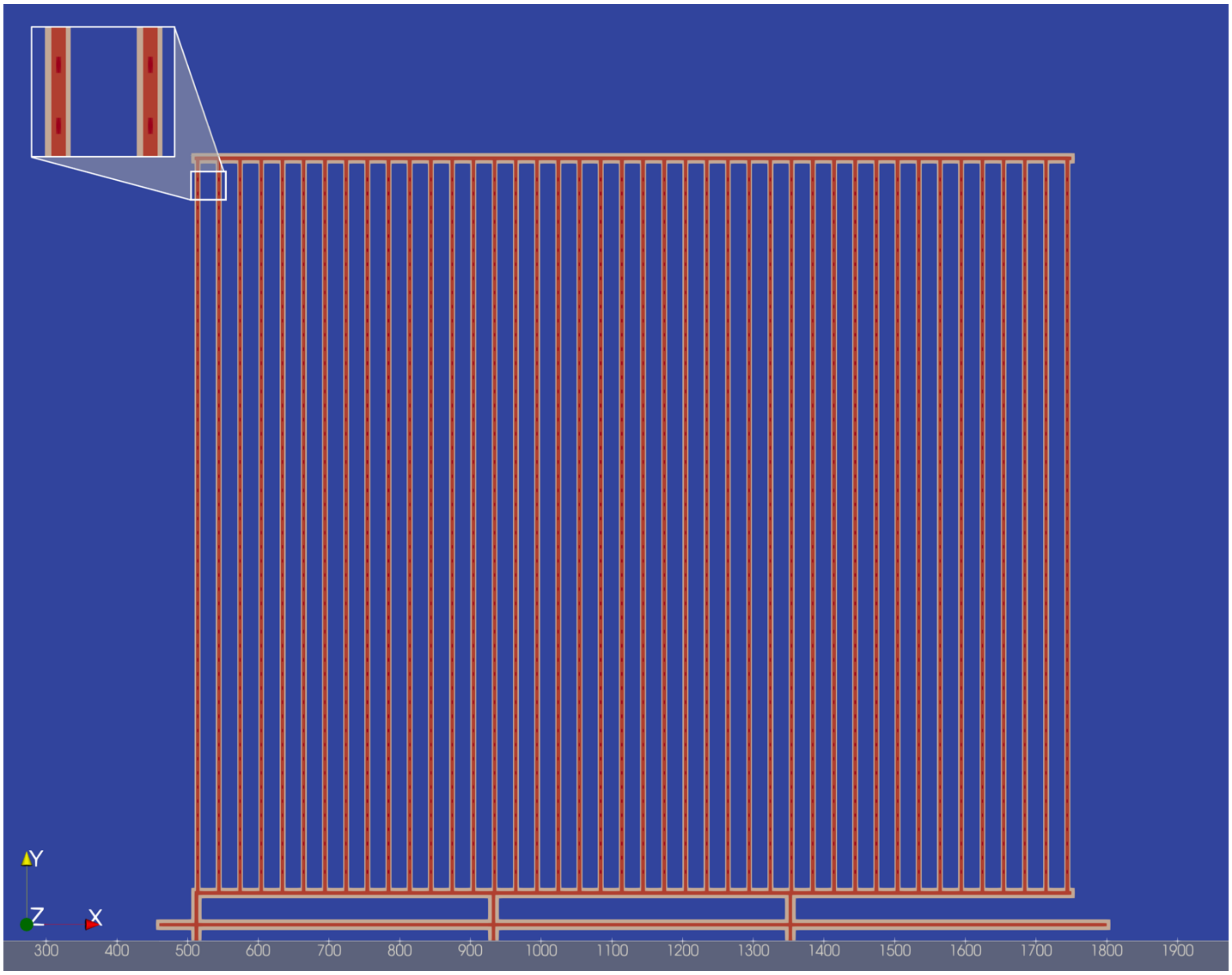

NOTE: Inset zoom on top left corner shows a close-up of four waste packages.

Figure 3-2. Horizontal (*x–y*) Slice through the Repository Colored by Material: Shale Host Rock (blue), DRZ (tan), Buffer/Backfill (orange), and Waste Package (red)

Table 3-2. Inputs to PFLOTRAN for Each Element

Element	Solubility (M)	K_d in Backfill (kg/m^3)	K_d in DRZ and Shale (kg/m^3)	K_d in Aquifer (kg/m^3)
Am	4×10^{-7}	2.1×10^{7}	1.08×10^{8}	2.17×10^{5}
Pu	2×10^{-7}	1.76×10^{6}	1.94×10^{6}	1.09×10^{6}
Np	4×10^{-9}	1.76×10^{6}	1.94×10^{6}	3.44×10^{4}
U	7×10^{-7}	1.76×10^{8}	1.73×10^{3}	1.88×10^{3}
Th	6×10^{-7}	5.27×10^{6}	1.73×10^{7}	6.43×10^{6}
I	Infinitely soluble	Nonsorbing	Nonsorbing	Nonsorbing
Cs	Infinitely soluble	6.67×10^{5}	8.64×10^{5}	1.22×10^{6}
Sr	Infinitely soluble	Nonsorbing	Nonsorbing	Nonsorbing

NOTE: DRZ = disturbed rock zone.

See Mariner et al. (2017) for more detail on parameter values, and PFLOTRAN User's Guide (Lichtner et al. 2020a; http://documentation.plotran.org) for process model implementation.

Source: Mariner et al. 2017.

3.2.2 Description of Hypothetical Unsaturated Alluvial Model

The model domain includes a single waste package positioned in a backfilled emplacement drift (tunnel) in a repository situated in unsaturated alluvium at a depth of 250 m. The waste package and drift are both approximated as having square cross sections rather than the circular cross sections described for the reference case in Mariner et al. (2018). For this analysis, the cross sections are 1.67 × 1.67 m for the waste package and 4 × 4 m for the emplacement drift. The centerline-to-centerline drift spacing is 40 m. The waste packages are 5 m long with centers spaced at 40 m along the drift. The drift and waste package volumes are consistent with the Geologic Disposal Safety Assessment unsaturated zone reference case design (Sevougian et al. 2019, Table 4.1; Hardin and Kalinina 2016). By symmetry, only one quarter of the waste package and 20 m of the drift are modeled. In addition to the waste package internals, a shell/overpack with thickness of 0.1 m (assumed for ease of gridding) is included in the mesh. The model domain extends from the land surface to the water table in the vertical direction. Figure 3-3 shows detail from a portion of the computational mesh in the vicinity of the waste package and drift.

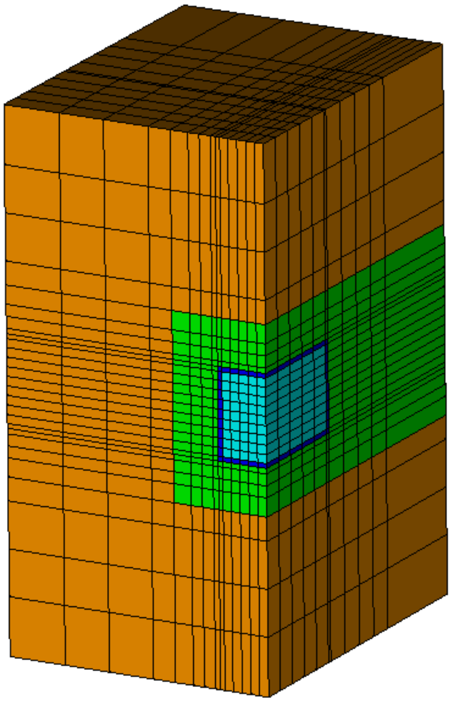

NOTE: This three-dimensional (3D) perspective is cut through the drift centerline and waste package midpoint and thus shows only one-quarter of the waste package. Green = backfilled drift, brown = host formation, light blue = waste package internals, and dark blue = waste package shell.

Figure 3-3. Cut Through of the Computational Domain Showing a 6 × 6 × 12 m Detail of the Mesh

In the reference case, the alluvium host medium for the repository is assumed to have a dry thermal conductivity of 1.0 W/(m·K) and a wet thermal conductivity of 2.0 W/(m·K). Backfill material is assumed to have the same thermal properties as the alluvium but with higher permeability (10^{-14} m^2 for the host medium versus 10^{-13} m^2 for the backfill). The internals of the waste package are assumed to have the same moisture retention properties as the backfill material. This assumption is conservative because it prevents the formation of a capillary barrier once the waste package fails. The waste package outer shell is assigned a very low permeability to prevent water from flowing through it.

The simulations were initially spun up without the repository. Repository closure is assumed at t = 0 using results from the spin-up phase as initial conditions, but with waste package internals, shell, and drift backfill in place. The DPCs are assumed to contain 37 PWR assemblies from a reactor that was shutdown prior to 2000. Decay heat in the DPC as calculated by ORIGEN (Croff 1983) produces about 4 kW at the time of repository closure (assumed to be in 2100), but the value is only 249 W at 9,000 years postclosure, the assumed time of waste package breach in this work.

3.3 Thermal Conductivity

The heat generated by postclosure criticality and the heat from radioactive decay could result in significant perturbation to the local temperature field. It is important to capture the capacity for the repository host-rock system to dissipate this heat. This heat can also affect, potentially irreversibly, the temperature-dependent material and geochemical properties of the natural and engineered barriers that are part of the repository system. For example, as presented in Section 4.2, the heat emission from a criticality event in the canister is liable to affect the properties of the surrounding buffer, which could directly affect the performance in the repository. Because of the importance of the thermal effects of a postclosure criticality event on modeling repository performance, PFLOTRAN was modified to account for the temperature dependence of a material's thermal conductivity. The mathematical basis for this modification, along with how the model was developed and implemented, is described below.

3.3.1 Thermal Characteristic Curves

New developments in thermal modeling were driven by a desire to broaden insight into postclosure criticality consequences by accommodating several phenomena affecting the dynamic temperature field between multiple emplacements of hot waste packages. These developments take a generalized form in thermal characteristic curves (TCCs), which are extendable classes of thermal conductivity relationships relating state variables like temperature or water saturation to thermal conductivity.

PFLOTRAN now includes saturation- and temperature-dependent thermal conductivity by way of TCCs. This functionality was added to impart higher modeling fidelity for scenarios in which significant thermal loading can lead to localized temperature anomalies in a repository. Heat dissipation is linked to the overall thermal conductivity, which can vary locally if there is significant local contrast in the temperature field and strong temperature dependence.

The previous implementation of thermal conductivity (κ_T) for use with PFLOTRAN nonisothermal flow modes involved using wet ($\kappa_\mathrm{T}^\mathrm{wet}$) and dry ($\kappa_\mathrm{T}^\mathrm{dry}$) endpoint conductivity values in a function with saturation (S_l) from Somerton et al. (1974) as shown in Equation 3-1. In the context of the current version, this equation is still used as the default (*D*) for effective thermal conductivity.

$$\kappa_T^D(S_l) = \kappa_T^{dry} + \sqrt{S_l}\left(\kappa_T^{wet} - \kappa_T^{dry}\right) \qquad \textit{Equation 3-1}$$

In TH mode, there is also an option to specify a frozen thermal conductivity ($\kappa_\mathrm{T}^\mathrm{fr}$) and related exponents (α and α_fr) for use in the freezing submode. As shown in Equation 3-2, the liquid saturation and ice saturation (S_{ice}) are used to evaluate the effective thermal conductivity in a partially unsaturated frozen medium, where ε is a small number employed for numerical stability when calculating derivatives (Painter 2011).

$$\begin{aligned}\kappa_T(S_l, S_{ice}) = \kappa_T^{wet}(S_l + \epsilon)^\alpha + \kappa_T^{fr}(S_{ice} + \epsilon)^{\alpha_{fr}} \\ + \kappa_T^{dry}[1 - (S_l + \epsilon)^\alpha - (S_{ice} + \epsilon)^{\alpha_{fr}}]\end{aligned} \qquad \textit{Equation 3-2}$$

In the previous version of the code for a given problem thermal conductivity, parameters were specified by material property along with heat capacity and density, but there were no additional parameters to determine temperature dependence. The new implementation creates flexibility to parameterize thermal conductivity as a function of other state variables like temperature. Regardless, the effective thermal conductivity between two cells is applied at cell interfaces by computing a harmonically averaged thermal conductivity between the two cells. This average value is then used with the temperature difference between cells to evaluate the heat flux and, depending on the phases involved, the derivative of energies with respect to temperature and saturation.

In the new TCC feature, the standard function types employed to evaluate κ_T are shown in Table 3-3. In most cases, a call to a temperature-dependent thermal conductivity function results in the evaluation of Equation 3-1 to determine saturation dependence and then calculation of a temperature-dependent function using that result. The only exceptions are the constant TCC (Equation 3-3), which is neither saturation nor temperature dependent, and the frozen TCC, which has modified saturation dependence.

The linear resistivity TCC (Equation 3-4) assumes that the reciprocal of thermal conductivity can be modeled as a linear function with temperature. This form was suggested by Birch and Clark (1940) and fitted empirically by Blesch et al. (1983) for granite, basalt, shale, and salt. The latter study was a far-field thermal analysis intended to evaluate the environmental impact based on temperature changes in various regions. In the linear resistivity function, a_1 is the resistivity shift parameter and a_2 is the scaling factor with the change in temperature. The temperature change is defined with respect to a reference temperature (T_{ref}), such that when $T_{ref} = 0$°C, κ_T^{dry} and κ_T^{wet} are assumed to be evaluated at 0°C as well.

The cubic polynomial TCC (Equation 3-5) adds three orders of temperature dependence to κ_T and includes a reference temperature (T_{ref}) with a default of 0°C. This polynomial form was used by Flynn and Watson (1969) to evaluate effective thermal conductivity in soils reaching temperatures up to 1,700°C. This study was conducted in the context of reentry and earth-impact scenarios for space vehicles containing radioisotopes, and the soils that were sampled included limestone, granitic detritus, sand, and others within a particle diameter of 1.7 mm. The order of polynomial was chosen to reduce the residuals in a least-squares fit of test data. Third-order least squares polynomial fits were also used to describe effective thermal conductivities for boiling water reactor (BWR) and PWR assemblies in Yucca Mountain studies (TRW Environmental Safety Systems 1996). A cubic polynomial can be applied to rock and buffer regions near a waste form susceptible to being affected by high temperature transients, or perhaps to regions intended to model SNF assemblies. Laboratory analyses of salt samples from Waste Isolation Pilot Plant (WIPP) showed strong temperature dependence of thermal conductivity with an applied heat flux (Kuhlman et al. 2020). The κ_T values decreased with temperature and appeared to conform to a cubic polynomial.

A power law TCC (Equation 3-6) employs an exponent (γ) and a reference temperature (T_{ref}). The default reference temperature is defined as absolute zero, or −273.15°C, which implies κ_T^{dry} and κ_T^{wet} values being evaluated at 26.85°C. The temperature change is normalized by 300 K and then raised to the exponent γ. This type of model is relevant to studies of crystals, ceramics, and engineering materials, and can be useful in characterizing heat transfer through the SNF, canister, and overpack.

Table 3-3. The Standard TCC Options in PFLOTRAN

Name	Application	Function	
Constant	Nonporous media not subject to strong temperature gradients Sensitivity studies	$\kappa_T = \kappa_T^C$	*Equation 3-3*
Default	All soils not subject to strong temperature gradients	$\kappa_T^D(S_l) = \kappa_T^{dry} + \sqrt{S_l}\left(\kappa_T^{wet} - \kappa_T^{dry}\right)$	*Equation 3-1* (repeat)
Linear Resistivity	Host rock in far-field thermal analyses such as granite, basalt, and shale	$\kappa_T(S_l,T) = \dfrac{\kappa_T^D(S_l)}{a_1 + a_2\left(T - T_{ref}\right)}$	*Equation 3-4*
Cubic Polynomial	Elevated soil temperatures (e.g., high temperature transients, ground impact scenarios) Backfilled SNF assemblies WIPP salt	$\kappa_T(S_l,T) = \kappa_T^D(S_l) \cdot \left[1 + \beta_1\left(T - T_{ref}\right) + \beta_2\left(T - T_{ref}\right)^2 + \beta_3\left(T - T_{ref}\right)^3\right]$	*Equation 3-5*
Power Law	Crystals, ceramics, and engineering materials (e.g., overpack, neutron absorbers)	$\kappa_T(S_l,T) = \kappa_T^D(S_l)\left(\dfrac{T - T_{ref}}{300}\right)^{\gamma}$	*Equation 3-6*
Frozen	Permafrost modeling	$\kappa_T(S_l,S_{ice}) = \kappa_T^{wet}(S_l + \epsilon)^{\alpha} + \kappa_T^{fr}(S_{ice} + \epsilon)^{\alpha_{fr}} + \kappa_T^{dry}\left[1 - (S_l + \epsilon)^{\alpha} - (S_{ice} + \epsilon)^{\alpha_{fr}}\right]$	*Equation 3-2* (repeat)

NOTE: The term $\kappa_T^D(S_l)$ is given by Equation 3-1 above. It is shown in red in that equation as well as the three other equations in which it appears.

SNF = spent nuclear fuel

WIPP = Waste Isolation Pilot Plant

For backwards compatibility, a frozen TCC is defined that uses the functional forms for effective thermal conductivity in TH/TH-TS mode (Equation 3-2). It is a derived type of the default TCC but utilizes an additional procedure for frozen thermal conductivity to account for ice saturation dependence. The model requires the dry and wet thermal conductivity and the exponent of the soil Kersten number (α), which is defined in the base class for use by all curves (initialized as 1.0) to give the user control over flux behavior in TH/TH-TS mode. Frozen soil analysis requires definition of the frozen soil Kersten number exponent (α_{fr}), the frozen thermal conductivity (κ_T^{fr}), and the name of the freezing model (provided in the documentation, Lichtner et al. 2020a). The freezing analysis is restricted to TH/TH-TS mode, and when freezing is active, only TCCs of the frozen type are allowed. When freezing is inactive in TH/TH-TS mode, or when the frozen curve is used outside of TH/TH-TS modes, only the dry and wet components of the equation are used.

Altogether, the TCC feature was implemented with a new source code file that contained all variables and subroutines used to process TCC-related user input, evaluate effective thermal conductivity, and provide error messages. A list of inputs for the deployed TCCs is shown in Table 3-4. The user can activate the TEST feature to print out a table of evaluated effective thermal conductivity values, along with $\frac{d\kappa_T}{dT}$ and $\frac{d\kappa_T}{dS_l}$, for a list of temperature and saturation coordinates. (Entries for ice saturation and $\frac{d\kappa_T}{dS_{ice}}$ are provided for the frozen curve.)

Table 3-4. User Inputs for the Standard TCCs

User Input	Value(s)	Applicability
THERMAL_CHARACTERISTIC_CURVES	<name>	All
THERMAL_CONDUCTIVITY_FUNCTION	<TCC type>	All
THERMAL_CONDUCTIVITY_CONSTANT	κ_T^C	CONSTANT
THERMAL_CONDUCTIVITY_DRY	κ_T^{dry}	DEFAULT and below
THERMAL_CONDUCTIVITY_WET	κ_T^{wet}	
THERMAL_CONDUCTIVITY_FROZEN	κ_T^{fr}	FROZEN (TH mode only)
KERSTEN_EXPONENT_FROZEN	α_{fr}	
ICE_MODEL	<model>	
KERSTEN_EXPONENT	α	FROZEN
REFERENCE_TEMPERATURE	T_{ref}	LINEAR_RESISTIVITY and below
LINEAR_RESISTIVITY_COEFFICIENTS	$[a_1, a_2]$	LINEAR_RESISTIVITY
CUBIC_POLYNOMIAL_COEFFICIENTS	$[\beta_1, \beta_2, \beta_3]$	CUBIC_POLYNOMIAL
EXPONENT	γ	POWER
END		
TEST		All
END		

To preserve backwards compatibility with PFLOTRAN v2, when the input format specifies κ_T^{dry} and κ_T^{wet} by material, a default TCC (Equation 3-1) is created and tied to these parameters. For frozen thermal conductivity in TH mode, κ_T^{fr}, α_{fr}, and α are tied to a frozen curve. The legacy input format cannot be combined with the usage of TCCs in a given input file. Verification of basic TCC functionality is provided in Appendix B. When coupled to a temperature-dependent criticality heat source, temperature-dependent thermal conductivity will be an important mechanism for modulating the power output from a criticality event. Now that PFLOTRAN contains a flexibly structured implementation of TCCs, specialized functional forms can be added in a straightforward manner to meet the needs of process modelers studying different repository concepts.

3.3.2 Thermal Conductivity Anisotropy

The TCC feature accommodates directional dependence via optional anisotropy ratios. An anisotropy tensor may be specified for a TCC to modify dry and wet thermal conductivity values depending on the direction traversed in the material. This is intended to be useful for characterizing layered repository strata with different conductivity behavior, for example, in the *x*- and *y*-directions compared to the *z*-direction.

In addition, there is a new “composite” TCC that allows for conductivity along certain axes to be governed by separate models altogether. This flexibility accommodates the special thermal conductivity characteristics of packages containing SNF, such as DPCs, for which different models are applied for the axial and radial directions to account for the lattice characteristics of the assemblies.

3.3.2.1 Model Development

Thermal conductivity is defined as a symmetric tensor **K** with six unique components κ_{ij} and unit vectors $\hat{n}_i$, as shown in Equation 3-7.

$$\mathbf{K} = \begin{bmatrix} \kappa_{xx} & \kappa_{xy} & \kappa_{xz} \\ \kappa_{xy} & \kappa_{yy} & \kappa_{yz} \\ \kappa_{xz} & \kappa_{yz} & \kappa_{zz} \end{bmatrix} \qquad \textit{Equation 3-7}$$

The thermal conductivity tensor relates the heat flux ($\vec{q}$) to the temperature gradient (∇T or $\vec{\theta}$) via Fourier’s Law (Equation 3-8). Therefore, the component κ_{xz} would characterize the heat flux induced in the *x*-direction from the temperature gradient measured in the orthogonal *z*-direction.

$$\vec{q} = -\mathbf{K}\cdot\nabla \mathrm{T} = -\mathbf{K}\cdot\left(\frac{\partial T}{\partial x}\hat{n}_x + \frac{\partial T}{\partial y}\hat{n}_y + \frac{\partial T}{\partial z}\hat{n}_z\right) = -\mathbf{K}\cdot\left(\theta_x\hat{n}_x + \theta_y\hat{n}_y + \theta_z\hat{n}_z\right) = -\mathbf{K}\cdot\vec{\theta} \qquad \textit{Equation 3-8}$$

The directional thermal conductivity (κ_θ) is defined as the value of thermal conductivity in the direction of the gradient ($\hat{\theta}$), as shown in Equation 3-9.

$$\kappa_\theta = \frac{\left|\vec{q}\cdot\hat{\theta}\right|}{\left|\vec{\theta}\right|} = \frac{1}{\left|\vec{\theta}\right|}\cdot\frac{\vec{q}\cdot\vec{\theta}}{\left|\vec{\theta}\right|} \qquad \textit{Equation 3-9}$$

The heat flux is expanded in terms of the direction cosines in Equation 3-10, where $\phi_{\theta i}$ is the angle between $\vec{\theta}$ and $\hat{n}_i$ (where i = {x,y,z}, as exemplified in Figure 3-4) and $\left|\vec{\theta}\right|$ is the magnitude of the temperature gradient.

$$\vec{q} = -\begin{bmatrix} \kappa_{xx} & \kappa_{xy} & \kappa_{xz} \\ \kappa_{xy} & \kappa_{yy} & \kappa_{yz} \\ \kappa_{xz} & \kappa_{yz} & \kappa_{zz} \end{bmatrix} \cdot \begin{bmatrix} |\vec{\theta}| \cos\phi_{\theta x} \\ |\vec{\theta}| \cos\phi_{\theta y} \\ |\vec{\theta}| \cos\phi_{\theta z} \end{bmatrix} \qquad \textit{Equation 3-10}$$

The result of the dot product in Equation 3-10 is shown in Equation 3-11.

$$\begin{aligned} \vec{q} = &-\left(\kappa_{xx}|\vec{\theta}| \cos\phi_{\theta x} + \kappa_{xy}|\vec{\theta}| \cos\phi_{\theta y} + \kappa_{xz}|\vec{\theta}| \cos\phi_{\theta z}\right)\hat{n}_x \\ &- \left(\kappa_{xy}|\vec{\theta}| \cos\phi_{\theta x} + \kappa_{yy}|\vec{\theta}| \cos\phi_{\theta y} + \kappa_{yz}|\vec{\theta}| \cos\phi_{\theta z}\right)\hat{n}_y \\ &- \left(\kappa_{xz}|\vec{\theta}| \cos\phi_{\theta x} + \kappa_{yz}|\vec{\theta}| \cos\phi_{\theta y} + \kappa_{zz}|\vec{\theta}| \cos\phi_{\theta z}\right)\hat{n}_z \end{aligned} \qquad \textit{Equation 3-11}$$

The dot product of the heat flux and the temperature gradient is shown in Equation 3-12. When that result is applied to Equation 3-9, the directional conductivity is shown in Equation 3-13.

$$\begin{aligned} \vec{q} \cdot \vec{\theta} = &-\Big[\kappa_{xx}\left(|\vec{\theta}| \cos\phi_{\theta x}\right)^2 + \kappa_{xy}|\vec{\theta}|^2 \cos\phi_{\theta y} \cos\phi_{\theta x} \\ &+ \kappa_{xz}|\vec{\theta}|^2 \cos\phi_{\theta z} \cos\phi_{\theta x}\Big] \\ &- \Big[\kappa_{xy}|\vec{\theta}|^2 \cos\phi_{\theta x} \cos\phi_{\theta y} + \kappa_{yy}\left(|\vec{\theta}| \cos\phi_{\theta y}\right)^2 \\ &+ \kappa_{yz}|\vec{\theta}|^2 \cos\phi_{\theta z} \cos\phi_{\theta y}\Big] \\ &- \Big[\kappa_{xz}|\vec{\theta}|^2 \cos\phi_{\theta x} \cos\phi_{\theta z} + \kappa_{yz}|\vec{\theta}|^2 \cos\phi_{\theta y} \cos\phi_{\theta z} \\ &+ \kappa_{zz}\left(|\vec{\theta}| \cos\phi_{\theta z}\right)^2\Big] \end{aligned} \qquad \textit{Equation 3-12}$$

$$\begin{aligned} \kappa_\theta = \ &\kappa_{xx}(\cos\phi_{\theta x})^2 + \kappa_{yy}\left(\cos\phi_{\theta y}\right)^2 + \kappa_{zz}(\cos\phi_{\theta z})^2 + 2\kappa_{xy} \cos\phi_{\theta x} \cos\phi_{\theta y} \\ &+ 2\kappa_{xz} \cos\phi_{\theta x} \cos\phi_{\theta z} + 2\kappa_{yz} \cos\phi_{\theta y} \cos\phi_{\theta z} \end{aligned} \qquad \textit{Equation 3-13}$$

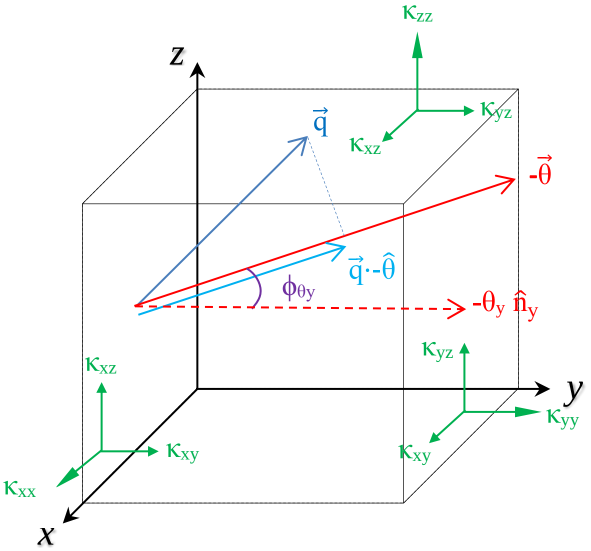

Figure 3-4. Diagram of a Possible Heat Flux and Temperature Gradient Alignment along with Thermal Conductivity Tensor Components

In PFLOTRAN, given a cartesian grid system, the upwind and downwind cell faces are normal to some unit vector in the *x*-, *y*-, or *z*-direction. Therefore, in such a discretization, the gradient is defined using the temperature difference across the cell and the distance, so it must be aligned with the unit vector traversing the two opposite cellular faces. For example, when the cell is traversed by $\hat{n}_x$, $\cos\phi_{\theta x} = 1$ while $\cos\phi_{\theta y} = \cos\phi_{\theta z} = 0$, which cancels the terms with the off-diagonal tensor components. Only when the principal axes of the thermal conductivity tensor are misaligned with the cartesian grid, or else when a polyhedral grid or flexed hex mesh is used, can multiple direction cosines be nonzero and allow the off-diagonal components to be usable. If the grid is always oriented along the principal axes of conductivity, the off-diagonal elements will be zero.

The eigenvectors (Λ_1, Λ_2, Λ_3) of Equation 3-7 yield the principal axes of the heat flux and the associated eigenvalues (λ_1, λ_2, λ_3) represent the extreme values. Since the tensor is symmetric, if the unit vectors $\hat{n}_i$ are rotated to align with Λ_i, **K** can be represented as a diagonal matrix in λ_i with basis Λ_i, as shown in Equation 3-14. If only diagonal components are specified by the user, those components are the eigenvalues, and the eigenvectors are the original unit vectors in *x*, *y*, and *z*. Therefore, it is acceptable to specify anisotropy ratios of one since the extreme values will always be the user-specified wet and dry values. However, the eigenvalues for a full tensor may result in extreme values exceeding the user-specified values of κ_T. Furthermore, the tensor must be positive semidefinite (Powers 2004). Therefore, the user must choose anisotropy ratios such that $\lambda_i \geq 0$ and $\lambda_i \leq \kappa_T$ (wet or dry).

$$\mathbf{K}' = \begin{bmatrix} \lambda_1 & 0 & 0 \\ 0 & \lambda_2 & 0 \\ 0 & 0 & \lambda_3 \end{bmatrix}$$

Equation 3-14

3.3.2.2 Anisotropy Implementation

The anisotropy routines are triggered when the user specifies anisotropy ratios (f_{ij}) in the input deck for the default TCC or its temperature-dependent, derived types, as shown Table 3-5. Currently, κ_T^{dry} and κ_T^{wet} are still specified as usual, and as of the writing of this report, the user cannot specify wet and dry anisotropic components in a piecemeal manner. Rather, ratios are used to modify both wet and dry values when the tensor operations are called. The upwind and downwind thermal conductivities are modified by these tensor operations right before the effective thermal conductivity functions are called to evaluate average dry and wet thermal conductivities.

To ensure that previous regression tests with isotropic thermal conductivity are unperturbed, the anisotropy routines check if the user has inadvertently specified a diagonal, isotropic tensor. If that is true, the tensor operations are skipped to maintain the previous computational speed, as mathematically, the tensor operation would not affect the upwind/downwind values of κ_T. If the user specifies one off-diagonal component, they are required to initialize the other two components as well. If no off-diagonal components are initialized, they are set to zero. All diagonal components must be initialized, and if no components are specified at all, the previous functionality with isotropic thermal conductivities is not affected. When a user specifies a full tensor, the eigenvalues are checked to ensure that the tensor is positive semi-definite. There is also a warning if eigenvalues may cause the user input thermal conductivity values to be exceeded along the tensor's principal axes. The new anisotropy feature is evaluated in detail in Appendix B.

Table 3-5. User Inputs for Thermal Conductivity Anisotropy

User Input	Value	Applicability and Implementation
THERMAL_CHARACTERISTIC_CURVES	<name>	
THERMAL_CONDUCTIVITY_FUNCTION	<func>	DEFAULT and derived types
THERMAL_CONDUCTIVITY_DRY	κ_T^{dry}	Instance modified after tensor operation
THERMAL_CONDUCTIVITY_WET	κ_T^{wet}	Instance modified after tensor operation
ANISOTROPY_RATIO_X	f_{xx}	$\kappa_{xx}^{dry}=f_{xx}\kappa_T^{dry}$, $\kappa_{xx}^{wet}=f_{xx}\kappa_T^{wet}$
ANISOTROPY_RATIO_Y	f_{yy}	$\kappa_{yy}^{dry}=f_{yy}\kappa_T^{dry}$, $\kappa_{yy}^{wet}=f_{yy}\kappa_T^{wet}$
ANISOTROPY_RATIO_Z	f_{zz}	$\kappa_{zz}^{dry}=f_{zz}\kappa_T^{dry}$, $\kappa_{zz}^{wet}=f_{zz}\kappa_T^{wet}$
ANISOTROPY_RATIO_XY	f_{xy}	$\kappa_{xy}^{dry}=f_{xy}\kappa_T^{dry}$, $\kappa_{xy}^{wet}=f_{xy}\kappa_T^{wet}$
ANISOTROPY_RATIO_XZ	f_{xz}	$\kappa_{xz}^{dry}=f_{xz}\kappa_T^{dry}$, $\kappa_{xz}^{wet}=f_{xz}\kappa_T^{wet}$
ANISOTROPY_RATIO_YZ	f_{yz}	$\kappa_{yz}^{dry}=f_{yz}\kappa_T^{dry}$, $\kappa_{yz}^{wet}=f_{yz}\kappa_T^{wet}$
END		
TEST		DEFAULT and derived types
END		

3.3.2.3 *Composite Curve*

A composite curve has been defined that applies previously defined TCCs along specific principal axes. This development was motivated by the need to incorporate different models for the transverse and axial extents of a DPC for criticality studies. The composite TCC uses scaling parameters derived from the unit vectors of the gridded domain, which in turn modify and sum the results of the constituent functions. The composite TCC is specified in the input deck downstream of the constituent functions according to Table 3-6. The test feature has not been implemented for this curve due to directional dependence.

For example, if "cct_radial" and "cct_axial" are defined upstream in the input deck, the first can be applied in the *x*- and *y*-directions and the second along the *z*-direction in a composite TCC named "dpc_1". When the TCC for “dpc_1” is called, a weighted average of all directional thermal conductivities is given depending on the unit vector involved, preserving all temperature and saturation dependencies of the constituent functions.

The anisotropy ratio capability does not conflict and can also be used with the composite TCC if such a level of detail is desired. It is recommended that the constituent curves do not have anisotropy ratios of their own to avoid a nonphysical result.

Table 3-6. User Inputs for a Composite TCC

User Input	Value	Applicability and Implementation
THERMAL_CHARACTERISTIC_CURVES	<name>	
THERMAL_CONDUCTIVITY_FUNCTION	<func>	COMPOSITE
COMPOSITE_X	<name>	A previously defined TCC applied along the *x*-axis
COMPOSITE_Y	<name>	A previously defined TCC applied along the *y*-axis
COMPOSITE_Z	<name>	A previously defined TCC applied along the *z*-axis
END		
END		

3.3.3 Special Thermal Conductivity Models

Thermal models have been developed for the radial and axial extents of a DPC, as discussed in Nole et al. (2021). The radial model κ_T^{radial} uses the format of the default TCC but represents the dry and wet components with special functions. The dry conductivity is represented with a temperature-dependent power law derived from backfilled assembly measurements (TRW Environmental Safety Systems 1996). This model assumes that thermal radiation controls heat transfer in a dry assembly and that thermal conductivity may be represented with a power law using a temperature coefficient (α_0), an exponent (α_1), and a scaling factor ($\kappa_{T,0}^{dry}$), as shown in Equation 3-15.

$$\kappa_T^{dry}(T) = \kappa_{T,0}^{dry} + \alpha_0 T^{\alpha_1} \qquad \text{Equation 3-15}$$

Over time, canisters may be susceptible to failure allowing for the influx of water, which can flood the assemblies. The model for κ_T^{wet} is derived from a model on the effective thermal conductivity of an array of cylinders surrounded by stagnant water (Cheng and Hsu 1999). Such an analysis could apply to the transverse direction across assemblies in a DPC when this reference model is modified to account for their square cross sections. The parameter κ_T^{wet} can be estimated from the thermal conductivity of flooding groundwater ($\kappa_T^{H_2O}$), the thermal conductivity of solid components like the fuel pins (κ_T^S), and the porosity of the assembly (ϕ), as shown in Equation 3-16.

$$\kappa_T^{wet}(\phi) = \kappa_T^{H_2O}\left[1 - \sqrt{1-\phi} + \frac{\sqrt{1-\phi}}{1 + \left(\frac{\kappa_T^{H_2O}}{\kappa_T^S} - 1\right)\sqrt{1-\phi}}\right] \qquad \textit{Equation 3-16}$$

The dry and wet components are then combined into the default-type analysis to describe the radial thermal conductivity of a DPC, as shown in Equation 3-1.

$$\kappa_T^{radial}(S_l, T, \phi) = \kappa_T^{dry}(T) + \sqrt{S_l}\left[\kappa_T^{wet}(\phi) - \kappa_T^{dry}(T)\right] \qquad \textit{Equation 3-17}$$

A related function assumes parallel heat conduction of solid assembly components and water along the *axial* extent of a DPC. The assembly porosity is used to separate solid and water components of thermal conductivity, where the water component is multiplied by the liquid saturation. This approach assumes that the thermal conductivity component of air, which comprises the volume fraction $\phi(1 - S_l)$, is negligibly small. Therefore, the model is only dependent on liquid saturation and ϕ, as shown in Equation 3-18.

$$\kappa_T^{axial}(S_l, \phi) = (1-\phi)\kappa_T^S + \phi\kappa_T^{H_2O} S_l \qquad \textit{Equation 3-18}$$

The models are defined in the input deck according to Table 3-7. In general, they require specification of the thermal conductivities for water and the assembly solids as well as the assembly porosity. The radial function requires additional input of the dry-state temperature coefficient and exponent as well as the reference value of dry thermal conductivity. The user may also use Equation 3-15 or Equation 3-16 independently as standalone functions by specifying those individual TCCs and optionally including constant κ_T^{wet} or κ_T^{dry}, respectively, to impart saturation dependence via the default relationship.

As mentioned in Section 3.3.2, directional variation in a waste form containing SNF can be simulated by incorporating the axial and radial models into a composite TCC. The subfunctions for this TCC would be specified depending on the orientation of the waste form centerline with respect to the main axes of the coordinate system.

Table 3-7. User Inputs for Assembly-Specific TCCs

User Input	Value(s)	Applicability
THERMAL_CHARACTERISTIC_CURVES	<name>	All
THERMAL_CONDUCTIVITY_FUNCTION	<TCC type>	All
THERMAL_CONDUCTIVITY_WATER	$\kappa_T^{H_2O}$	ASM_AXIAL/ASM_RADIAL/ASM_WATER_FILLED
THERMAL_CONDUCTIVITY_SOLID	κ_T^S	ASM_AXIAL/ASM_RADIAL/ASM_WATER_FILLED
POROSITY_ASSEMBLY	φ	ASM_AXIAL/ASM_RADIAL/ASM_WATER_FILLED
ASM_DRY_COEFFICIENT	α_0	ASM_RADIAL/ASM_DRY
ASM_DRY_EXPONENT	α_1	ASM_RADIAL/ASM_DRY
THERMAL_CONDUCTIVITY_DRY	κ_T^{dry}	ASM_RADIAL/ASM_DRY/ASM_WATER_FILLED[a]
THERMAL_CONDUCTIVITY_WET	κ_T^{wet}	ASM_DRY[a]
END		
TEST		All
END		

NOTE: [a] Optional to impart saturation-dependence in standalone functions.

3.4 Biosphere Model

The analyses by Price et al. (2019b) calculated concentrations of radionuclides in the shale adjacent to the drift, both with and without a steady-state criticality event. Because repository postclosure performance measures are based on dose to a member of the public, the results of the analyses presented in Section 5 utilize the full reactive transport capabilities of PFLOTRAN and the biosphere model in PFLOTRAN to calculate dose to a member of the public, both with and without the occurrence of a criticality event.

The biosphere model in PFLOTRAN calculates the annual dose to an individual drinking radioactive water from a well and is based on the International Atomic Energy Agency's Example Reference Biosphere (ERB) Model 1 (IAEA 2003). The user can specify whether to use Model 1A, which explicitly simulates the well, or Model 1B, which does not explicitly simulate the well (Lichtner et al. 2020a,b). Other pathways of exposure (e.g., inhalation, ingestion of food other than water) are not included. This approach is sufficient for this criticality study, which compares the dose to a member of the public assuming the occurrence of an in-package, steady-state, postclosure criticality event to the dose to a member of the public in the absence of an in-package, steady-state, postclosure criticality event.

To use the biosphere model in PFLOTRAN, the user must specify the region in the model that contains the well and the rate at which the modeled individual consumes water. The user must also specify which radionuclides are to be included in the dose assessment. Radionuclides that are included can be either "supported" or "unsupported." The transport of "supported" radionuclides from the repository to the hypothetical well is explicitly modeled, while the transport of "unsupported" radionuclides is not explicitly modeled in the simulation because of the short half-lives of the latter radionuclides. However, the dose from an "unsupported" radionuclide can be calculated even if the transport of that radionuclide from the repository to the well has not been explicitly modeled by assuming that the "unsupported" radionuclide is in secular equilibrium with its “supported” parent radionuclide. More detail concerning the mathematical implementation of the biosphere model in PFLOTRAN is given in Mariner et al. (2017).

For “supported” radionuclides, the following information must be provided: the sorption coefficient within the material where the screen portion of the well resides, the decay rate, and the ingestion dose coefficient. For “unsupported” radionuclides, the same information is required, as well as the emanation factor and the “supported” parent with which the “unsupported” radionuclide is in secular equilibrium. The emanation factor accounts for the movement of radon, which is formed from the decay of radium, into the air from the soil grains to which the radium is attached. Radon is a gas at biosphere-relevant conditions. The radionuclides considered and their parameter values are discussed in Section 4.5.

This page is intentionally left blank.

4. MODELING STEADY-STATE POSTCLOSURE CRITICALITY

Section 3 describes the two undisturbed hypothetical repository models. With the exception of Section 4.3.1, which focuses on an unsaturated alluvial repository, Section 4 presents the model developed to simulate a steady-state postclosure criticality occurring in a hypothetical saturated shale repository. The various subsections address the following:

- Section 4.1 describes two different approaches for modeling steady-state postclosure criticality in a waste package.
- Section 4.2 discusses how the thermal effects of postclosure criticality on near-field conditions were modeled.
- Section 4.3 explains how the thermal effects of postclosure criticality on groundwater flow and radionuclide transport were modeled, both in the unsaturated alluvial repository (Section 4.3.1) and in the saturated shale repository (Section 4.3.2).
- Section 4.4 presents how the thermal effects of postclosure criticality on DPC components were modeled.
- Section 4.5 evaluates the radionuclides that need to be considered for transport calculations and/or dose calculations in the event of a postclosure criticality.

4.1 Waste Package

This subsection presents two different ways to model steady-state postclosure criticality in a waste package. The first, discussed in Section 4.1.1, looks at the approach to loosely couple the neutronics, in-canister TH processes, and repository heat transfer. The second, discussed in Section 4.1.2, focuses on examining the oscillatory nature of a steady-state postclosure criticality.

4.1.1 Simulations of a Critical DPC in a Saturated Shale Repository

This subsection discusses work performed in computing the power level of a DPC in a saturated repository. While the canisters under consideration are MPC-32 DPCs and the repository under consideration is shale, the numerical algorithms described herein can be applied to any critical DPC in any saturated repository, provided the coupling between the neutronics, in-canister TH processes, and repository heat transfer remains loose and roughly linear. Section 4.1.1.1 describes the methodology used to compute the quasi-steady-state power in a critical canister. In this context, quasi-steady state means that the fuel rods, the water inside the canister, and the host rock are all in thermal equilibrium, but the radionuclides in the fuel are gradually depleted or decay. Section 4.1.1.2 presents initial results for a critical DPC not in thermal equilibrium with the surrounding host rock. Finally, Section 4.1.1.3 examines the effect of depletion on the reactivity and sustainable power level of a critical DPC.

4.1.1.1 Calculating the Quasi-Steady-State Power Level of a Critical DPC

The initial multiphysics methodology for estimating the steady-state power in a DPC involves spanning the theoretical TH space for a given DPC, starting by assuming a canister boundary temperature. Using the Shift Monte Carlo neutronics code (Pandya et al. 2016) and the RELAP5-3D TH code (The RELAP5-3D Code Development Team 2018), the study team performed a search to find the power level of a DPC such that k_{eff} is approximately unity. The algorithm for performing this criticality search is as follows:

1. For a set of plausible power levels (~1–100 kW), calculate the associated steady-state fluid temperatures and densities using the RELAP5-3D DPC model.
2. Calculate k_{eff} for each TH state point using the Shift DPC model.
3. From the resulting k_{eff}, interpolate the critical moderator density.
4. Use the predicted critical moderator density to interpolate the critical power level using the TH data.
5. Recompute the fluid temperatures and densities at the predicted critical power level using RELAP5-3D.
6. Recalculate k_{eff} for the new state point and iterate steps 3 through 5 to convergence within ~0.001 of unity.
7. Once the power level for a given DPC boundary temperature is computed, another DPC boundary temperature is assumed, and the process is repeated.

The initial implementation of this method spanned DPC boundary temperatures ranging from that of the ambient host rock (300 K) to near the boiling temperature of water at 50 bar (530 K). The coarse application of the methodology resulted in the power estimates shown in Table 4-1.

Because of the low power levels, the coupling between the various physical phenomena (i.e., neutronics, in-canister TH, and repository heat transfer) is loose and roughly linear. Therefore, fully coupled, multiphysics simulations can be avoided in favor of linear interpolation of precomputed tabular results. Moreover, while initially power shapes generated by Shift were used to compute TH properties with RELAP5-3D, it was observed that the flow mixing within the DPCs was sufficient to provide a nearly uniform density and temperature. Therefore, a single value for fluid temperature and corresponding fluid density were sufficient for use in the neutronics calculations. This conclusion justifies the use of the TH fluid properties provided by the PFLOTRAN (Lichtner et al. 2020a,b) repository model data in the next iteration of the methodology discussed below. The Shift calculations performed as part of this initial effort to estimate critical moderator densities and temperatures are also essential when the repository proxy data are used to estimate DPC power more accurately.

With this knowledge in hand, the study team employed a geological repository model to explore the plausible combinations of DPC power and boundary temperatures for a realistic repository environment. The PFLOTRAN repository model was set in saturated shale host rock at a depth of 500 m, with several different DPC power levels (~1, 2, 4, and 6 kW). Proxy data were then generated for each of these conditions, including TH state points within the waste package as a function of time, ultimately resulting in thermal equilibrium between the DPC and the repository for each power level. Finally, these data were combined with the previously generated critical moderator density curves to enable a more accurate steady-state power estimate via interpolation.

This new methodology addresses the fact that the prior analysis was uncoupled from the larger repository environment, essentially stopping at the outer canister boundary and the associated temperature. However, as shown in Table 4-1, the power strongly depends on the canister surface temperature, which in turn depends on the heat transfer from the canister into the host rock. Thus, the PFLOTRAN geological repository model was leveraged to impose realistic limits on what values the canister boundary temperature could sustain given the postulated power levels within the canister and the thermal properties of the surrounding host rock. This additional restraint ultimately bounded the sustainable powers that were theoretically possible to less than ~6 kW.

Table 4-1. Initial Steady-State DPC Power Estimates (uncoupled from repository host rock)

Canister Surface Temperature (K)	Power (kW)	Fluid Density (kg/m^3)	Fluid Temperature (K)
MPC-32-162			
375.15	84.07	906	437.15
387.65	66.36	905.74	437.42
400.15	48.99	905.32	437.85
412.65	31.49	905.2	437.96
425.15	14.44	905.31	437.86
MPC-32-TSC-079			
325.15	76.23	948.54	389.06
337.65	61.05	948.39	389.24
350.15	45.8	948.16	389.54
362.65	30.51	947.93	389.83
375.15	15.2	947.98	389.77

The results from the PFLOTRAN calculations yielded three steady-state power levels at 1, 2, and 4 kW with their associated canister boundary temperatures. To ensure that the two TH models agreed, the study team re-ran the RELAP5-3D model with these parameters, with the result being nearly identical fluid temperatures and densities at these new, lower power levels. These three PFLOTRAN state points are shown in Table 4-2. The converged critical power levels for the two example DPCs based on the new set of TH results supported by the PFLOTRAN calculations are also shown in Table 4-2. As a final check, the two cases were re-run using Shift, confirming that a k_{eff} of near unity was predicted for the MPC-32-162 canister (1.00077 ± 0.00022) and the MPC-32-TSC-079 canister (1.00049 ± 0.00021) given the stated fluid properties.

An updated depletion analysis was also completed for the MPC-32-162 canister using the integrated radiation transport/depletion capabilities found in Shift, which has inline coupling to the ORIGEN nuclide depletion code (Gauld 2011). The power shown in Table 4-2 was used to predict the radionuclide inventory as a function of time resulting from the postulated criticality event. The MPC-32-162 model created with the Used Nuclear Fuel – Storage, Transportation & Disposal Analysis Resource and Data Systems (UNF-ST&DARDS) software included a 20,000-year decay step, which was followed by a 10,000-year-long, steady-state criticality event. This 20,000-year decay step represents time allowed for the canister to fail and flood, but it also represents another conservative “worst-case” assumption because the multiplication factor within the canister reaches a maximum during this timeframe (Wagner and Parks 2003). A base case (i.e., no fission power) was also simulated to serve as a comparison to the 2.47 kW, steady-state criticality case.

Table 4-2. PFLOTRAN Equilibrium Cases and Improved DPC Steady-State Power Estimates

Canister Surface Temperature (K)	Power (kW)	Fluid Density (kg/m3)	Fluid Temperature (K)
PFLOTRAN Cases (steady state)			
521	4	797.94	524.71
412	2	927.56	414.39
358	1	969.81	359.53
MPC-32-162 Converged Case			
436	**2.47**	905.93	437.22
MPC-32-TSC-079 Converged Case			
387	**1.61**	948.17	389.52

Figure 4-1, Figure 4-2, and Figure 4-3 illustrate various sets of nuclide densities for the MPC-32-162 case, including stable fission products, radioactive fission and activation products, and actinides with their decay products. Figure 4-4 shows the ratio of the densities of specific nuclides with and without a 2.47 kW, steady-state criticality event; it should be noted that this plot only shows the ratio for nuclides present in nonnegligible concentrations in the base case. Most radioactive fission products are not shown in Figure 4-4 because the ratio would be infinite.

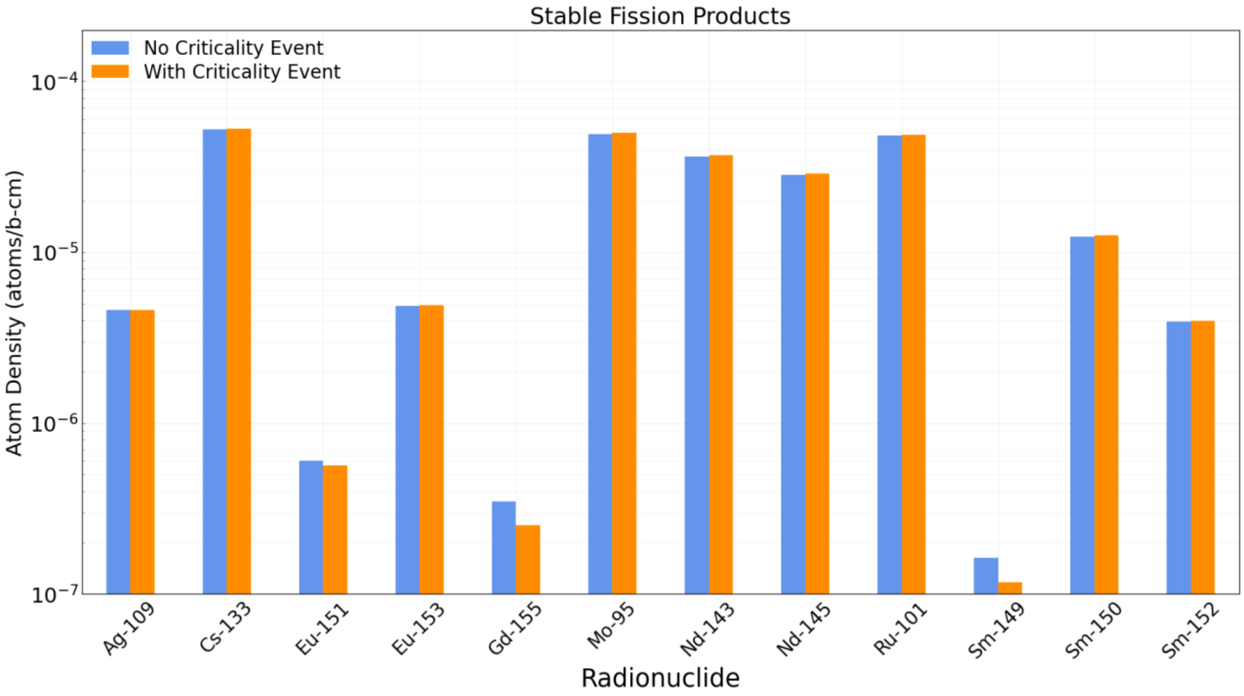

Figure 4-1. Comparison of Stable Fission Product Densities in the MPC-32-162 Model with and without a 10,000-Year-Long, Steady-State Criticality Event Producing 2.47 kW

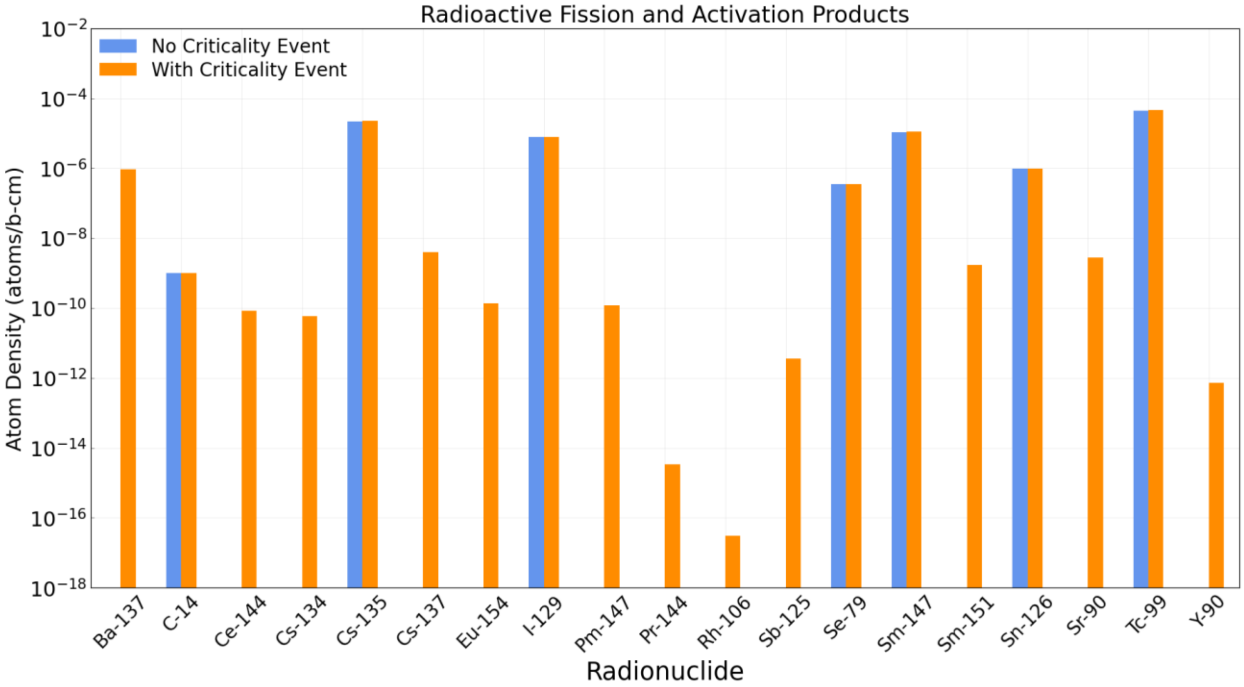

Figure 4-2. Comparison of Radioactive Fission Product Densities in the MPC-32-162 Model with and without a 10,000-Year, Steady-State Criticality Event Producing 2.47 kW

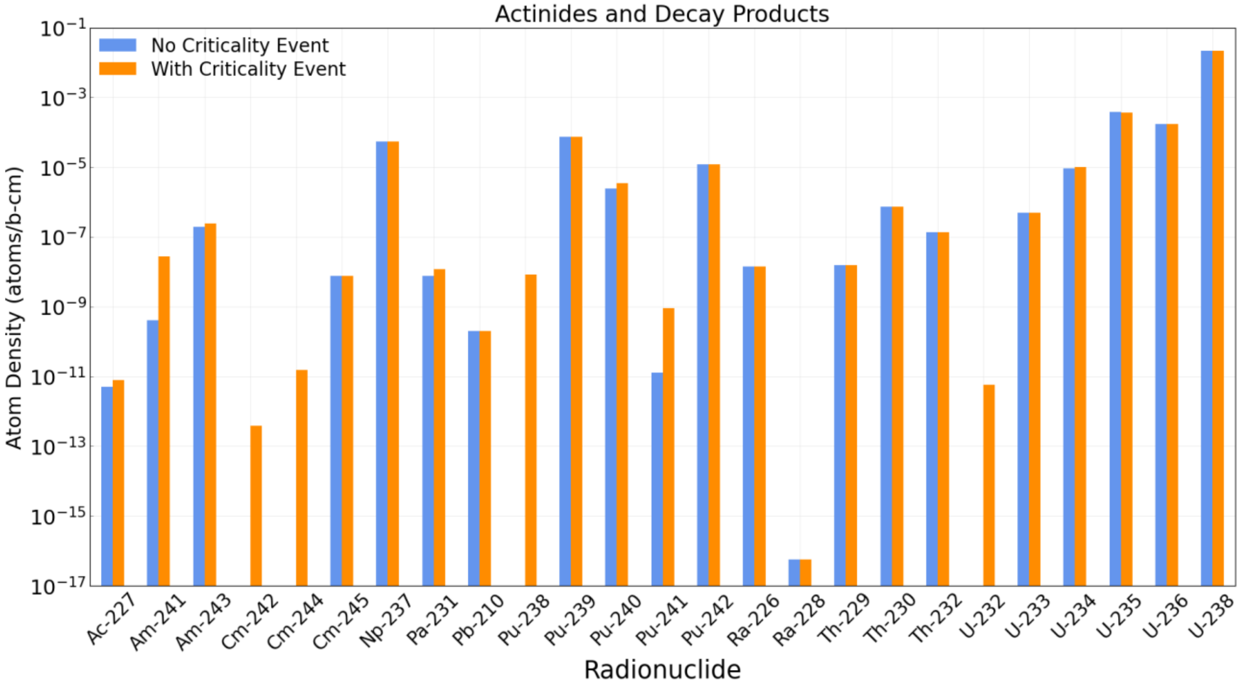

Figure 4-3. Comparison of Actinide Densities in the MPC-32-162 Model with and without a 10,000-Year-Long, Steady-State Criticality Event Producing 2.47 kW

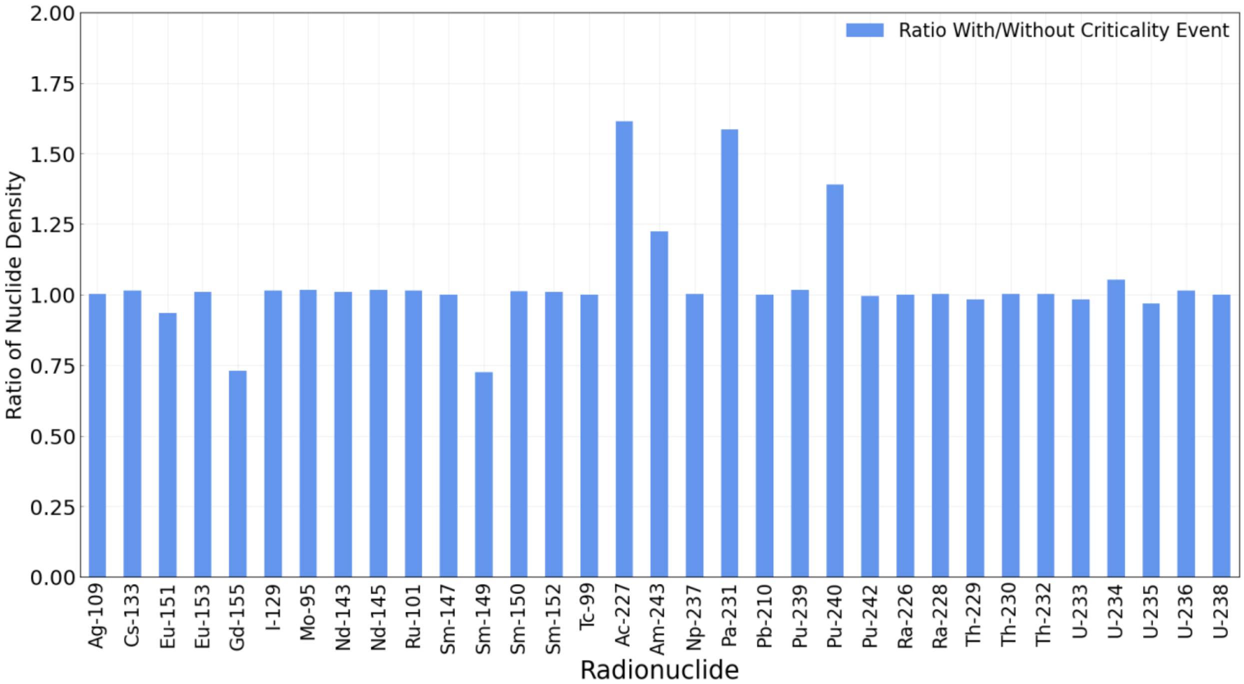

Figure 4-4. Ratio of Selected Nuclide Densities in the MPC-32-162 Model with and without a 10,000-Year-Long, Steady-State Criticality Event Producing 2.47 kW

As expected, the nuclide inventory of stable fission products remains largely unchanged except for the major neutron poisons ^{155}Gd and ^{149}Sm, which get noticeably depleted by the extended low-power criticality. This behavior is likely due to the soft neutron spectrum resulting from modeling the water as fresh, with no neutron absorbers, and at a higher moderator density than typically found in reactor operations. The inventory of short-lived fission products is predictably impacted because most of the pre-existing inventory has decayed away; therefore, the criticality event generates a small inventory of short-lived fission products that would otherwise not be present. This additional nuclide inventory could be relevant to the performance of a repository, but the impact would likely be mitigated by the relatively quick decay of most of these nuclides as they are transported slowly to the boundary of the repository. Some of the nuclides that may be of interest include ^{151}Sm (~90 years), ^{90}Sr (~30 years), and ^{137}Cs (~30 years). Some of the actinides fall into a similar category, particularly ^{244}Cm (~18 years), ^{238}Pu (~88 years), and ^{232}U (~69 years). Most of the other “short-lived” nuclides have substantially shorter half-lives and should decay prior to reaching the public receptor.

Finally, there are a few longer-lived actinide inventories that get noticeably impacted by the prolonged criticality event. The inventories of ^{243}Am (~7,400 years), ^{240}Pu (~6,600 years), ^{231}Pa (~33,000 years) and its daughter ^{227}Ac (~22 years) all see an increase on the order of approximately 20% to 60%. The overall impact of these modest differences in nuclide inventory on the performance of a specific geologic repository remains to be quantified in future work.

4.1.1.2 Analysis of a Critical DPC in a Saturated Shale Repository Undergoing Heating

Section 4.1.1.1 presents an algorithm for computing the quasi-steady-state power level in a critical DPC. The primary assumption in that method is that the fuel rods, the water filling the canister, and the host rock are all in thermal equilibrium. Given the relatively low temperatures within a critical DPC, the assumption of thermal equilibrium between the fuel rods and in-canister water is probably reasonable for the timescales relevant to the consequences of criticality in a deep geologic repository. However, the assumption that the host rock is also in thermal equilibrium is somewhat more difficult to justify because it can take decades for a repository to reach thermal equilibrium, even for the low powers postulated by the current model. Therefore, an additional effort was undertaken to capture the early-time evolution of the power produced by a DPC more accurately as it reaches the predicted steady-state power level. This work entailed interpolating the associated critical moderator properties on time-dependent PFLOTRAN proxy data. These results are shown in Figure 4-5. Although the power initially exceeds ~7 kW, it drops below 4 kW within the first couple of years as the DPC heats up the surrounding environment. The power continues to decrease as it approaches the eventual steady-state power level in the first few centuries. A comparison of these results to the quasi-steady-state power assumption for the first 350 years reveals that the time-dependent model results in approximately 6% more total power, which may be of slight importance depending on the timescale of concern. Obviously, this extra 6% power produced early on will become negligible as longer timescales are studied (< 0.002% over 10,000 years).

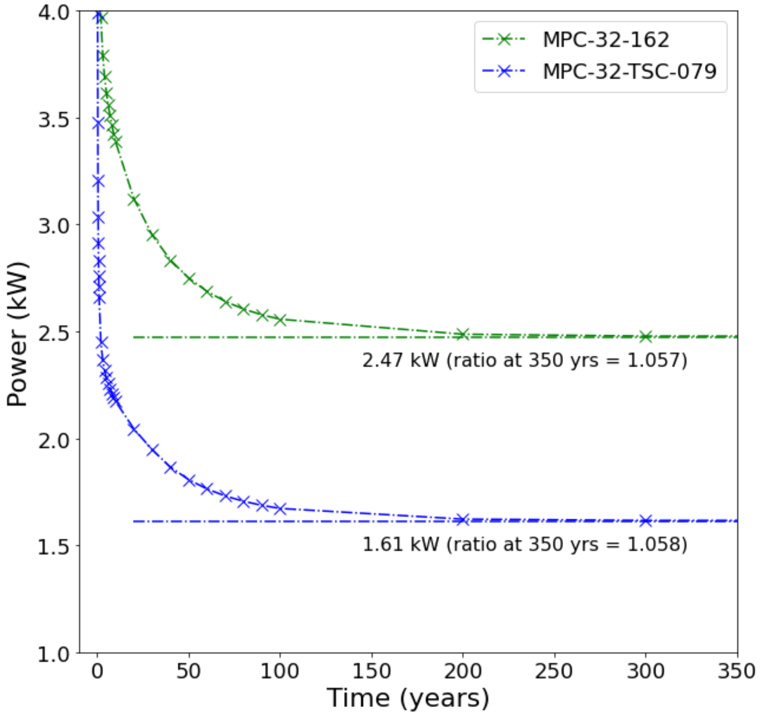

Figure 4-5. Time-Dependent Power History for Two MPC-32 DPCs Incorporating Thermal Imbalance in Host Rock

4.1.1.3 Initial Investigation into the Effect of Nuclide Depletion on DPC Power

An initial investigation of the effect of nuclide depletion on the power a critical DPC can sustain over long time periods is currently underway. Although the power level within a DPC has been shown to be relatively low (less than 4 kW), over the course of millennia the fuel will deplete, the reactivity of the DPC will decrease, and thus the power level the DPC can sustain will decrease as well. Figure 4-6 shows the effect of depletion on the multiplication factor in the two example DPCs investigated thus far. These data suggest that, within the first ~30,000 years, both DPCs will undergo a significant drop in reactivity (> 5,000 pcm) because of depletion within the fuel as well as the decay of ^{239}Pu. A peculiar effect is also seen within this timeframe: a relatively brief increase or ‘peak’ in multiplication factor within the DPCs.

Upon further investigation, the cause of this behavior stems from the somewhat localized power distribution within the DPCs. For the first ~20,000 years, the power is generated primarily in the top (axially) of the fuel assemblies, where most of the excess fissile material resides.[1] Fuel pins near the top of the assembly experience less depletion during reactor operation because control rods are inserted from the top in PWRs. The top of assemblies also tends to have a higher concentration of ^{239}Pu due to a harder neutron spectrum resulting from lower moderator densities relative to the middle and bottom of the core. Therefore, when a DPC experiences a criticality event, the bulk of the fissions occur near the top, where the fuel is less depleted. Gradually, as this fissile inventory is exhausted, the power begins to shift downward, toward the bottom of the assemblies. As the neutron flux increases significantly at the bottom portion of the assemblies, the stable neutron poisons (primarily ^{155}Gd and ^{149}Sm) deplete, resulting in a relatively quick increase in fission density at the bottom of the assemblies. This phenomenon causes power to shift to the bottom of the assemblies for a brief period, which in turn causes the neutron poison depletion to accelerate. The peaks in k_{eff} near years 0 and 20,000 are both likely due to these neutron poisons depleting from the ‘active’ part of the fuel, first at the top of the assemblies, followed by the bottom. This trend is currently under investigation, along with other potential components including the decay of important isotopes over the timescale of interest and spectral effects that may impact fissile and absorber isotope generation and depletion rates.

After these power shifts, the power shape appears to stabilize, although it is still somewhat peaked at the top and bottom of the fuel. This result is illustrated in Figure 4-7, which shows the percentage of the total power generated in each of the 18 axial nodes over the course of ~200,000 years in the MPC-32-162 canister. It should be noted that a criticality event would likely terminate much sooner than this limit due to the reduced k_{eff}. Incorporating the effect of depletion into the power history model of the DPCs is currently underway.

---

[1] In this discussion, “top” and “bottom” refer to the top and bottom of the fuel assemblies when the fuel assemblies are oriented vertically in the reactor. For disposal purposes, the fuel assemblies are oriented horizontally such that the portion of the assembly that was the top or bottom in the reactor is now on either end of the cylindrical DPC.

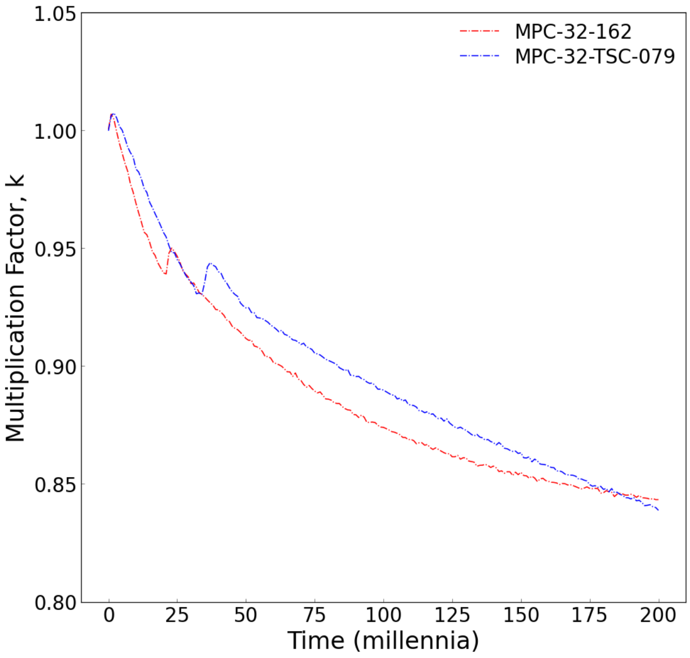

Figure 4-6. Depletion Effects on Multiplication Factor for the Two Example DPCs

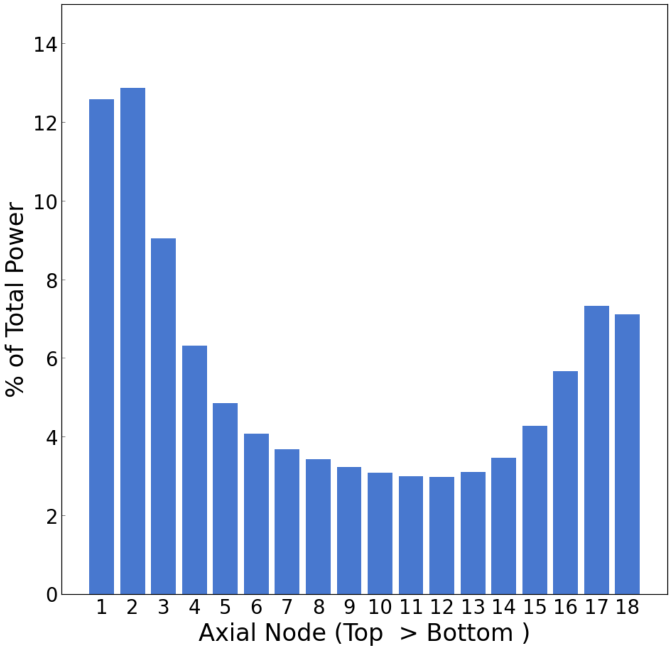

Figure 4-7. Axial Power Distribution in the MPC-32-162 DPC over a 200,000-Year Criticality Event

4.1.2 Oscillatory Nature of Steady-State Criticality

Preliminary investigation of postulated uncontrolled reactivity excursions has been completed. This event notionally occurs over a time scale ranging from weeks to many years, involving a slow ingress (filling the cask over 50 days at the fastest rate) of water submerges a mostly intact fuel lattice to insert reactivity. Poison elements are assumed to have been eroded and displaced. The moderating water results in a thermalized spectrum similar to PWR operating spectra, and the intact fuel lattice within each fuel bundle is near the optimal reactivity configuration. Thus, criticality events are plausible, even when credit is taken for the depleted fuel and the cask internal carbon-steel structure separating the fuel assemblies.

Progress was made in developing Monte Carlo N-Particle (MCNP) and Fluent models of a 37-assembly MAGNASTOR cask. Evaluations of cask reactivity were completed for a range of conditions such as water level. Geometry and meshing for the Fluent model were also completed. Loosely (explicit) coupled neutronic and TH processes are planned but have not been completed yet.

4.1.2.1 MCNP Model

The neutronic and criticality behavior of the casks was simulated using MCNP6.2 (i.e., “MCNP”). The input deck was created from scratch, rather than adopting and modifying an existing input model. Major geometric features of the 37-assembly cask were taken from the nonproprietary version of the MAGNASTOR Final Safety Analysis Report (NAC International 2010). Generic 15 × 15 Westinghouse PWR assembly information was used to fill any missing geometry information, such as assembly lattice specifics (e.g., pin pitch). Geometry inputs for the MCNP model and material inputs, including a detailed burnup inventory provided by Oak Ridge National Library (ORNL), are described in the two unnumbered subsections below.

MCNP Geometry Inputs

Figure 4-8 depicts the unit cell of the MCNP model, which includes the interior basket walls separating the individual fuel bundles. The fuel assemblies are 15 × 15 with nominal lattice pitch and are comprised of 204 fuel rods, 20 control rod guide tubes, and 1 central instrument tube. Zircaloy-4 clads the fuel and comprises the guide and instrument tubes, which are filled with either water or air. The blue material represents water for a submerged assembly or pressurized air if the assembly is above the water level. The ivory material is UO_2 fuel of various nuclide composition depending on the assembly; it includes long-lived actinides and stable fission products corresponding to the specific assembly’s burnup history and decay time. The grey material represents the carbon-steel basket walls. Zircaloy-4 is depicted by the green-colored material surrounding the fuel pins, which is somewhat difficult to see in the figure given its thickness. The fuel–cladding gap is modeled but not visible on this figure. No poison elements are treated in the MCNP model.

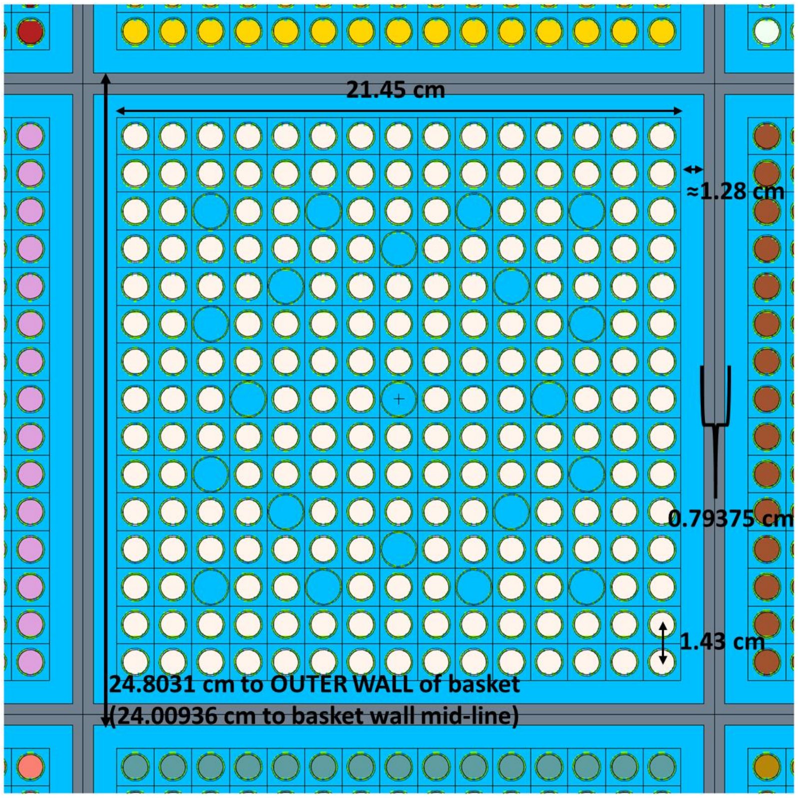

NOTE: Blue = water for a submerged assembly or pressurized air if the assembly is above the water level
Ivory = UO_2 fuel of various nuclide composition depending on the assembly, including long-lived actinides and stable fission products corresponding to the specific assembly's burnup history and decay time
Grey = carbon-steel basket walls
Green = Zircaloy-4 surrounding the fuel pins

Figure 4-8. MCNP Model Geometric Unit Cell for 37-Assembly Cask

Water or air is assumed to fill a near-nominally sized, fuel–cladding gap. In essence, outside water or air permeates the comprised cladding, which presumes corrosive degradation of the cladding pressure boundary. Likewise, the fission gas plena and guide/instrument tubes are filled with water or air depending on the water level. The existence of a nominal fuel–cladding gap is likely dubious given long-term degradation of the fuel from burnup, long decay time, and corrosion. Nonetheless, moderator ingress into the fuel rods is evaluated to significantly affect predicted eigenvalue. Water–fuel mixing such as water filling cracks and voids within the UO_2 or mixing with UO_2 dust may have a further reactivity influence not considered here. The impact of water filling the fuel rod gaps is discussed in Section 4.1.2.3.

Figure 4-9 shows the radial geometry of the MCNP model. In these analyses, the cask is resting on its side where flood water fills the cask laterally across the assemblies (i.e., not along the fuel axis). The cask is surrounded by earth, the thickness of which was evaluated to be rather insignificant when the neutron spectrum is thermalized following flooding. A few neutron mean free paths in earth are included around the cask. The outer cask wall is stainless steel, while the inner steel basket structure is carbon steel. Both are assumed to have not corroded away in the neutronic model, i.e., a porous structure of reduced gross density is not considered, despite the fact that some damage to the outer basket must have occurred to allow water ingress. A slice view through the horizontal midplane of the cask and along the fuel axis is shown by Figure 4-10.

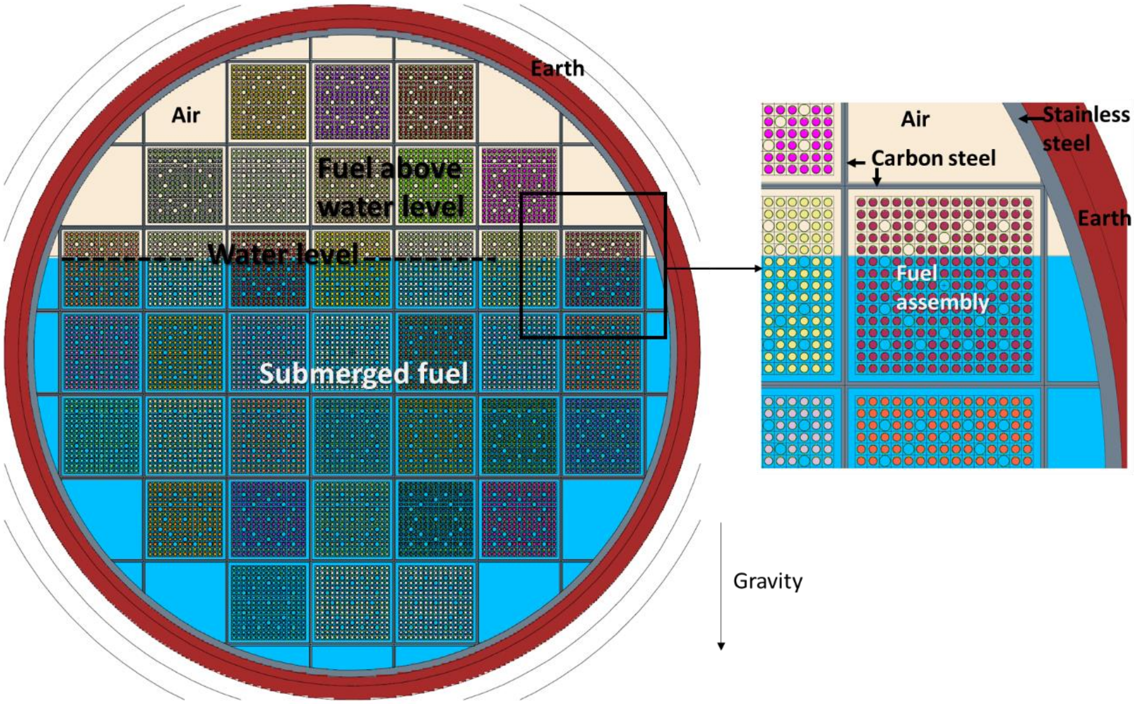

Figure 4-9. Radial (vertical) Geometry of MCNP Model with Near-Critical Water Level

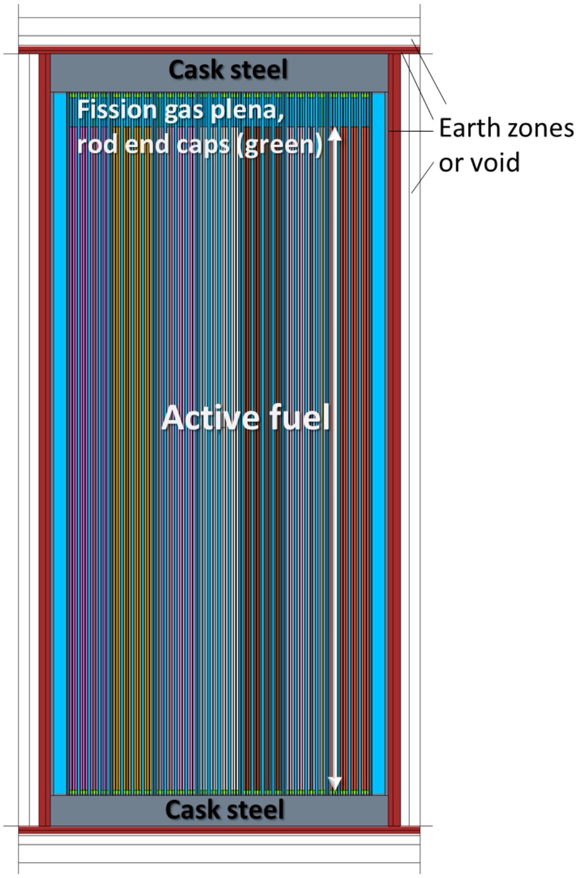

NOTE: The slice is through the horizontal midplane.

Figure 4-10. Axial Geometry of MCNP Model

Table 4-3 lists several model features and dimensions of the MCNP model geometry. Radial and axial dimensions are listed for the fuel lattice, basket dimensions, overall cask diameter and height, and other important features.

Table 4-3. MCNP Model Facets and Dimensions

Aspect	Value
Fuel assembly type	15 × 15
Number of active fuel elements per assembly	204
Number of control rod guide tubes	20
Number of instrument tubes	1
Number of assemblies / basket tubes	37
Total number of fuel rods	7,548
Dimension	**Value (cm)**
Fuel outer diameter	0.9484
Cladding inner diameter	0.9654
Cladding outer diameter	1.0719
Fuel–cladding gap thickness	0.0085
Cladding thickness	0.05325
Guide/instrument tube inner diameter	1.3004
Guide/instrument tube outer diameter	1.3868
Guide/instrument tube thickness	0.0432
Fuel lattice pitch	1.43
Interstitial gap between assembly and basket wall	1.28
Basket wall thickness	0.79375
Basket pitch (assembly-to-assembly center)	24.01
Active fuel height	365.76
Fission gas plenum length	16
Axial cladding end caps length	2
Cask outer stainless-steel wall thickness	2
Cask wall inner diameter	91.44
Surrounding earth thickness	10
Overall cask outer length	430

Material Properties and Fuel Inventory for MCNP Model

An overview of the materials in the MCNP model is provided in Table 4-4. Detailed listings of atom fractions for metal alloys are not given here. Total cask inventories of key actinides and other nuclides are provided, which reflect the depletion of the fuel and 9,000 years of decay time. All neutron cross sections are at 293.6 K and utilize ENDF/B-VII.1 data.

Table 4-4. Materials in MCNP Model

Aspect	**Value**	**Nominal Density (g/cm^3)**
Fuel material	UO_2	10.52
Cladding material	Zircaloy 4	6.55
Flood water	Pure H_2O (no sediments)	1.0
Cask outer wall	stainless steel 304L	7.86
Basket internal structure	A508 carbon steel	7.8
Surrounding earth	Generic western US avg.	1.52
Air above the water level	78.4% N, 21.1% O, 0.5% Ar, trace C	0.06 (near 50 bar)
Total Cask Inventories	**Mass (kg)**	
Total UO_2 mass	20,517	
Uranium (reflects depletion)	17,821.0	
^{235}U	216.5	
^{236}U	80.88	
^{238}U	17,518.3	
^{237}Np	30.96	
^{239}Pu	88.08	
^{240}Pu	15.67	
^{241}Pu	2.287×10^{-5}	
^{242}Pu	6.943	
^{243}Am	0.7044	
^{99}Tc	11.42	
^{103}Rh	7.594	
^{147}Sm	4.158	
^{151}Eu	0.2222	

The detailed isotopic compositions of each assembly are implemented into MCNP model, reflecting the individual final burnups and ^{235}U content of each assembly as shown in Figure 4-11 and Figure 4-12, respectively. These inventories were provided by ORNL from UNF-ST&DARDS. The nuclide inventories entail 9,000 years of decay time. The intermediate burnups, and corresponding higher ^{235}U content, in the center of the cask result in very center-peaked power distributions when moderating water floods the cask.

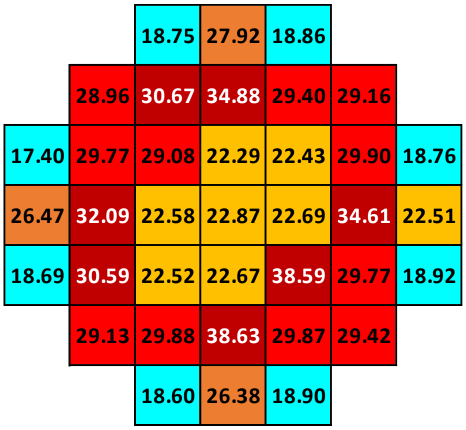

		18.75	27.92	18.86		
	28.96	30.67	34.88	29.40	29.16	
17.40	29.77	29.08	22.29	22.43	29.90	18.76
26.47	32.09	22.58	22.87	22.69	34.61	22.51
18.69	30.59	22.52	22.67	38.59	29.77	18.92
	29.13	29.88	38.63	29.87	29.42	
		18.60	26.38	18.90		

Figure 4-11. Assembly Burnup (GWd/t) Distribution in 37-Assembly Cask

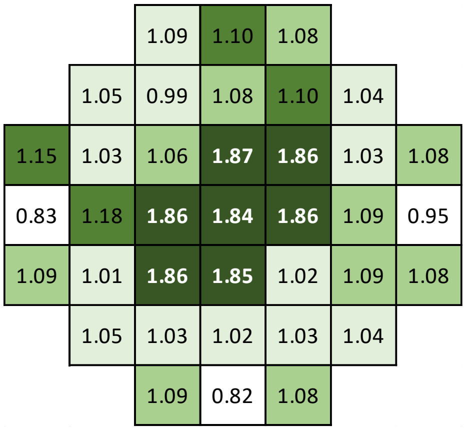

		1.09	1.10	1.08		
	1.05	0.99	1.08	1.10	1.04	
1.15	1.03	1.06	1.87	1.86	1.03	1.08
0.83	1.18	1.86	1.84	1.86	1.09	0.95
1.09	1.01	1.86	1.85	1.02	1.09	1.08
	1.05	1.03	1.02	1.03	1.04	
		1.09	0.82	1.08		

Figure 4-12. Final ^{235}U Weight Fractions after Depletion and 9,000-Year Decay Time

4.1.2.2 Key Neutronic Results

This subsection addresses reactivity, neutron spectra, and power distribution predictions. The quantities were calculated using MCNP6.2 for a range of conditions. The analysis considers variations in water level in addition to degraded geometries. A quick evaluation of source neutron level using SCALE6.2 is also presented. The source neutron population is necessary for accurate prediction of uncontrolled reactor startup due to the slow ingress of moderator into the lattice.

Near-Critical Configuration

Given the model inputs and assumptions, the critical water level is estimated to completely submerge the bottom four rows of fuel baskets. The critical level is just above the middle of the next (fifth) row of assemblies. Predicted eigenvalue in this configuration is slightly subcritical. The corresponding reactivity is −\$0.083, which utilizes an MCNP-estimated effective delayed neutron fraction of 0.00533 (σ=0.00008). This β_{eff} value reflects the actinide content of the burned fuel, as plutonium fission entails lower delayed neutron fraction. Flooding another pin row results in a slightly supercritical state with greater reactivity magnitude.

The critical water level position is shown by Figure 4-13, which also lists k_{eff} and the standard deviation. Reactivity results for two water levels around the critical position are listed in Table 4-5. Point kinetics parameters are calculated at the critical position (i.e., row 5 half flooded + 2 rows of pins) and are listed in Table 4-6. The transient analysis of the cask using point kinetics, typically using six delayed neutron precursor groups, requires these parameters.

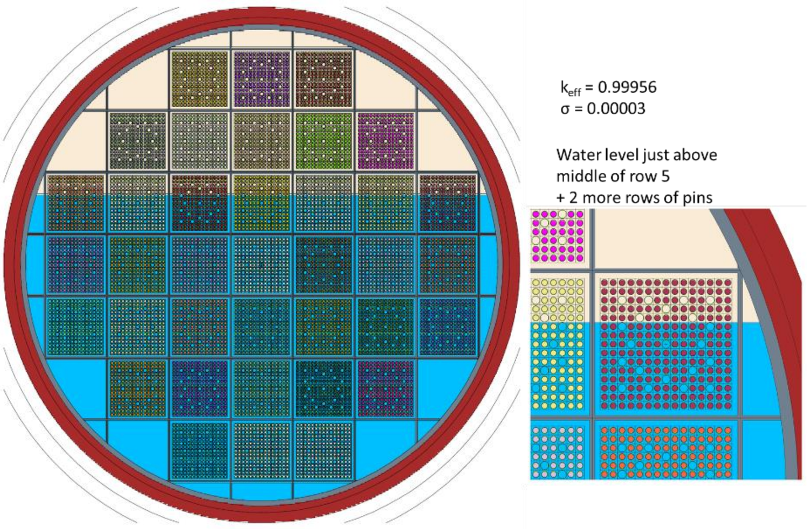

Figure 4-13. Predicted Critical Water Level and Eigenvalue

Table 4-5. Eigenvalues and Reactivity for Near-Critical Water Level

Flood Level	Water Level above Center (cm)	Water Level above Bottom (cm)	k_{eff}	k_{eff} σ	k_{eff} −2σ	k_{eff} +2σ	Reactivity	React ($)
row 5 half + 2 pin rows	27.58	119.02	0.99956	0.00003	0.99950	0.99962	−0.00044	−0.083
row 5 half + 3 pin rows	29.01	120.45	1.00103	0.00006	1.00091	1.00115	0.00103	0.193

Table 4-6. MCNP-Calculated Point Kinetics Parameters

Parameter	Value	Std. Dev.
β_{eff}	0.00533	0.00008
Generation time (μs)	29.36646	0.03715
Precursor 1 β_{eff}	0.00018	0.00001
Precursor 2 β_{eff}	0.00094	0.00003
Precursor 3 β_{eff}	0.00087	0.00003
Precursor 4 β_{eff}	0.00208	0.00005
Precursor 5 β_{eff}	0.00087	0.00003
Precursor 6 β_{eff}	0.00038	0.00002
Precursor 1 E_{avg} (MeV)	0.41211	0.00247
Precursor 2 E_{avg} (MeV)	0.48990	0.00107
Precursor 3 E_{avg} (MeV)	0.43538	0.00106
Precursor 4 E_{avg} (MeV)	0.54906	0.00095
Precursor 5 E_{avg} (MeV)	0.50930	0.00143
Precursor 6 E_{avg} (MeV)	0.53951	0.00257
Precursor 1 λ (s^{-1})	0.01335	0.00000
Precursor 2 λ (s^{-1})	0.03219	0.00000
Precursor 3 λ (s^{-1})	0.11988	0.00001
Precursor 4 λ (s^{-1})	0.30518	0.00002
Precursor 5 λ (s^{-1})	0.86498	0.00008
Precursor 6 λ (s^{-1})	2.88952	0.00052

Reactivity Effects of Moderator Ingress into Fuel Rods

The assumption of water ingress into the fuel cladding has significant reactivity impacts. The cladding is treated as being largely intact, but water has filled the fuel–cladding gap through small defects and holes in the cladding, perhaps because of corrosion. Given the burnups (20−40 GWd/t) and long decay time (9,000 years), the fuel material will not be perfect cylindrical pellets. Rather, the outer fuel surface will likely irregular, and the UO_2 will be cracked and fractured with internal voids. The 9,000 years of actinide decay might create fuel debris or dust in the rods. Further water–fuel mixing with the fuel in a degraded state will have different reactivity effects. Nonetheless, these analyses assume a nominal (i.e., cylindrical shell) fuel–cladding gap.

Calculated reactivity changes due to cladding water vaporization/removal are summarized in Table 4-7. It is interesting to note that if the cask became slightly supercritical, thereby increasing fission power to the point of adding heat to the fuel, the reactivity feedback due to voiding the gap water might turn over the power transient. The immediate reactivity feedback would be from fuel Doppler broadening, but the water around the fuel would heat and increase in temperature before the effects spread to the cladding and the bulk of the surrounding water in the fuel lattice. The vaporization or removal of water in the fuel–cladding gap results in −34 cents of reactivity change, which could be sufficient to terminate (or perhaps stabilize) the transient in conjunction with Doppler feedback.

Table 4-7. Cladding Moderator Reactivity Impact

Water Level	k_{eff} with Water in Fuel–Cladding Gaps below Water Level	k_{eff} with No Water in Fuel–Cladding Gaps	$\Delta k \times 10^4$	Δρ	Δρ ($)
Near critical	0.99956 ± 0.00006	0.99776 ± 0.00006	−18.0	−0.00180	−0.34
Fully filled with water	1.01003 ± 0.00006	1.00830 ± 0.00006	−17.3	−0.00170	−0.32

Reactivity, Power Distribution, and Neutron Spectrum with Increasing Water Level

Water level is progressively raised in the cask to determine the critical level. Eigenvalue and reactivity for the various water levels are tabulated in Table 4-8. Estimated 95% confidence intervals are also provided. The critical water level is about 120 cm above the bottom of the cask inner surface.

Three-dimensional (3D) power distributions (i.e., relative fission reaction rates) are tallied for a range of flood levels. Relative fission reaction rates are resolved radially on the assembly level over 20 evenly spaced axial nodes. These power distributions can be used as inputs for separate TH analyses. Figure 4-14 illustrates the water level being raised discretely over each fuel assembly row, starting from completely dry to completely flooded. The associated two-dimensional (2D) radial power peaking factors and k_{eff} values for each state are also shown. Power peaking is normalized to the average fission reaction rate in each assembly. Therefore, near the critical water level (5 rows submerged), the center assembly is generating about 4.5 times more fission power than the average assembly power. Fission power peaking is more pronounced when water is pooling near the bottom of the cask, but the cask is also sufficiently subcritical in these states. With a harder neutron spectrum in the dry cask, relative fission reaction rates are flatter across the assemblies, owing to the longer mean free paths and tighter neutronic coupling at the fast spectrum. The cask is very subcritical (k_{eff} ~ 0.3) with no significant moderator within the fuel lattice, and thus the associated power distribution is not very meaningful.

Table 4-8. Reactivity and Eigenvalue for Different Water Levels

					95% Confidence			
Flood Level	**Water Level above Center (cm)**	**Water Level above Bottom (cm)**	k_{eff}	k_{eff} **σ**	k_{eff} **−2σ**	k_{eff} **+2σ**	**Reactivity**	**React ($)**
dry	–91.44	0.00	0.31550	0.00003	0.31544	0.31556	−2.16957	–407.049
≈1/4 fill	–48.73	42.71	0.80471	0.00006	0.80459	0.80483	−0.24268	–45.532
≈1/2 fill	0.72	92.16	0.96035	0.00006	0.96023	0.96047	−0.04129	−7.746
row 5 dry	11.61	103.05	0.98881	0.00007	0.98867	0.98895	−0.01132	−2.123
row 5 half filled	24.72	116.16	0.99680	0.00006	0.99668	0.99692	−0.00321	−0.602
row 5 half + 2 pin rows	27.58	119.02	0.99956	0.00003	0.99950	0.99962	−0.00044	−0.083
row 5 half + 3 pin rows	29.01	120.45	1.00103	0.00006	1.00091	1.00115	0.00103	0.193
row 5 filled	35.62	127.06	1.00734	0.00006	1.00722	1.00746	0.00729	1.367
row 6 filled	59.63	151.07	1.00972	0.00006	1.00960	1.00984	0.00963	1.806
row 7 half filled	72.74	164.18	1.00979	0.00006	1.00967	1.00991	0.00970	1.819
top reflector dry	83.64	175.08	1.00979	0.00006	1.00967	1.00991	0.00970	1.819
100% water fill	91.44	182.88	1.01003	0.00003	1.00997	1.01009	0.00993	1.863

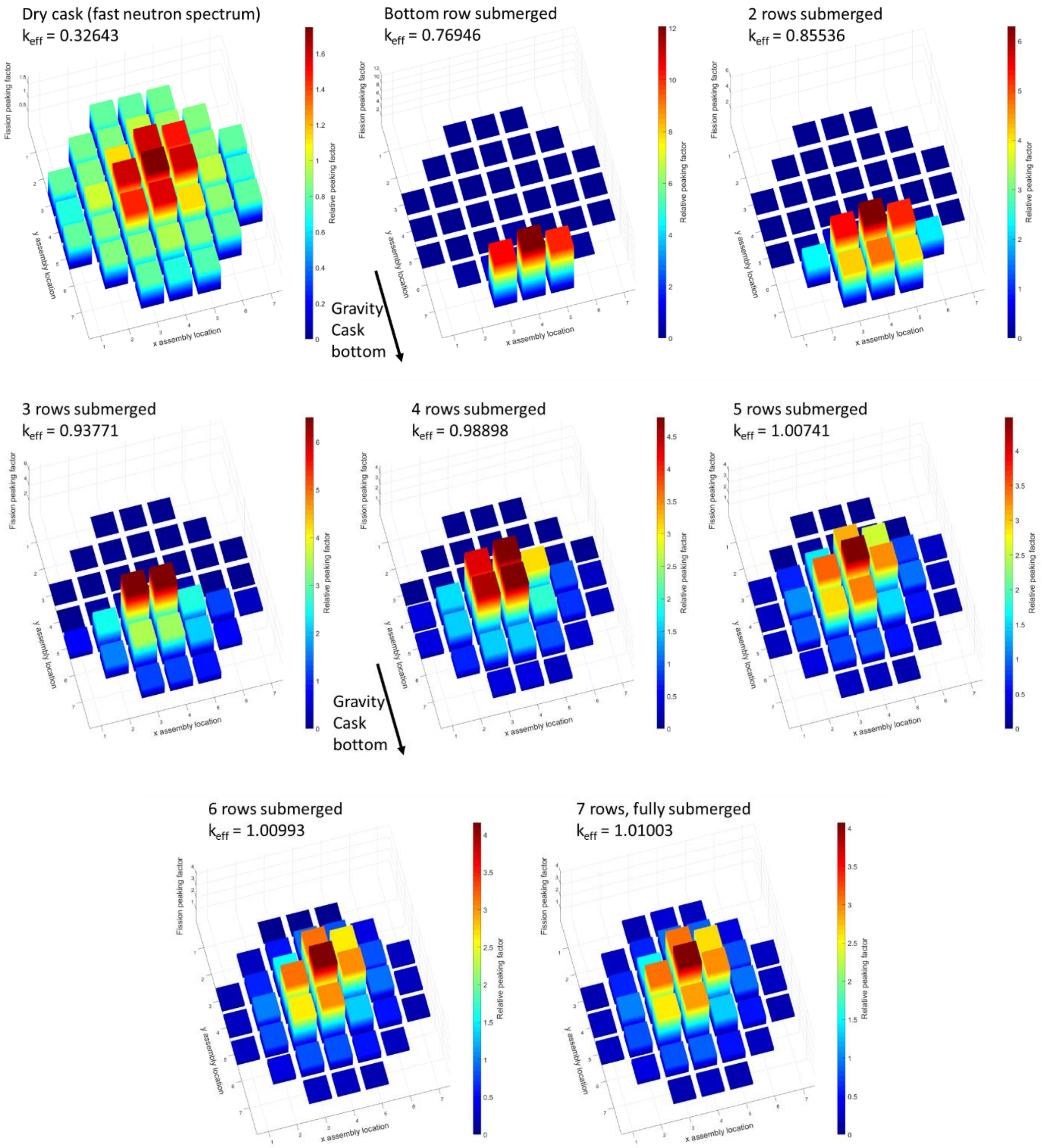

Dry cask (fast neutron spectrum)
k_{eff} = 0.32643

Bottom row submerged
k_{eff} = 0.76946

2 rows submerged
k_{eff} = 0.85536

Gravity
Cask
bottom

3 rows submerged
k_{eff} = 0.93771

4 rows submerged
k_{eff} = 0.98898

5 rows submerged
k_{eff} = 1.00741

Gravity
Cask
bottom

6 rows submerged
k_{eff} = 1.00993

7 rows, fully submerged
k_{eff} = 1.01003

Figure 4-14. Radial Distribution Power Peaking Factor for Variable Water Level

Neutron spectra for the cask at various water levels are depicted in Figure 4-15. The four curves illustrate the thermalization of the neutron spectrum starting from completely dry (blue); to three bottom rows being submerged in water (green); to five rows submerged, at which point the cask is supercritical (yellow), and then fully submerged (red). Significant neutron thermalization has already occurred once three rows have been flooded, reflecting the dramatic increase in reactivity relative to the dry case. The highest reactivity case—red curve signifying a fully submerged cask—has the greatest relative neutron flux at around 10^{-7} MeV, which increases thermal neutron absorption in fuel.

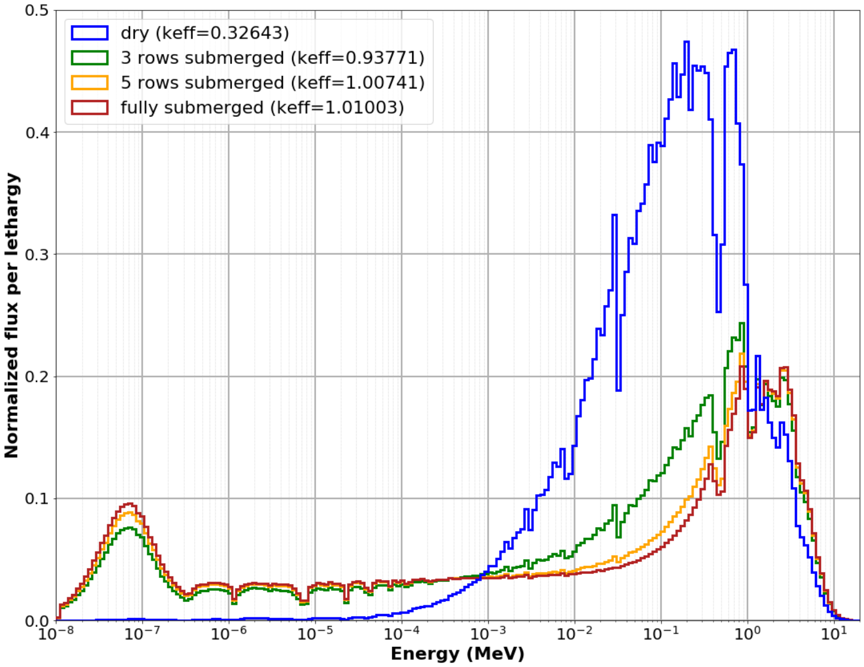

Figure 4-15. Overall Cask Neutron Spectra for Variable Water Level

Reactivity Insertion Rate, Source Neutron Level, and Feedback for Uncontrolled Reactor Startup

The postulated reactivity excursion due to flooding is analogous to a slow, prolonged, uncontrolled reactor startup. The fastest flooding rate might be anticipated to flood the cask over a ≈50-day period. Therefore, to facilitate transient analyses, the study team evaluated a reactivity insertion rate for the cask using the k_{eff} values as a function of water level and the hypothesized flood rate. Furthermore, the neutron source level of the cask was calculated using SCALE6.2, and the fuel Doppler coefficient was estimated. These inputs are required for simple, coupled neutronic and TH models, in addition to the point kinetic parameters already presented (if using point kinetics).

Figure 4-16 shows k_{eff} and total reactivity as a function of rising water level. The information plotted in this figure is from Table 4-8. The total reactivity of the fully submerged cask is just under \$2. Figure 4-17 shows the integral reactivity worth of the water. It also depicts the differential reactivity worth per cm of rising water level, focused near the critical water level. Differential reactivity worth is greater for rising water near the bottom and center of the cask, as expected, relative to the upper portions of the cask as the neutron spectrum has already been thermalized in much of the fuel lattice.

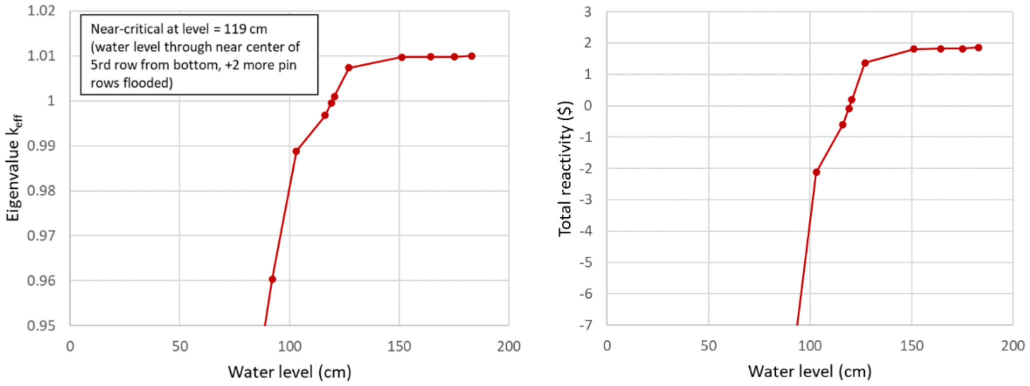

Near-critical at level = 119 cm (water level through near center of 5rd row from bottom, +2 more pin rows flooded)

Figure 4-16. Reactivity with Flooding Water Level

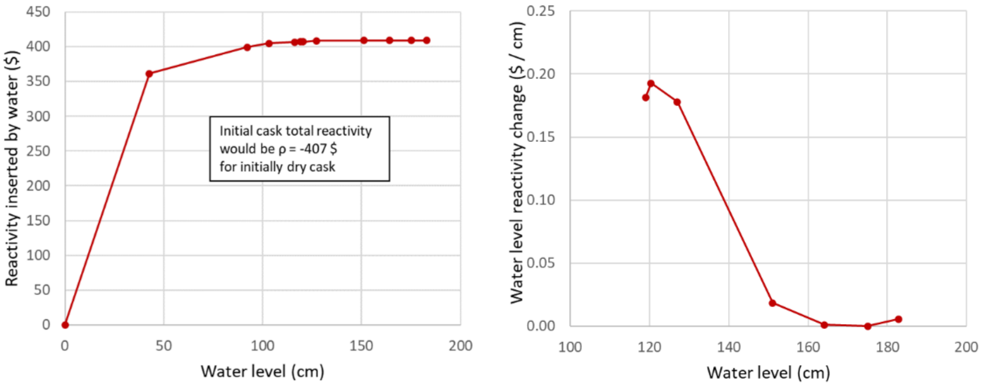

Initial cask total reactivity would be ρ = -407 $ for initially dry cask

Figure 4-17. Integral and Differential Reactivity Worths of Flood Water

For simplicity, a fill time of 50 days to completely flood the cask is assumed to result in a constant rate of change in water level. In actuality, a constant volumetric flow rate would entail faster elevation change at the lower and upper portions of the horizontal cask. The 50-day fill time corresponds to 3.66 cm/day of elevation change. The subsequent reactivity insertion rate, given the different reactivity worth, is provided by Figure 4-18. Peak reactivity insertion rates near the critical water level (120 cm) are about $0.7 per day but decrease to less than $0.1 per day as the cask continues to fill. With no reactivity feedback, the maximum overall cask reactivity is predicted to be about $1.86.

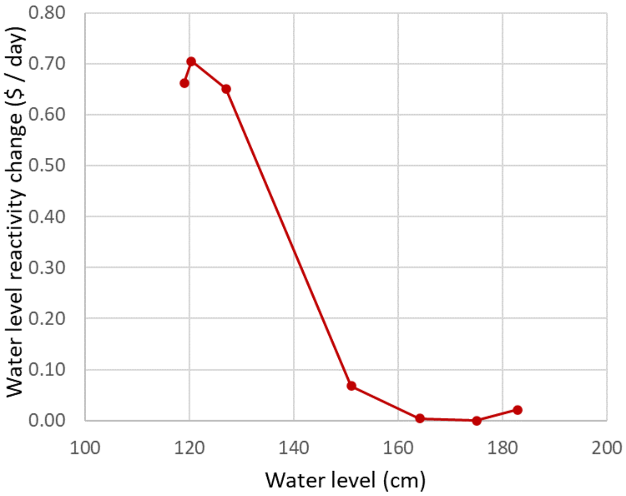

Figure 4-18. Reactivity Insertion Rate for Constant Water Level Rise

Source neutron levels after 9,000 years of decay are evaluated using SCALE6.2. The source neutron level provides an initial neutron population (i.e., initial fission power level) for transient simulations of the uncontrolled startup event. A summary of the overall neutron sources is provided in Table 4-9. The total source level after 9,000 years is roughly 3 × 10^7 n/s for the entire cask inventory. The neutron source is mostly driven by spontaneous fission from ^{240}Pu and ^{242}Pu. Spontaneous fission of ^{238}U and ^{236}Cm ($t_{1/2}$ ~ 4,760 years) is also significant. The usual dominant sources of spontaneous fission neutrons in spent LWR fuel—^{242}Cm ($t_{1/2}$ ~ 163 days) and ^{244}Cm ($t_{1/2}$ ~ 18.1 years)—have long decayed away by 9,000 years. Nuclear reactions with oxygen isotopes (^{18}O and ^{17}O) also contribute to neutron source level. Actinide decay and the abundance of oxygen in UO_2 result in significant α,n reaction rates. The dominant α,n contributors are ^{239}Pu, ^{240}Pu, and ^{243}Am. Using averages of 2.6 neutrons/fission and 190 MeV/fission, the source neutron level is roughly equivalent 0.37 mW of fission power. The decay heat at 9,000 years is about 250 W.

Table 4-9. Neutron Source for 9000-Year Decay Inventory

Neutron Source	Neutrons/s
α,n	4.4465×10^6
Spontaneous fission	2.6961×10^7
Total	3.1407×10^7

The first significant reactivity feedback after the cask becomes supercritical would be fuel Doppler feedback as the fuel temperature increases. A series of MCNP calculations is executed at increasing temperatures with the water level near the critical position. Fuel cross-section libraries (Evaluated Nuclear Data File/Version B – Rev. 7.1 [ENDF/B-VII.1]) are used at 293.6 K, 600 K, 900 K, 1,200 K, and 2,500 K. The fuel Doppler coefficient is estimated to be −2 pcm/ΔK, as shown in Figure 4-19. This is equivalent to $-\$3.75 \times 10^{-3}$ per ΔK using the calculated β_{eff} of 0.00533.

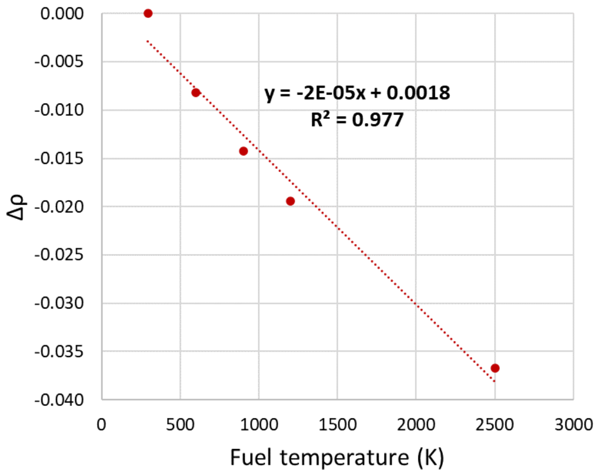

Figure 4-19. Fuel Doppler Coefficient

Scoping Evaluations of Degraded Cask Geometry

Given the low enrichment and burnup of the fuel, the geometry of the fuel lattice is of first-order importance for the overall reactivity of the cask. The cask cannot become critical without significant moderating material *within* the fuel lattice. The volume fractions of fuel and moderator are also important. Several degraded geometry cases are presented here for demonstration purposes.

Figure 4-20 depicts the flooded cases with nominal geometry (case a) compared to six alternative arrangements (cases b–g). For example in case b, if the fuel pitch in each assembly collapses to the point that the rods are in contact (1.43–1.072 cm), the cask is subcritical (k_{eff} = 0.70634) even when fully submerged (Section 6.2.2.5). Despite the abundance of moderator *surrounding* the fuel assemblies (which acts mostly to absorb neutrons rather than effectively thermalize the spectrum within the lattices), the lattices are too undermoderated (excessive fuel to moderator volume ratio in the lattices) to reach criticality. The neutron spectrum is hardened (Figure 4-21) with associated increase in neutron mean free path, and less neutrons are absorbed in the lattice regions due to less water volume ratio in the lattices. Therefore, the interstitial water gap and carbon-steel basket regions between the assemblies have increased neutron absorption (Table 4-10). The interstitial water gap thickness between the assemblies is reduced in case c, which entails a reduction in basket pitch from 24.009 cm to 18.64 cm (in addition to the collapsed lattice pitch); this situation increases reactivity, but the cask is still significantly subcritical (k_{eff} = 0.87297). *With* the reduced lattice pitch and subsequent larger-water-gap thickness, the interstitial water has significantly increased reactivity worth compared to cases with nominal lattice pitch. Replacing the carbon-steel basket with water in this configuration results in another significant reactivity increase (case c to case d, k_{eff} = 0.99730), as expected due to high neutron absorption in the carbon steel. Further reduction of the basket pitch from 18.64 cm to 16.1 cm in case e, such that fuel rods between assemblies are also touching, results in a reduction in reactivity (k_{eff} = 0.85936) compared to the previous two cases, thus demonstrating how bringing the assemblies closer can eventually decrease reactivity. Case f has a nominal lattice pitch and reduced basket pitch of 22.25 cm. With reduced interstitial water around the assemblies, neutron absorptions decrease in the interstitial water and carbon-steel basket, thus resulting in an increase in reactivity (k_{eff} = 1.03825) compared to the base case a. Case a and f are identical except for the basket pitch, suggesting the interstitial water has a reactivity worth of about $5 when the lattice pitch is nominal. While this is significant, the carbon-steel basket has a reactivity worth of roughly $15 to $27 depending on the other geometric factors. Reducing the lattice pitch can decrease reactivity by as much as $80. Case e shows that further reduction of the interstitial gap between assemblies can decrease overall reactivity, depending on other key factors like lattice pitch. The greatest reactivity configuration of the cask likely resembles a PWR core with near-nominal lattice pitch, the carbon-steel basket removed, and with the excessive interstitial gaps reduced. Such a configuration is given by case g in Figure 4-20 (k_{eff} = 1.10136). Higher reactivity configurations probably exist entailing slightly increased separation of fuel; examples include increased lattice pitch or slightly increased interstitial spacing between assemblies.

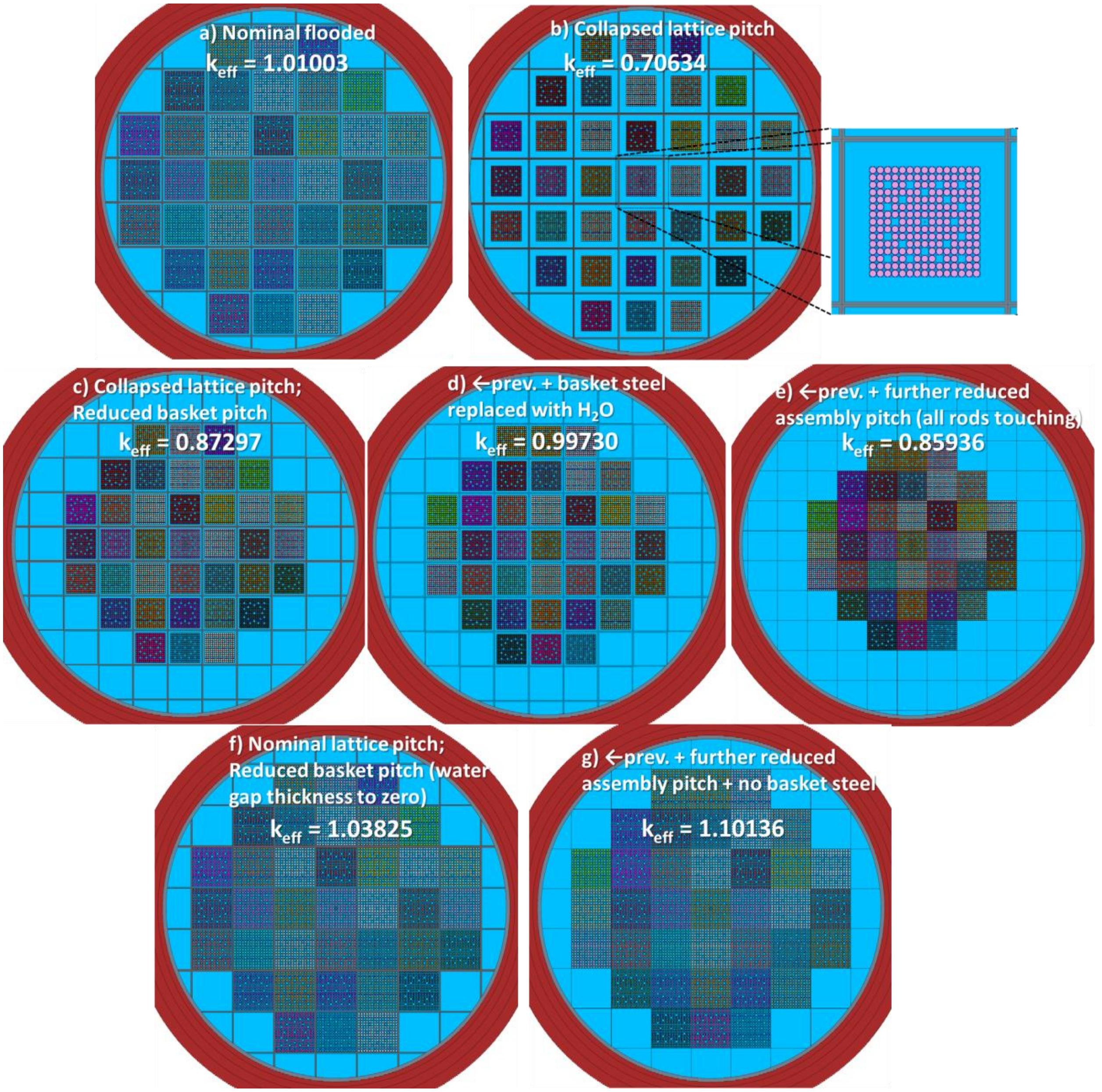

Figure 4-20. Degraded Geometries and Associated k_{eff} Values

Neutron absorption distributions for select cases are listed in Table 4-10. For the nominal geometry, the interstitial gap water between the assemblies contributes a relatively low fraction of neutron absorptions. The carbon-steel basket absorbs about 4 times as many neutrons. Hence, reducing the amount of interstitial gap water (i.e., assembly pitch reduction) does not drastically increase reactivity as much compared to changes in the basket geometry/material or lattice pitch. Comparing neutron absorption fractions in cases a and c demonstrates the importance of lattice pitch and resulting spectrum in the lattice regions: these cases have similar absorption fractions in the interstitial water gaps, yet case c is significantly subcritical while case a (nominal geometry) has $1.86 of excess reactivity despite the fuel assemblies being closer together in case c.

Table 4-10. Neutron Balances for Select Cases: k_{eff} Values and Fraction of Total Neutron Absorptions

	Case a: Nominal	**Case b: Rods Touching; Nominal Assembly Pitch**	**Case c: Rods Touching; Reduced Assembly Pitch**
Cask region/material	k_{eff} = 1.01003	k_{eff} = 0.70634	k_{eff} = 0.87297
Fuel	0.8017	0.5874	0.8269
Channel water	0.0664	0.0109	0.0140
Interstitial water gap	**0.0242**	**0.1985**	**0.0226**
All outer water regions	0.0067	0.0078	0.0253
Channel Zircaloy	0.0063	0.0052	0.0078
Inner steel baskets	**0.0882**	**0.1816**	**0.0913**
All outer steel baskets	0.0029	0.0044	0.0105
Outer stainless steel	0.0028	0.0032	0.0012
Outer earth	0.0009	0.0009	0.0003

The ten degraded geometry cases presented herein illustrate the importance of the near-nominal lattice geometry. The k_{eff} results for the various degraded geometry cases are summarized in Table 4-11, including the cases shown in Figure 4-20. Over 9,000 years of decay, aging, and corrosion, the lattice geometry may no longer reflect the design arrangement. A few more drastic geometry changes are also investigated but are not intended to identify the limiting case. Rather, these geometry changes aim to further demonstrate how conglomeration of low enriched LWR fuel can often reduce criticality concerns. If all 20,517 kg of fuel were to relocate (e.g., collapse or melt) into a solid sphere of UO_2, k_{eff} is substantially subcritical even when the fuel sphere is surrounded by water. This calculation assumes the entire fuel debris was at the maximum depleted ^{235}U content of 1.87 w/o. Even with 7 w/o enrichment and no fission products or other actinides, a sphere of 20,517 kg of UO_2 is subcritical if no significant moderating material is interspersed among the fuel.

Table 4-11. k_{eff} for Degraded Geometries

Degraded Case	Lattice Pitch (cm)	Assembly Pitch (cm)	k_{eff}	σ
Case b in Figure 4-20: Fully submerged; lattice pitch reduced (rods touching)	1.072	24.00935 (design value)	0.70634	0.00006
Case c in Figure 4-20: Fully submerged; lattice pitch reduced (rods touching); assembly/basket pitch reduced;	1.072	18.64	0.87297	0.00006
Case d in Figure 4-20: Fully submerged; lattice pitch reduced (rods touching); assembly/basket pitch reduced; carbon-steel basket replaced with water	1.072	18.64	0.99730	0.00006
Case e in Figure 4-20: Fully submerged; lattice pitch reduced (rods touching); assembly/basket pitch further reduced such that all rods are touching; carbon-steel basket replaced with water	1.072	16.12	0.85936	0.00006
Case f in Figure 4-20: Fully submerged; nominal lattice pitch; assembly/basket pitch reduced (interstitial water gap thickness reduced to zero)	1.43	22.25	1.03825	0.00006
Case g in Figure 4-20: Fully submerged; nominal lattice pitch; assembly/basket pitch further reduced (interstitial water gap thickness reduced to zero); carbon-steel basket removed	1.43	21.46	1.10136	0.00006
5 rows submerged; nominal geometry; basket carbon steel voided	1.43	24.00935	1.09625	0.00006
5 rows submerged; nominal geometry; basket carbon steel replaced with water	1.43	24.00935	1.08344	0.00006
All fuel reformed into solid UO_2 sphere surrounded by water (1.87 w/o enrichment)	NA	NA	0.57967	0.00006
All fuel reformed into solid UO_2 sphere surrounded by water (7 w/o enrichment)	NA	NA	0.89809	0.00006

Table 4-11 lists results for which the carbon-steel basket material is assumed to be degraded for both full and partially flooded cases. This material is potentially severely corroded after thousands of years. Replacing the carbon-steel basket material with void inserts $15.1 of reactivity when the cask is near the critical flood level (about 5 rows of assemblies submerged). Replacing the basket volume with additional water results in less reactivity compared to simply voiding this space. The carbon steel acts to neutronically isolate the fuel assemblies as a mild poison material. Hence, its removal significantly increases cask reactivity. Filling the basket volume with additional water still increases reactivity relative to the base case with carbon steel. However, in this arrangement the cask mimics a PWR core with excessive interstitial space between assemblies. The cask is thus overmoderated and the additional water acts to absorb neutrons relative to the case that voided the basket volume. The neutron spectra associated with some of the degraded geometries are shown in Figure 4-21. The figure demonstrates how squeezing out moderator volume in the case with reduced pin pitch (the green curve being case b from Figure 4-20) produces a harder, undermoderated spectrum compared to the base geometry with critical water level (i.e., near 5 rows submerged). The case with voided basket volume exhibits a more thermalized spectrum, reflecting the increased reactivity.

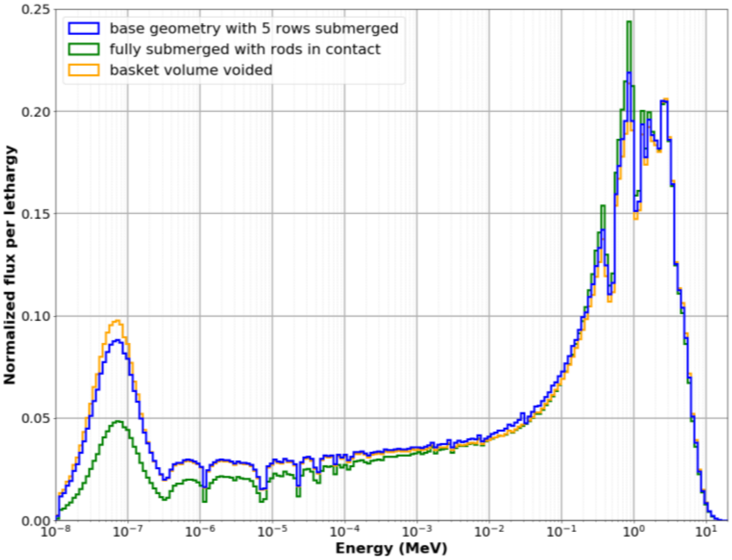

Figure 4-21. Degraded Geometry Neutron Spectra

4.1.2.3 *Summary*

The study team created an MCNP model of a 37-assembly MAGNASTOR cask and completed a series of criticality predictions. The analyses indicate the cask may become supercritical if the cask floods above the midplane of the cask (on its side). This prediction is predicated on the assumption that the poison elements within each tube are removed by corrosion and degradation. The flood water results in a potential total excess reactivity of $1.86. However, the reactivity insertion occurs slowly over about 50 days. Thus, reactivity feedback due to evolving fuel and moderator TH conditions would gradually reduce total reactivity after the cask is supercritical. These analyses also assume the fuel–cladding gap is full of water because of some degradation of the cladding pressure boundary, which adds about $0.34 of reactivity. For detailed predictions of power oscillations, coupled reactor kinetic and TH calculations are necessary to evaluate the temporal details of fuel temperature feedback, gap water heating and density feedback, and the reactivity feedback of the bulk water in the assembly channels, in addition to the hydraulic conditions outside cask. The study team began preliminary model development using computational fluid dynamics (CFD) and system codes, but these efforts have not been completed yet.

Power distributions and k_{eff} values were calculated as a function of rising water level. Fuel Doppler reactivity feedback was estimated for uniform temperature changes over the cask fuel rods. Neutron spectra for various conditions were presented. Some additional studies including source neutron level (i.e., mostly spontaneous fission) and reactivity associated with some degraded geometries were completed. As expected, collapse of the lattice pitch would dramatically decrease reactivity, while assembly pitch can have different effects depending on other geometric and material conditions, such as the basket structure. The carbon-steel basket separating the fuel assemblies was found to have a significant negative reactivity influence. Hence, removal or degradation of this structure due to corrosion would significantly increase cask reactivity, especially in conjunction with flooding.

4.2 Thermal Effects on Near-Field Conditions

As discussed in Section 2.1, the heat generated by a steady-state criticality event would affect groundwater flow, radionuclide transport, near-field conditions, and DPC components. Of the many FEPs identified in that section, some were implemented in PFLOTRAN as a part of this study. A newly developed model of alteration of the smectite to illite in the backfill is discussed in Section 4.2.2. The already-existing capability of PFLOTRAN to model heat distribution in the EBS and the host rock is demonstrated in Section 4.2.3.

4.2.1 Waste Package Heat Generation

As in Price et al. (2019b), DPCs are assumed to contain 37 PWR assemblies from a reactor that was shutdown prior to 2000. Spent fuel decay heat in the base case is modeled using a piecewise linear curve that decreases monotonically from 4,002.73 W at time 0 (closure) to 249.02 W at 9,000 years after closure (Table 4-12). Without a criticality event, DPCs produce heat from radioactive decay throughout the 1,000,000-year analysis period. With a steady-state criticality event occurring in all waste packages between 9,000 and 19,000 years, each DPC produces about 400 W from the prompt fissions occurring during the criticality and produces additional decay heat from the increase in fission products (Section 4.2.3 and Section 5.1). Table 4-12 shows the total heat generated by both these sources, and Figure 4-22 illustrates the total heat generated for the two modeling cases over the entire simulation period. Note that previous analyses assumed that the steady-state criticality event produced 4kW of heat for 10,000 years (Price et al. 2019a,b). In contrast, the analyses described in this report assume that the steady-state criticality event produces 0.4 kW of heat; the reason for this assumption is discussed in Section 4.2.3.

Table 4-12. Total Heat Generation in a 37-PWR DPC With and Without Criticality

Time after Closure (years)	Total Heat without Criticality[a] (W)	Total Heat with Criticality[b] (W)
0	4,002.73	4,002.73
25	3,459.25	3,459.25
50	3,097.82	3,097.82
75	2,843.38	2,843.38
100	2,653.15	2,653.15
125	2,502.66	2,502.66
150	2,377.76	2,377.76
200	2,174.78	2,174.78
250	2,009.67	2,009.67
300	1,868.45	1,868.45
350	1,744.46	1,744.46
400	1,633.90	1,633.90
500	1,444.05	1,444.05
600	1,286.46	1,286.46
700	1,153.87	1,153.87
800	1,041.46	1041.46
900	945.72	945.72
1,150	762.89	762.89
1,400	638.45	638.45
1,650	552.99	552.99
1,900	493.68	493.68
2,150	451.92	451.92
2,400	421.97	421.97
2,900	383.32	383.32
3,900	343.34	343.34
4,900	319.02	319.02
5,900	299.20	299.20
6,900	281.51	281.51
7,900	265.36	265.36
8,900	250.52	250.52
9,000	249.02	649.02
9,050	248.31	897.47
9,100	247.61	899.16
9,500	242.10	901.65
10,000	235.47	898.92
11,000	222.97	889.36
12,000	211.43	879.13
15,000	181.70	852.13
18,000	157.89	830.91
19,000	151.01	824.88
20,000	144.59	154.29
21,025	138.48	146.03
21,100	138.05	145.50
21,250	137.19	144.46
21,500	135.77	142.76
22,000	133.00	139.51
23,000	127.72	133.43
49,900	54.18	54.17
99,900	18.76	19.13
199,900	9.78	10.44
499,900	8.47	8.94
999,900	6.52	6.75

NOTE: [a] For the base case, all waste packages breach at 9,000 years but don't see an increase in heat.

[b] For the steady-state criticality case, between 9,000 and 19,000 years after closure all waste packages are critical with the total heat shown above.

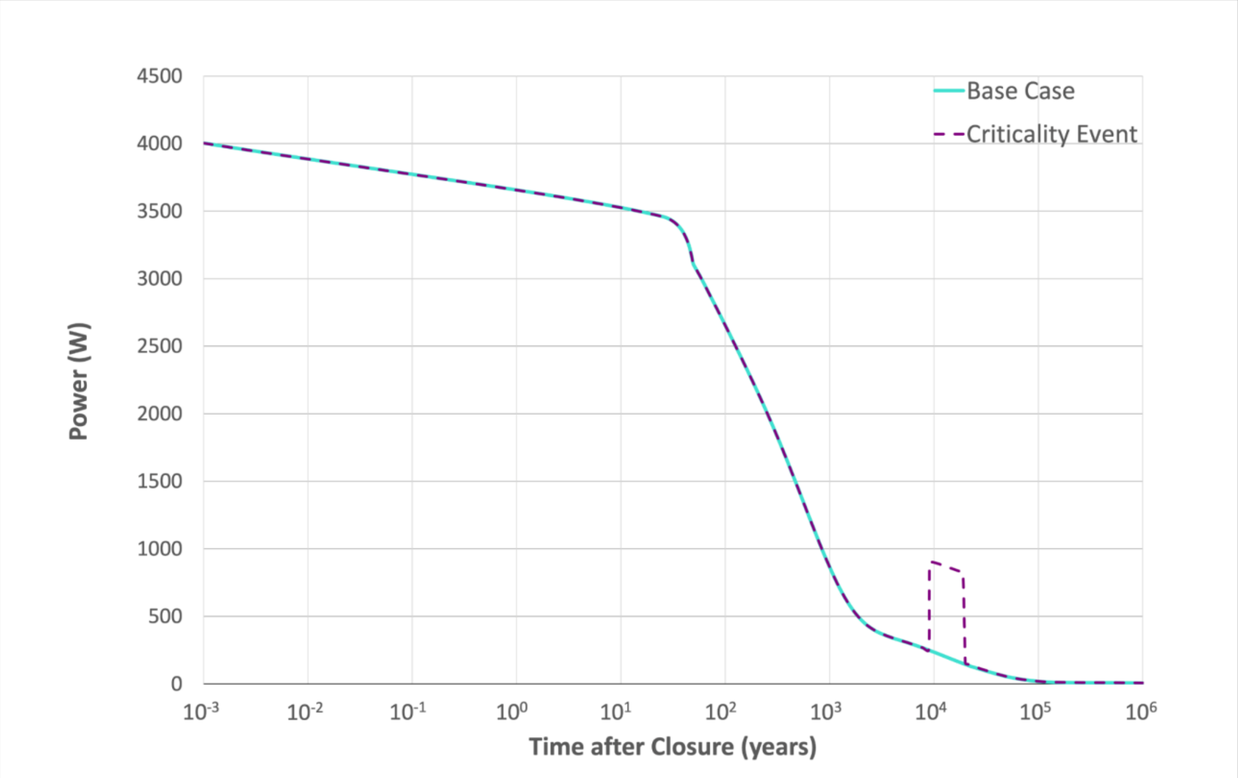

Figure 4-22. Total Heat Generation Comparison per 37-PWR DPC over the 1,000,000-Year Simulation for the Base Case and Steady-State Criticality Case

4.2.2 Smectite-to-Illite Transition

In a repository, the waste package is surrounded by an EBS containing a buffer of bentonite, which provides an effective barrier to radionuclide transport because of low hydraulic conductivity and favorable swelling characteristics. Bentonite is comprised largely of the montmorillonite mineral of the smectite group, which has an articulated, laminar structure allowing for the adsorption of water and subsequent expansion. Thermodynamic equilibrium of the smectite can be affected by the silica reactivity and potassium concentration in the repository environment (Karnland and Birgersson 2006). A potassium cation (K^+) can act as a counter-ion and affect the net-negative layer charge of the smectite. If quartz (SiO_2) can precipitate (crystallize) in the presence of potassium, there is reduced water interaction and reduced swelling from the interlayer collapse in smectite as it transforms to illite. This loss of swelling capacity and plasticity from the smectite-to-illite (S–I) transition is susceptible to inducing volume shrinkage and increased permeability in the buffer. There is also a counteracting effect from increased radionuclide sorption on illite. This mineral transition is found to be correlated with temperature, so the transition can be driven by elevated waste package temperatures during a criticality event.

PFLOTRAN has reactive transport modeling capabilities that could potentially be used to account for the reagents of the S–I transition, including quartz, potassium, sodium, etc. However, changes in soil physical properties corresponding to such mineral reactions have not been implemented. Rather than introduce physical changes in materials via the reactive transport side of the code, a reduced-order model can be used on the flow side to handle material transformations (including the S–I transition) and remove dependence on chemical parameters.

In this new model, the approach assumes that the S–I transition can be directly translated into a change in the original permeability and sorption characteristics. The scale of this change would have to be estimated a priori as part of the surrogate model. Furthermore, it must be assumed that the geochemical conditions needed for illitization are present either at time zero or when the threshold temperature is exceeded.

Alteration of the buffer permeability is considered part of an irreversible time- and temperature-dependent mineral transition. The rate of illitization is temperature dependent and the reaction only takes place when the temperature of a grid cell is above the user-specified threshold (default of 0°C). The rate of illitization is used to determine the fractional increase in illite in the material for a given time step. In a sense, the surrogate model incorporates the effects of mineral phase transitions without detailed reactive transport calculations and without modifying the gridded domain despite the decrease in buffer swelling capacity.

The time rate of change of smectite into illite is taken from the Huang et al. (1993) study and shown in Equation 4-1 for a given time step $i+1$.

$$-\left.\frac{df_S}{dt}\right|^{i+1} = \begin{cases} [K^+]\cdot\left(f_S^i\right)^2\cdot A\exp\left(-\dfrac{E_a}{\mathcal{R}\cdot T^{i+1}}\right) & T^{i+1}\geq T_{th} \\ 0 & T^{i+1}<T_{th} \end{cases} \qquad \textit{Equation 4-1}$$

The equation is based on the potassium cation concentration $[K^+]$ in mol/L and the previous smectite fraction f_S^i, where A is the frequency term in L/(mol·s), E_a is the activation energy in J/mol, $\mathcal{R}$ is the ideal gas constant, T^{i+1} is the temperature in Kelvin of the grid cell, and T_{th} is the threshold temperature below which the reaction does not take place. The value of $[K^+]$ is currently implemented as a fixed input value and is not evaluated from transport. The expression implies that, at steady-state temperature, the rate of illitization is reduced as more smectite is replaced with illite.

By integrating Equation 4-1 over the time period, the smectite fraction is evaluated in Equation 4-2.

$$f_S^{i+1} = \frac{f_S^i}{1-[K^+]\cdot A\exp\left(-\dfrac{E_a}{\mathcal{R}\cdot T^{i+1}}\right)\cdot\left(t^{i+1}-t^i\right)\cdot f_S^i} \qquad \textit{Equation 4-2}$$

The illite fraction is defined in Equation 4-3 as the complement of the smectite fraction. For this reason, the code only keeps track of f_S as a variable for checkpointing and output.

$$f_I^{i+1} = 1 - f_S^{i+1} \qquad \textit{Equation 4-3}$$

The change in a given permeability component k_j^{i+1} at time step $i+1$ as a result of illitization is computed with Equation 4-4 using the proportional change in the smectite fraction and a shift factor C_k along with the original permeability tensor k_j^0.

$$k_j^{i+1} = k_j^0\left[1+\left(\frac{f_I^{i+1}-f_I^0}{f_S^0}\right)\cdot C_k\right] \qquad \textit{Equation 4-4}$$

This equation suggests that when all the original smectite is transformed to illite, the permeability has been modified by a factor of $1+C_k$. The original permeability is employed as opposed to a recursive solution to maintain the relevance of C_k if a simulation needs to be restarted. This reference permeability tensor is saved within the illitization object before it is replaced with the checkpoint value in the auxiliary variables. Also, given the intermittent nature of the function's temperature dependence (via the temperature threshold), Equation 4-4 ensures that the permeability does not change if the mineral fractions do not change over a given time step.

4.2.3 Heat Distribution in EBS and Host Rock

In past simulations (Price et al. 2019a,b), the model domain included only a single waste package, and that waste package experienced a steady-state postclosure criticality event. For the current work, the steady-state criticality case assumes all the waste packages in the repository fail 9,000 years after repository closure, fill with water, and achieve a state of steady-state criticality. This assumption was made for calculational expediency and does not represent an expected event. Future studies will examine the effects of varying the onset of postclosure criticality spatially and temporally.

PFLOTRAN's governing equations include the necessary equations to model heat transport in the repository, so it was not necessary to modify PFLOTRAN to account for a nonuniform heat distribution in the repository. Figure 4-23 depicts an *x*–*z* (i.e., vertical) slice through the model domain from the centermost waste package within the repository of the half-symmetry model. The various colors reflect the temperature distribution at 19,000 years postclosure, which is when the 10,000-year-long, steady-state criticality event is assumed to terminate. This figure shows the extent of repository heating from the steady-state criticality event. The maximum temperature reached at the centermost waste package of the half-symmetry model, called "wp0," was 266.1°C at 19,000 years.

Note that the temperature distribution below and above the repository is not uniform; the heat generated by the criticality event extends farther below the repository than it does above the repository. Two explanations for this nonuniform temperature distribution have been identified. One explanation is that the thermal properties of the geologic layers above and below the hypothetical repository are different from each other, resulting in a nonuniform flow of heat. The other explanation is that this situation is an artifact of the distance from the repository to the lower boundary and the imposed lower boundary condition. This nonuniform temperature distribution affects radionuclide diffusion, as discussed in Section 5.2. One other thing to note is that the temperature gradient above the repository does reach the top of the model. A temperature difference of ~2°C at 19,000 years occurs (not shown) directly above the centermost region of the repository at the top face of the model domain.

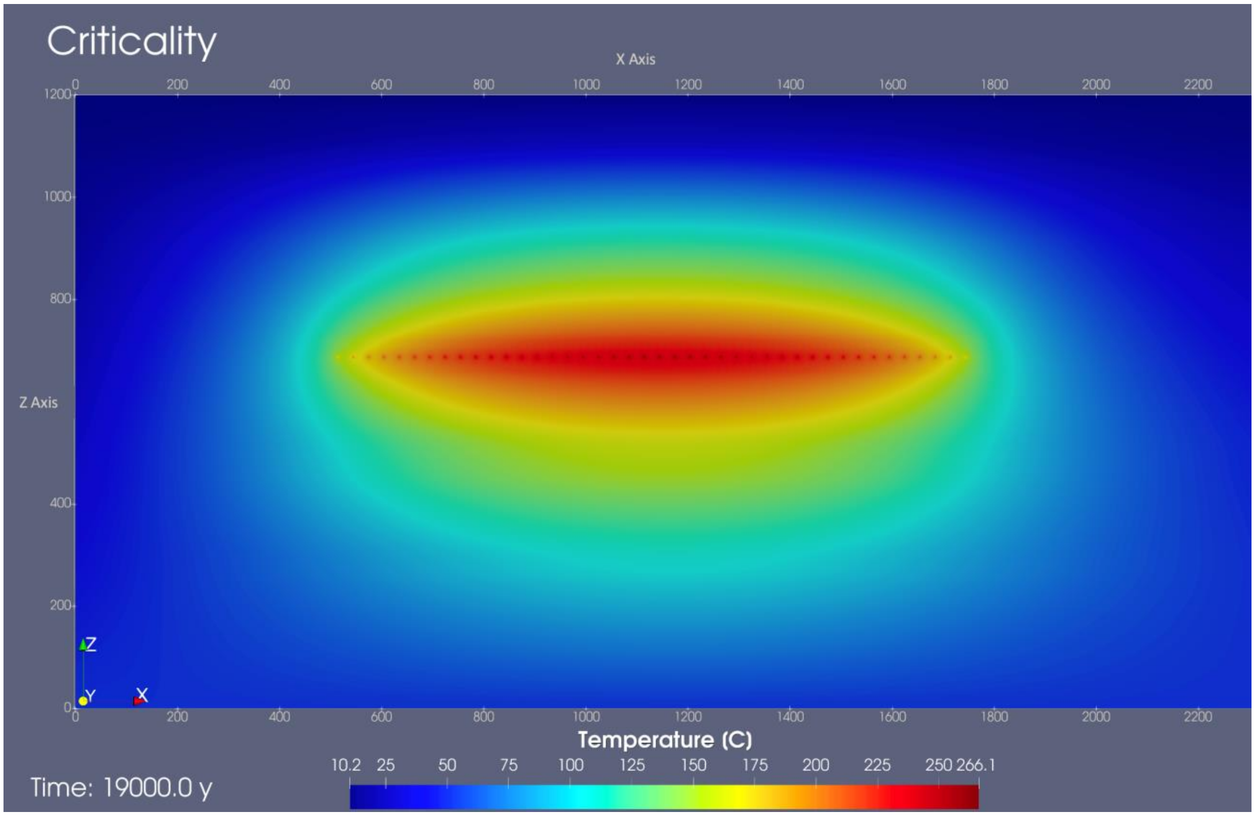

NOTE: Figure shows *x*–*z* (vertical) slice through the model domain from the centermost waste package within the repository of the half-symmetry model.

Figure 4-23. Repository Temperatures after 0.4 kW, 10,000-Year-Long, Steady-State Criticality Event at 19,000 Years

Figure 4-24 is an *x*–*y* (horizontal) slice through the model domain showing the temperature at 19,000 years postclosure, which is when the 10,000-year-long, steady-state criticality event is assumed to terminate. As expected, the centermost waste packages reach the highest temperature, 266.1°C.

Previous thermal analyses of a single waste package found that, based on the ability of the backfill and host rock to transport heat away from the waste package, the maximum power that could be generated by a steady-state criticality event in the hypothetical shale repository is about 4 kW. This value relies on the assumption that the boiling of water terminates a criticality event, imposing a maximum waste package temperature of 264°C. However, imposing this maximum waste package temperature and assuming that all the waste packages experience a steady-state criticality event at the same time results in limiting the power that can be generated by the innermost waste packages to 0.4 kW. This heat is from both the prompt fission associated with the criticality event and fission product decay heat. Note that the calculated change in radionuclide inventory assumes a 4 kW, 10,000-year-long, steady-state criticality event (Section 4.5), which is about 10 times higher than what is assumed in the repository-scale PA calculations documented here. For the only radionuclide that contributes to dose, ^{129}I, this situation has the effect of overestimating the increase in ^{129}I inventory due to steady-state criticality by about a factor of 10.

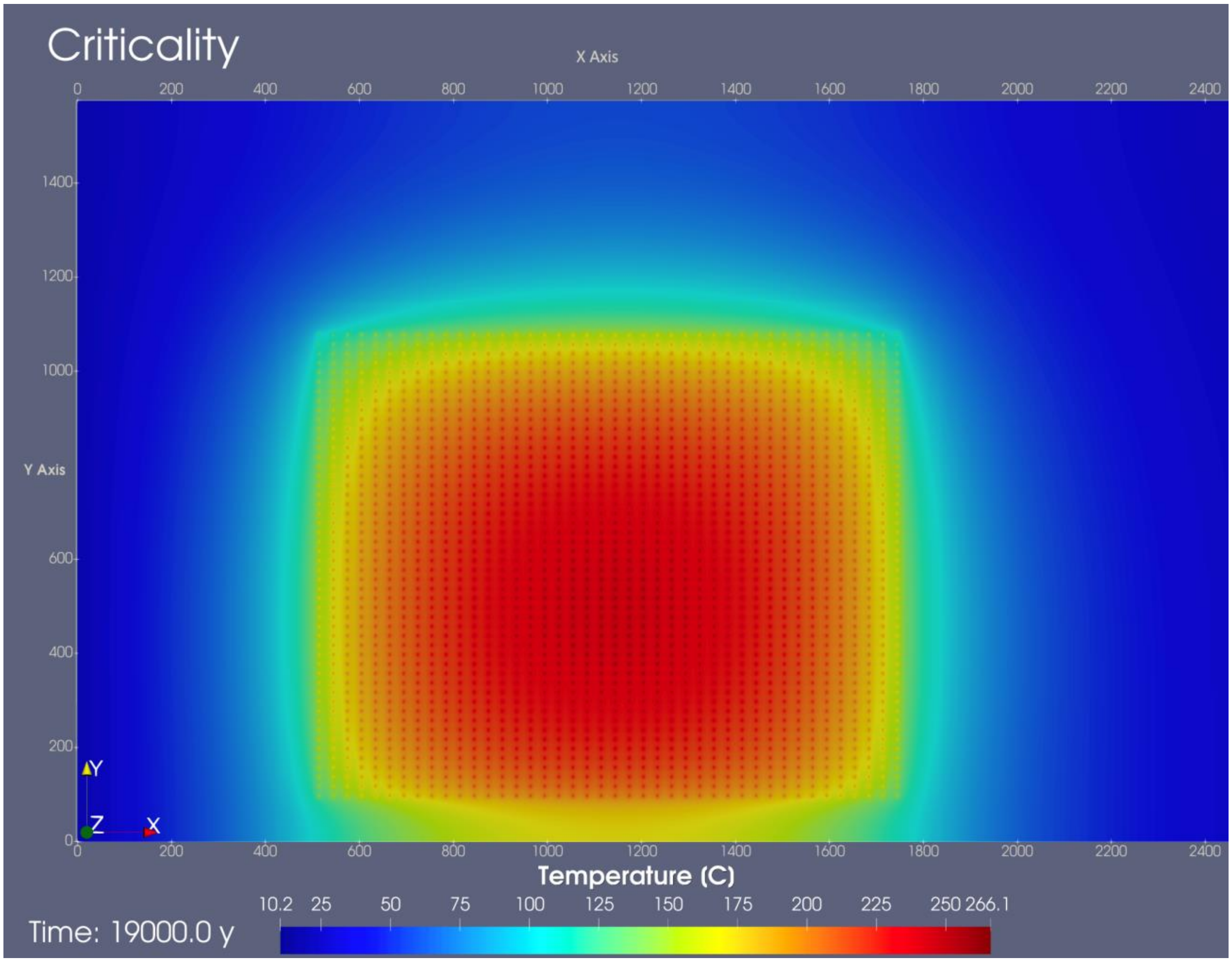

NOTE: Figure shows *x*–*y* slice through repository.

Figure 4-24. Repository Temperatures after 0.4 kW, 10,000-Year-Long, Steady-State Criticality Event at 19,000 Years

4.3 Thermal Effects on Flow and Transport

As discussed in Section 2.1, the heat generated by a steady-state criticality event can affect groundwater flow and radionuclide transport. PFLOTRAN (Lichtner et al. 2020a,b) possesses the ability to model thermal effects on groundwater flow and on diffusion and advection of radionuclides. It factors in the equation of state for water to determine densities, enthalpies, viscosities, etc. during the thermal evolution of the system. When PFLOTRAN is run in GENERAL mode, the conservation of energy from heat emitting sources is coupled with the conservation of momentum for the mass flux of groundwater and radionuclides in the porous medium.

This section presents an analysis of thermal effects on groundwater flow for the hypothetical unsaturated alluvial repository (Section 4.3.1) and an analysis of the effects of illitization on transport properties in the backfill (Section 4.3.2).

4.3.1 Thermal Effects on Groundwater Flow in the Unsaturated Alluvial Repository

The hypothetical unsaturated alluvial model was described in Section 3.2.2. Modeling the occurrence of steady-state criticality in the hypothetical unsaturated alluvial model is described below.

At 9,000 years, the top of the DPC outer shell is assumed to be breached, which is modeled by replacing some or all of the mesh cells associated with the top of the DPC shell with those associated with drift backfill. For this analysis, the geometry of the DPC is presumed to remain unaltered except for the loss of the top part of that shell. That is, the low permeability cells of the DPC shell sides and bottom remain intact, allowing the waste package to fill with water. The criticality event is assumed to start after the DPC has filled to ~1 m depth with water. For each combination of percolation rate (see below) and assumed thermal and hydrological properties of the host medium, backfill, and DPC internals, different power outputs from the criticality event are considered. The objective is to identify the power output that could be produced by a criticality event without driving water out of the DPC by boiling and evaporation.

The deep percolation rate for the reference case is 2 mm/yr. Variant cases of 1 and 10 mm/yr were also considered. It should be noted that a percolation rate of 10 mm/yr is very high for an unsaturated site. Other variant cases explore sensitivity to how the DPC internals are represented and the fraction of the waste package shell that is breached on top.

An analysis was done to identify what TH conditions and criticality power output might lead to retaining enough water in a breached DPC in unsaturated alluvium to maintain a steady-state criticality event. This analysis assumes that the DPC is breached at 9,000 years postclosure. The criticality event starts only after the waste package has filled with water.

Figure 4-25 shows the simulated liquid saturation index inside the DPC for several different power levels. Infiltrated water fills the DPC to a level of about 1 m around year 17,100 (Figure 4-25a), at which time the criticality event is assumed to start. Assuming a 50 W power output from the criticality event, the DPC remains filled with water for at least 1,000 years after the criticality event (i.e., at 18,100 years postclosure; Figure 4-25b). In contrast, 100 W power output from the criticality event will drive water from the DPC by 500 years (i.e., at 17,600 years postclosure) and stop the criticality event (Figure 4-25c). Figure 4-25d shows that the waste package would be completely dry if the power level was 100 W for 1,500 years (i.e., at 18,600 years postclosure). Thus, the lower bound on the power output from the criticality event is 50 W, and the upper bound is 100 W.

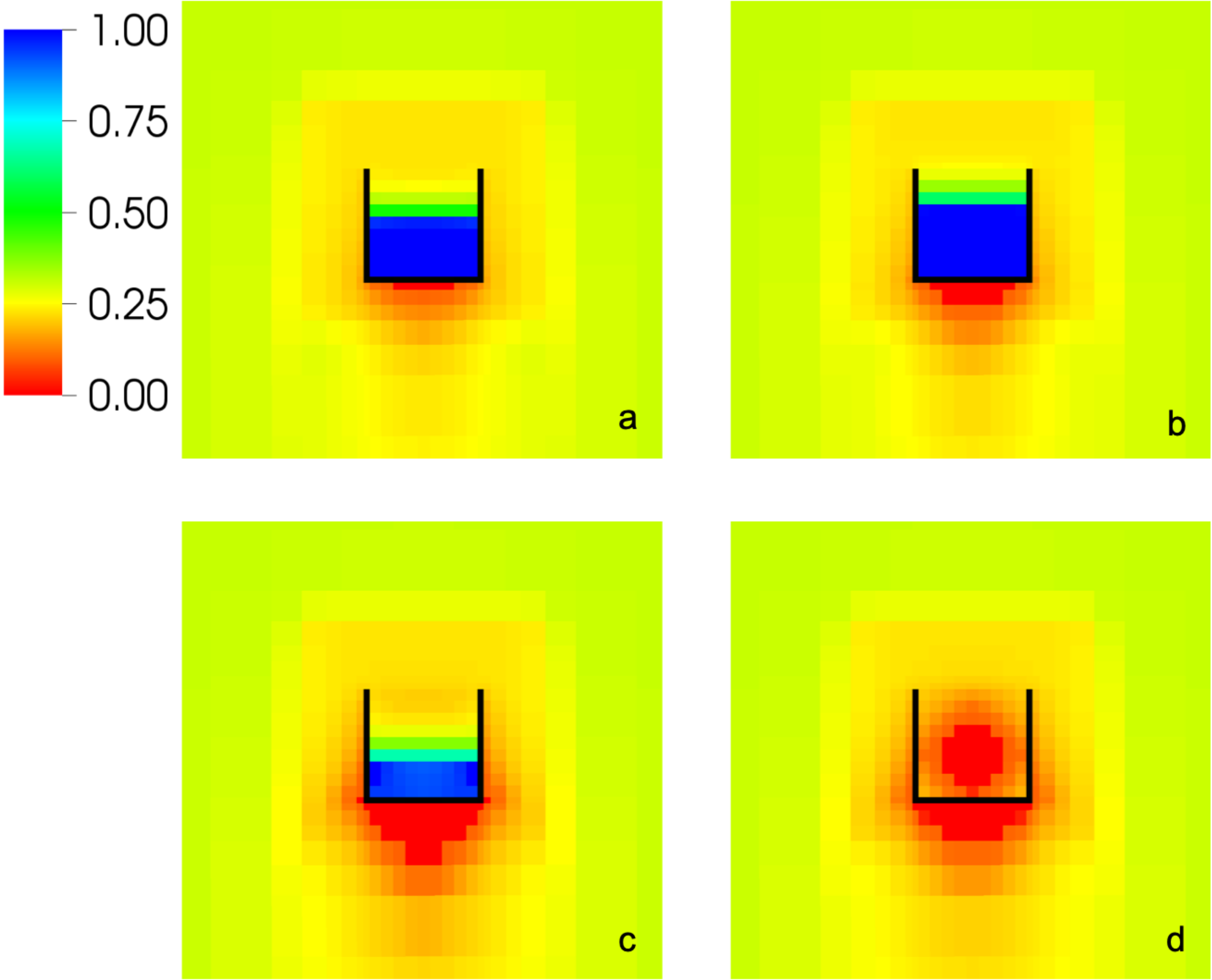

NOTE: Black lines indicate the DPC shell.

Figure 4-25. Simulated Liquid Saturation Index inside the DPC for Several Different Power Levels at (a) 17,100 Years (DPC fills allowing criticality event to initiate); (b) 18,100 Years (50 W power output); (c) 17,600 Years (100 W power output); and (d) 18,600 Years (100 W power output)

Sensitivity to various modeling assumptions is shown in Table 4-13. Two of the sensitivity cases pertain to deep percolation rates that are different from the reference case of 2 mm/yr. In the partial breach case, the assumed breach in the top of the DPC is 0.6 × 1.0 m^2 or approximately 14% of the cap area. The final two sensitivity cases address representation of the DPC internals. The reference case uses a dry thermal conductivity κ_{dry} of 1.0 W/(m·K) for the DPC internals and sets the moisture retention properties to be the same as the drift to prevent the formation of a capillary barrier. One of the sensitivity cases decreases the dry thermal conductivity to 0.5 W/(m·K). The other sensitivity case for DPC internals sets the moisture retention properties to be that of coarse gravel.

Results are sensitive to the deep percolation rate. For a 1 mm/yr rate, decay heat alone is sufficient to delay water return to the DPC to 25,300 years postclosure. Moreover, only 50 W of additional power from a criticality event is sufficient to drive off the water. For a 10 mm/yr percolation rate, the DPC fills with water faster (year 10,600) and between 300 W and 400 W of power output from the criticality event can be maintained.

If the top of the DPC is only partially breached, then it takes longer to fill the DPC as compared to the reference case of a full breach. Greater power output from the criticality event can also be supported. In particular, 100 W is sufficient to drive off water in the fully breached case, but not in the partially breached case because the partially intact lid reduces the rate of diffusion-driven loss of water vapor from the DPC internals.

A lower thermal conductivity in dry conditions κ_{dry} also delays the return of water to the DPC. Lowering κ_{dry} from the reference case assumption of 1 W/(m·K) to 0.5 W/(m·K) delays filling of the DPC and initiation of the criticality event from 17,100 years to 18,600 years. This change is expected because the lower thermal conductivity results in a warmer DPC and steeper temperature gradient, thus increasing the evaporation rate of the incoming water.

PFLOTRAN is based on a porous-medium formulation and can only provide an approximate representation of the heat and mass transport internal to the DPC. As described in Section 5.1, heat transfer processes can be accurately represented with a temperature-dependent thermal conductivity. Transport of water mass is more approximate. In particular, porous-medium representations require a relationship between capillary pressure and water content, which describes moisture retention in the porous medium and is uncertain for the DPC internals. The reference case sets the water retention properties of the DPC internals equal to those of the drift to prevent the formation of a capillary barrier that would delay water from entering the DPC. An alternative assumption is to assume weaker moisture retention for DPC internals. The last variant case sets the water retention properties inside the DPC to those of a coarse gravel, which is regarded as more realistic than the reference case. As expected, weaker retention does delay filling of the DPC, but the effect is modest (17,700 years as opposed to 17,100 years for the reference case). This result confirms that the reference case assumption provides a reasonable and conservative bound.

Table 4-13. Results for Different Sensitivity Cases

Case	Time of Criticality Event (years postclosure)	Lower Bound on Power Output (W)	Upper bound on Power Output (W)
Reference (deep percolation = 2 mm/yr)	17,100	50	100
Deep percolation = 1 mm/yr	25,300	0	50
Deep percolation = 10 mm/yr	10,600	300	400
Partial breach	22,600	100	200
κ_{dry} of DPC internals = 0.5 W/(m·K)	18,600	50	100
Weaker water retention for DPC internals	17,700	50	100

In this model, various background percolation rates were sampled to identify the conditions under which a given power produced by a criticality event would not completely drive out water from a DPC through evaporation and boiling. These multiphase simulations were run in PFLOTRAN and proved numerically very challenging due to the balancing of competing evaporative, boiling, and capillary forces acting on the water in the domain. To resolve these processes and achieve numerical convergence, the simulator was forced to take prohibitively small, time steps precluding a more detailed analysis of this system.

Over the course of the last year under the PFLOTRAN Development work package (Nole et al. 2021), steps were taken to address limitations in PFLOTRAN relating to multiphase flow near the residual water saturation limit of the capillary pressure curve, which until now had been treated with a hard cap on capillary pressure at water saturation values below residual saturation. By smoothing this cusp, the development team saw dramatic improvement in runtime and time stepping of multiphase flow simulations with boiling and evaporation. This function-smoothing feature for capillary pressure and relative permeability has allowed users to finish many previously unrunnable simulations.

This smoothing functionality for capillary pressure and relative permeability was released in PFLOTRAN in June 2021, and an effort is currently underway to apply these smoothing algorithms to the unsaturated alluvium model for DPC criticality consequence analysis. This model is currently being reworked to include these features as part of an inter-laboratory effort between the PFLOTRAN development team at Sandia National Laboratories (SNL) and PFLOTRAN modelers at ORNL.

4.3.2 Effects of Illitization of Backfill

4.3.2.1 Permeability Test Problem

A simple problem was devised in PFLOTRAN to test the ability of the S–I model to modify permeability given the times and temperatures needed for the mineral transformation in backfill in a hypothetical saturated, shale repository. The test domain is a water-saturated block of soil measuring 4 × 4 × 20 m with a porosity of 25%, a tortuosity of 50%, a permeability of 10^{-12} m^2, and a hydrostatic pressure of 1 MPa. The soil has an initial temperature of 20°C, a density of 2,650 kg/m^3, and a heat capacity of 830 J/(kg·K). The domain is discretized into 1 m^3 grid blocks and has a boundary condition at the northern face with water at 5 MPa and 260°C. A 1-m-thick layer of smectite-rich bentonite buffer exists 2 m into the soil from the northern face, as shown in Figure 4-26.

The buffer is split into "Buffer 1" on the east with an initial permeability of 10^{-20} m^2 and "Buffer 2" on the west with an initial permeability of 10^{-16} m^2. The two buffer regions have unique initial smectite fractions but otherwise have the same material properties, including a porosity of 35%, a density of 2,700 kg/m^3, a heat capacity of 830 J/(kg·K), and a default TCC from 0.6 to 1.5 W/(m·K). There is 90% initial smectite in Buffer 1 and 75% in Buffer 2, with a reaction threshold temperature of 40°C in the first region and 60°C in the second. The activation energy is defined as 1.18×10^5 J/mol, the frequency term is 8.08×10^4 L/(mol·s), and the potassium concentration is 2.16×10^{-3} M. The permeability in each material is set to increase by 1,000-fold when the fraction of illite reaches 100% (i.e., $C_k = 999$).

Results for temperature and permeability over time are shown in Figure 4-27 for Buffer 2 grid cells. The boundary condition introduces a temperature gradient that heats the region beyond the threshold temperature of 60°C around 0.0244 years (9 days). A maximum steady-state temperature of 260°C is reached by 94.9 years, while the fastest rate of change of the permeability from the illitization reaction occurs at around 11.7 years. A significant fraction of smectite is transformed to illite by 10^4 years, with a final illite fraction of 99.5% compared to the original fraction of 25%. This transformation corresponds to increase in permeability to 9.94×10^{-14} m^2 from the original 10^{-16} m^2. Likewise, in Buffer 1, the permeability increases from 10^{-20} m^2 to 9.95×10^{-18} m^2 with a final illite fraction of 99.5% compared to the original 10%. These results demonstrate the asymptotic behavior expected from Equation 4-2 and Equation 4-3 as the smectite fraction decreases over time. This behavior is plotted visually in Figure 4-28, which indicates that the smectite quantities in the two buffer regions eventually align despite different initial conditions.

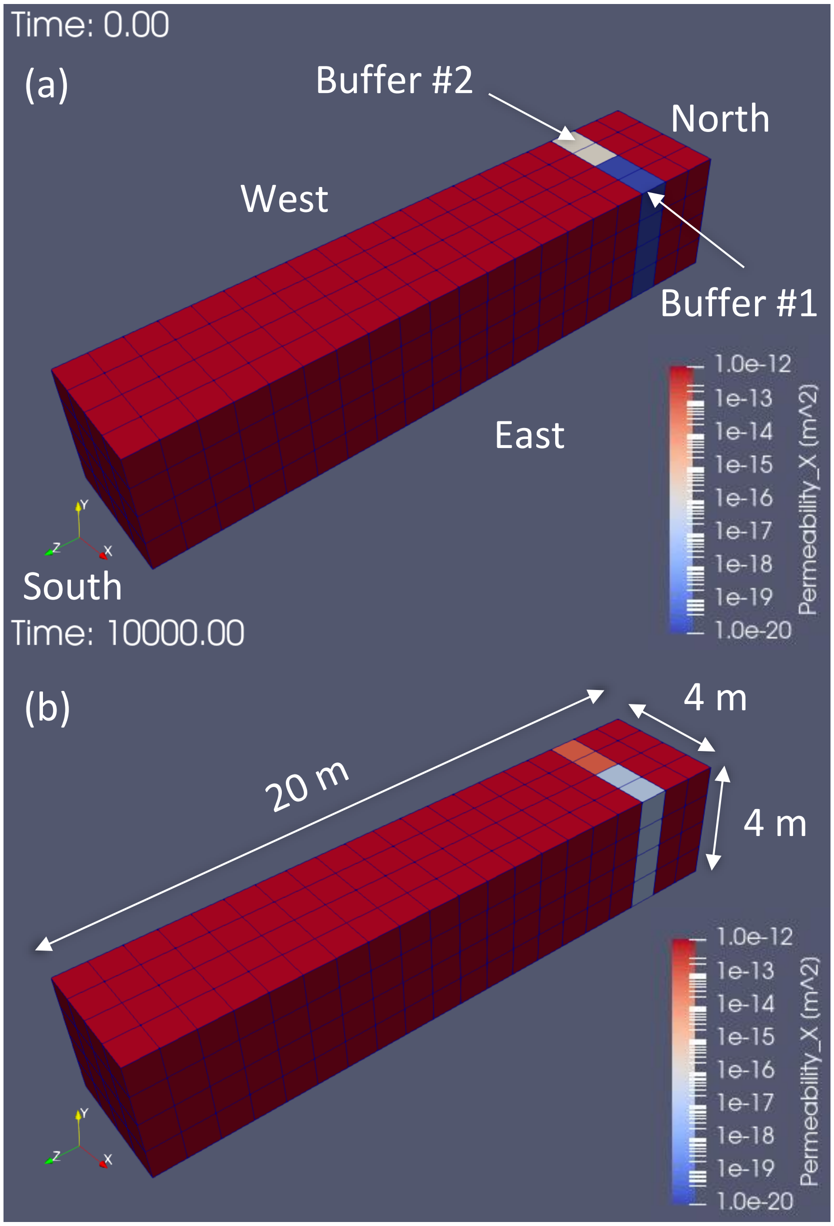

Figure 4-26. Test Domain Showing Change in Permeability in the Buffer from (a) 0 Years to (b) 10^4 Years

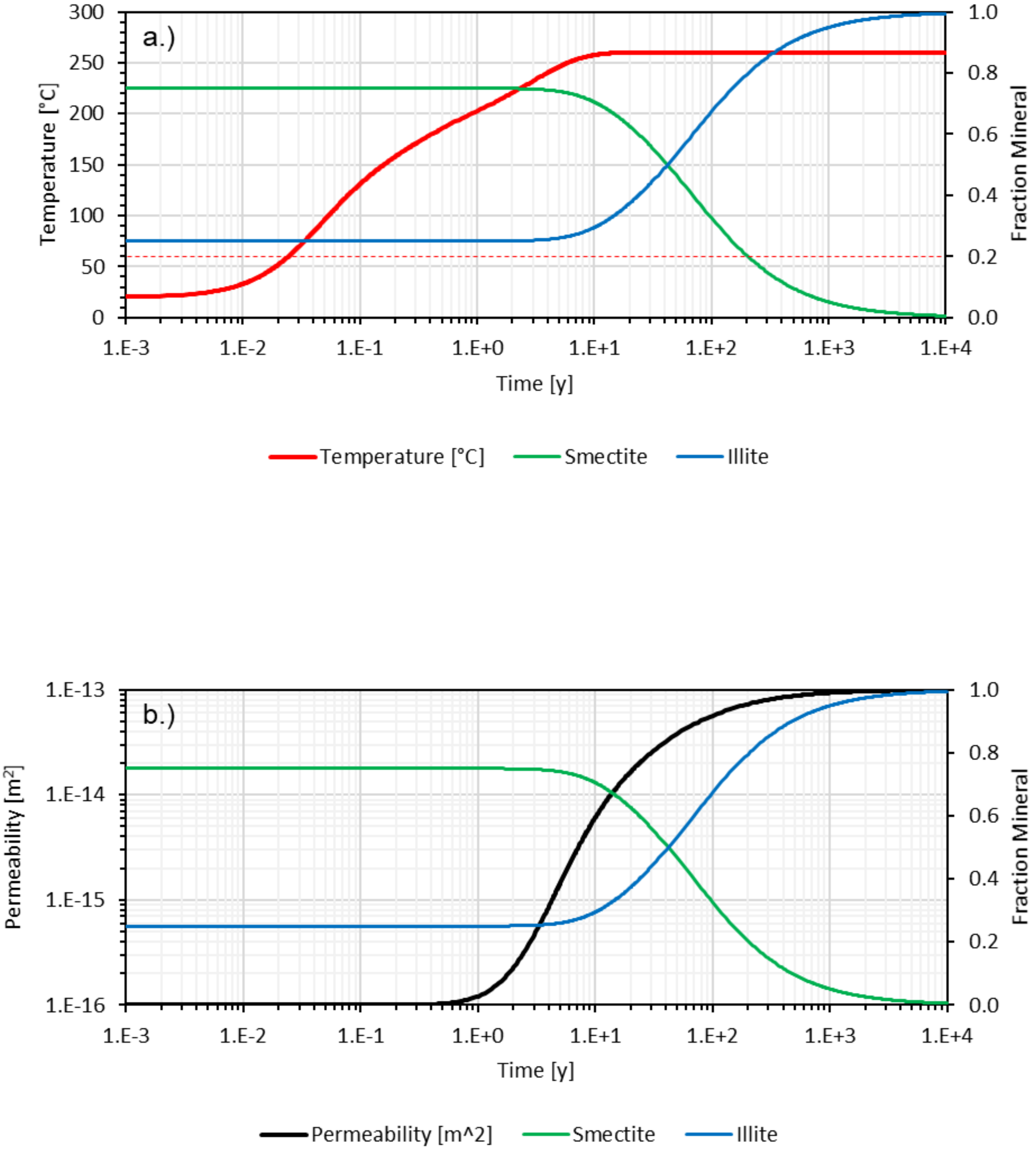

Figure 4-27. (a) Temperature and (b) Permeability over Time for Grid Cells Undergoing S–I Transition in Buffer #2 in the Test Problem

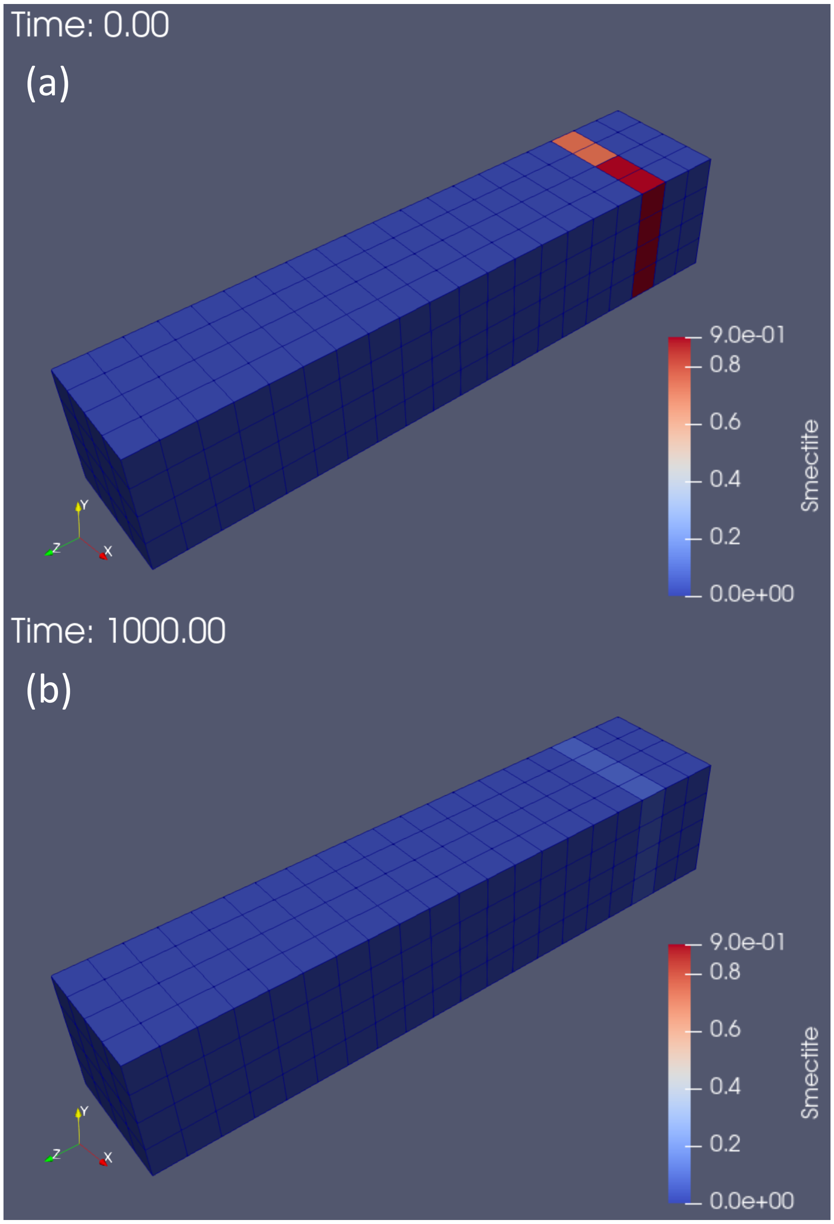

Figure 4-28. Smectite Fractions at (a) 0 Years and (b) 10^3 Years Using a Scale from 0% to 90%

4.3.2.2 Future Work

When the plots were generated for Section 4.3.2, the illitization feature formed its own module in the same hierarchy as characteristic curves and TCCs. It was applied within GENERAL mode during the modification of those auxiliary variables. The plan is to expand the overall programming into a generalized module for material transformations that extend beyond the effects from illitization, with illitization being just one type of process that can affect the system permeability.

The illitization type can be expanded with additional models. Another model for the illitization rate is provided by Cuadros and Linares (1996) and is shown in Equation 4-5. In this expression, the potassium concentration is modified with the exponent m and the order for the smectite fraction is raised to order n. The rate constant k is also a temperature-dependent Arrhenius term.

$$-\frac{df_S}{dt} = [K^+]^m {f_S}^n \cdot k(T) \qquad \textit{Equation 4-5}$$

Using the time-step notation from earlier, the time-integrated value for the smectite fraction is shown for two solutions of n in Equation 4-6. When employing $m = 1$ and $n = 2$, the solution for the Huang et al. (1993) is obtained, demonstrating that the Cuadros and Linares model is a generalization to arbitrary order. Therefore, including such an option will expand modeling fidelity and impart more realism to a simulation. It can also be convenient for fitting to on-site data for a given PA.

$$f_S^{i+1} = \left\{[K^+]^m \cdot k(T) \cdot (n-1)\left(t^{i+1} - t^i\right) + \left(f_S^i\right)^{1-n}\right\}^{1/1-n}, n > 1$$

Equation 4-6

$$f_S^{i+1} = f_S^i \cdot \exp\left\{-k(T) \cdot [K^+]^m \cdot \left(t^{i+1} - t^i\right)\right\}, n = 1$$

The next conceptual development to take place for the feature will be expansion of S–I effects to sorption distribution coefficient (K_d). This effort may require special interfacing with the existing reactive transport process models in PFLOTRAN. Use of the model will also be expanded beyond the buffer region into the host rock, as the temperatures of the host rock can become elevated and susceptible to similar mineralogical changes affecting permeability and K_d.

4.4 Thermal Effects on DPC Components

As mentioned in Section 2.1.5, a model of the corrosion of grid spacers that includes the effects of radiolysis was developed and implemented in PFLOTRAN. The model is based on rates of Zircaloy corrosion proposed by Brady and Hanson (2020). This process is important to repository performance because it represents one of the mechanisms for permanently terminating the criticality event. The PFLOTRAN implementation of Zircaloy grid spacer degradation is described below.

Although the grid spacer degradation model is now available in PFLOTRAN, it was not used in the analyses described in Section 5. Implementing the grid spacer model in the PA calculations would require a tighter coupling between neutronics and depletion calculations and the PA calculations than was available when this report was prepared. The reason is that implementing the grid spacer degradation model in PA calculations leads to termination of the criticality event at times that are not known a priori. However, estimating the change in radionuclide inventory, which was done prior to running PFLOTRAN, requires knowing a priori how long the criticality event will last. For the PA calculations described in

Section 5, it was assumed that the steady-state criticality event lasted 10,000 years. Future efforts will focus on developing a way to estimate inventory changes without having to know a priori when the steady-state criticality event will terminate.

4.4.1 Overview

PFLOTRAN now features a grid spacer degradation option for waste packages containing SNF. This option is a time-, temperature-, and saturation-dependent corrosion model that monitors the fraction of uncorroded Zircaloy in the SNF assemblies, or the “grid spacer vitality.” Its purpose is to introduce a corrosion model that in turn provides a criticality termination mechanism for steady-state criticality in SNF. When the grid spacers (Figure 4-29) have extensively degraded, the fuel rods are assumed to lose their critical configuration from spatial self-shielding effects and reduced moderation from interstitial water upon rod collapse/consolidation (Section 6.2.2.5).

The feature is implemented at the same hierarchy as the waste form mechanism and criticality mechanism within the waste form process model. It requires input of the total mass and surface area of all assemblies in the package, along with governing rate parameters. Since the model treats the corrosion phenomenon globally within the waste package with no fidelity for individual assembly characteristics, the user must employ averaged values for the assemblies in the package. When the grid spacer vitality falls below 1% of the original total mass, all criticality events associated with the waste package permanently cease because of an assumed loss of critical configuration.

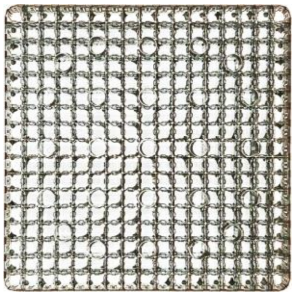

Figure 4-29. Zircaloy Grid Spacer for a 17 × 17 PWR Assembly

4.4.2 Grid Spacer Degradation Model

The grid spacer vitality (V) is determined using the corrosion rate (R) for time steps t^i to t^{i+1} and a total initial grid mass M_0^{SG}, as shown in Equation 4-7.

$$V^{i+1} = V^i - \frac{R^{i+1} \cdot \left(t^{i+1} - t^i\right)}{M_0^{SG}} \qquad \text{Equation 4-7}$$

To account for the role of water level in a system with evolving saturation (e.g., unsaturated alluvium), a saturation-dependent ramp function can be used to alter the corrosion rate given partial inundation of the assemblies. This saturation-dependent ratio $f(\bar{S}_l)$ for water level correction is defined in Equation 4-8, where S_l^{exp} is the saturation for which the grid spacers are considered fully inundated with water.

$$f\left(\bar{S}_l^{i+1}\right) = \begin{cases} \dfrac{\bar{S}_l^{i+1}}{S_l^{exp}} & \bar{S}_l^{i+1} < S_l^{exp} \\ 1 & \bar{S}_l^{i+1} \geq S_l^{exp} \end{cases} \qquad \textit{Equation 4-8}$$

The corrosion rate is governed by an Arrhenius term with constant $\mathcal{C}$, activation energy Q, and the average waste package temperature $\bar{T}$. This term is further modified with the cumulative grid spacer surface area A_0^{SG} and $f(\bar{S}_l)$, as shown in Equation 4-9.

$$R^{i+1} = f\left(\bar{S}_l^{i+1}\right) \cdot A_0^{SG} \cdot \mathcal{C} \exp\left(-\frac{Q}{\mathcal{R} \cdot \bar{T}^{i+1}}\right) \qquad \text{Equation 4-9}$$

The grid spacer degradation model is intended to be combined with the neutronics surrogate model and illitization model to test interplay between the heat of criticality and the physical properties of the EBS. In addition, the new thermal modeling capabilities will be incorporated to demonstrate potential anisotropy effects within the larger heat transfer context.

4.4.3 Test Problem

The study team constructed a simple test problem to verify that the new model can successfully terminate steady-state criticality events in multiple waste forms. Since representative corrosion parameters would require long simulation times for the effects to be realized, artificially elevated parameters were employed for purposes of inspection. The test domain is a 4 × 4 × 20 m, water-saturated block of soil with a porosity of 25%, tortuosity of 1.0, permeability of 10^{-12} m^2, and hydrostatic pressure of 1 atm. The domain is discretized into 1 m^3 grid blocks; a boundary condition exists at the northern face (concurrent with the origin) with water at 1 atm and 100°C. The soil has an initial temperature of 20°C, a density of 2,650 kg/m^3, and heat capacity of 830 J/(kg·K). Thermal conductivity is governed by a default TCC from 5.5 to 7.0 W/(m·K), and the characteristic curve uses a Van Genuchten relationship for saturation and Mualem relationship for liquid and gas permeability.

Within the soil there are three regions defining waste forms of 4 m^3 volume at z = 3–5 m, 10–12 m, and 14–16 m, where all are defined at x = 2–4 m and y = 2–4 m (Figure 4-30). The waste form characteristics, as defined in the waste form process model block, are shown in Table 4-14, where the waste packages are numbered along the +z-axis. The waste packages all have unique breach times, waste form mechanisms, and criticality mechanisms, and WF (waste form) #1 and WF #2 also feature a grid spacer degradation mechanism. Of the criticality mechanisms, the start and end times are unique and overlap for some extent of time. The criticality mechanisms also feature the same time-dependent, decay heat dataset, which is one quarter of the heat emission used in Price et al. (2019b). For the short time period of the simulation, the dataset provides an essentially constant power output of 1 kW. Constant heats of criticality are employed for ss_crit_1 and ss_crit_3, while ss_crit_2 employs a temperature-dependent lookup table with a maximum of 4 kW (plotted in Figure 4-31) to test the mix of specifications. A critical water saturation is defined within each mechanism, while a critical water density is further specified for WF #1 and WF #3. As mentioned previously, the components of the grid spacer degradation mechanisms for WF #1 and WF #2 were selected to terminate steady-state criticality within the simulation period of 90 days. Therefore, the choices for $\mathcal{C}$ are very high and those for Q are low. Saturation dependence is active for spc_02 by specifying an S_l^{exp} of 80%, while it is inactive for spc_01.

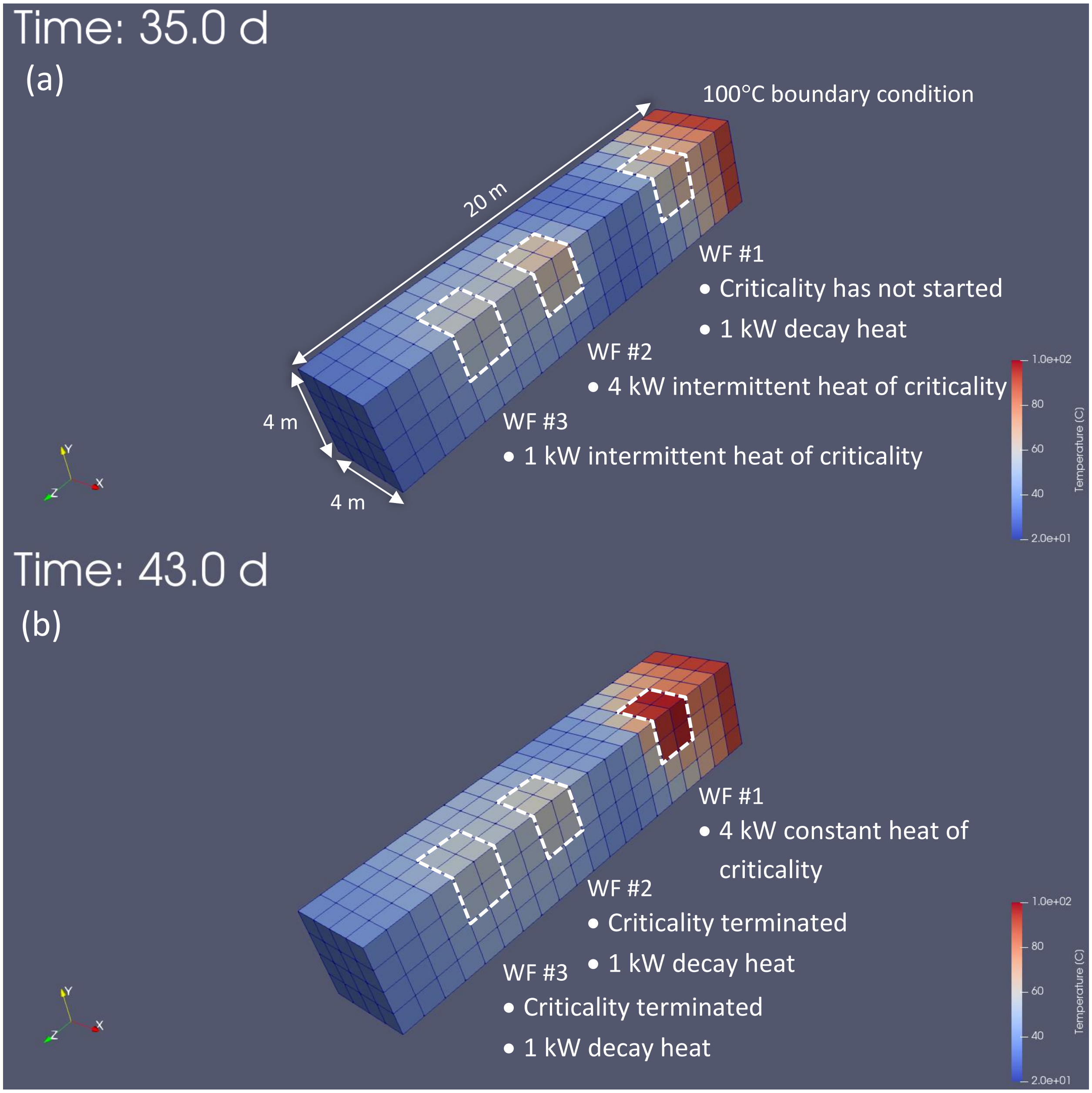

Figure 4-30. Diagram of Test Problem Showing Temperature at (a) 35.0 d and (b) 45.0 d

Table 4-14. Parameters Employed for the Zircaloy Grid Spacer Degradation Test Problem

PFLOTRAN Input	WF #1	WF #2	WF #3	Units
WASTE_FORM				
REGION	wf1	wf2	wf3	
CANISTER_BREACH_TIME	5.0d+0	1.0d+0	2.5d+0	d
MECHANISM_NAME	DSNF	CUSTOM	GLASS	
CRITICALITY_MECHANISM_NAME	ss_crit_1	ss_crit_2	ss_crit_3	
SPACER_MECHANISM_NAME	spc_01	spc_02	N/A	
END				
CRITICALITY_MECH				
NAME	ss_crit_1	ss_crit_2	ss_crit_3	
CRIT_START	4.0d+1	3.0d+1	5.0d+0	d
CRIT_END	7.0d+1	6.0d+1	9.0d+1	d
CRITICAL_WATER_SATURATION	6.0d-1	7.0d-1	3.0d-1	
CRITICAL_WATER_DENSITY	8.5d+2	N/A	9.0d+2	kg/m^3
HEAT_OF_CRITICALITY				
(C)ONSTANT_POWER/(D)ATASET	(C) 4.0d+0	(D) Figure 4-31	(C) 1.0d+0	kW
END				
END				
SPACER_DEGRADATION_MECHANISM				
NAME	spc_01	spc_02	N/A	
Q	5.75d+04	5.70d+04		J/mol
MASS $\left(\boldsymbol{M_0^{SG}}\right)$	8.00d+04	1.00d+05		g
SURFACE_AREA $\left(\boldsymbol{A_0^{SG}}\right)$	1.00d+03	2.20d+03		dm^2
EXPOSURE_LEVEL $\left(\boldsymbol{S_l^{exp}}\right)$	0.00d+00	8.00d-01		
C	2.50d+07	3.50d+07		mg/(s·dm^2)
END				

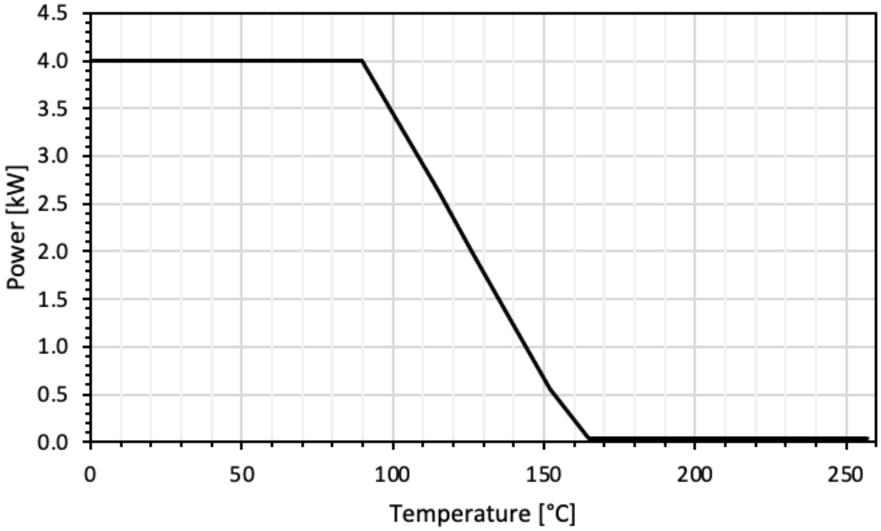

Figure 4-31. Heat of Criticality for Given Temperature during the Steady-State Criticality Event

4.4.4 Results

Information on the criticality source term and grid spacer vitality was reported through print statements and extracted from the standard output using a Perl script, and as such output options were not available as of this report. Figure 4-32 shows the grid spacer vitality within WF #1 and WF #2 along with their average temperatures. The vitality decreases monotonically with time as the average temperature increases in each waste package, which is indicative of a linearly increasing rate from Equation 4-9. However, the rates of degradation are observed to increase noticeably when the average temperature rises in each waste package. The degradation rate for WF #2 is less severe because it is reduced by the saturation-dependent term, where the exposure limit of 80% is crossed at 31 days. After 31 days, S_l decreases to about 69% and $f(\overline{S}_l) \approx 0.87$.

Figure 4-33 shows the grid spacer vitality and the heat of criticality along with important time markers including the breach times of the waste packages, the original start and end times of criticality, and the actual times when criticality is terminated. The vitality is confirmed to remain at 1.0 until the packages are breached. The heat of criticality in WF #1 remains at 4 kW until the grid spacer vitality falls below 1% at 43.1 days, preempting the original end time of 70 days for the steady-state event. The region containing WF #1 remains saturated, so the critical water saturation has no effect. However, in WF #2, the soil becomes unsaturated during the criticality event, leading to intermittent criticality oscillating between 0 and 4 kW. Despite the intermittent heat output, the loss of vitality can terminate the criticality event at 35.7 days, which is before the original end time of 60 days. It should be noted that although the heat of criticality in WF #2 was determined through a lookup table, the region did not get hot enough to require an interpolation of different powers; therefore, only the 4 kW maximum in the table is observed.

Figure 4-30 shows the temperature of the gridded domain at two different times. The increase in temperatures in the region defined for WF #1 from 35 to 43 days is visually demonstrative of the effects of the criticality event. Likewise, the decrease in temperatures of the region defined for WF #2 in the same time frame is indicative of the loss of criticality from grid spacer degradation, where the source term is restricted to decay heat (1 kW). The same phenomenon applies to WF #3 (as will be demonstrated with vitality data) although this effect is visually indeterminate since the contribution from criticality is only 1 kW.

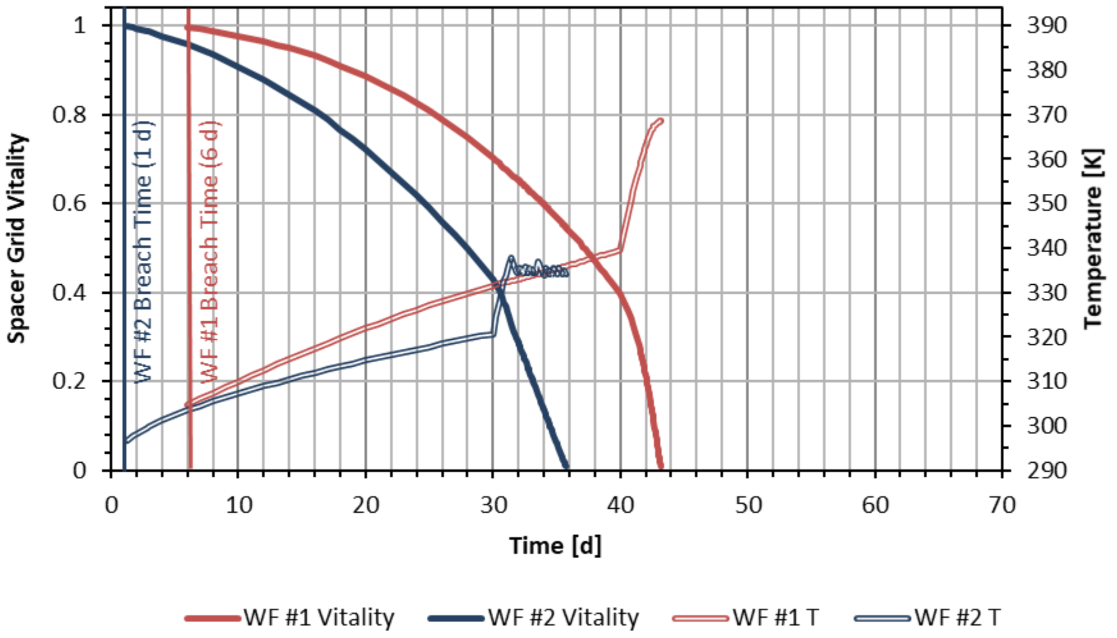

Figure 4-32. Grid Spacer Vitality and Average Waste Form Temperature over Time

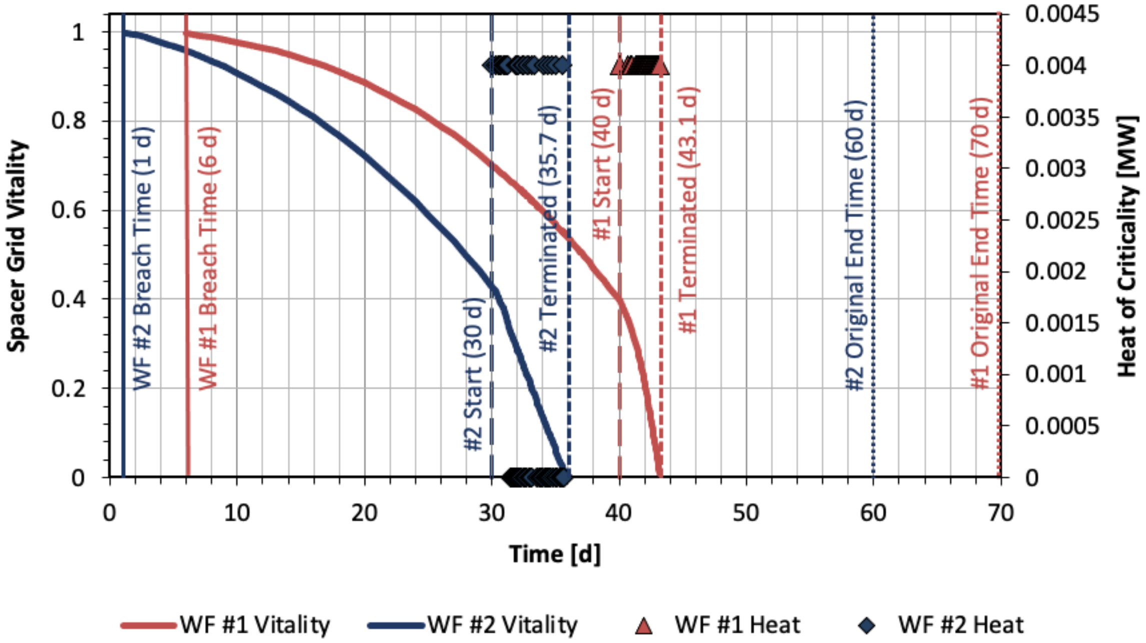

Figure 4-33. Grid Spacer Vitality and the Heat of Criticality over Time along with Time Markers for Breach Time, Criticality Termination, and the Original Criticality End Time

Because of the boundary conditions employed, the water densities in the inner half of the domain (from the origin) fluctuate while retaining some level of water saturation, as shown in Figure 4-34. The liquid densities in the soil do not fall below 960 kg/m^3, so the critical water density limits specified for ss_crit_1 and ss_crit_3 in Table 4-14 are never triggered. However, the liquid saturation fluctuates throughout the outer half of the domain in the +z-direction, where the medium becomes unsaturated to as low as 18%. Therefore, the average liquid saturation levels of the waste forms in this region (WF #2 and WF #3) appear to impart an intermittent effect to criticality events.

The intermittent power output, as influenced by liquid saturation, is plotted in Figure 4-35. For WF #2, intermittent power output occurs as S_l bifurcates about the critical limit of 70% until the loss of vitality terminates the event. For WF #3 (which has no grid spacer mechanism), an intermittent, 1 kW criticality occurs around 31.5 days when the 30% limit is met. At 38 days, the steady loss of saturation effectively terminates the criticality event before the original end time of 90 days.

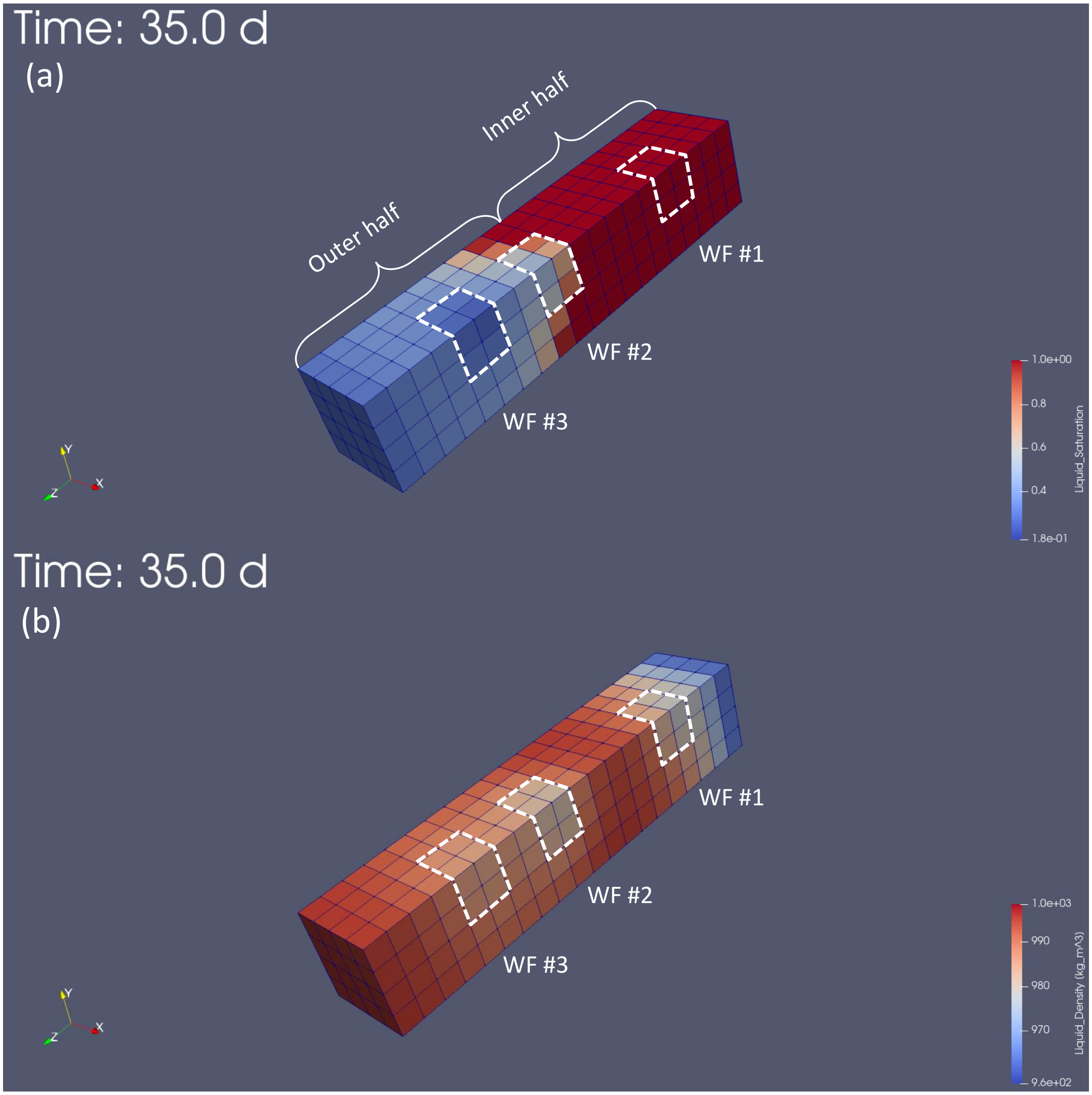

Figure 4-34. (a) Liquid Saturation and (b) Liquid Density at 35 days, When WF #3 Nears its Critical Water Saturation and WF #2 Oscillates along its Critical Water Saturation

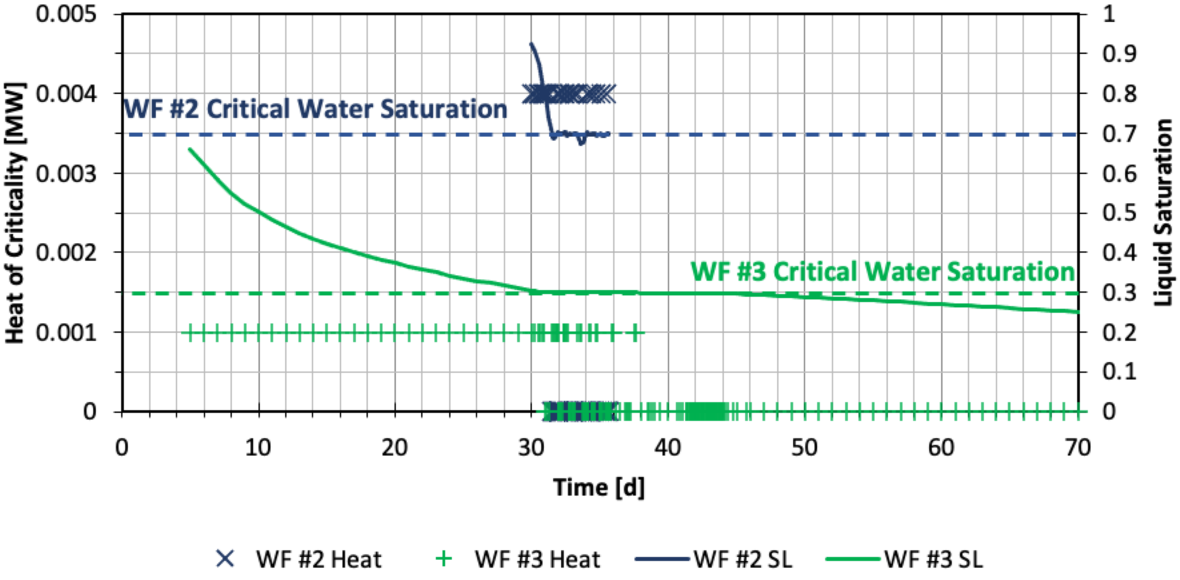

Figure 4-35. Grid Spacer Vitality and the Liquid Saturation over Time along with Lines Indicating Critical Water Saturations

4.5 Inventory Effects—Radionuclides Included in Transport and Dose Calculations

Previous analyses (Price et al. 2019b) examined the change in the inventory of 58 nuclides: 46 radionuclides and 12 stable fission products. Radionuclide selection for the inventory analyses was based on whether the radionuclide might be important to dose, it provided burnup credit, it is a source of decay heat, or some combination of those three reasons. Subsequent SNF inventory calculations (Price et al. 2019b) included these 58 radionuclides, both without a criticality event (base case) and with a 4 kW, steady-state criticality event lasting 10,000 years (steady-state criticality case). A comparison of the calculation results of the two cases indicates that the inventory of some radionuclides increases significantly for the steady-state criticality case compared to the base case. This outcome is due to the short half-lives of theses radionuclides; by 19,000 years after repository closure in the absence of a criticality, the inventories of the short-lived radionuclides have decayed to either very low levels or to zero. The assumed 10,000-year-long, steady-state criticality event produces these radionuclides, which leads to the significant percent increases. Another result of the inventory analysis is that the inventory of some radionuclides decreases with the occurrence of the criticality event. This behavior is caused by fission or neutron capture of that radionuclide or its parent. Finally, the inventory of long-lived fission and activation products increases by a few percent, reflecting their production by the 10,000-year-long, steady-state criticality event.

However, modeling the transport and dose of all 58 nuclides included in the inventory is unnecessary as well as impractical because of computational requirements. The following discussion provides a basis for excluding some of the 58 radionuclides included in inventory calculations from the PFLOTRAN calculations that include transport to the biosphere and dose to a receptor.

For the purposes of analyzing the consequences of a postclosure criticality event on repository performance, a nuclide selected solely because it provides burnup credit does not need to be considered for nuclide transport and dose calculations, particularly if it is stable. Future studies might analyze whether transport of burnup-credit radionuclides away from the waste package could affect the reactivity inside the waste package, but that effort is outside the scope of the analyses described in this report. Therefore, the 12 nuclides included solely because they provide burnup credit (^{109}Ag, ^{133}Cs, ^{151}Eu, ^{153}Eu, ^{155}Gd, ^{95}Mo, ^{143}Nd, ^{145}Nd, ^{101}Ru, ^{149}Sm, ^{150}Sm, ^{152}Sm) do not need to be considered in the PFLOTRAN transport and dose calculations.

The remaining 46 nuclides can be divided into 26 actinides and 20 fission (and activation) products (Table 3-3 and Table 3-4 of Price et al. [2019b], respectively). Of the 26 actinides identified in Table 3-3 of Price et al. (2019b), three radionuclides—^{242m}Am, ^{242}Cm, and ^{244}Cm—do not need to be included in the PFLOTRAN radionuclide transport and dose calculations. The two Cm isotopes do not need to be included in radionuclide transport and dose calculations because of the following: (1) they have short half-lives (0.446 years for ^{242}Cm and 18.1 years for ^{244}Cm), (2) they are not produced via a radioactive decay chain, and (3) they were included solely for their contribution to decay heat (Price et al. 2019a, Table 5). Their daughter products (^{238}Pu and ^{240}Pu, respectively, see Figure 4-36) are included in transport and dose calculations. The isotope ^{242m}Am does not need to be included because its activity in SNF is negligible compared to its daughter, ^{238}Pu, which is included in transport and dose calculations.

In addition, four radionuclides do not need to be included in the radionuclide transport calculation, but they should be included in the dose calculations by assuming that each is in secular equilibrium with its parent radionuclide. These four radionuclides are ^{228}Ra ($t_{1/2}$ = 5.85 years), ^{241}Pu ($t_{1/2}$ = 14.33 years), ^{210}Pb ($t_{1/2}$ = 22.2 years), and ^{227}Ac ($t_{1/2}$ = 21.77 years). Furthermore, PFLOTRAN has the ability to model dose from ^{222}Rn, a gas produced by decay of ^{226}Ra. Thus, ^{222}Rn is added to the list of radionuclides for which dose is calculated. The dose from ^{222}Rn is calculated based on the assumption that it is in secular equilibrium with its parent; due to its short half-life (3.8 days), transport of ^{222}Rn from the repository is not calculated.

Therefore, 19 actinides are designated for possible inclusion in the radionuclide transport calculations (26 – 3 – 4), while 24 actinides are designated for possible inclusion in the biosphere model dose calculations (26 – 3 + 1). The actinide radionuclides possibly included in the radionuclide transport calculations and/or the dose calculations are shown in Table 4-15. In this table, a radionuclide designated as “unsupported” is not explicitly included in the radionuclide transport calculations but would be considered in the dose calculation by assuming it is in secular equilibrium with its parent radionuclide.

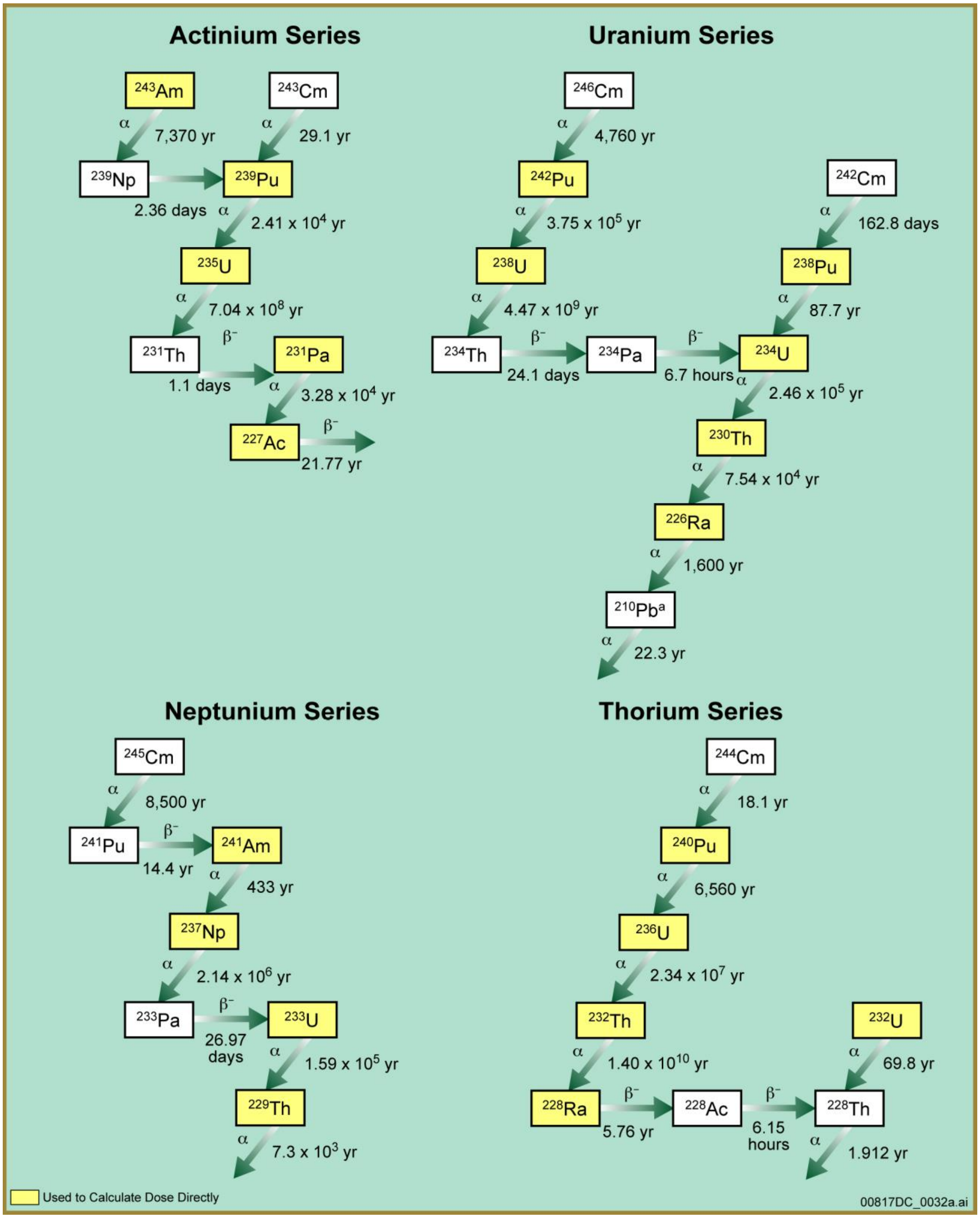

Source: DOE 2010, Figure 6.3.7-4.

Figure 4-36. Actinide Decay Chains

Table 4-15. Actinides Considered for Inclusion in the Radionuclide Transport and/or Dose Calculations

Nuclide	Half-life (years)[a]	Daughter	Ingestion Dose Coefficient (Sv/Bq)[b]	Supported or Unsupported	Parent Radionuclide (if unsupported)	Emanation Coefficient
Thorium Series						
^{240}Pu	6,561	^{236}U	2.5×10^{-7}	Supported	N/A	N/A
^{236}U	2.34E+07	^{232}Th	4.7×10^{-8}	Supported	N/A	N/A
^{232}Th	1.40E+10	^{228}Ra	2.3×10^{-7}	Supported	N/A	N/A
^{228}Ra[d]	5.75		6.9×10^{-7}	Unsupported	^{232}Th	N/A
^{232}U	68.9		3.3×10^{-7}	Supported	N/A	N/A
Neptunium Series						
^{245}Cm	8,423	^{241}Pu	2.1×10^{-7}	Supported	N/A	N/A
^{241}Pu[d]	14.33	^{241}Am	4.8×10^{-9}	Unsupported	^{245}Cm	N/A
^{241}Am	432.6	^{237}Np	2.0×10^{-7}	Supported	N/A	N/A
^{237}Np	2.14E+06	^{233}U	1.1×10^{-7}	Supported	N/A	N/A
^{233}U	1.59E+05	^{229}Th	5.1×10^{-8}	Supported	N/A	N/A
^{229}Th	7.93E+03		4.9×10^{-7}	Supported	N/A	N/A
Uranium Series						
^{242}Pu	3.75E+05	^{238}U	2.4×10^{-7}	Supported	N/A	N/A
^{238}U	4.47E+09	^{234}U	4.5×10^{-8}	Supported	N/A	N/A
^{238}Pu	87.7	^{234}U	2.3×10^{-7}	Supported	N/A	N/A
^{234}U	2.46E+05	^{230}Th	4.9×10^{-8}	Supported	N/A	N/A
^{230}Th	7.54E+04	^{226}Ra	2.1×10^{-7}	Supported	N/A	N/A
^{226}Ra	1.6E+03	^{222}Rn, ^{210}Pb	2.8×10^{-7}	Supported	N/A	N/A
^{222}Rn[e]	1.05E-02		3.5×10^{-9}	Unsupported	^{226}Ra	0.4[c]
^{210}Pb[d]	22.2		6.9×10^{-7}	Unsupported	^{226}Ra	N/A
Actinium Series						
^{243}Am	7,364	^{239}Pu	2.0×10^{-7}	Supported	N/A	N/A
^{239}Pu	2.41E+04	^{235}U	2.5×10^{-7}	Supported	N/A	N/A
^{235}U	7.04E+08	^{231}Pa	4.7×10^{-8}	Supported	N/A	N/A
^{231}Pa	3.28E+04	^{227}Ac	7.1×10^{-7}	Supported	N/A	N/A
^{227}Ac[d]	21.77		1.1×10^{-6}	Unsupported	^{231}Pa	N/A

Notes: [a] Half-lives taken from the National Nuclear Data Center (BNL n.d.).

[b] From Table F.1 of ICRP (2012) except for ^{222}Rn, which is from UNSCEAR (2000).

[c] From Mariner et al. (2017).

[d] This nuclide is not transported but dose is computed assuming secular equilibrium with its parent or grandparent.

[e] This nuclide is not transported but dose from this nuclide is calculated by release in the gas phase from the soil in the vicinity of the dose recipient, assuming secular equilibrium with its parent nuclide.

Of the 20 fission and activation products identified in Table 3-4 of Price et al. (2019b) that are included in the inventory for both the base case and the steady-state criticality case, 7 radionuclides—^{144}Ce, ^{134}Cs, ^{154}Eu, ^{147}Pm, ^{144}Pr, ^{106}Rh, and ^{125}Sb—do not need to be included in the PFLOTRAN radionuclide transport or dose calculations because they were included in the inventory solely for their contribution to decay heat, their half-lives are short (shorter than 8.6 years), and they are not generated in significant quantities during the steady-state postclosure criticality event (Price et al. 2019b, Table 3-4). In addition, ^{147}Sm, and ^{151}Sm are included in the inventory solely because they provide burnup credit (Price et al. 2019a, Table 5); therefore, these two radionuclides do not need to be included in the PFLOTRAN radionuclide transport or dose calculations. Two additional radionuclides, ^{90}Y and ^{137m}Ba are included in the inventory solely because they contribute to decay heat. However, ^{90}Y and ^{137m}Ba are daughters of ^{90}Sr and ^{137}Cs, respectively, which were designated for inclusion in radionuclide transport and dose calculations. Therefore, ^{90}Y and ^{137m}Ba do not need to be included in radionuclide transport calculations, but they should be included in dose calculations. The same is true of ^{126m}Sb, the daughter of ^{126}Sn. Note that ^{126m}Sb was not previously included in inventory calculations.

Therefore, 9 fission and activation products (20 – 7 – 2 – 2) need to be considered for inclusion in the radionuclide transport calculations and an additional 3 radionuclides need to be considered in the dose calculations, assuming that each of those 3 is in secular equilibrium with its parent. Table 4-16 shows these 12 fission and activation product radionuclides considered in the PFLOTRAN transport and dose calculations.

Table 4-16. Fission Products and Activation Products Considered for Inclusion in the Radionuclide Transport and/or Dose Calculations

Nuclide	Half-life (years)[a]	Daughter	Ingestion Dose Coefficient (Sv/Bq)[b]	Supported or Unsupported	Parent Radionuclide (if unsupported)	Emanation Coefficient
^{137m}Ba[c]	4.85E-06	^{137}Ba (stable)	Not available[d]	Unsupported	^{137}Cs	N/A
^{14}C	5,700	^{14}N (stable)	5.8×10^{-10}	Supported	N/A	N/A
^{36}Cl	3.01E+05	^{36}Ar, ^{36}S (stable)	9.3×10^{-10}	Supported	N/A	N/A
^{135}Cs	2.30E+06	^{135}Ba (stable)	2.0×10^{-9}	Supported	N/A	N/A
^{137}Cs	30.08	^{137m}Ba	1.3×10^{-8}	Supported	N/A	N/A
^{129}I	1.57E+07	^{129}Xe (stable)	1.1×10^{-7}	Supported	N/A	N/A
^{126m}Sb[c]	3.49E-07	^{126}Te (stable)	3.6×10^{-11}	Unsupported	^{126}Sn	N/A
^{79}Se	3.26E+05	^{79}Br (stable)	2.9×10^{-9}	Supported	N/A	N/A
^{126}Sn	2.30E+05	^{126m}Sb	4.7×10^{-9}	Supported	N/A	N/A
^{90}Sr	28.9	^{90}Y	2.8×10^{-8}	Supported	N/A	N/A
^{99}Tc	2.11E+05	^{99}Ru (stable)	6.4×10^{-10}	Supported	N/A	N/A
^{90}Y[c]	7.3E-03	^{90}Zr (stable)	2.7×10^{-9}	Unsupported	^{90}Sr	N/A

NOTE: [a] Half-lives taken from the National Nuclear Data Center (BNL n.d.).

[b] From ICRP (2021, Table F.1).

[c] This nuclide is not transported but dose is computed assuming secular equilibrium with its parent or grandparent.

[d] The ingestion dose coefficient for ^{137m}Ba is not available from ICRP (2012, Table F.1); however, this situation does not affect the dose calculations. Because the ^{137m}Ba is in secular equilibrium with ^{137}Cs, ^{137m}Ba is included in the dose calculations through the ^{137}Cs.

5. PERFORMANCE ASSESSMENT RESULTS

This section presents the PA results for the work conducted this year using the hypothetical saturated repository in shale from Mariner et al. (2017). This study is focused on calculating dose to a member of the public in the host rock with and without the occurrence of a steady-state criticality event (i.e., steady-state criticality case versus base case). Note that, for the purposes of this study, the steady-state criticality case assumes that all waste packages experience a steady-state criticality event when they are breached 9,000 years after repository closure. This assumption was made for calculational expediency and does not represent an expected event. Future studies will examine the effects of varying the onset of postclosure criticality spatially and temporally.

As noted in Section 3.2.1, changes made to the existing PFLOTRAN input used for the saturated shale repository from Mariner et al. (2017) include implementing the criticality submodule, running the simulation in GENERAL mode (previously run in TH mode), modeling DPCs that contain 37 PWR assemblies, implementing the newly developed illitization model of the buffer, and implementing anisotropic, temperature-dependent thermal conductivity.

5.1 Studies Conducted

Two modeling cases—a base case and a steady-state criticality case—were run, and several different outputs from the two cases were compared with each other. The outputs used for the comparison include (1) temperature and liquid pressure at a specific observation point within the model, (2) effects of the illitization model on permeability, (3) transport of ^{129}I, ^{237}Np, ^{90}Sr, and ^{137}Cs over the course of the 1,000,000-year simulation time, and (4) ^{129}I dose to a member of the public.

A vertical (x–z) slice through the model domain shows the location of four observation points (Figure 5-1). Three of these observation points are located in the centermost region of the repository: “wp0” represents the centermost waste package of the half-symmetry repository, “bf0” represents an observation point directly to the right of “wp0” within the buffer region, and “drz0” represents an observation point to the right of “bf0” within the DRZ. The fourth observation point is “sand_obs1”, located in the upper sandstone aquifer, ~30 m downgradient from the edge of the repository and 425 m above it.

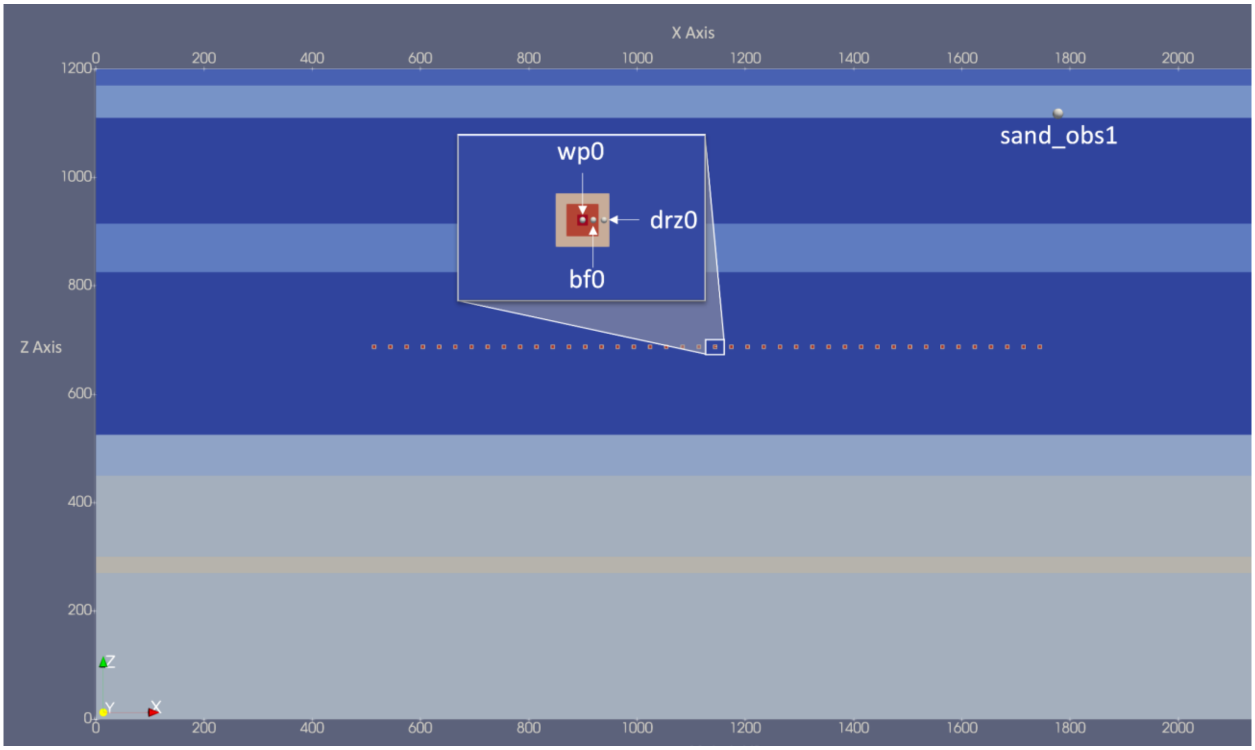

NOTE: Inset zoom on top center shows a close-up of the centermost region of the repository.

Figure 5-1. Vertical (*x*–*z*) Slice through Model Domain Colored by Material, Showing the Location of Observation Points "wp0", "bf0", "drz0", and "sand_obs1"

5.2 Results

A comparison of the simulated temperature at observation point "wp0" over the 1,000,000-year simulation time between the steady-state criticality case (dashed purple line) and the base case (solid turquoise line) is shown in Figure 5-2. As expected, the temperature is identical for the first several thousand years up until the start of the criticality event 9,000 years after repository closure, when the temperature for the steady-state criticality case begins to increase. The temperature for the steady-state criticality case continues to increase reaching a maximum temperature of 266.1°C at 19,010 years. By 70,000 years, "wp0" for the steady-state criticality case has cooled to the point that the two cases have similar temperatures once again. For both cases, the final temperature (~29.5°C) after 1,000,000 years never fully reaches the initial temperature (27.8°C).

The liquid pressure at wp0 as a function of time is presented for both cases in Figure 5-3. At 9,000 years the temperature for the steady-state criticality case begins to climb as seen in Figure 5-2, and as a result so does the liquid pressure, reaching a maximum value of 6.6 MPa at 13,720 years.

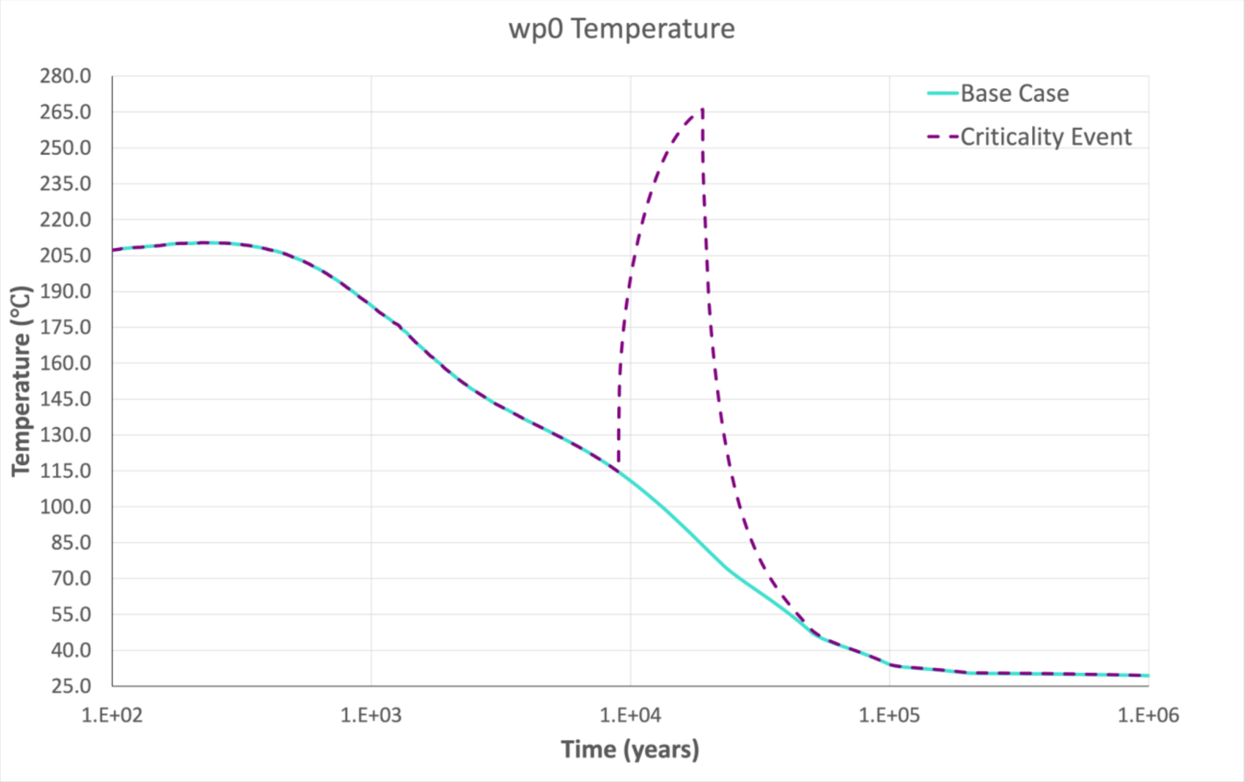

Figure 5-2. Temperature Comparison for the Centermost Waste Package of Half-Symmetry Model Domain, "wp0", for the Base Case and the Steady-State Criticality Case

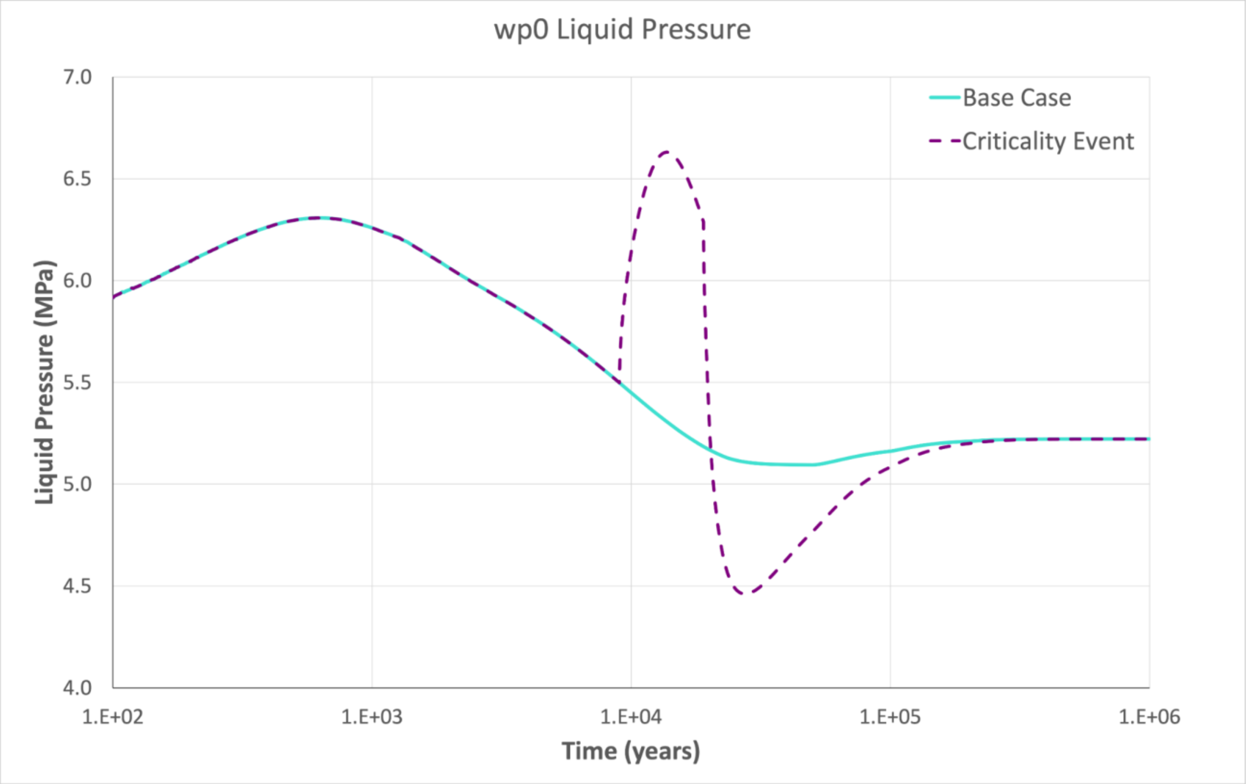

Figure 5-3. Liquid Pressure Comparison for the Centermost Waste Package of Half-Symmetry Model Domain, "wp0", for the Base Cases and the Steady-State Criticality Case

Three *x*–*z* slices through the repository at the centermost waste package (wp0) are shown in Figure 5-4. The first vertical slice (Figure 5-4a) shows the location of the centermost buffer observation point (bf0) and the previously mentioned wp0. The colors in the figure indicate material ID: burgundy for waste packages, red for buffer, tan for DRZ, and blue for host rock. The second vertical slice (Figure 5-4b) shows permeability results at 19,000 years for the base case. The third vertical slice (Figure 5-4c) shows permeability results at 19,000 years for the steady-state criticality case. In comparing the two cases, differences can be seen specifically within the buffer region in which the criticality event case shows a greater difference in permeability. This result is due to the implementation of the PFLOTRAN illitization model within the two cases. Figure 5-5 shows a plot comparison between the two cases for a simulation period between 100 and 1,000,000 years at observation point bf0. Within this plot the first increase in permeability is from decay heat, and the second increase in the steady-state criticality case is due to the occurrence of the criticality event, which commences 9,000 years after repository closure. The decay heat causes the permeability to increase by a factor of 180; the initial permeability is 1.0E-20 m^2 while it is 1.8E-18 m^2 at 8,986 years right before the criticality event commences. The heat from the criticality event causes a five-fold increase in the permeability for the steady-state criticality case compared to that for the base case. At 1,000,000 years, the permeability of the steady-state criticality case at bf0 is 9.8E-18 m^2 while it is 1.8E-18 m^2 for the base case.

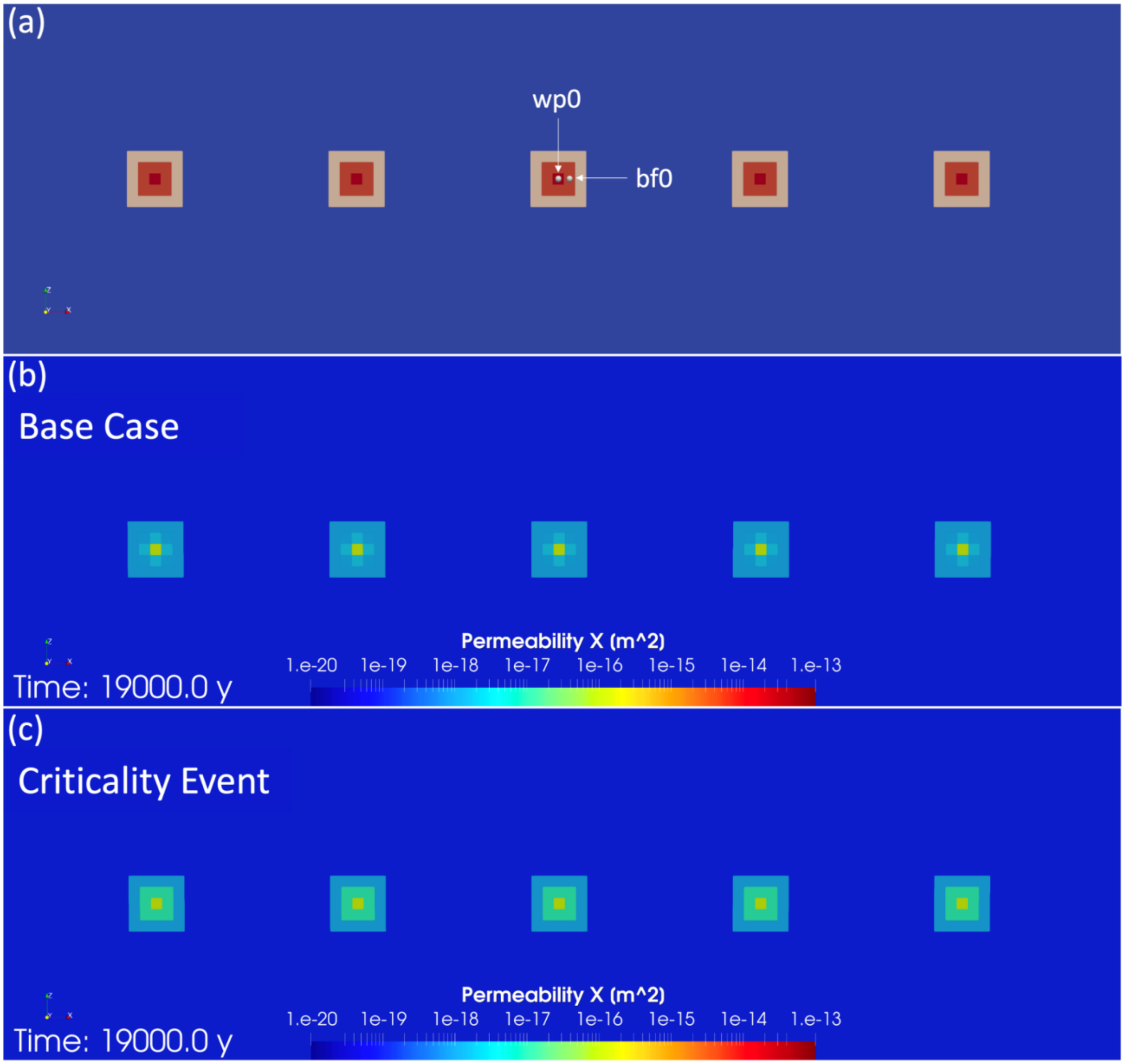

NOTE: In (a), burgundy represents waste packages, red represents the buffer, tan represents the DRZ, and blue represents the host rock. In (b) and (c), the color coding for permeability is indicated by the graduated color strip (low of 1.0E−20 m^2 [dark blue] to high of 1.0E−13 m^2 [dark red]).

Figure 5-4. Vertical (*x*–z) Slice through Repository at Centermost Waste Package, wp0, Showing (a) Schematic of Waste Packages, Buffer, DRZ, and Host Rock, (b) Permeability at 19,000 Years for the Base Case, (c) Permeability at 19,000 Years for the Steady-State Criticality Case

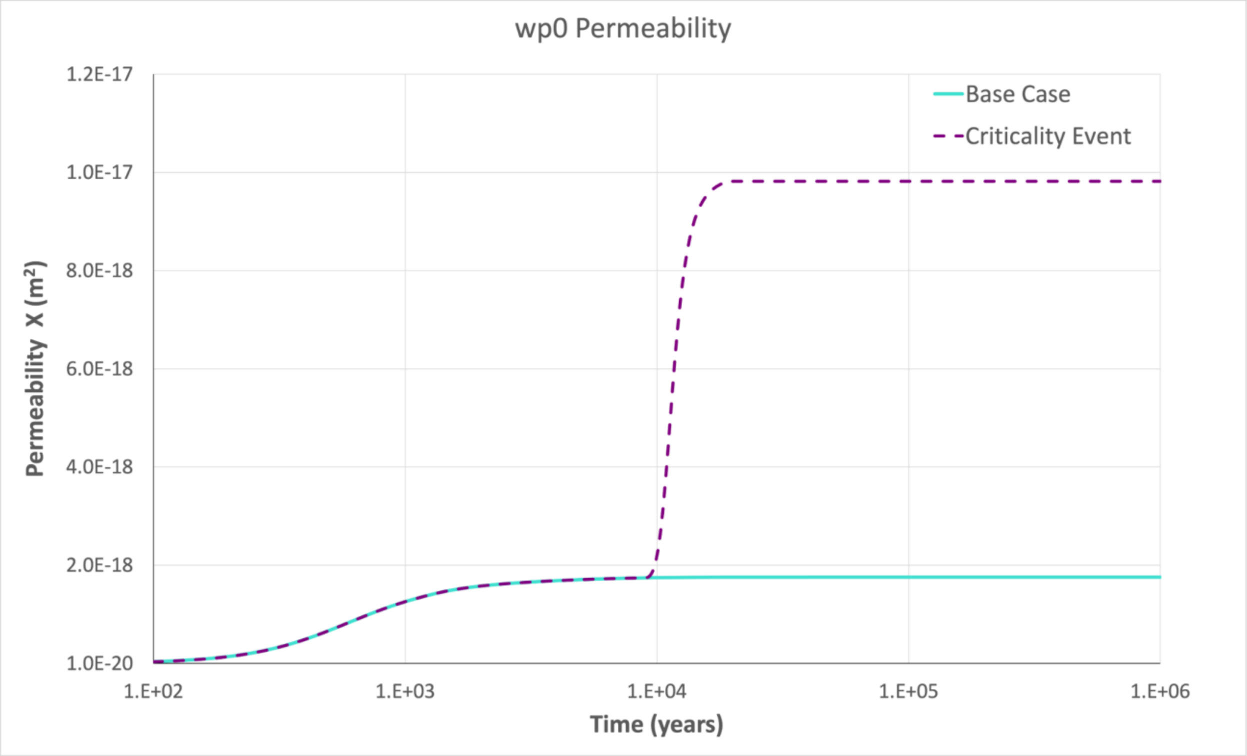

Figure 5-5. Permeability Comparison for the Base Case and the Steady-State Criticality Case between 100- and 1,000,000-Year Simulation Period at Observation Point bf0

Simulation results for both the base case and the steady-state criticality case involving the transport of ^{129}I through the model domain and dose to a member of the public are presented in the next several figures. The nuclide ^{129}I does not have a solubility limit and does not sorb to any of the geologic materials (Table 3-2); therefore, transport of this nuclide is not retarded. At 9,000 years, all waste packages are set to breach for both cases and, as a result, ^{129}I can be seen directly at the location of all waste packages (Figure 5-6). At 19,000 years, ^{129}I remains confined to the near field but very small differences can be seen between the two cases (Figure 5-7). As shown in Figure 5-7, the ^{129}I plume has expanded slightly more in the steady-state criticality case, both above and below the repository as compared to the base case. This result stems from a series of related factors; the higher temperatures associated with the steady-state criticality case increase the pressure of the pore water, which leads to an increase in porosity (because of the soil compressibility model), which increases tortuosity, which leads to increased diffusion of ^{129}I. Because the backfill and the host rock are nearly impermeable (see permeability values in Table 3-1), diffusion is the only significant transport mechanism; therefore, the increased temperatures associated with the steady-state criticality case lead to slightly increased diffusive transport of ^{129}I, as shown in Figure 5-7.

By 50,000 years, ^{129}I has reached the limestone aquifer 160 m beneath the repository, but the ^{129}I has transported slightly farther downgradient within this aquifer in the steady-state criticality case than in the base case (Figure 5-8). This outcome is due to increased diffusion in the steady-state criticality case, which causes ^{129}I to reach the lower aquifer earlier than in the base case. By 50,000 years, ^{129}I has been transported slightly farther downstream in the steady-state criticality case than in the base case. By 200,000 years, ^{129}I has advected through the limestone aquifer to the end of the model domain, 5 km beyond the edge of the repository (Figure 5-9), and it has started to diffuse into the less permeable geologic layers. At this point, no differences can be seen between the two cases, a trend that continues through the remainder of the 1,000,000-year simulation time. By 500,000 years, ^{129}I has continued to advect through the lower limestone aquifer as well as through the upper sandstone aquifer, located 425 m above the repository (Figure 5-10). The concentration is higher in the lower aquifer, and ^{129}I has continued to diffuse from the lower aquifer into the less permeable geologic layers. By 1,000,000 years, ^{129}I has continued to advect through both aquifers to the well located 5 km downstream from the repository (Figure 5-11), and diffusion into less permeable layers continues.

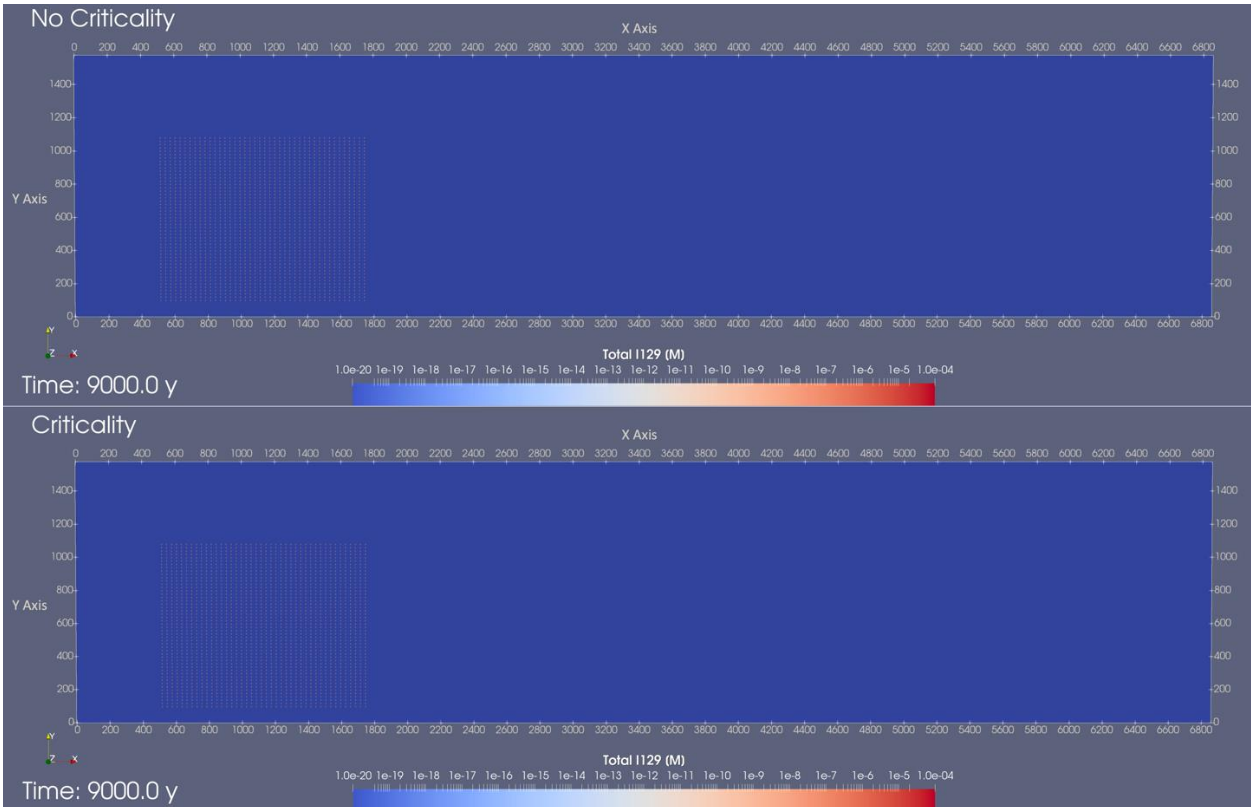

Figure 5-6. ^{129}I Concentration at 9,000 Years for the Base Case and the Steady-State Criticality Case Plotted in a Horizontal Slice through the Model Domain at the Elevation of the Repository

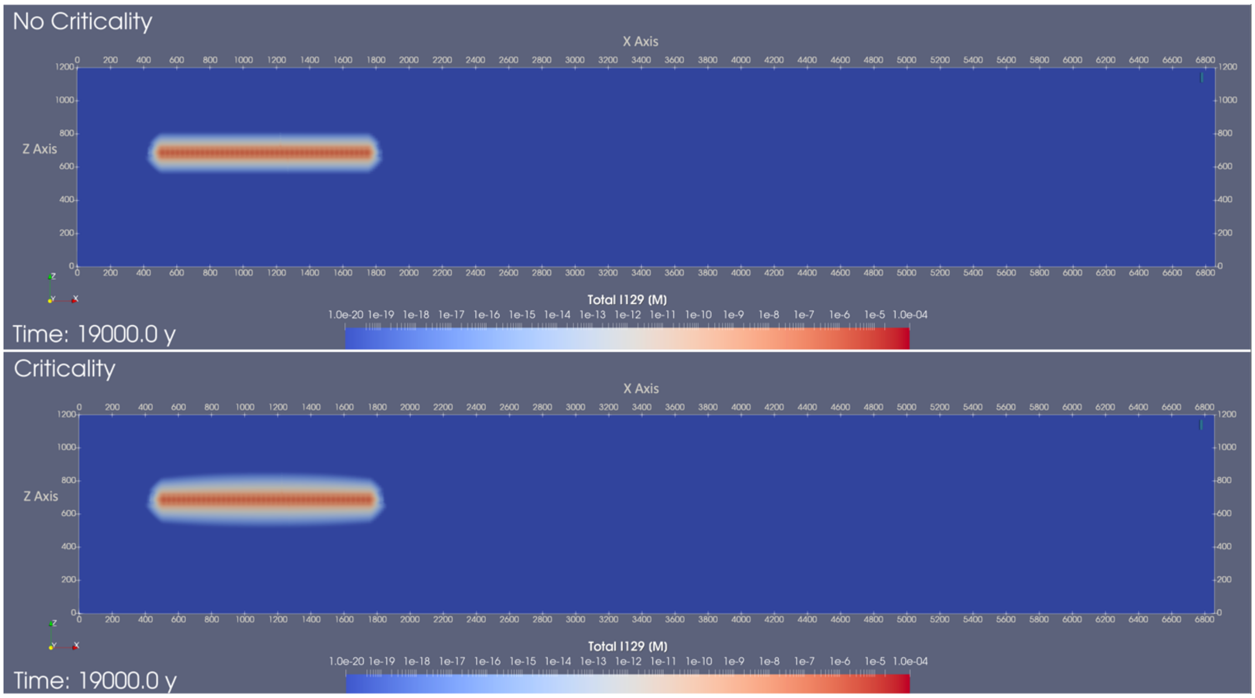

Figure 5-7. ^{129}I Concentration at 19,000 Years for the Base Case and the Steady-State Criticality Case Plotted in a Vertical Slice through the Model Domain at the *y* Midpoint of the Repository

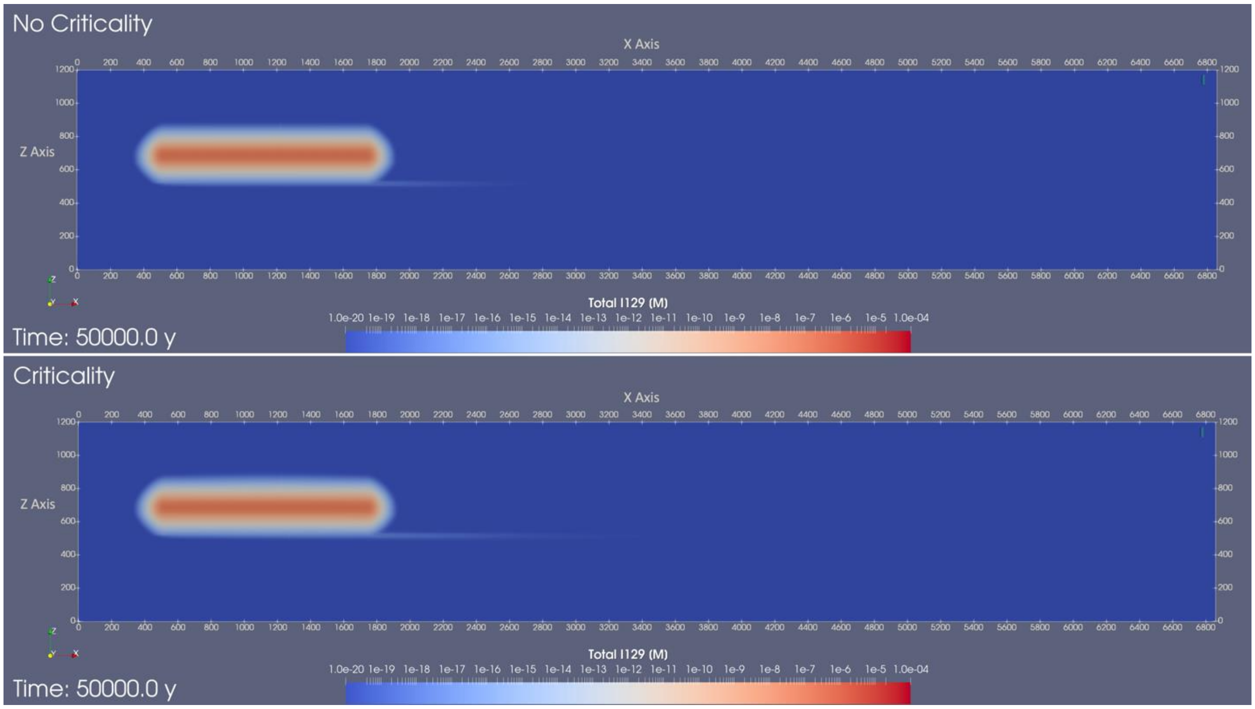

Figure 5-8. ^{129}I Concentration at 50,000 Years for the Base Case and the Steady-State Criticality Case Plotted in a Vertical Slice through the Model Domain at the *y* Midpoint of the Repository

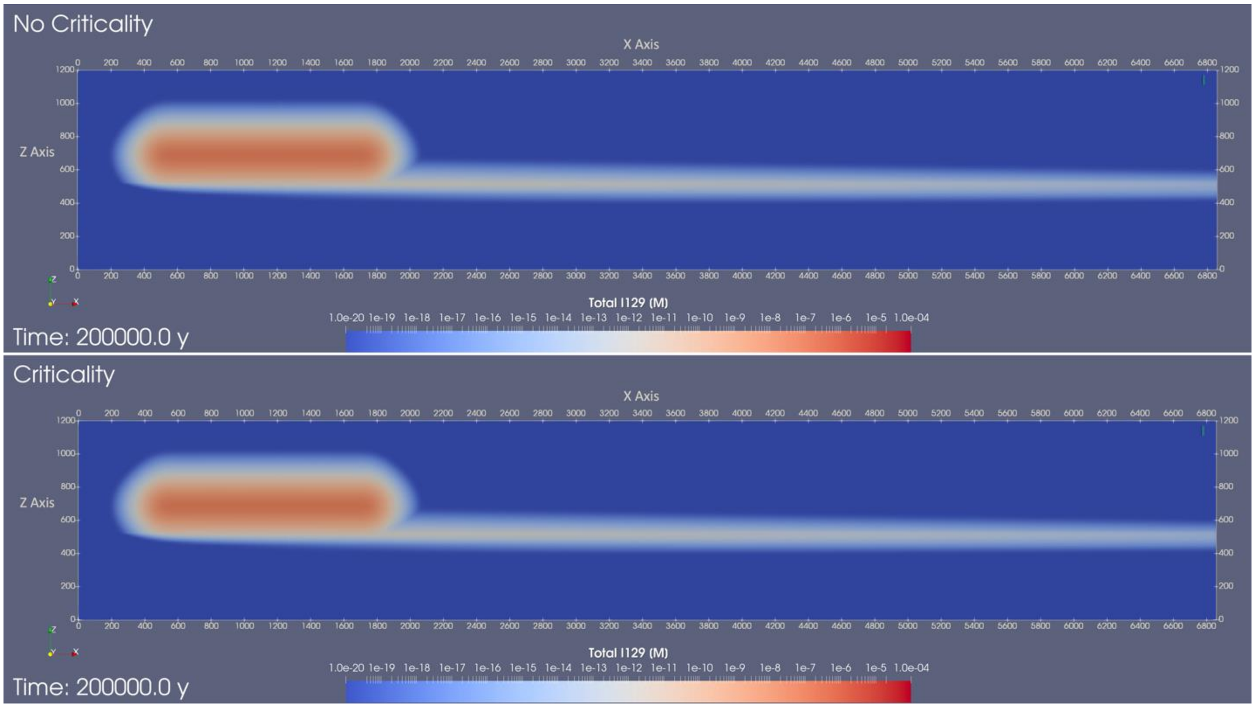

Figure 5-9. ^{129}I Concentration at 200,000 Years for the Base Case and the Steady-State Criticality Case Plotted in a Vertical Slice through the Model Domain at the y Midpoint of the Repository

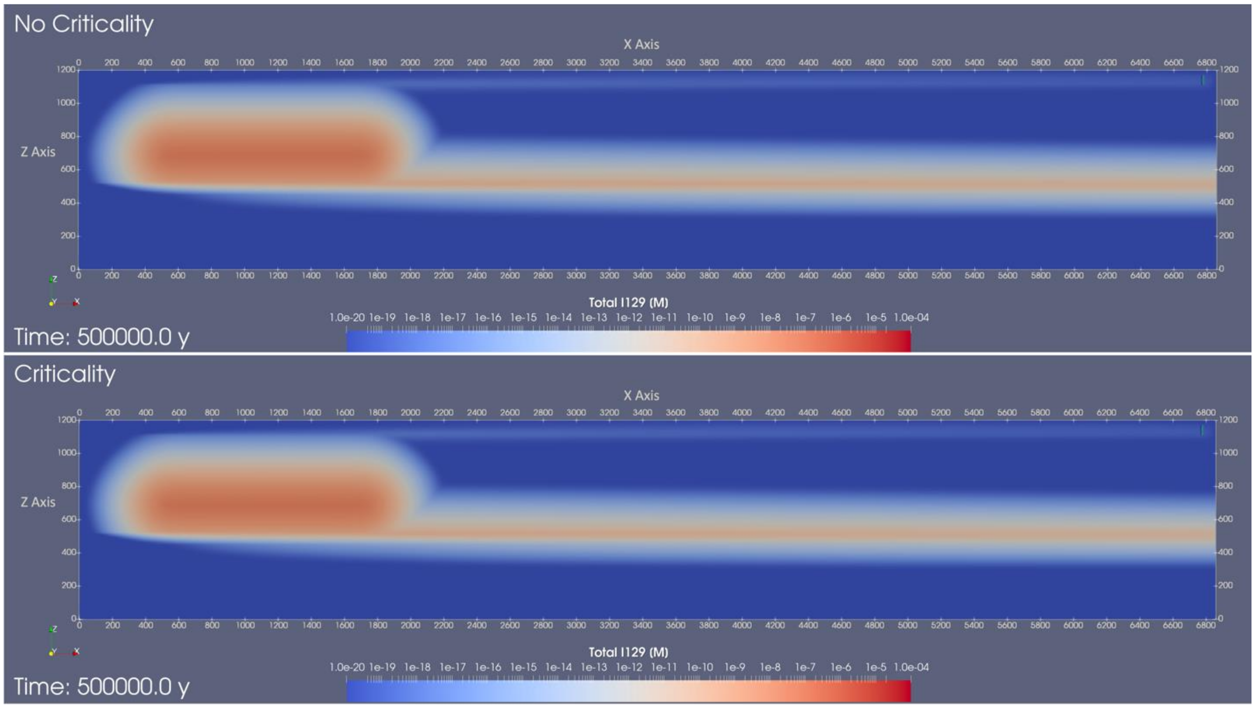

Figure 5-10. ^{129}I Concentration at 500,000 Years for the Base Case and the Steady-State Criticality Case Plotted in a Vertical Slice through the Model Domain at the *y* Midpoint of the Repository

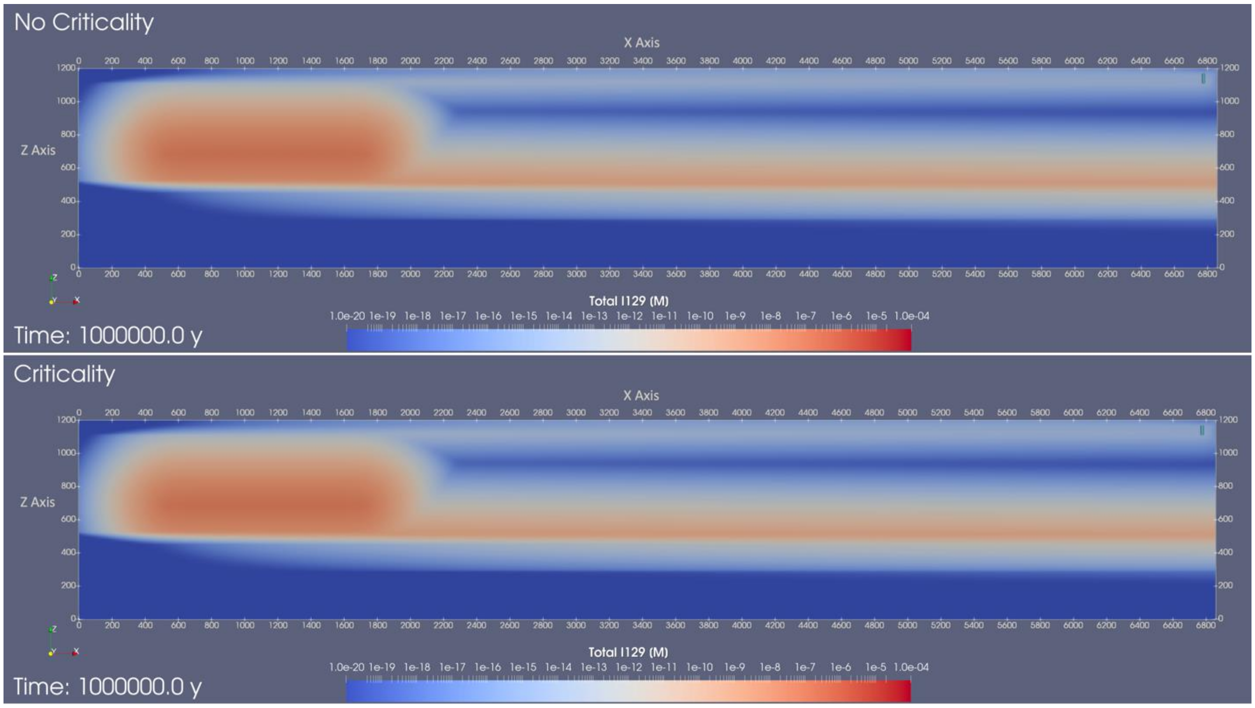

Figure 5-11. ^{129}I **Concentration at 1,000,000 Years for the Base Case and the Steady-State Criticality Case Plotted in a Vertical Slice through the Model Domain at the *y* Midpoint of the Repository**

The dose to a member of the public from ^{129}I over 1,000,000 years is shown in Figure 5-12 for the base case and the steady-state criticality case. By about 443,000 years, both cases show an ^{129}I dose of 10^{-15} Sv/yr, and by 1,000,000 years both reach a dose slightly above 10^{-10} Sv/yr. At 1,000,000 years, the ^{129}I dose associated with the steady-state criticality case is 0.46% lower than that associated with the base case, which is within numerical accuracy and is insignificant. Although the inventory of ^{129}I increases by about 3.5% over the course of the 10,000-year-long, steady-state criticality event (Price et al. 2019b), this slight increase in inventory does not translate to an increase in dose to a member of the public.

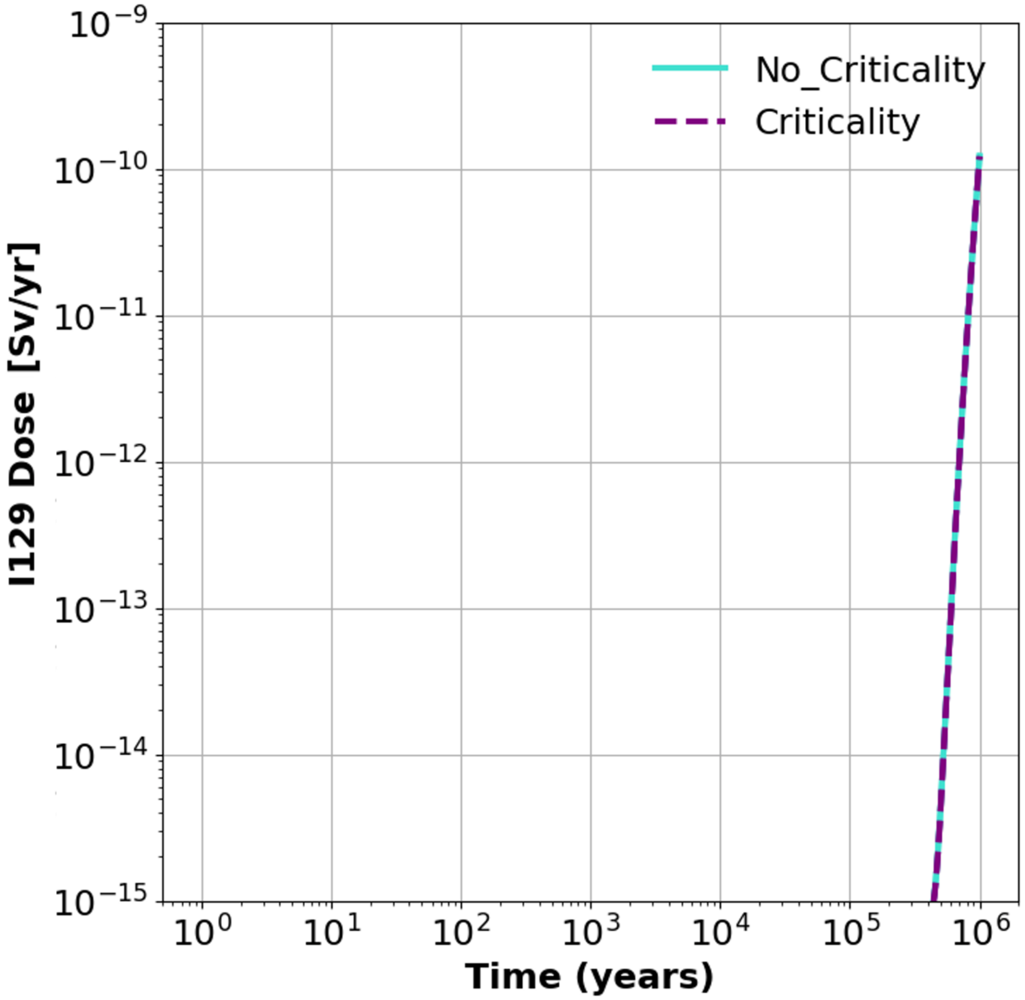

Figure 5-12. ^{129}I Dose Comparison for the Base Case and the Steady-State Criticality Case

Simulation results involving the transport of ^{237}Np for both the base case and the steady-state criticality case are shown in Figure 5-13. This figure shows the concentration of ^{237}Np at various points in the repository after 1,000,000 years. Besides being solubility limited, ^{237}Np is a radionuclide species that sorbs (Table 3-2); this figure indicates that ^{237}Np remains within the vicinity of the repository over the course of the 1,000,000-year simulation, regardless of whether steady-state criticality event occurs, because its transport is slowed by sorption. Because this isotope does not get transported to the well that is part of the exposure pathway, ^{237}Np cannot result in a dose to a member of the public. Based on these results, it was determined that it was not necessary to model the transport of other long-lived sorbing radionuclides that sorb more than ^{237} Np (i.e., with sorption coefficients greater than that of ^{237}Np).

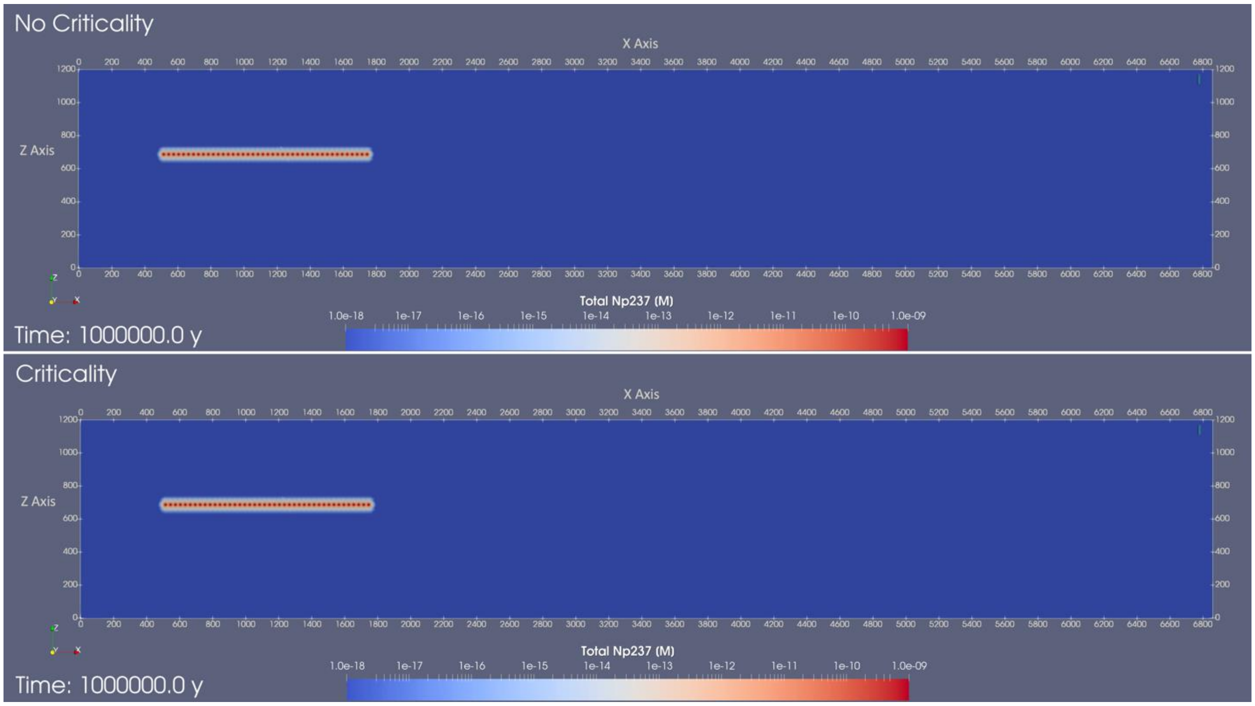

Figure 5-13. ^{237}Np Concentration at 1,000,000 Years for the Base Case and the Steady-State Criticality Case Plotted in a Vertical Slice through the Model Domain at the *y* Midpoint of the Repository

As discussed in Section 4.5, the steady-state criticality event produces short-lived fission products that do not usually need to be considered in a PA because their half-lives are short enough that either they have decayed to insignificant quantities or they no longer exist by the time the waste package fails and radionuclide transport commences. Two such radionuclides are ^{137}Cs and ^{90}Sr. Shown in Figure 5-14 and Figure 5-15 are concentration histories for ^{137}Cs and ^{90}Sr, respectively, at four observation points. These plots show that the concentration of ^{137}Cs, which is a sorbing element with a half-life of about 30 years, drops by about 6 orders of magnitude between the waste package and the DRZ with no noticeable concentration in the upper sand aquifer. The farther out from the repository, the lower the molar concentration. This observation is also true of ^{90}Sr, which is a nonsorbing element that also has a half-life of about 30 years. The ^{90}Sr plots show that the concentration of ^{90}Sr decreases by about two orders of magnitude between the waste package and the DRZ. Like the ^{137}Cs, the ^{90}Sr never reaches the upper sand aquifer. Therefore, given the long travel time between the repository and the well used by a member of the public, it is not necessary to include short-lived fission products in the PA.

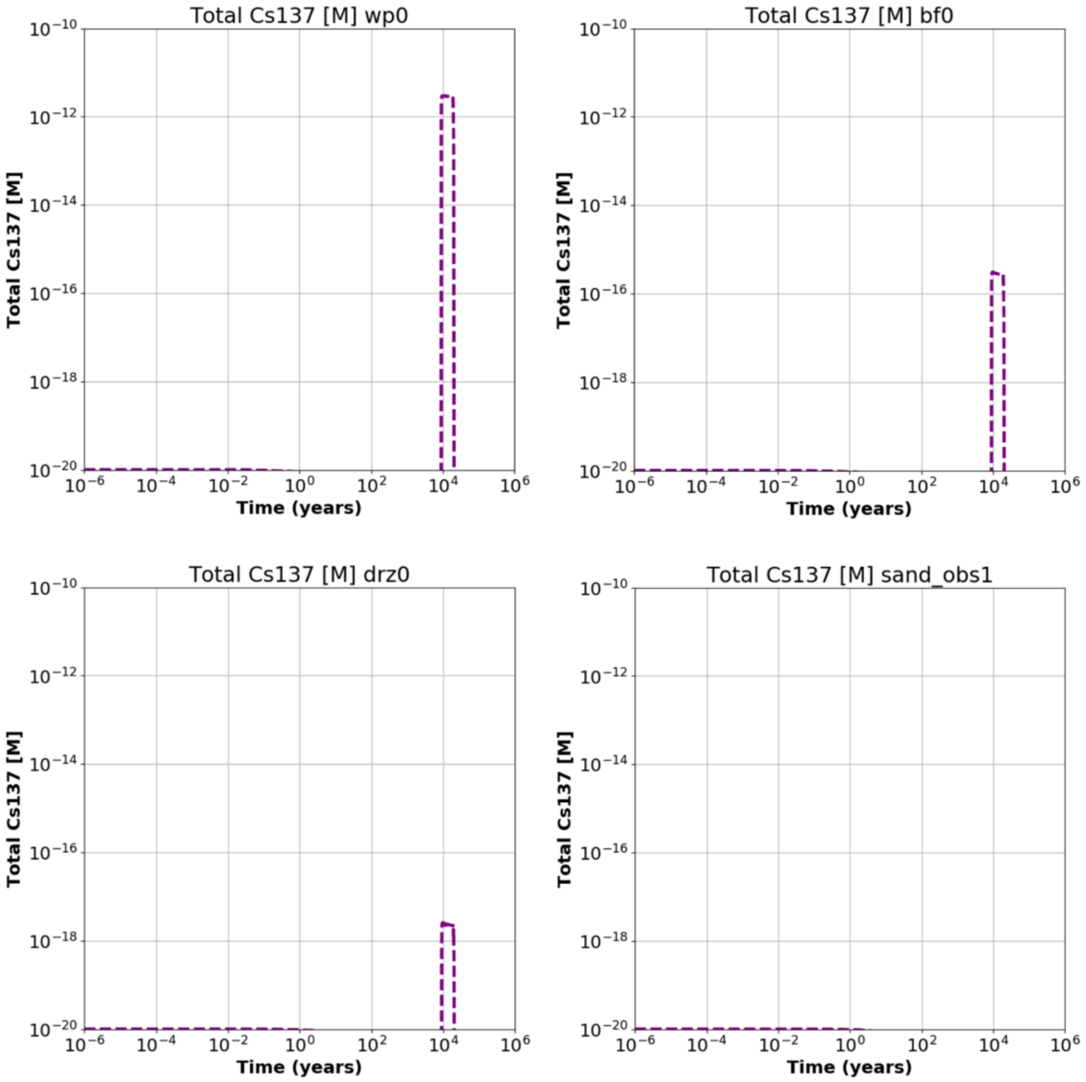

NOTE: The four observations points are the following: wp0, centermost waste package in the half-symmetry model domain; bf0, buffer surrounding wp0; drz0, DRZ nearest to wp0 and bf0; sand_obs1, located in the upper sandstone aquifer ~30 m downgradient from the edge of the repository and 425 m above it.

Figure 5-14. ^{137}Cs Concentration History for the Steady-State Criticality Case Plotted at Four Observation Points

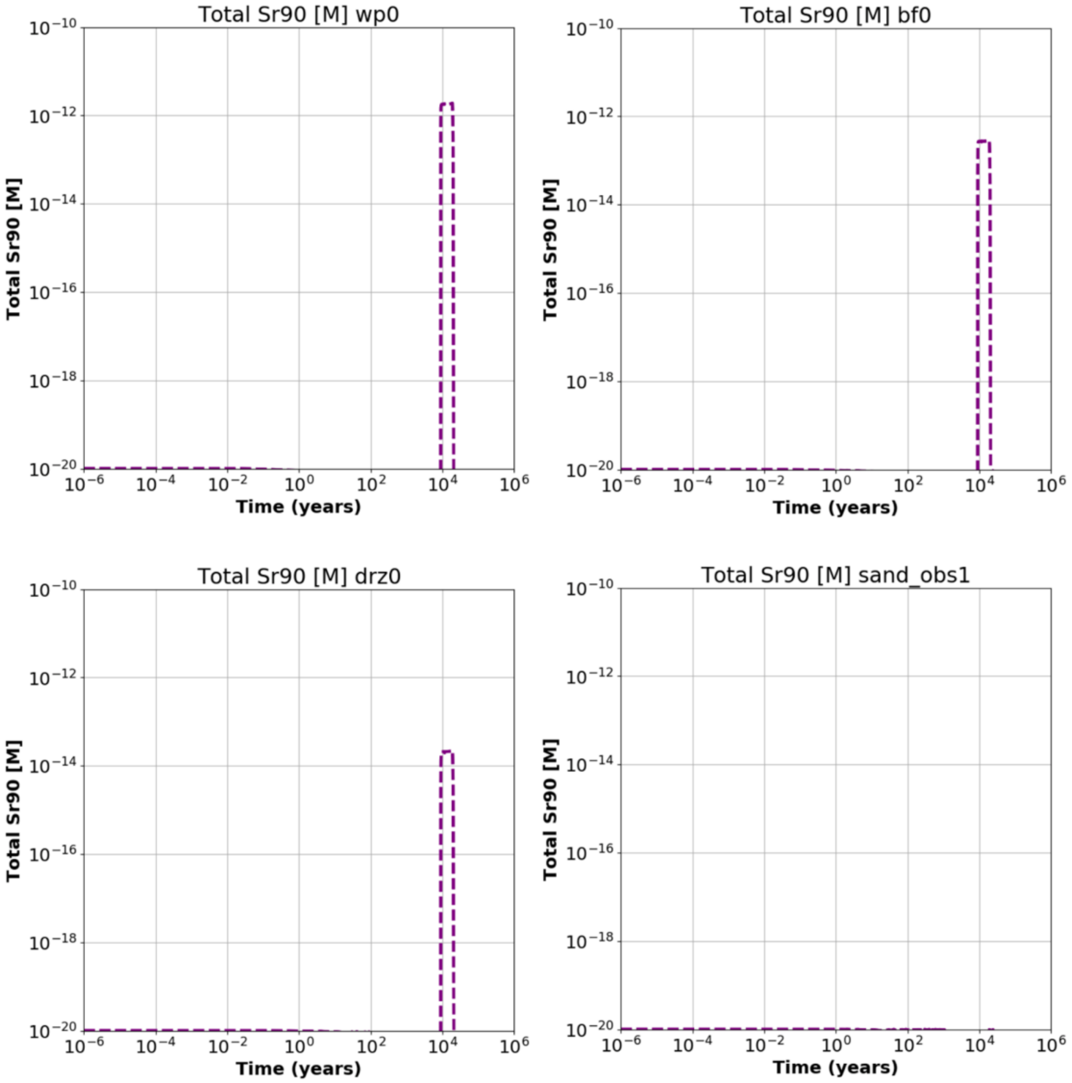

NOTE: The four observations points are the following: wp0, centermost waste package in the half-symmetry model domain; bf0, buffer surrounding wp0; drz0, DRZ nearest to wp0 and bf0; sand_obs1, located in the upper sandstone aquifer ~30 m downgradient from the edge of the repository and 425 m above it.

Figure 5-15. ^{90}Sr Concentration History for the Steady-State Criticality Case Plotted at Four Observation Points

6. MODELING TRANSIENT CRITICALITY EVENT

This section presents three different approaches to modeling a transient criticality event. The first approach uses a Monte Carlo solver Shift to perform high-fidelity calculations (Section 6.1); the second approach uses MCNP to characterize reactivity feedback coefficients for use in the RAZERBACK code (Talley 2017a,b; 2018) to model a transient criticality event in the unsaturated repository (Section 6.2); and the third approach uses the commercially available SIMULATE-3K (S3K; Studsvik AB n.d.) code to simulate a transient criticality event in the saturated repository (Section 6.3).

6.1 Shift Transient Implementation

Using the Monte Carlo solver Shift (Pandya et al. 2016) to solve transient criticality problems enables high-fidelity calculations of energy deposition throughout the DPC as a function of time that do not suffer from approximations to the continuous-energy physics or problem geometry. Once coupled to a thermal hydraulics code, these calculations can be used to determine if the transient event causes materials to fail by exceeding maximum temperatures or thermal stress limits. The release version of Shift currently only supports steady-state (k-eigenvalue) criticality calculations. This section details the efforts to benchmark a development branch of Shift modified to support time-dependent criticality problems. Shift's transient capabilities have been benchmarked for the 2D C5G7 reactor geometry using multigroup cross sections as a verification that the accumulation of the delayed neutron source and generation of point kinetics parameters are correct.

6.1.1 Transient Model

Shift has been modified to solve the time-dependent, neutron transport process by passing a particle bank in between k-eigenvalue criticality calculations at discrete time steps. Closely following the implementation from Jo et al. (2016), this modified Shift implementation uses particles to carry a weighting factor that is determined by the random walk process and that accounts for the accumulation of delayed neutrons across time steps. To prescribe a transient event in a Shift input file, the user must provide neutron kinetics data (delayed neutron fractions, fission spectra, and decay constants) and time-dependent reactivity insertions. Reactivity insertions are specified by providing a multiplicative scaling factor to the number densities of individual materials for each Monte Carlo time step. For example, specifying an increase in the moderator number density would act as a positive reactivity insertion because of increased neutron thermalization. Additional reactivity insertions, such as time-dependent changes to the problem geometry, have not yet been implemented.

Simulating the time-dependent neutron transport process directly with Monte Carlo can be computationally prohibitive because very small time steps are required to capture accumulation of the delayed neutron source accurately. The transient method implemented in Shift is a quasi-static method (Dulla et al. 2008) that factorizes the neutron flux into the product of a shape function ($\varphi(\boldsymbol{x}, \widehat{\boldsymbol{\Omega}}, E, t)$), which is loosely dependent on time, and an amplitude function ($p(t)$), which is dependent exclusively on time. Quasi-static methods assume that the shape function varies much more slowly in time than the amplitude function and can be updated much less frequently, as seen in Figure 6-1. The amplitude function should therefore be much less computationally expensive to solve than the higher-fidelity shape function.

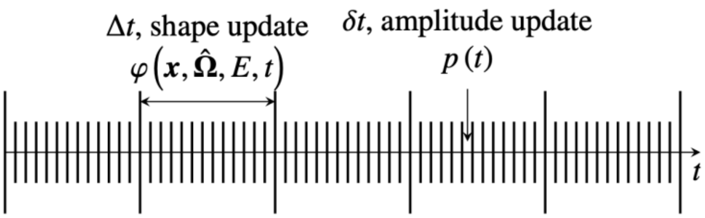

Figure 6-1. Quasi-Static Method Time Discretization

Shift uses a specific quasi-static method, called the predictor-corrector quasi-static method (PCQM) (Dulla et al. 2008). This PCQM relies heavily on the assumption that the shape function varies slowly in time and updates the entire neutron flux, called the "predictor" flux, on the macro time scale instead of the shape function. The amplitude solver is then marched through the micro time scale to "correct" the predictor flux. Though work involving implementation of the full PCQM is planned for the near future, the full PCQM was not available for use in the preparation of this report; thus the predictor flux, generated by solving the time-dependent neutron transport equation with Shift, is used for all results presented herein. The amplitude function is computed as the solution to the Exact Point Kinetics Equations (EPKE), which is a globally integrated and adjoint-weighted system of ordinary differential equations solving for the system's power and delayed neutron precursor concentrations.

6.1.2 Benchmark Problem

The C5G7-TD benchmark (Hou et al. 2017) simulates various time-dependent reactivity insertions applied to a small light water reactor with eight UO_2 assemblies and eight mixed oxide (MOX) assemblies. This benchmark problem was selected because it is qualitatively similar to the application and it is a standard problem within the nuclear engineering community for verifying these methods.

Figure 6-2 (left) shows the southeast quadrant cross-section of the C5G7 reactor. The benchmark specification defines seven energy groups and eight delayed neutron precursor groups. Multigroup cross sections for all materials, delayed neutron precursor group decay fractions, decay constants, and fission spectra are all provided. More specific details about the C5G7 reactor can be found in the benchmark specification (Hou et al. 2017). Exercise TD3 of the benchmark simulates four transient events by linearly varying the core moderator density for a 2D version of the reactor geometry with the time-dependent profile seen in Figure 6-2 (right). The TD3 simulation results from Shift for this report have been compared against the same transient simulation with MPACT, a 2D/1D deterministic code maintained by the University of Michigan and ORNL. MPACT uses Method of Characteristics in the radial direction and an SP_3 (third-order simplified spherical harmonic expansion) nodal method in the axial direction (Kochunas et al. 2013). A detailed description of the C5G7-TD benchmark results with MPACT is provided in (Shen et al. 2018).

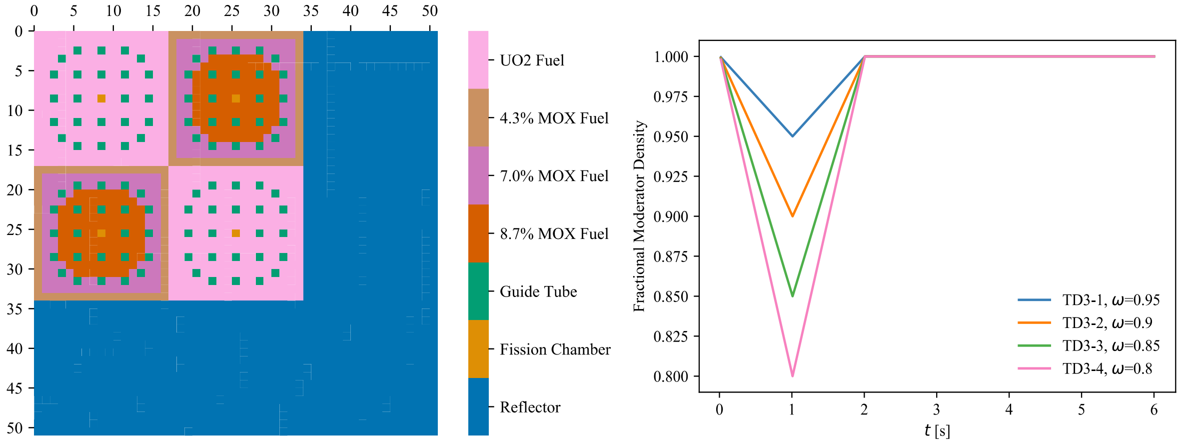

Figure 6-2. C5G7 Reactor Pincell Layout (left) and Time-Dependent Change in the Moderator Density for Case TD3 (right)

6.1.3 Benchmark Results

Point kinetics parameters, such as the prompt neutron generation time and effective delayed neutron fractions, were derived from steady-state Shift Monte Carlo tallies and approximated as constant in time. The adjoint-weighting function was generated using the Denovo deterministic solver developed at ORNL (Evans et al. 2010). In its current state, Denovo only supports SP$_3$ adjoint eigenvalue calculations that are untested and unadvertised at the time of writing. The dynamic reactivities generated by Shift and MPACT for each of the TD3 cases are shown in Figure 6-3 (left) with time steps of 1×10^{-2} seconds. Each TD3 case simulated with Shift was executed up until $t = 6$ seconds with 10^5 particle histories per cycle, 150 inactive cycles, and 250 active cycles. The corresponding fractional core fission rate profiles are generated by using the reactivity profiles from Shift as input into the EPKE solver before being compared against the MPACT solution in Figure 6-3 (right). The Shift and MPACT solutions agree after stochastic noise has been removed from the Shift dynamic reactivity ($t > 2$ seconds). A summary of various norm comparisons for the Shift and MPACT fractional core fission rate profiles is shown for each TD3 case in Table 6-1, where p_i is the fractional core fission rate at time step i.

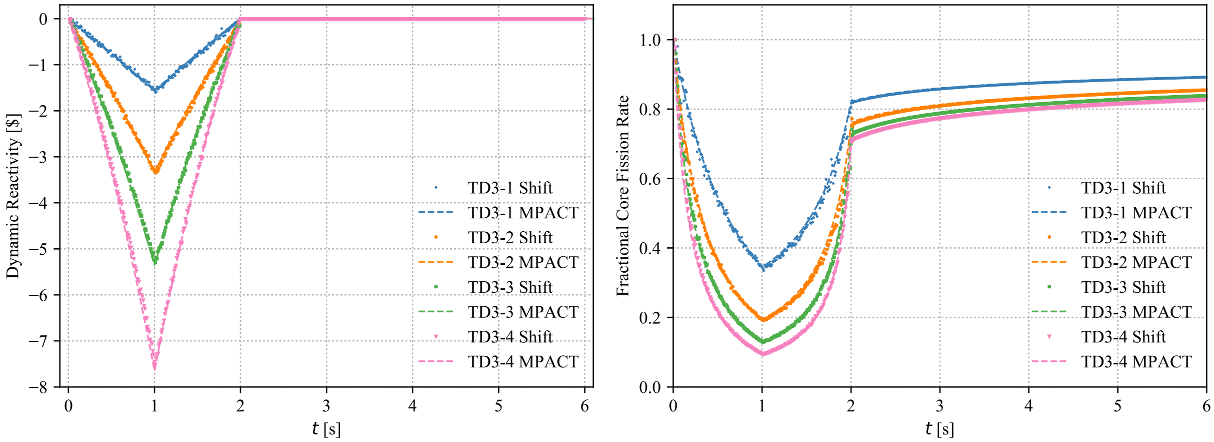

Figure 6-3. Dynamic Reactivity from Shift (left) and EPKE Fractional Core Fission Rate (right) for Each of the TD3 Cases with Stochastic Noise Removed for *t* > 2 seconds

Table 6-1. Norm Comparisons between Shift and MPACT Solutions for Each TD3 Case

TD3 Case	1	2	3	4
$\max_i \left\lvert \frac{p_{i,\text{Shift}} - p_{i,\text{MPACT}}}{p_{i,\text{MPACT}}} \right\rvert$	6.81%	11.07%	7.61%	11.86%
$\frac{1}{N_{\text{time steps}}} \left[\sum_i \left(\frac{p_{i,\text{Shift}} - p_{i,\text{MPACT}}}{p_{i,\text{MPACT}}} \right)^2 \right]^{1/2}$	0.22%	0.31%	0.22%	0.29%
$\frac{1}{N_{\text{time steps}}} \sum_i \frac{p_{i,\text{Shift}} - p_{i,\text{MPACT}}}{p_{i,\text{MPACT}}}$	−1.09%	−2.25%	−0.12%	1.09%

6.1.4 Conclusions and Ongoing Work

Shift’s transient capabilities have been verified with the MPACT code for the C5G7-TD3 benchmark problem with stochastic noise removed from segments of the transient for which no reactivity change is being imposed. Increasing the number of particle histories per fission source iteration cycle might reduce the variance in the stochastic noise for the dynamic reactivity generated by Shift at great computational expense. Notably, the fractional core fission rate does not appear to be sensitive to the stochastic noise while changes to the reactor are being imposed for $t < 2$ seconds. This observation might suggest that more significant computational resources need to be devoted to “critical points” throughout the transient, when the dynamic reactivity is approximately zero. Additionally, before Shift can accurately simulate a transient criticality event inside a DPC repository, its transient capabilities need to be extended to support:

- Sampling of delayed neutron precursor groups with continuous-energy kinetics data
- Mechanisms for simulating reactivity feedback. For the super-prompt critical nature of the transients being examined in this project, fuel Doppler broadening will be the dominant feedback mechanism. Shift already has native on-the-fly Doppler broadening (OTFDB) capabilities that will be leveraged as the implementation progresses.

6.2 Alluvial Repository

This section presents an evaluation of the power pulse from hypothetical transient criticality events in an unsaturated alluvial repository. The primary parameters of interest are the power profile, the fuel temperature profile (peak and average), and the water temperature profile (localized and global). A reactor kinetics calculation with RAZORBACK (Talley 2017a,b; 2018) can illuminate the pulse characteristics given the thermal properties of the SNF and infiltrated groundwater along with the particular reactivity insertion characteristics. RAZORBACK is a research reactor transient analysis computer code designed to simulate the operation of a research reactor. The code provides a coupled numerical solution of the point reactor kinetics equations; the energy conservation equation for fuel element heat transfer; the equation of motion for fuel element thermal expansion; and the mass, momentum, and energy conservation equations for cooling of the fuel elements by water.

The study team conducted a preliminary series of steady-state criticality calculations with MCNP to characterize reactivity feedback provided the conditions for baseline criticality are achieved. These feedback coefficients are used in the kinetics analysis to characterize the transient pulse given a positive insertion of reactivity for given length of time. The time-integrated behavior of the pulse can be used to model effects on the DPC and surrounding barriers in future studies and determine if transient criticality event effects are consequential.

6.2.1 Approach

6.2.1.1 Host Rock Effects

The host rock consists of unsaturated alluvium. Assuming an emplacement depth of 500 m and 18°C surface temperature, a geothermal gradient of ~25°C/km provides an ambient temperature of 30°C. For the static neutronics analyses, a precriticality average canister temperature of 60°C is assumed to account for the decay heat at 9,000 years of cooling (Price et al. 2019b, Figure 3-19).

The groundwater flooding the canister is modeled as pure water with no dissolved species, although the effects of dissolved species can be easily accommodated in future studies. Since the alluvium host rock is unsaturated and the DPC lies at or above the water table, a hydrostatic pressure of 1 atm is used. Therefore, fluid densities inside the DPC are determined at 1 atm and 60°C, with the exception of unbreached DPCs in which the pressure is 8 bar from the helium backfill. This hydrostatic pressure was a factor in the selection of the proper reactor kinetics code to handle the problem, as some codes are tailored to reactor conditions at higher pressures.

6.2.1.2 Canister Model

The DPC used for this study is based on a NAC MAGNASTOR TSC-37 containing 37 spent Westinghouse 15 × 15 PWR assemblies from Zion. As shown in Figure 6-4, the assemblies are mounted in a basket made of 21 square tubes made of ASME SA537 Class 1 carbon steel joined at the corners. These tubes are about 0.8 cm thick and form 16 adjoining void spaces when welded for a total of 37 insertion channels, where the center-to-center pitch is about 11.8 cm. Outside of the basket, the structural trusses joining the basket to the stainless-steel canister are modeled as empty space filled with fluid. As mentioned, the DPC is assumed to be backfilled with helium for storage and flooded with pure water (i.e., no dissolved species) when breached. The basket has a density of 7.85 g/cm^3.

The tubes contain four 21.4-cm-wide absorber assemblies of 1/8-in.-thick, boron carbide (B_4C)/aluminum composite plates mounted internally with 28-gauge (1/64 in.), 316 stainless-steel retainers. The adjoining void spaces do not contain absorber assemblies. The composite is assumed to contain 65 at% B_4C

(43.2 wt%), with boron comprised of the natural abundance of 81.6 wt% B-11 and 18.4 wt% B-10. The (n,γ) cross sections of B-11 and B-10 are 0.005 b and 0.5 b, respectively, while B-10 has an additional (n,α) cross section of 3840 b. The aluminum component is assumed to be pure ^{27}Al metal with no alumina. Altogether, the absorber has a density of 2.619 g/cm^3, and constituent atoms are modeled as a homogeneous mixture.

The inner radius of the canister is assumed to be 90.2 cm to circumscribe the edges of the basket, while an assumed thickness of 1.25 cm results in an outer radius of 91.45 cm. The canister is placed into a 316 stainless-steel overpack of 5 cm thickness and is separated by a 5 mm gap filled with fluid. The EBS would be outside of the overpack, although this area is modeled in the neutronics study as void since the reflective effects of the EBS materials are assumed to be minimal and not worth the computational expense for additional particle tracking. The stainless-steel components are modeled with a density of 8.0 g/cm^3.

The assemblies consist of 204 spent fuel rods and 21 vacant control rod guide tubes. Using pre-operation dimensions, the fuel rods consist of UO_2 fuel pellets of 0.46 cm radius surrounded by a 0.0095 cm, fluid-filled gap and Westinghouse ZIRLO (a zirconium-based alloy) cladding of 0.06 cm thickness. The fuel has a density of 10.2 g/cm^3 (93% of the maximum theoretical density of 10.95 g/cm^3), and the cladding has a density of 6.6 g/cm^3. The rods and guide tubes are separated by a center-to-center pitch of 1.4 cm and have a uniform length of 400 cm; the fuel and cladding edges are assumed to be flush with no plenum regions or springs. Dishing of fuel pellets and gaps between fuel pellets are ignored, making the fuel a continuous cylindrical volume. The SNF is assumed to be disposed with no control rods. While present physically, the grid spacers, guide tubes, tie plates, and other nonfuel components are ignored in the neutronics model and replaced with water like the other void spaces in the system.

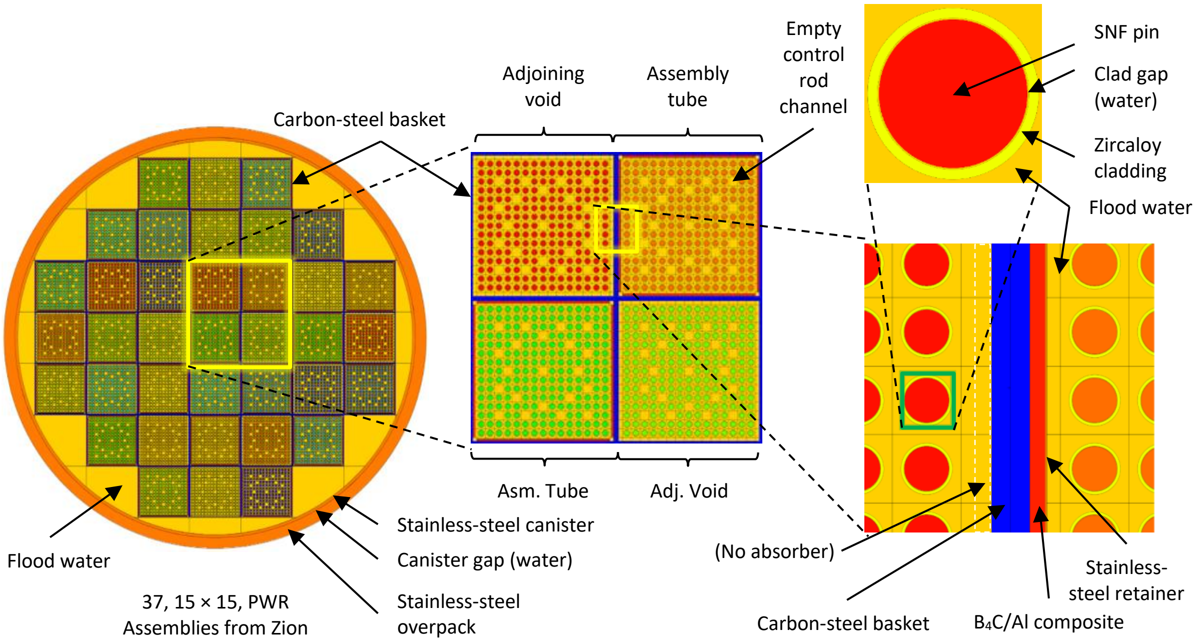

NOTE: Asm. = Assembly
Adj. = Adjoining

Figure 6-4. Radial Model of NAC TSC-37 Used in MCNP Simulations

The longitudinal extent of the DPC is shown in Figure 6-5, where dimensions are nonprototypic and chosen to reduce effects of asymmetry in the results. The assemblies are imagined as lying within the center of the 219-cm-long tubes, where fluid fills the void spaces above and below. There is also a 7 mm, fluid-filled gap between the basket and canister lid and a 5 mm gap between the canister and overpack. The canister lid has an average thickness of 14.9 cm for a total canister length of 470 cm, while the overpack is made 560 cm long (Sevougian et al. 2019).

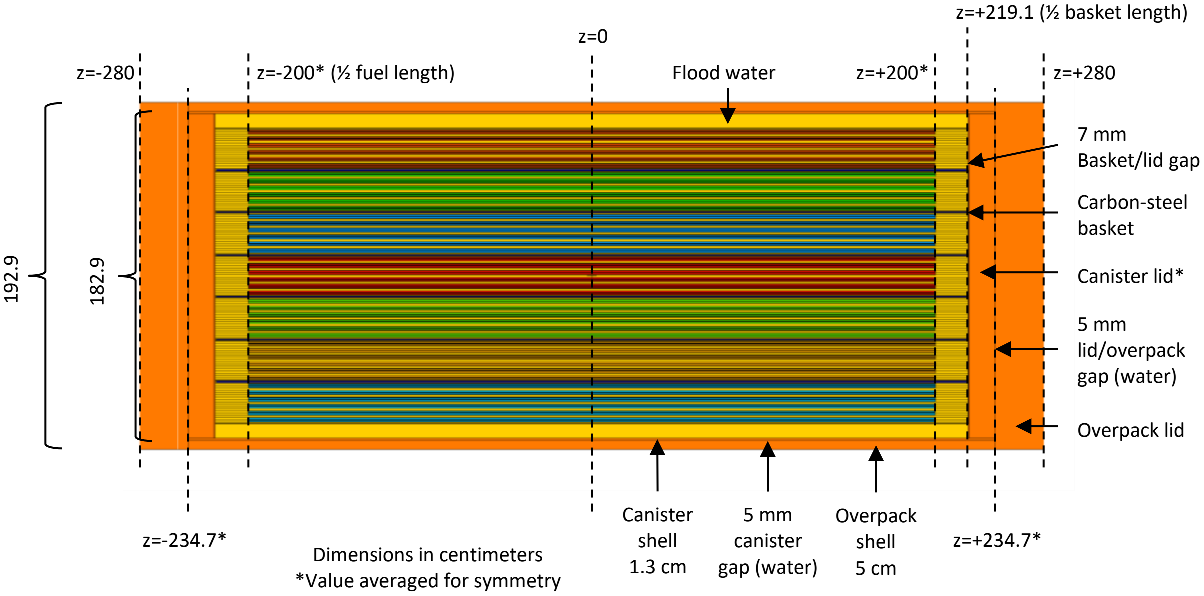

Figure 6-5. Axial Model of NAC TSC-37 Used in MCNP Simulations

6.2.1.3 Fuel Composition

The fuel composition was provided by ORNL from SCALE evaluations on an assembly basis, and results were postprocessed for MCNP isotope labeling and formatting using a Perl script. The results assume emplacement at 2100. Figure 6-6 shows the initial enrichment and burnup of the 37 assemblies, which constitute initial conditions in the depletion calculation. The median operational values for the assemblies are 2.81 wt% initial enrichment, 455.0 kg initial uranium, 27.9 GWd/t burnup, and 122.4 years cooling time after reactor discharge (around 1977). The span of discharge dates is between 1975 and 1996, while burnup ranges from 17.4 to 38.6 GWd/t and initial enrichment ranges from 2.24 wt% to 3.56 wt%. Loading of the DPC has assemblies with higher initial enrichments and burnups around 22.5 GWd/t biased towards the center, while the lowest initial enrichments and burnups are placed on the periphery.

The time points of interest in the depletion results are zero years (emplacement) and 9,000 years, which is the assumed start of the criticality event. After reactor operation and cooling, there are of course fission products and various decay daughters, but there is also additional fissile material present in the SNF besides ^{235}U, which includes ^{233}U, ^{239}Pu, and ^{241}Pu.

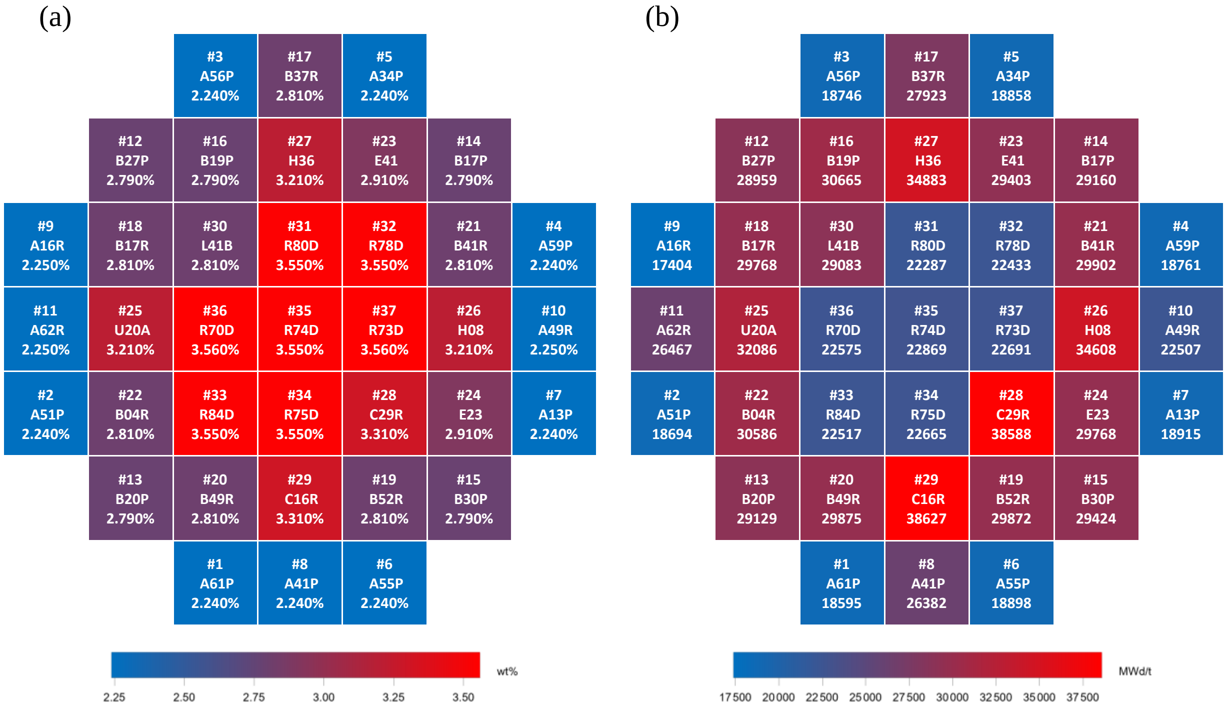

(a)

		#3 A56P 2.240%	#17 B37R 2.810%	#5 A34P 2.240%		
	#12 B27P 2.790%	#16 B19P 2.790%	#27 H36 3.210%	#23 E41 2.910%	#14 B17P 2.790%	
#9 A16R 2.250%	#18 B17R 2.810%	#30 L41B 2.810%	#31 R80D 3.550%	#32 R78D 3.550%	#21 B41R 2.810%	#4 A59P 2.240%
#11 A62R 2.250%	#25 U20A 3.210%	#36 R70D 3.560%	#35 R74D 3.550%	#37 R73D 3.560%	#26 H08 3.210%	#10 A49R 2.250%
#2 A51P 2.240%	#22 B04R 2.810%	#33 R84D 3.550%	#34 R75D 3.550%	#28 C29R 3.310%	#24 E23 2.910%	#7 A13P 2.240%
	#13 B20P 2.790%	#20 B49R 2.810%	#29 C16R 3.310%	#19 B52R 2.810%	#15 B30P 2.790%	
		#1 A61P 2.240%	#8 A41P 2.240%	#6 A55P 2.240%		

(b)

		#3 A56P 18746	#17 B37R 27923	#5 A34P 18858		
	#12 B27P 28959	#16 B19P 30665	#27 H36 34883	#23 E41 29403	#14 B17P 29160	
#9 A16R 17404	#18 B17R 29768	#30 L41B 29083	#31 R80D 22287	#32 R78D 22433	#21 B41R 29902	#4 A59P 18761
#11 A62R 26467	#25 U20A 32086	#36 R70D 22575	#35 R74D 22869	#37 R73D 22691	#26 H08 34608	#10 A49R 22507
#2 A51P 18694	#22 B04R 30586	#33 R84D 22517	#34 R75D 22665	#28 C29R 38588	#24 E23 29768	#7 A13P 18915
	#13 B20P 29129	#20 B49R 29875	#29 C16R 38627	#19 B52R 29872	#15 B30P 29424	
		#1 A61P 18595	#8 A41P 26382	#6 A55P 18898		

Figure 6-6. As-Loaded Configuration of the TSC-37 with Assembly Numbers and identification Labels, Colored by (a) Initial Enrichment and (b) Burnup (MWd/t)

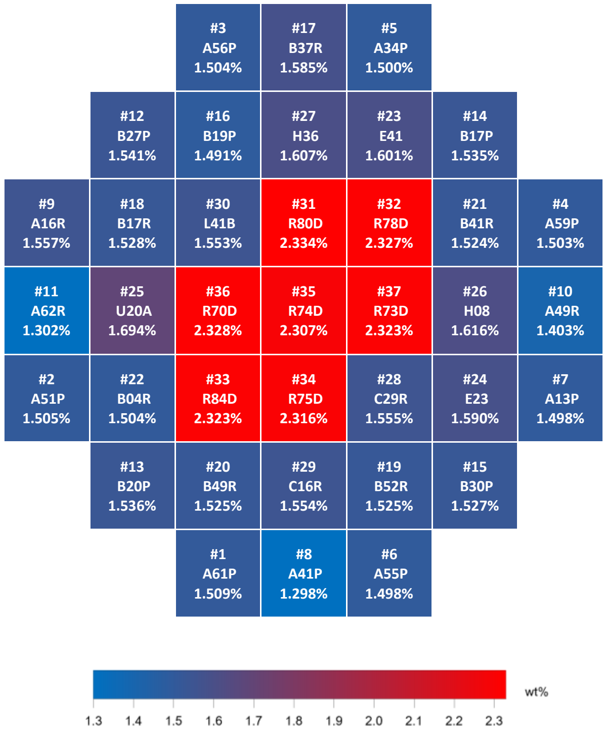

		#3 A56P 1.504%	#17 B37R 1.585%	#5 A34P 1.500%		
	#12 B27P 1.541%	#16 B19P 1.491%	#27 H36 1.607%	#23 E41 1.601%	#14 B17P 1.535%	
#9 A16R 1.557%	#18 B17R 1.528%	#30 L41B 1.553%	#31 R80D 2.334%	#32 R78D 2.327%	#21 B41R 1.524%	#4 A59P 1.503%
#11 A62R 1.302%	#25 U20A 1.694%	#36 R70D 2.328%	#35 R74D 2.307%	#37 R73D 2.323%	#26 H08 1.616%	#10 A49R 1.403%
#2 A51P 1.505%	#22 B04R 1.504%	#33 R84D 2.323%	#34 R75D 2.316%	#28 C29R 1.555%	#24 E23 1.590%	#7 A13P 1.498%
	#13 B20P 1.536%	#20 B49R 1.525%	#29 C16R 1.554%	#19 B52R 1.525%	#15 B30P 1.527%	
		#1 A61P 1.509%	#8 A41P 1.298%	#6 A55P 1.498%		

Figure 6-7 shows the content of fissile isotopes at 9,000 years, at which time most fissile material appears to be concentrated near the center of the DPC mostly as a consequence of the initial conditions in Figure 6-6. The maximum fissile content at the onset of criticality is 2.33 wt% as shown in these central assemblies, although the median value is only 1.54 wt%.

The aforementioned Perl script calculated normalized mass fractions for all unique nuclides in the ORNL inventory results per assembly per time point. It then provided MCNP material input lines for each assembly at a given time for nuclides with mass fractions above 10^{-8}, which usually amounted to 35 or 36 nuclides. For reference, an average composition across all 37 assemblies at 9,000 years is shown in Table 6-2 in decreasing order of mass fraction. The material consists of 99.5 wt% actinides with 98.7 wt% uranium and 0.6 wt% plutonium. The most abundant nonactinides are stable fission products ^{133}Cs and ^{143}Nd, with ^{99}Tc as the most abundant radioactive nonactinide followed by ^{135}Cs and ^{129}I. Notable absorbers ^{149}Sm and ^{155}Gd are present in small quantities, but there are other stable fission products in the list with appreciable (n,γ) cross sections.

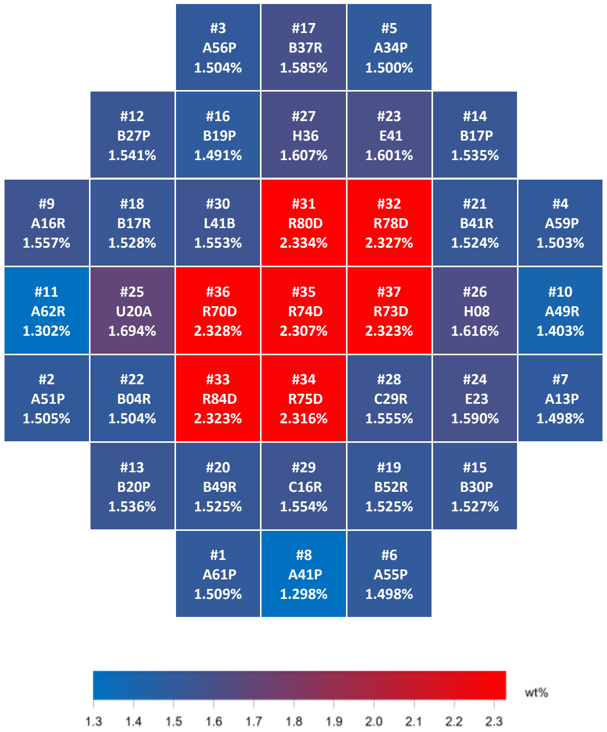

		#3 A56P 1.504%	#17 B37R 1.585%	#5 A34P 1.500%		
	#12 B27P 1.541%	#16 B19P 1.491%	#27 H36 1.607%	#23 E41 1.601%	#14 B17P 1.535%	
#9 A16R 1.557%	#18 B17R 1.528%	#30 L41B 1.553%	#31 R80D 2.334%	#32 R78D 2.327%	#21 B41R 1.524%	#4 A59P 1.503%
#11 A62R 1.302%	#25 U20A 1.694%	#36 R70D 2.328%	#35 R74D 2.307%	#37 R73D 2.323%	#26 H08 1.616%	#10 A49R 1.403%
#2 A51P 1.505%	#22 B04R 1.504%	#33 R84D 2.323%	#34 R75D 2.316%	#28 C29R 1.555%	#24 E23 1.590%	#7 A13P 1.498%
	#13 B20P 1.536%	#20 B49R 1.525%	#29 C16R 1.554%	#19 B52R 1.525%	#15 B30P 1.527%	
		#1 A61P 1.509%	#8 A41P 1.298%	#6 A55P 1.498%		

Figure 6-7. As-Loaded Configuration of the TSC-37 with Assembly Numbers and Identification Labels, Colored by the wt% of Fissile Isotopes at 9,000 Years of Cooling

Table 6-2. Average Composition of All 37 Assemblies at 9,000 Years along with Half-Lives

Symbol	A	kg/kg	$t_{½}$ (year)
U	238	9.700E-01	4.468E+09
U	235	1.196E-02	7.035E+08
Pu	239	4.776E-03	2.409E+04
U	236	4.625E-03	2.340E+07
Np	237	1.730E-03	2.142E+06
Cs	133	9.415E-04	*Stable*
Pu	240	7.785E-04	6.556E+03
Nd	143	7.007E-04	*Stable*
Mo	95	6.429E-04	*Stable*
Ru	101	6.389E-04	*Stable*
Tc	99	6.325E-04	2.109E+05
Nd	145	5.493E-04	*Stable*
Cs	135	3.849E-04	2.313E+06
Pu	242	3.730E-04	3.739E+05
U	234	2.890E-04	2.453E+05
Sm	147	2.334E-04	1.062E+11
Sm	150	2.326E-04	*Stable*
I	129	1.285E-04	1.569E+07
Eu	153	9.377E-05	*Stable*
Sm	152	9.234E-05	*Stable*
Ag	109	6.692E-05	*Stable*
Am	243	3.260E-05	7.383E+03
Sn	126	1.676E-05	2.301E+05
Eu	151	1.229E-05	1.711E+18
Th	230	7.046E-06	7.539E+04
Gd	155	6.202E-06	*Stable*
U	233	4.655E-06	1.591E+05
Se	79	3.743E-06	2.950E+05
Sm	149	3.304E-06	*Stable*
Th	232	1.092E-06	1.401E+10
Cm	245	5.649E-07	8.556E+03
Ra	226	1.113E-07	1.584E+03
Pa	231	9.106E-08	3.273E+04
Th	229	6.719E-08	7.874E+03
Am	241	2.898E-08	4.322E+02
C	14[a]	2.518E-08	5.704E+03

NOTE: [a] **Not modeled in the doppler broadening study**.

6.2.1.4 Neutronics

The MCNP code (version 6.1.1) is used to evaluate effective multiplication in the DPC using the canister model and ORNL inventory results. The code and its cross-section libraries have been benchmarked for low-enriched-uranium (LEU; < 10 wt%) criticality studies via data from the International Criticality Safety Benchmark Evaluation project handbook (Briggs et al. 2003). However, the results shown in this report are not compared with these benchmarks pending further refinement.

For criticality calculations, three source points are defined per fuel rod at one quarter, one half, and three quarters of the length. Physically, these points represent neutrons from spontaneous fission or neutrons emitted as a result of decay. The calculations use 10,000 neutron histories per cycle, with 100 inactive cycles and 500 total cycles. The initial guess for k_{eff} is assumed to be 1.0 until refined with baseline results.

Static calculations maintain cross sections from the ENDF/B-VII.1 library at 20.45°C. Calculations incorporating effects of Doppler broadening modify cross sections in the fuel as the temperature increases using the OTFDB code.

The materials defining the fuel in each assembly were obtained from the postprocessed ORNL results. Perl scripts were used to calculate evolving material compositions and fluid densities and create MCNP input files using a template file with flagged regions of the input deck. Effective densities of compound materials were obtained using the composition script from Salazar (2018).

The canister model is implemented using a nested hierarchy of universes, beginning with the components of a fuel rod, the fuel rods in a given assembly, an assembly in a tube/void space, a tube/void space in the basket grid, and the basket inside of the canister and overpack. The initial composition of the fuel rods is assumed to be uniform per assembly. The assembly materials are numbered sequentially, but the as-loaded configuration does not follow this numbering scheme in any pattern. Therefore, special attention was paid to ensure proper mapping of the assemblies in the tubes and void spaces in the basket for the as-loaded configuration. A consequence of employing this nested cell definition is less convenience in defining a water level in the DPC, which is slated for future work. The uniform fuel assumption also prevents employing spatial variation in fuel temperatures.

6.2.1.5 Criticality Scenario

A generalized, high-level timeline of the criticality scenario is shown in Figure 6-8, showing the conceptual evolution of the reactivity (ρ) state over time along with time periods affecting the inventory and degradation state of the canister. Engineering considerations for preventing criticality events in the repository begin with the properties of the fuel itself, including the original type (e.g., UO_2, accident-tolerant) and enrichment (e.g., LEU), and then its utilization in a particular reactor type (e.g., PWR, BWR) for commercial production, which includes burnup, operation/shutdown cycles, and fuel shuffling. After the fuel has reached end-of-life (EOL), assemblies are placed into a spent fuel pool for approximately ten years of cooling. The assemblies are then moved into dry cask interim storage in DPCs, where the void space is backfilled with inert gas such as helium. After some period in interim storage, the DPC is emplaced in an alluvial repository surrounded by an EBS, and the timeline for postclosure criticality begins.

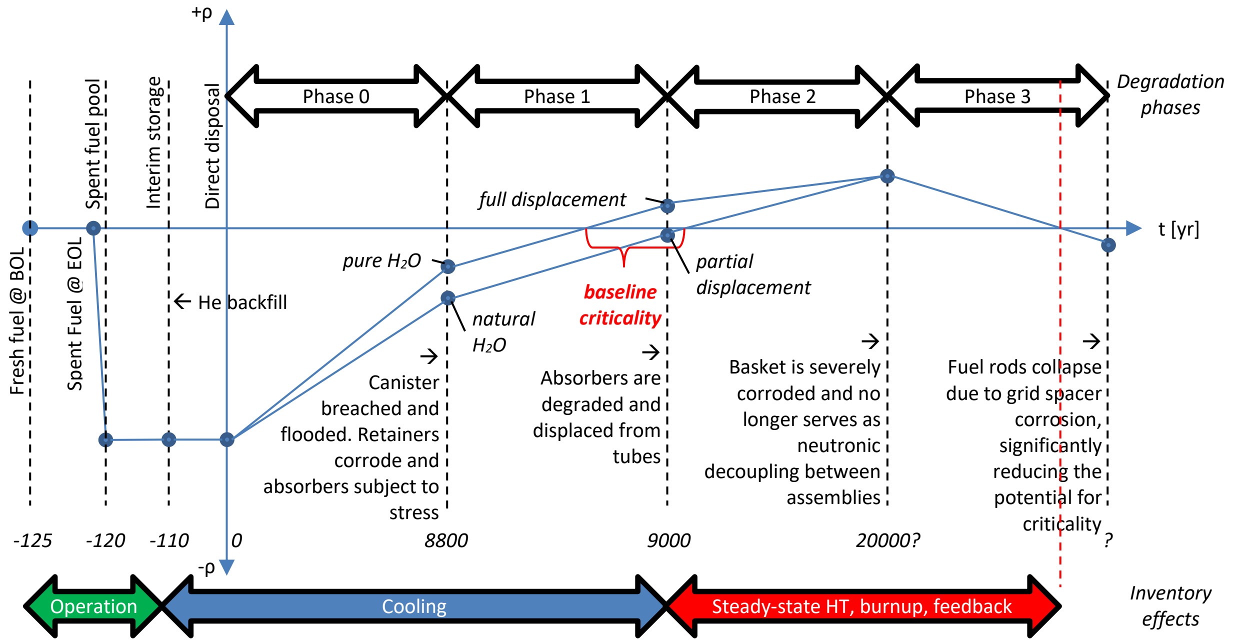

NOTE: BOL = beginning-of-life
EOL = end-of-life
HT = high temperature

Figure 6-8. General Timeline of Events in the Criticality Scenario along with General Reactivity Behavior and Anticipated Time Frames

After emplacement, the canister is subject to corrosion and other phenomena that can result in a breach, which serves as the gateway for water infiltration. However, the packaged absorbers are designed to be robust in such failure scenarios, so only until they are extensively degraded can the effect of water lead to appreciable increases in system reactivity. The absorbers are hypothesized to degrade first followed by the canister basket, and both phenomena would increase the reactivity. For the purposes of this study, it is assumed that baseline criticality can be achieved with such extensive degradation provided an appropriate quantity of water in the canister.

A baseline critical state is required before transient events can be considered. However, it is also possible that the approach to the initial critical state is itself intermittent and time dependent, especially in an unsaturated repository where water is less likely to fill the whole DPC (see Section 4.3.1). That is, just as criticality is achieved, the heat of criticality may cause water to evaporate or boil at a rate that matches or exceeds the replenishment from infiltration or condensation. The effects of decay heat and subcritical heating may also be nonnegligible. The steady state is therefore defined with respect to effectively achieving heat transfer equilibrium with the surroundings in the repository, where the boundary conditions needed for prolonged criticality are consistent over geological time until major reactivity feedback effects decrease reactivity on a system-wide level. Such feedback effects include depletion of the fissile material, thermal expansion, voiding, and warping of the fuel, introduction of natural poisons into the groundwater, loss of reactivity from fission product buildup, or loss of moderator from evaporation or boiling without replenishment.

At some point in time, the basket is so thoroughly degraded that assemblies are no longer effectively separated, which increases neutronic coupling between neighboring fuel rods (as less neutrons are lost to capture or leakage) and increases the reactivity. However, the Zircaloy grid spacers in the SNF are also susceptible to a thermally driven corrosion process (Section 4.4). Given the heat from criticality events, this corrosion process can be accelerated, and when the grid spacers have extensively corroded, the fuel rods will become less separated and eventually agglomerate from grid collapse. This situation leads to a decrease in reactivity from an increase in spatial self-shielding, which can ultimately terminate the steady-state criticality if other forces such as depletion, thermal expansion, or loss of water have not done so already.

The following sections will describe how the different phases of degradation can be modeled to understand the preliminary baseline criticality cases before undertaking a transient analysis.

Phase 0

The TSC-37 is modeled with a backfill of 95 at% (83.9 wt%) helium and 5 at% (16.1 wt%) air with a gas density corresponding to 60°C and 8 bar. The model uses the as-loaded configuration of assemblies and includes the effects of the basket and neutron absorbers but ignores the effects of the structural components of the assemblies (i.e., grid spacers, tie plates, guide tubes, etc.) This phase represents conditions of interim storage as a baseline reference case for the subcritical state before the effects of water flooding can be considered.

Phase 1

The model progresses to include the infiltration of groundwater. In an alluvial repository, the water level is susceptible to change as the DPC lies above the water table. However, this report considers a fully flooded canister in an effort to de-couple the water level from this initial criticality scoping analysis. The effects of partial flooding are slated for future work.

Seismic events combined with erosion of the EBS can be postulated to tilt or perhaps fully invert a canister. Seismicity can also elicit mechanical failure and displacement of the absorber plates. While the composite material is strongly resistant to dissolution, suspensions of small, solid particles may be susceptible to transport (e.g., Brownian motion) and can displace absorbers from their original location. In a situation in which the DPC is heavily tilted or inverted, B_4C particles from degraded absorbers can traverse the length of the tube and accumulate below the fuel, removing shielding between fuel rods in neighboring assemblies and increasing reactivity in the DPC (Figure 6-9). If the canister maintains horizontal emplacement, B_4C particles from the degraded absorber can accumulate on the bottom of the tube and still increase reactivity to some degree. These scenarios are termed Phase 1a and Phase 1b, respectively.

For modeling Phase 1a, engineered absorbers are gradually replaced with water and effectively removed from neutron transport. This situation is hypothesized to constitute a larger reactivity insertion, although the insertion period would be limited by the transit time of the particles to the bottom of the assemblies.

For modeling Phase 1b, while top and lateral absorbers are removed, the lower region of the tube still contains particles that interact with SNF. The lower absorber is therefore modeled with increasing density as atoms in the other absorbers are replaced with water, so the total mass of absorber is conserved. This situation is hypothesized to constitute a smaller reactivity insertion, and in terms of characterizing a potential transient event, this would be enhanced with a shorter transit time.

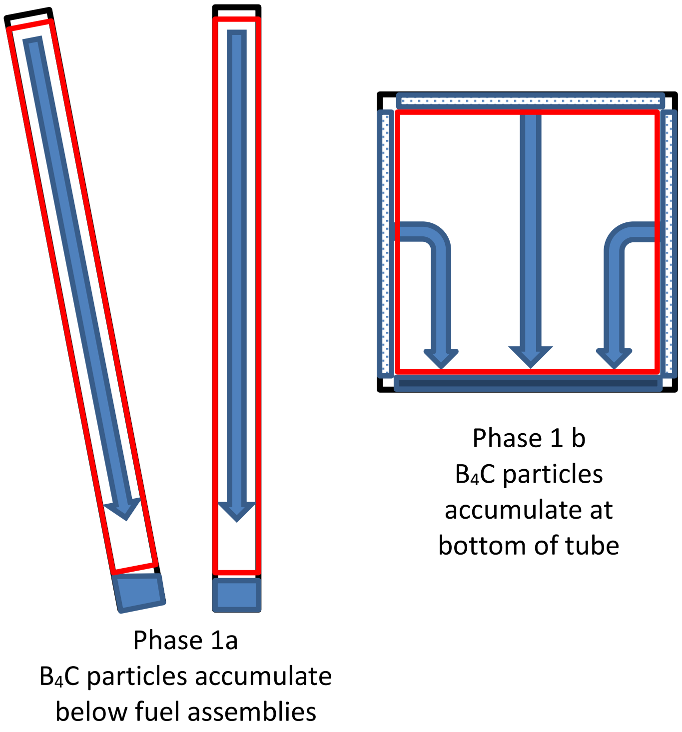

Figure 6-9. Phase 1 Scenarios with Assemblies Outlined in Red

A size distribution of B_4C particles from the absorber plates can be useful for estimating transit times for Phase 1 transient criticality events (Figure 6-10). Such a distribution could be obtained from a solid mechanics analysis of particles dislodged and resettled during a seismic event. The transit times can then be evaluated using a buoyancy-based analysis for the particles (modeled as spheres) suspended in the water column of the basket tube. Using the total mass of absorber, these time periods can then be used to configure the reactivity insertion as a function of time and space for RAZORBACK.

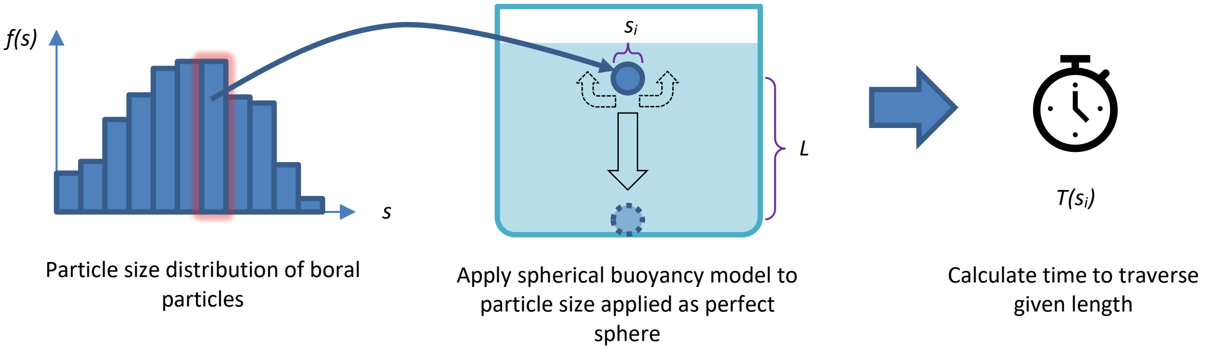

Figure 6-10. Proposed Approach To Evaluate Transit Time

Phase 2

The basket undergoes extensive corrosion such that it no longer provides neutronic decoupling between assemblies. This effect can be modeled as the metal in the carbon-steel basket being gradually replaced with water, which will increase the reactivity of the system from the end-state achieved in Phase 1. This basket corrosion effect is called Phase 2a, which is shown in Figure 6-11.

After the carbon-steel basket has extensively degraded, the assemblies (with grid spacers still intact) can progress to move closer to one another as the basket gradually collapses from the weight of fuel and the carbon steel is ineffective at shielding neutrons. This collapse effect is called Phase 2b. The carbon steel is modeled as being completely displaced with water, and from this state, the tube pitch is modeled as being gradually reduced until the assemblies are touching, emulating a reactor configuration, and giving a peak system reactivity. For purposes of reducing asymmetry effects, this close-contact configuration is hypothesized as occurring at the center of the canister (Figure 6-12).

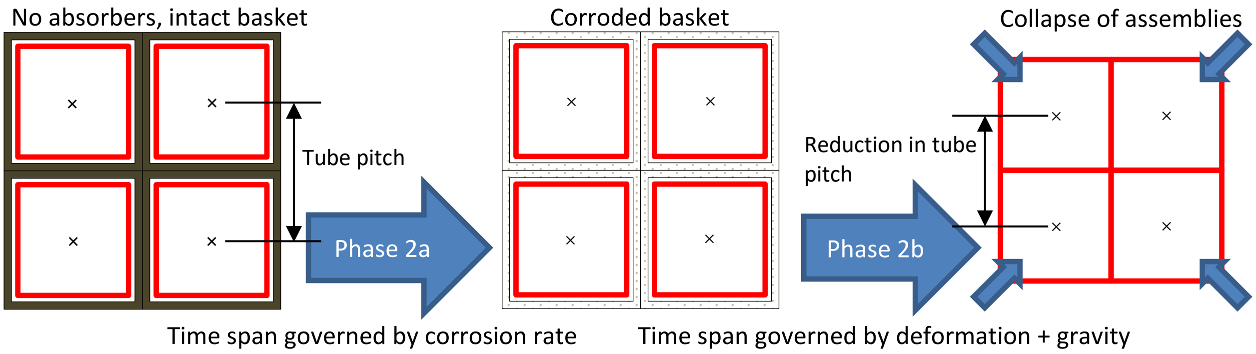

Figure 6-11. Phase 2 Scenarios with Assemblies Outlined in Red

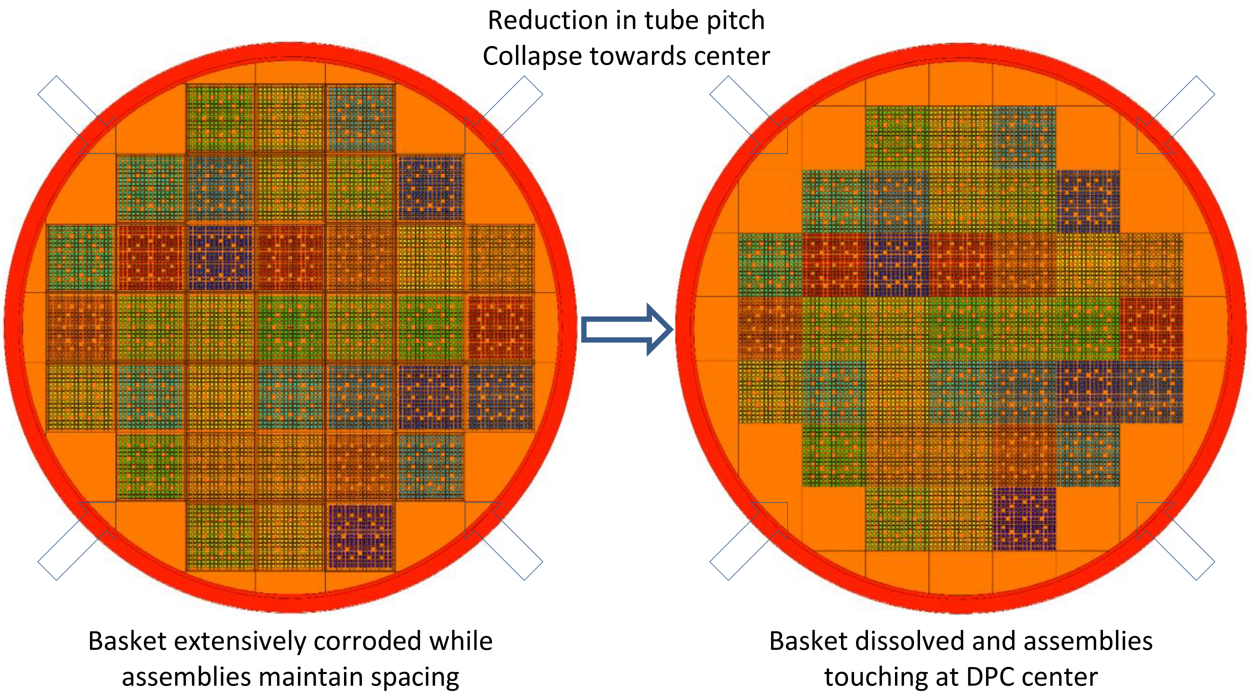

Figure 6-12. Start and End States of the Phase 2b MCNP Model

Phase 3

In Phase 3, rod collapse within an assembly occurs when zircaloy grid spacers have fully corroded and no longer maintain the original pitch of the fuel rods. The resultant undermoderated system is hypothesized to terminate baseline critical configuration and associated steady-state criticality heat generation. If the collapse occurs within a short period of time, however, it may be possible that a momentary increase in reactivity could occur before the full collapse. Nonetheless, this transient event may be less substantive than those occurring in the previously mentioned scenarios.

The fuel rod spacing in an assembly is gradually reduced until the rods are touching, i.e., when the rod pitch equals the diameter of the fuel clad (Figure 6-13). The rod collapse is modeled in MCNP for the flooded, no-absorber, basket-intact configuration at the end of Phase 1a and the flooded, no-basket, close-contact configuration at the end of Phase 2b. These two scenarios are called Phase 3a and Phase 3b, respectively, and are diagrammed in Figure 6-14 and Figure 6-15. While the control rod guide tubes are empty and not included in the model, the gap they introduce between rods is maintained.

These geometries are chosen to maintain a high degree of symmetry and reactivity. While gravity would cause accumulation of rods at the bottom of the canister, such a configuration would not be as reactive due to shielding effects from the stainless steel. Also, it is not clear if there would be more reactive configurations with off-parallel rod displacements.

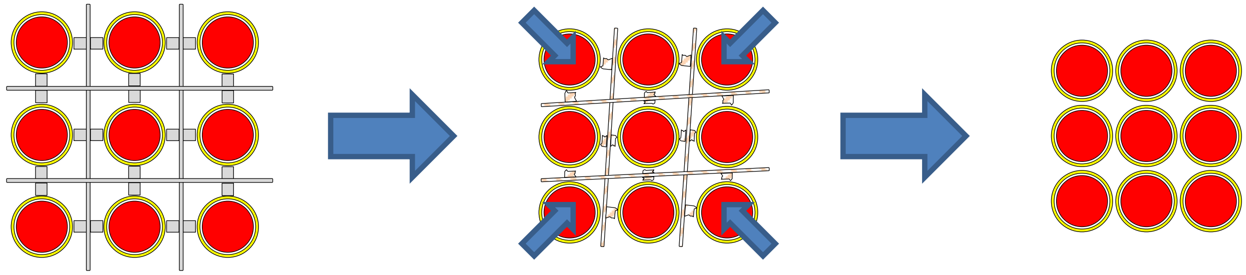

Figure 6-13. Phase 3 Scenario for Collapse of Fuel Rods with Grid Spacer Degradation

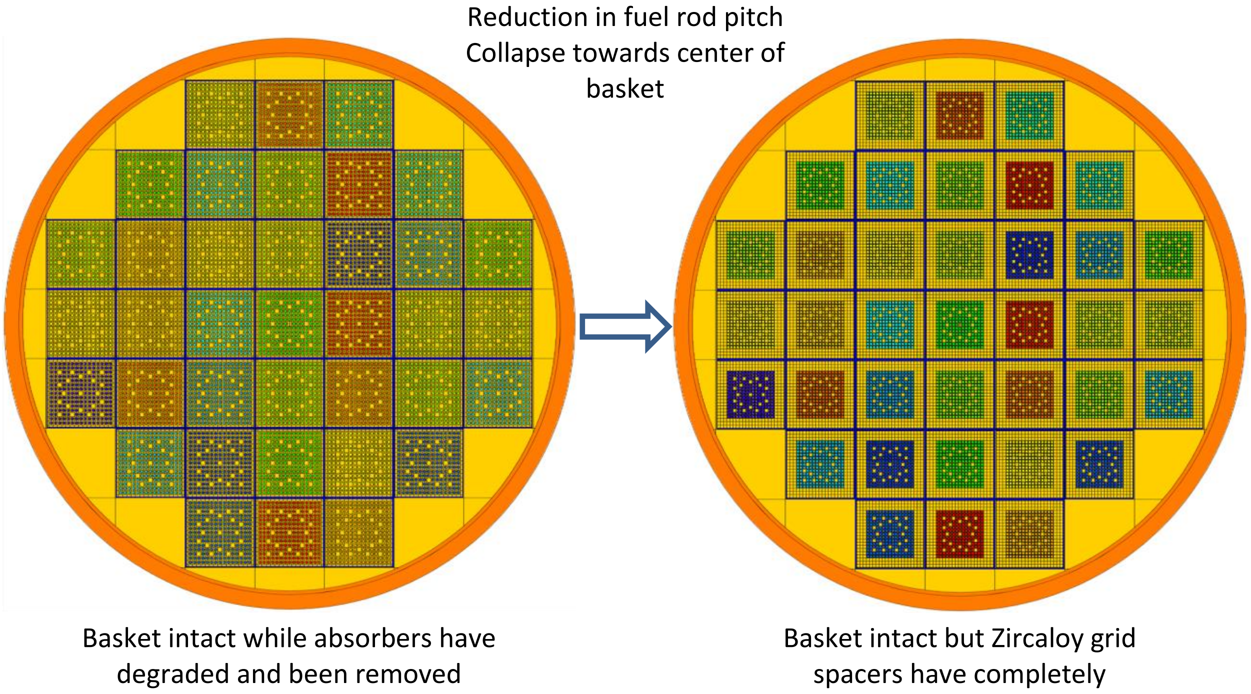

Reduction in fuel rod pitch
Collapse towards center of basket

Basket intact while absorbers have degraded and been removed

Basket intact but Zircaloy grid spacers have completely

Figure 6-14. Start and End States of the Phase 3a MCNP Model

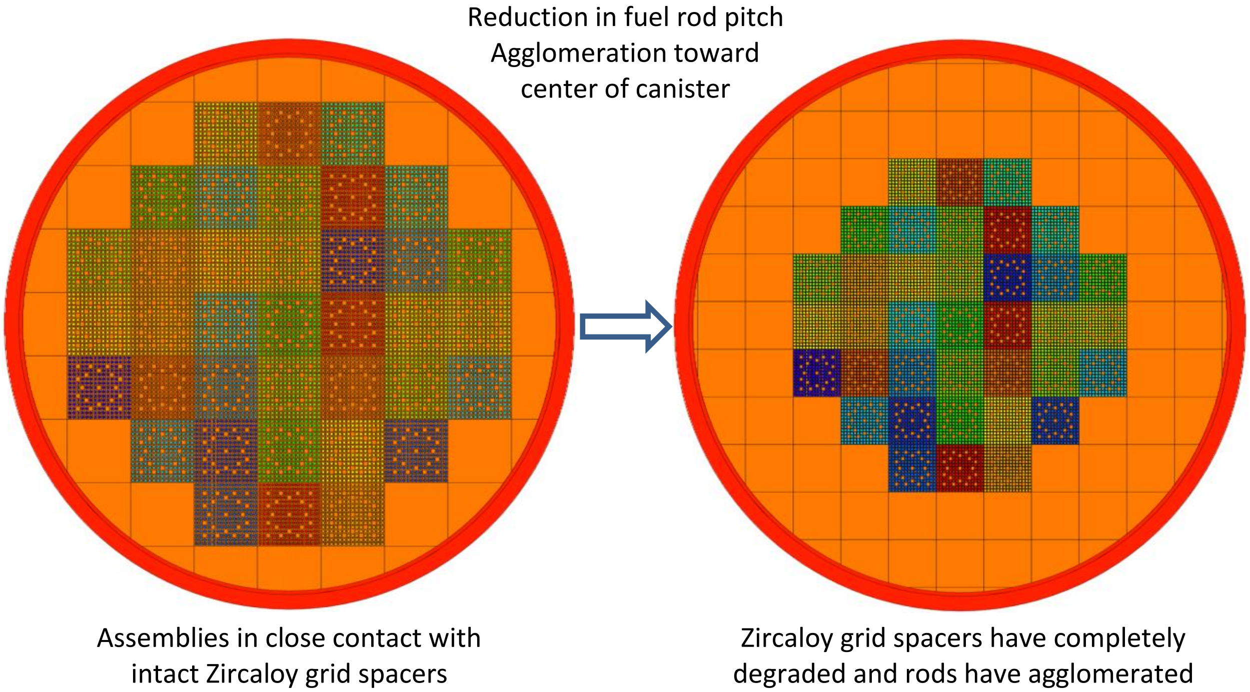

Figure 6-15. Start and End States of the Phase 3b MCNP Model

6.2.1.6 Reactivity Feedback

The series of steady-state neutronics analyses for the base case scenarios provide reactivity feedback information dealing with the introduction of water, the loss of absorber, and changes in DPC configuration. However, there are additional feedback mechanisms that can be investigated including voiding of the moderator, increasing temperature in the fuel, and thermal expansion in the fuel. These are necessary to understand in order to perform a calculation in RAZORBACK.

The increase in fuel temperature is hypothesized to reduce system reactivity through Doppler broadening of the fuel, which describes a smearing effect of resonances with increasing average temperatures. The peaked resonances for absorption become smeared and broadened in energy as a consequence of increased vibrational motion in the target nuclei. This results in a depression in absorption cross-section peaks and a spread in the range of applicable energies, where the latter effect ultimately leads to a net increase in absorptions.

For calculations incorporating Doppler broadening effects, the cross sections in the fuel are modified as the temperature increases using the OTFDB code (Martin 2012). The code uses ENDF data at different temperatures to create an interpolated energy grid based on a temperature range with set intervals. When a collision is scored in MCNP, OTFDB employs the user-specified cell temperature to alter both the collision kinematics and absorption cross sections based on the Cullen and Weisbin, exact Doppler broadening equation (Cullen and Weisbin 1976). There are 54 unique nuclides across all materials at 9,000 years; these nuclides are listed in the OTFDB card in the MCNP input deck. One exception is ^{14}C in the fuel, which is excluded from the broadening analysis as only natural-carbon cross sections were available.

A script was written to run the OTFDB preprocessor code for these nuclides and create interpolations based on a range of temperatures from 300 K (26.85°C) to 2,500 K (2,226.85°C). This temperature range corresponds to the temperatures of the "80c" (293.6 K) and "84c" (2,500 K) ENDF-B/VII.1 evaluations used in MCNP, where 300 K is used for rounding purposes. Eighth-order interpolations are made in 10 K intervals across this temperature range using an energy grid based on 100 K bins. The binary interpolation files are located in a central directory and symbolically linked to working directories with OTFDB calculations. These binaries are referenced when an interaction is scored in a material containing any of these isotopes and if the temperature is specified in that material. While the upper bound temperature is below the melting point of pure UO_2 fuel (around 2,800°C), it lies above the expected melting point of 2,000°C for zircaloy-based alloys. Therefore, the final temperatures in the analysis should cover the point at which significant fuel rod degradation is achieved and a transient criticality event would not be sustainable.

RAZORBACK employs the temperature feedback coefficient in the form of the power law shown in Equation 6-1. This type of temperature dependence is representative of feedback in a thermal reactor (Ott and Neuhold 1985). The coefficients $\mathcal{C}_0$ and $\mathcal{C}_1$ are fitted to the results of the static MCNP calculations with OTFDB to provide an approximation of the temperature coefficient.

$$\frac{\partial \rho}{\partial T} = \mathcal{C}_0 + \frac{\mathcal{C}_1}{\sqrt{T}} \qquad \textit{Equation 6-1}$$

The code also employs feedback coefficients for the coolant in terms of increasing temperature ("spectral") and voiding. The coolant temperature coefficient is implemented as reactivity per Kelvin while the voiding coefficient is implemented as reactivity per percent void. In the MCNP simulation, the temperature feedback coefficient is obtained by increasing coolant temperature and modifying coolant density up to 100°C at 1 atm (pure vapor data are considered unimportant for the transient). The voiding coefficient is found by increasing the steam quality at the 1 atm saturation temperature and using the homogenized density. While the characteristics of two-phase flow would be strongly influenced by the canister geometry and the level of steam separation, the analysis treats the mixture as homogeneous throughout the void space.

The water properties in the coolant analysis are obtained from the International Association for the Properties of Water and Steam (IAPWS) Industrial Formulation 1997 (IF97) for the Thermodynamic Properties of Water and Steam (Wagner et al. 2000). The open-source CoolProp thermophysical property database (version 6.4.1) is used to evaluate this formulation (Bell et al. 2014); the specific version of the IF97 backend used for compilation of the python wrapper was version 2.1.2. The python wrapper is called via another python script to facilitate command line usage in the larger Doppler broadening analysis. The inputs of temperature, pressure, steam quality, etc. can be specified for outputs of density, saturation temperature, and so on.

The two-phase analysis is applicable for the temperature range from 273.15 K to 647.096 K and the pressure range from 611.22 Pa to 22.064 MPa, which correspond to the transition from the triple point to the critical point. The single-phase analysis is restricted from 0°C to 100°C for the 1 atm scenario, as the transition from liquid to steam is sufficient to suppress criticality. However, a scenario can be devised in which the breach is sealed after water infiltrates the canister; this situation would allow for pressure build-up, which would expand the temperature range of the liquid phase for the Doppler broadening analysis in the coolant. The analysis could proceed at increasing temperatures and pressures along the saturation line up to 617.94 K and 15.5 MPa (the design pressure of the PWR assemblies) with the assumption that no steam is present in the mixture (i.e., use only saturated liquid properties). The coefficient can then be derived for the normal temperature range and maximal temperature range.

The outputs from CoolProp were cross-checked with the IF97 module in the “IAPWS” open-source python package (Gómez Romera et al. 2021). Results were obtained for single-phase points of temperature from 0°C to 100°C and pressure from 0.1 MPa to 8 MPa, and two-phase points for pressure and quality from 0 to 1. The density results were identical within the full 8 decimals of precision analyzed, showing that CoolProp results are replicable within the community.

6.2.1.7 Reactor Kinetics

RAZORBACK is a reactor transient analysis code designed to determine the response of a pool-type natural circulation research reactor via a coupled numerical solution of the point kinetics equations, the conservation of energy, and the conservation of momentum for coolant and fuel elements (Talley 2017b). It has been validated for transient analyses with data from SNL’s Annular Core Research Reactor (ACRR; Talley 2017a). In this study, it is used to evaluate the point kinetics equations given the reactivity feedback behavior provided by the neutronics scoping analysis discussed earlier. Calculations are meant to span the applicable time period of the postulated transient pulse for a given total reactivity insertion.

In the simulation, the flooded DPC with compromised absorber plates functions as a reactor, for which the maximum power $P_{100\%}$ is set to 1 MW. The problem acknowledges all N_{rods} = 7,548 SNF rods in the TSC-37 and employs an element peak-to-average factor $f_{r,peak}$ of 1.5096 to impart a maximum element power $P_{element}$ of 20 kW for fraction $\chi = 1$, as implied in Equation 6-2 (Talley 2017b). Before the transient begins, the problem is allowed to stabilize for 60 seconds with no feedback or reactivity insertion. It then initiates at 100.0% of the full reactor power and the reactivity insertion begins immediately at time zero.

$$P_{element} = \frac{\chi * P_{100\%}}{N_{rods}} f_{r,peak} \qquad \textit{Equation 6-2}$$

RAZORBACK features reactivity controls in the form of a control rod bank, safety rod bank, and transient rod bank, all of which behave in the same time- and space-dependent manner, although the transient rods have additional specifications. There is also an option to enter a generic time-dependent reactivity insertion function that can augment the rod reactivity for a specified time period. The calculations in this report use the control rods as means of controlling the time-dependent reactivity insertion, while the other options are turned off.

Use of the control rod bank required construction of a differential reactivity curve as a sine-squared function of the axial height of the control rod bank. This was done by iteratively changing parameters to adjust to the axial height of 400 cm while maintaining similar peaking behavior to the sample problem curve. The parameters were also adjusted to integrate to unity across the whole extent of the fuel so the curve could be scaled to the total worth of the control rod bank. This resulting function is shown in Equation 6-3 and plotted in Figure 6-16. The control rod is withdrawn at a fixed speed to a certain distance to insert the desired worth within a specified time period. The problem ends at 50 times the period of the control rod insertion, with an exception for the 0.01-second insertions for which an end time of 2.0 seconds is employed to capture the full range of results.

$$\left.\frac{d\rho}{dz}\right|_{CR} [cm^{-1}] = 0.00417395 \cdot \sin^2(0.006464969 \cdot z + 0.4) \qquad \textit{Equation 6-3}$$

The delayed neutron group decay constants and group fractions are taken from the eight-group formulation from Spriggs et al. (1998). The reactivity feedback coefficients from the MCNP studies are applied directly and no scaling factors are applied. However, the local feedback weighting factor for the particular location in the fuel element is determined using the product $F_r(r) \cdot F_z(z)$ with an exponent of 2.0, which characterizes data from ACRR tests. This approach is used since the neutronics study did not employ individual rod fidelity or any axial discretization to provide a custom exponent. In the following fits associated with this choice of exponent, a weighting factor of 0.894 is employed to scale the total reactivity feedback as an adjustment for the core location peaking factor.

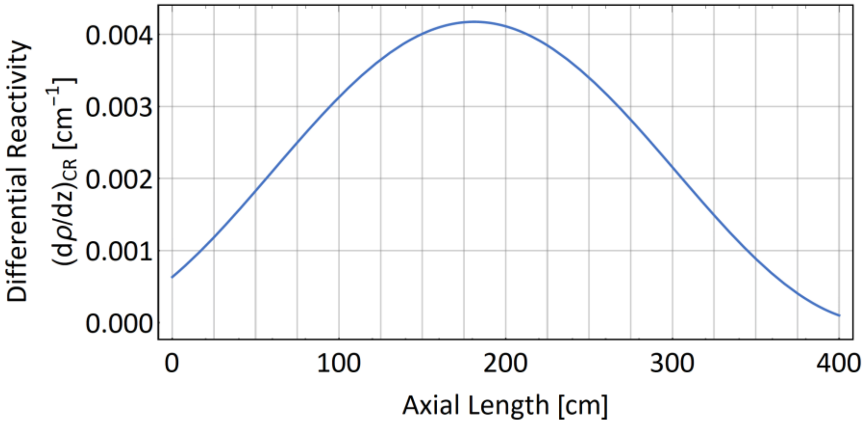

NOTE: This curve integrates to unity so it can be scaled to the total worth of the control rod bank.

Figure 6-16. Differential Reactivity Curve for the Control Rod Used in the Study

While the DPC is meant to be horizontally emplaced, the problem requires the configuration to be vertical to follow the reactor basis of the code and for the basket assemblies to be directly exposed to a column of water in a virtual tank. The pool tank height is set as 1,060 cm, providing a maximum 626 cm, water column above the coolant channel (described later) and 640 cm above the top of the fuel. The water column determines the pressure at the bottom and top of the coolant channel assuming 14.696 psia atmospheric pressure at the top of the tank. An exploratory analysis of the effects of the water level indicated marginal effects on final results for this initial problem setup. Therefore, this report shows results with water at 300 cm below the tank lip, which is 326 cm of water above at the top of the coolant channel. This approach gives a coolant channel pressure range of 19.3 psia to 25.5 psia top to bottom.

The tank area of 25,543.1 cm^3 represents the area from inner canister radius, as water outside the canister is assumed to play no role in the transient. There is no other displaced volume in the water apart from the reactor. The pool heating is determined by the reactor (DPC) power output and natural convection, and the initial pool temperature is 60°C. The ANS 5.1 Decay Heat specification is turned on to account for SNF decay heat prior to the transient.

The fuel is modeled with three zones: cylindrical UO_2 fuel, a clad gap filled with water, and ZIRLO cladding. The clad gap is necessary to model thermal expansion and radiative heat transfer effects. Dimensions are borrowed directly from the neutronics analysis for the Westinghouse 15 × 15 PWR configuration, including the nonprototypic fuel length of 400 cm as the active length. The fuel is divided into 30 radial nodes while the gap and clad are divided into 10 radial nodes. The 15th radial node in the fuel is used to evaluate an average temperature from the adjacent 5 nodes on either side. The axial extent is divided into 400 nodes, giving an axial node height of 1 cm, and the square pitch of 1.430 cm from the Westinghouse assembly is maintained. Pressure inside and outside of the fuel element is set initially at 14.696 psia (101,325 Pa), although the outer pressure does not change over time.

In terms of the coolant channel, there is a heated region adjacent to the fuel elements, an unheated coolant channel length of 14 cm above the heated region, and a lower unheated length of 20 cm, providing a total system length of 434 cm. In RAZORBACK, the coolant and fuel nodes are staggered such that there is one additional heated coolant node compared to the fuel nodes. A two-phase flow drift velocity of 8.5 cm/s is used as representative of saturated water with a surface tension of 0.072 N/m (via IF97). A boiling expansion suppression factor of 1.0 is employed to avoid numerical instabilities with saturated boiling. The atmospheric pressure above the pool water is 14.696 psia (101,325 Pa). The coolant node inlet/exit flow area is 1.36656 cm^2 with a wetted perimeter of 1.45988 cm, and a minor head loss coefficient of 1.50 is employed. The reactor protection features (e.g., scram) are turned off, and the loss-of-coolant and loss-of-heat-sink accident simulators are also turned off.

The radial fission density profile for a given fuel element is modeled with an exponential function $F_r(r)$. Since the MCNP simulations did not explore this profile through radial discretization of the pellets, the curve used in the sample problem from the RAZORBACK manual was used as a template and then iteratively modified until the integral was normalized with respect to the fuel pellet radius of 0.465 cm. The result is shown in Equation 6-4 and plotted in Figure 6-17, where the fission density peaks at the pellet surface.

$$F_r(r) = 0.019 \cdot e^{2 \cdot r} + 0.96866 \qquad \text{Equation 6-4}$$

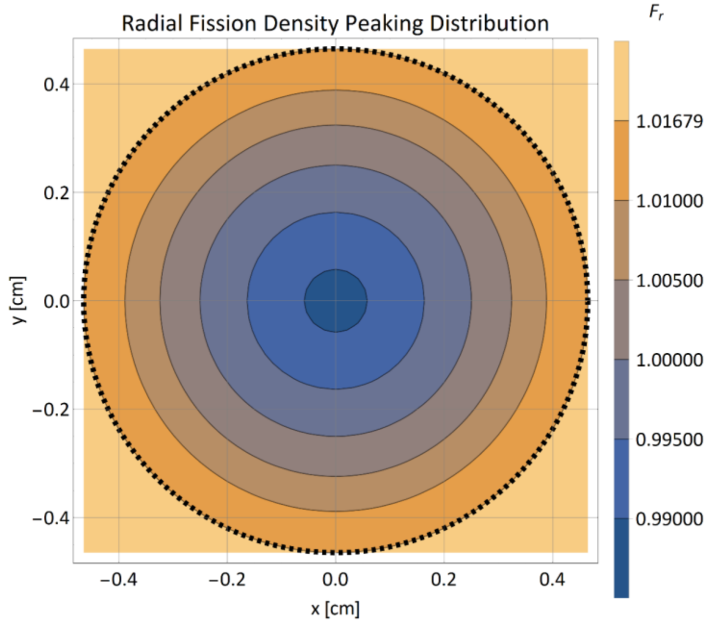

Figure 6-17. Radial Distribution of Fission Density Peaking $F_r(r)$ in the RAZORBACK Simulation

The axial fission density profile is a polynomial function in axial height that incorporates the fuel rod length. Given the lack of axial discretization in the MCNP input files, the fit used in the sample problem was applied verbatim to this study. This profile, plotted in Figure 6-18, indicates that the peak density occurs around 160 cm from the bottom. The integral of this profile is normalized to the fuel rod length.

Table 6-3 shows material properties of the fuel element components as implemented in the RAZORBACK simulation. The densities of UO_2 and Zircaloy (ZIRLO) are carried over from the neutronics analysis, while the density of water is the quantity obtained at 20°C from IF97. The MELCOR database is used to determine temperature-dependent thermal conductivity and specific heat for UO_2 and Zircaloy (Humphries et al. 2015). Figure 6-19 shows that two different temperature ranges are used to define κ_T and c_p for UO_2; the melting point of 3,113 K marks a transition point for evaluating constant values for the melt. This behavior is applied in RAZORBACK as piecewise equation with a polynomial for the solid region and a constant for the melt region.

Figure 6-20 shows that the thermal conductivity of Zircaloy rises with temperature until the melting point of 2,098 K, upon which a constant value is used for the melt. The specific heat behaves in more irregular manner. The region from 273.15 K to 1,090 K has c_p rising smoothly, and afterwards from 1,090 K to 1,248 K, there is a sharp increase to a peak value of c_p. After the peak, the Zircaloy c_p drops to a constant value. This behavior requires the heat capacity to be modeled piecewise with three functions in RAZORBACK.

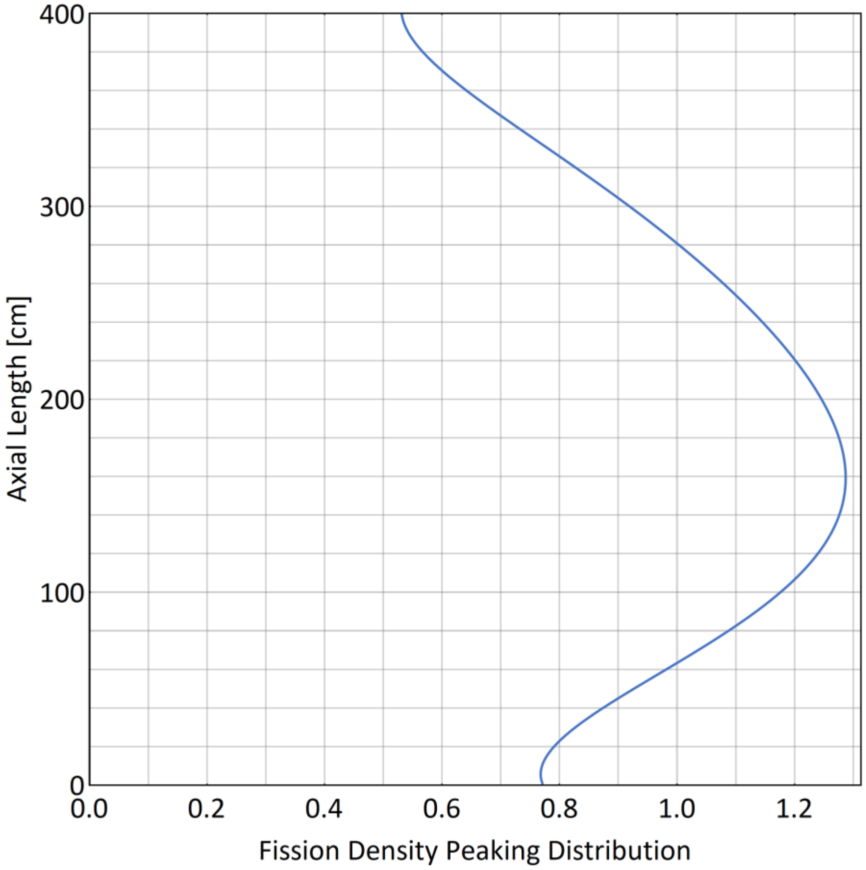

Figure 6-18. Axial Distribution of Fission Density Peaking $F_z(z)$ in the RAZORBACK Simulation

Table 6-3. Material Properties for a Fuel Element in RAZORBACK

Material / Property	UO_2	Water	Helium	Zircaloy (ZIRLO)
Density at 20°C (g/cm^3)	10.2	0.998206092	0.000166311	7.75
Thermal Conductivity (W/[cm·K])	MELCOR (Figure 6-19a)	IF97 (Figure 6-21a)	CoolProp (Figure 6-23a)	MELCOR (Figure 6-20a)
Specific Heat Capacity (J/[g·K])	MELCOR (Figure 6-19b)	IF97 (Figure 6-21b)	CoolProp (Figure 6-23b)	MELCOR (Figure 6-20b)
Thermal Radiation Surface Emissivity	0.8	0.95	1.0	0.325
Thermal Radiation Transmissivity	0.0	1.0	1.0	0.0
Linear Thermal Expansion Coefficient (K^{-1})	Equation 6-5	0.0[a]	0.0[a]	6.721E-6
Young's Modulus (GPa)	180	1.0E-20[b]	1.0E-20	89.9
Poisson's Ratio	0.303	0.3[b]	0.3[b]	0.35

NOTE: [a] RAZORBACK does not expand fluids and instead applies this property to solids, which in turn modifies adjacent gaseous volumes.

[b] Recommended values for gas in RAZORBACK

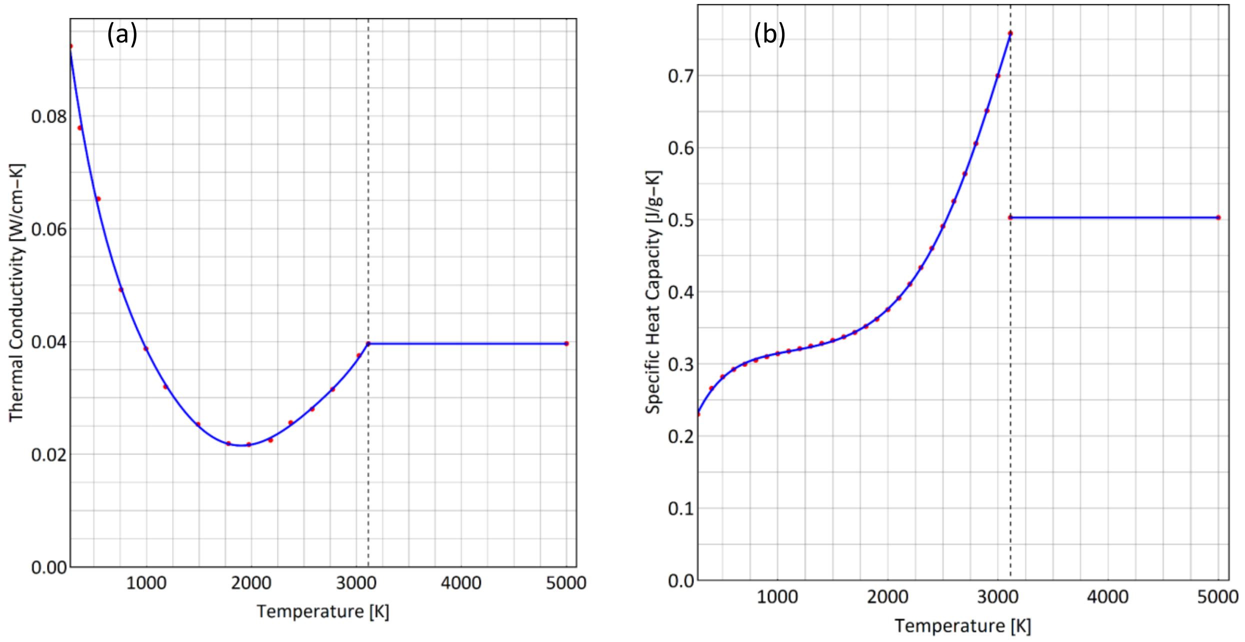

NOTE: Polynomial fits are shown in blue for different temperature ranges.

Figure 6-19. Temperature-Dependent (a) Thermal Conductivity and (b) Specific Heat for UO_2 from the MELCOR Data Library

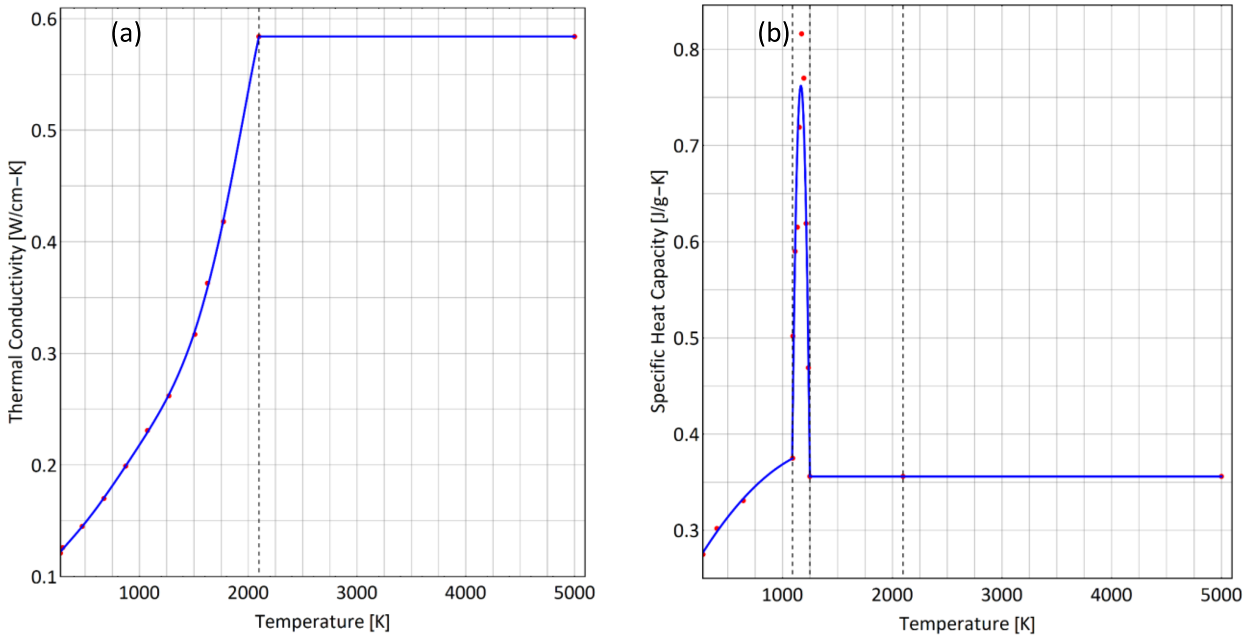

NOTE: Polynomial fits are shown in blue for different temperature ranges.

Figure 6-20. Temperature-Dependent (a) Thermal Conductivity and (b) Specific Heat for Zircaloy from the MELCOR Data Library

For UO_2, the default fuel surface emissivity from MELCOR of 0.8 is used. The linear strain from thermal expansion is found from a temperature-dependent fit from NEA (2016), which is featured in the code FRAPCON-3.5. To interpret this fit in a more convenient manner, the linear strain is evaluated from 273.15 K to 2,500 K and then fitted to a second-order polynomial function of temperature (in Kelvin). The derivative of this fit is then taken as the linear thermal expansion coefficient:

$$\alpha(T)[K^{-1}] = 5.333 * 10^{-6} + 5.078 * 10^{-9}\, T \qquad \textit{Equation 6-5}$$

Equation 6-5 is evaluated as 6.822×10^{-6}/K at 293.15 K and 1.802×10^{-5}/K at 2,500 K. For the remaining UO_2 properties, a transmissivity of 0.0 is used to follow the RAZORBACK convention of applying this value for solids (and 1.0 for gases.) The Young's modulus and Poisson's ratio are derived as average values of data from Munro (2002).

For Zircaloy, the surface emissivity is taken from the MELCOR database for conditions of no oxide layer formation. The strain from thermal expansion was obtained from a radial fit used in FRAPCON-3.5 via NEA (2016). The strain was evaluated from 273.15 to 2,500 K and then fitted to a line. The slope of this line provided the thermal expansion coefficient of 6.721×10^{-6}. The Young's modulus and Poisson ratio are obtained for ZIRLO from Weck et al. (2015).

The gap can be modeled as being filled with water (from rod breaching and water infiltration) or helium (unbreached). The former is more representative of the failed state, as rods would eventually be breached from corrosion, but the latter is a conservative choice for more accurately portraying the role of thermal expansion in the thermal system. The thermal conductivity and specific heat of water at 101,325 Pa are taken from IF97 via CoolProp and are plotted in Figure 6-21. Due to the phase transition at 100°C, two fits are provided as a piecewise function for each parameter for use in RAZORBACK. The thermal conductivity of helium as a gap-filling gas is based on correlations from Hands and Arp (1981), which is tabulated at 101,325 Pa via CoolProp and shown in Figure 6-22a. The specific heat is obtained via CoolProp from the equation of state described in Ortiz-Vega (2013). It is plotted in Figure 6-22b and shown with two separate polynomial fits divided at 725 K.

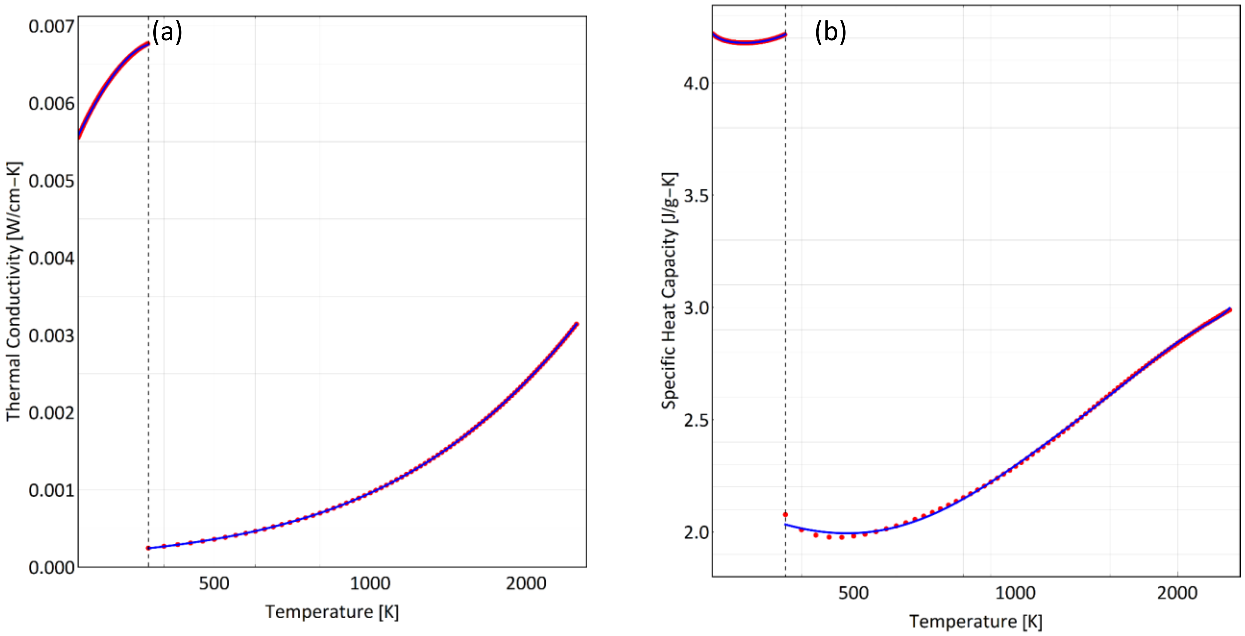

NOTE: Polynomial fits are shown in blue for the liquid and gas phases.

Figure 6-21. Temperature-Dependent (a) Thermal Conductivity and (b) Specific Heat for Water from IF97 at 101,325 Pa

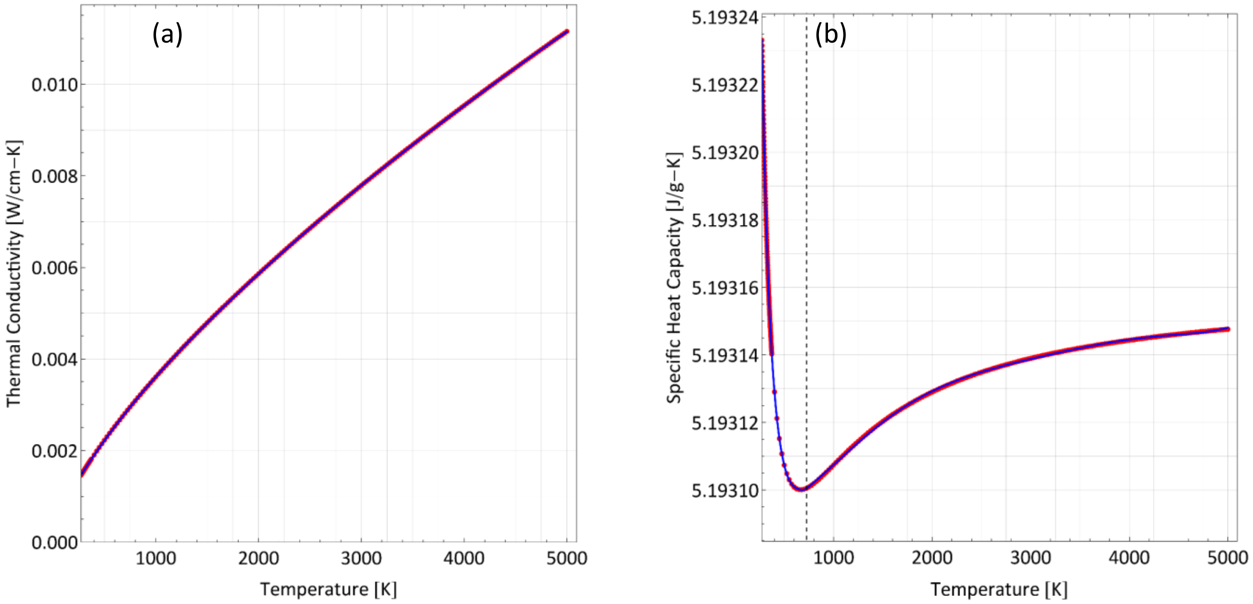

NOTE: Polynomial fits are shown in blue for the liquid and gas phases.

Figure 6-22. Temperature-Dependent (a) Thermal Conductivity and (b) Specific Heat for Helium from CoolProp at 101,325 Pa

6.2.1.8 Solid Mechanics

The results of the kinetics analysis can elucidate the total energy release and thermodynamic behavior from a transient event. If the final results appear significant, they can be applied in a solid mechanics analysis to determine if the net energy release and power from transient criticality could impact the EBS and host rock. The energy would be obtained from the time-integrated pulse and applied as a pressure shock inside of the canister, which is visualized in Figure 6-23. The mechanics analysis would propagate the shockwave throughout the stainless-steel canister and overpack, buffer material, and unsaturated alluvium. Codes proposed for use include Zapotec from SNL, which itself is a coupling of the CTH shock physics code with the finite element capabilities of Sierra/Solid Mechanics. The tool has the ability to sample gas-on-solid pressures from CTH, which could account for the rapid phase change in the water caused by the transient. This type of investigation is proposed as a form of consequence analysis when the kinetics analysis is refined.

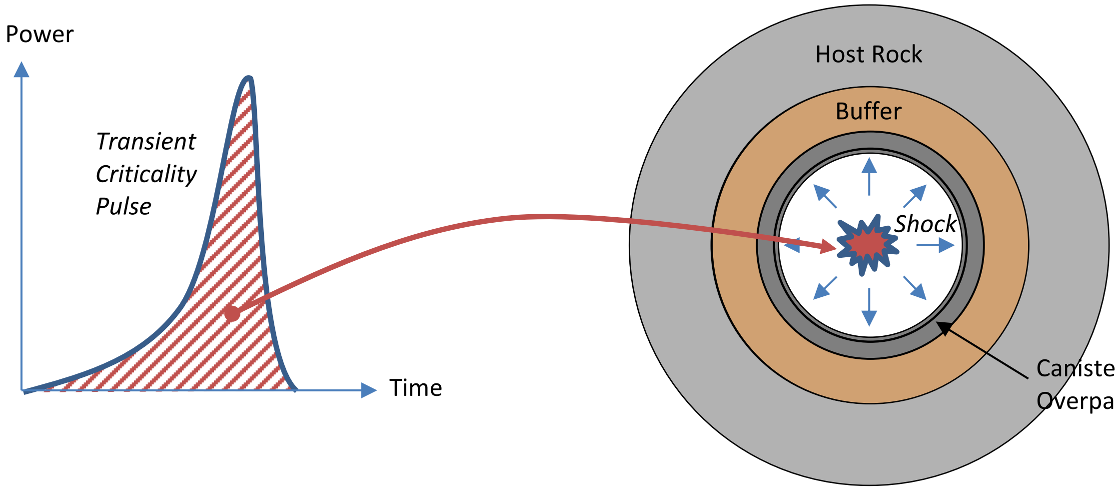

Figure 6-23. The Integrated Energy of the Transient Criticality Pulse Can Be Applied as the Shockwave in a Solid Mechanics Analysis

6.2.2 Neutronics Results

This section summarizes the preliminary neutronics calculations before moving on to the kinetics analysis. The summary includes the scoping tests for Phases 0 through 3 and then the calculations simulating various reactivity feedback mechanisms. Fits included in plots of results correspond to the units of the primary *y*-axis, while secondary units may be presented on the secondary *y*-axis for additional perspective. Advanced fits are provided using the Mathematica analysis software. All analyses use Perl scripts to modify the MCNP input deck using template files, while bash scripts are used to complete the test matrices using the Boca high performance computing cluster at SNL.

6.2.2.1 Intact Canister (Phase 0)

The results for the Phase 0 calculations for the normal, intact canister backfilled with helium are shown in Table 6-4. Subcritical conditions are confirmed for a 95 at% He and 5 at% air mixture at 8 bar, with a k_{eff} of 0.30 at emplacement and a slightly lower value after 9,000 years of decay (and no loss of pressure). The restriction to prompt neutron fission results in slightly lower values of k_{eff}.

Table 6-4. k_{eff} and β_{eff} for Normal Backfilled Base Case Scenario with Zion Assemblies in TSC-37

Intact canister backfilled w. 95 at% He, 5 at% Air	SNL (MCNP) 60°C, 8 bar, Neutrons - All		SNL (MCNP) 60°C, 8 bar, Neutrons - Prompt	
	0 years	9,000 years	0 years	9,000 years
k_{eff}	0.30167 ± 0.00013	0.29753 ± 0.00013	0.30019 ± 0.00013	0.29612 ± 0.00012
β_{eff}	0.00543 ± 0.00044	0.00581 ± 0.00048	—	—

6.2.2.2 Failure Base Case Scenarios

The base case scenarios involving DPC failure are shown in Table 6-5. The effective multiplication factor increases as the failure mode progresses. The results have reasonable agreement with sister calculations at ORNL with the Shift code.

The remainder of the report isolates the neutronics to the effects from prompt neutron fission except when discussing the effective delayed neutron fraction or dollar reactivity. While β_{eff} does vary with a margin of error per calculation, the convention will be to use a weighted mean per series of calculations.

Table 6-5. k_{eff} and β_{eff} for Failure Base Case Scenarios with Zion Assemblies in TSC-37

Condition	Parameter	SNL (MCNP) 60°C, 1 atm, 9,000 years, Neutrons - All	SNL (MCNP) 60°C, 1 atm, 9,000 years, Neutrons - Prompt	ORNL (Shift)[a] 263.85°C, 50 bar, 7,978 years
Flooded, intact basket + absorbers	k_{eff}	0.86699 ± 0.00031	0.86339 ± 0.00030	0.88756 ± 0.00023
	β_{eff}	0.00520 ± 0.00041	—	—
Flooded, intact basket, no absorbers	k_{eff}	1.03621 ± 0.00030	1.03076 ± 0.00029	1.03679 ± 0.00024
	β_{eff}	0.00548 ± 0.00037	—	—
Flooded, no basket, no absorbers	k_{eff}	1.11819 ± 0.00026	1.11216 ± 0.00026	1.11923 ± 0.00018
	β_{eff}	0.00576 ± 0.00042	—	—

Source: [a] Banerjee 2021.

6.2.2.3 Phase 1

Figure 6-24 shows the effective multiplication in the DPC as the absorber/retainer assemblies are degraded according to Phase 1a and 1b scenarios. The system begins in subcritical conditions when the DPC is flooded as the absorbers are adequate at poisoning chain reactions despite the introduced moderator. The k_{eff} for the common initial state is 0.86303 ± 0.0003 with a reactivity of -0.15871, or −\$29.15. The value of k_{eff} steadily increases as more absorber is degraded, with the full degradation state showing k_{eff} of 0.9739 ± 0.0003 for 1a and 1.02848 ± 0.00029 for 1b. These values bound the Phase 1 scenario for different perspectives of absorber displacement, from B_4C particles accumulating on the bottom of the tube in the original horizontal emplacement to particles accumulating at the bottom of the basket in a highly tilted DPC.

The weighted mean of the delayed neutron fraction is 0.00544 ± 0.00006 for Phase 1a and 0.00547 ± 0.00006 for Phase 1b, so the reactivity conditions for either approach should be comparable. Figure 6-25 shows the reactivity of the system as the last quantity of absorber and retainer are replaced with water. Criticality is achieved in Phase 1a when 99.13 vol% of the absorber assembly has degraded in the flooded DPC basket. The system is prompt-critical at 99.30 vol% degradation, and the maximum dollar reactivity of \$5.09 is achieved when all of the absorber is gone, which can be interpreted as the “worth” of the installed absorbers given a flooded DPC. Criticality is not achieved within Phase 1b, and the final reactivity is −\$4.90. It should be emphasized that the high reactivity values in this results section are influenced by the lack of control rods in the assemblies, as the model inspects the full excess reactivity from the SNF.

Phase 1a results show that the system proceeds from a subcritical state to prompt critical given catastrophic failure of the absorber plates. This outcome provides plausibility that it may be possible to have a transient criticality without an initial steady-state criticality if the degradation proceeds quickly enough. However, the assumption used for kinetics is that an initial steady-state criticality exists prior to initiation of the transient to exclude the need for external neutron sources. This assumption also allows results to be bounding for events proceeding from a subcritical state.

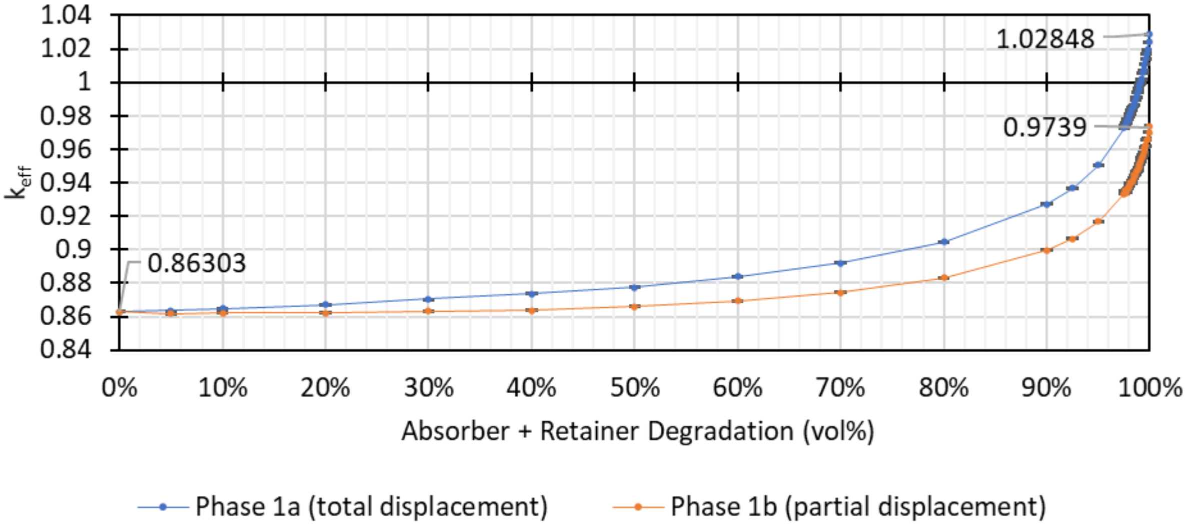

Figure 6-24. Effective Multiplication for Phase 1 in Terms of the Percent Volume Degraded in the Absorber and Retainer Assembly

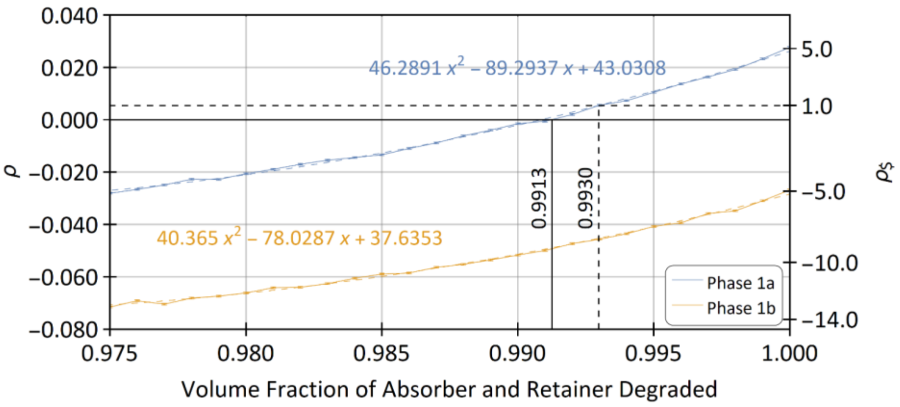

NOTE: The fit only applies for 97.5 vol% and above.

Figure 6-25. Reactivity of Phase 1 as the Remaining Amount of Absorber Is Displaced

6.2.2.4 Phase 2

The Phase 2a results in Figure 6-26a show a quadratic growth in k_{eff} as more of the carbon-steel basket is replaced with water, where the fully degraded state shows a k_{eff} of 1.11176 ± 0.00028. There is a discrepancy in k_{eff} between the end state of Phase 1a (1.02848 ± 0.00029, from Figure 6-24) and the initial state of Phase 2a (1.03025 ± 0.00029, from Figure 6-26a). This discrepancy is attributed to the treatment of the absorber and retainer regions as separate materials in Phase 1a. Although the Phase 1a end-state has these regions replaced with water, in Phase 2a, those regions are removed altogether and lumped with the water filling the tube. Therefore, in Phase 1a, collisions are scored in the B_4C/retainer regions despite there not being too many interactions in this part of the tube. This situation causes a poorer Monte Carlo estimation, which is most noticeable in the reduced absorption k_{eff} estimator, poorer correlation in the absorption/track length estimators, and different k_{eff} confidence intervals. The weighted mean of the delayed neutron fraction is 0.00540 ± 0.00009 for Phase 2a and 0.00548 ± 0.00010 for Phase 2b. Therefore, reactivity increases from $5.44 (the absorber worth) to $18.62 as the basket undergoes massive corrosion.

The results of Phase 2b are shown in Figure 6-26b, where the initial state is the original tube spacing with a k_{eff} of 1.11169 ± 0.00028. The end state corresponds to the grid spacers of adjacent assemblies adjoining one another (close contact) where the k_{eff} is 1.11019 ± 0.00029. The maximum k_{eff} of 1.12246 ± 0.00027 is achieved when the tube half-pitch is reduced by 34.8% to 11.4 cm. The maximum reactivity from Phase 2b is $19.90, which is likely representative of the full excess reactivity of the whole DPC given catastrophic failure.

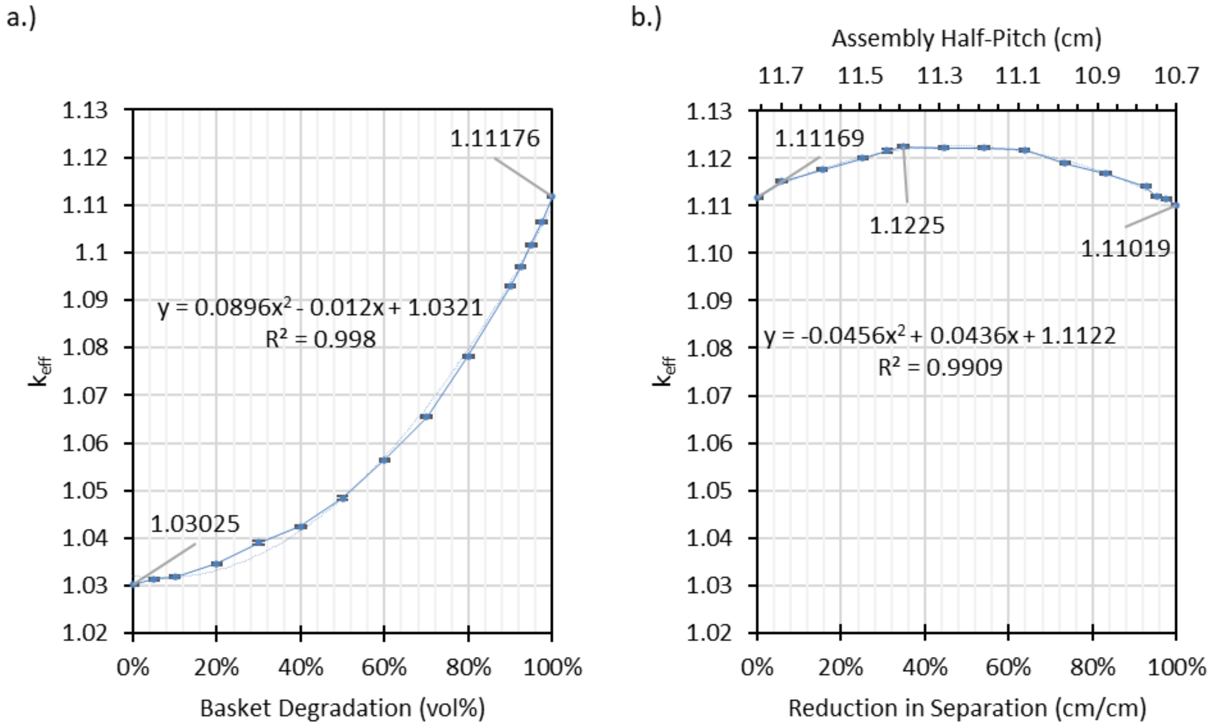

Figure 6-26. Effective Multiplication by (a) Percent Volume Degraded for Phase 2a and (b) Percent Separation Reduced in Phase 2b, along with Quadratic Fits

6.2.2.5 Phase 3

The results for Phase 3a are shown in Figure 6-27 for a simultaneous grid spacer collapse in each assembly, while the basket remains intact. The initial state is the end state of Phase 1a with a flooded DPC, no absorbers, and k_{eff} = 1.03076 ± 0.00029. The end state has all fuel clads touching, and the effective multiplication is reduced to 0.73157 ± 0.0003 due to spatial and energy self-shielding effects in the fuel with almost no interstitial moderator. The initial critical state from removing absorbers is lost when the Zircaloy spacers have allowed for a 14.7% reduction in the original rod half-pitch to 0.689 cm. The weighted mean of the delayed neutron fraction is 0.00546 ± 0.00007 for Phase 3a and 0.00557 ± 0.00007 for Phase 3b. Therefore, the reactivity drops from $5.46 (the absorber worth) to −$67.15 with grid spacer degradation.

Figure 6-28 shows results for k_{eff} when the close-contact configuration at the end of Phase 2b undergoes further collapse with the degradation of assembly grid spacers. The k_{eff} is 1.11019 ± 0.00029 for the initial state and then decreases quadratically with decreasing separation. The end state in which all rods are bundled together has a k_{eff} of 0.87109 ± 0.00029. Given that there is a greater density of fuel, the critical configuration is maintained until the fuel rod half-pitch is reduced by 63.3% to 0.602 cm. The reactivity of Phase 3b drops from $17.82 to −$26.58 with rod consolidation. These results support the grid spacer degradation model (Section 4.4), in which failure of the grid spacers is assumed to terminate a criticality event.

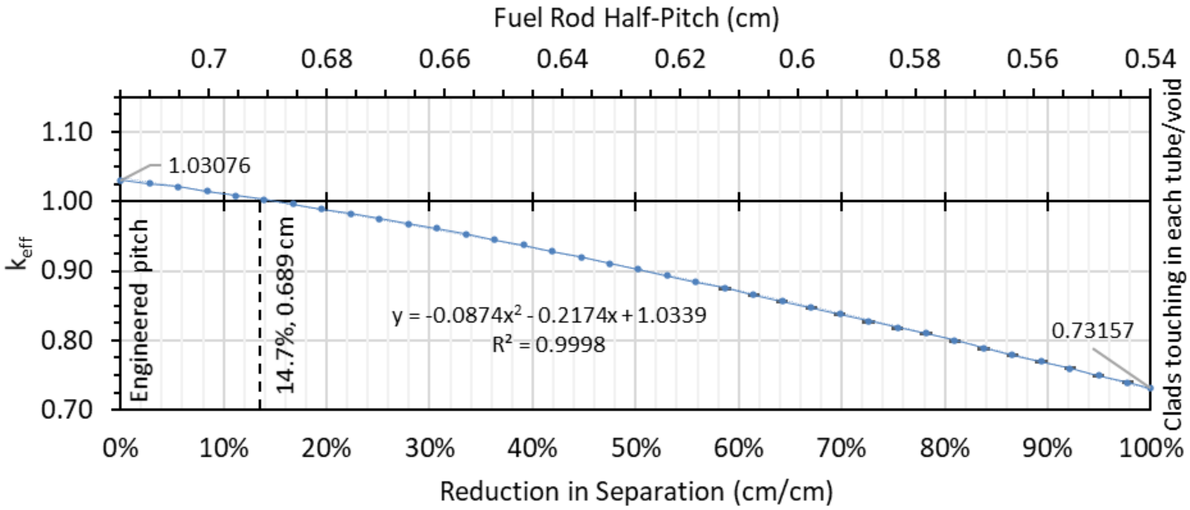

Figure 6-27. Effective Multiplication for Phase 3a in Terms of Percent Separation Reduced along with Quadratic Fit

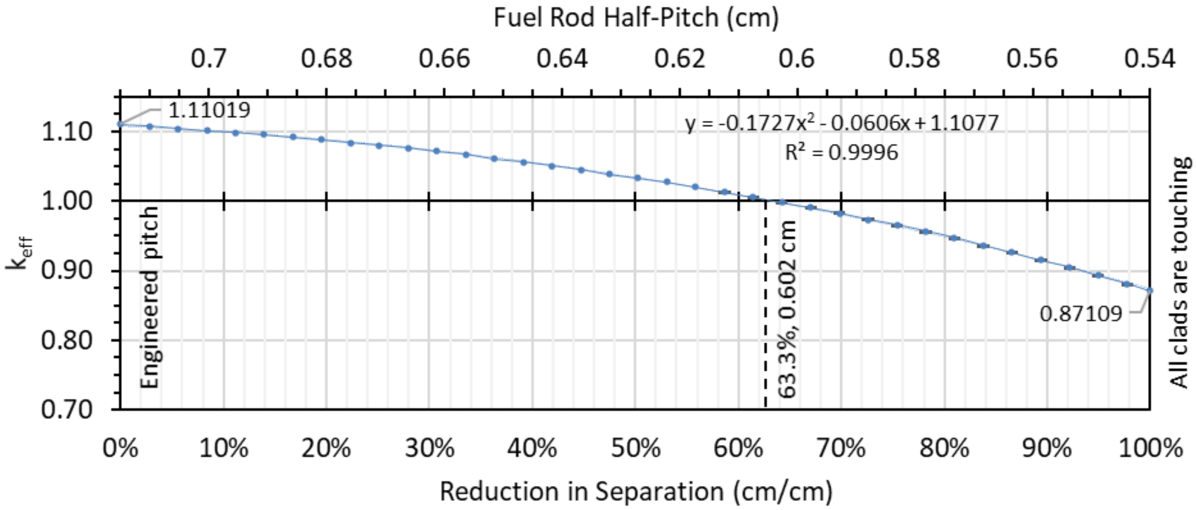

Figure 6-28. Effective Multiplication for Phase 3b in Terms of Percent Separation Reduced along with Quadratic Fit

6.2.2.6 *Temperature Feedback in the Fuel*

A series of neutronics calculations was implemented to estimate the temperature feedback coefficient in the fuel. The first iteration of the analysis involved sequentially broadening the UO_2 cross sections with increasing fuel temperatures in isolation. The lower bound temperature of 300.5 K is within the 300–2,500 K range using in the construction of the OTFDB binary lookup tables. The upper bound temperature of 2,500 K represents a temperature at which the Zircaloy cladding is likely to melt and the fuel geometry and critical configuration are compromised. The analysis assumes a rapid increase in fuel temperature such that (1) no significant heat is transferred to the surroundings, non-UO_2 components are fixed with cross sections at 300.5 K, and (2) the material properties are unaffected and the fuel geometry is intact.

The reactivity results for the first iteration are shown in Figure 6-29, which includes a generic power law fit and a specific $\sqrt{T}$ for purposes of fitting to RAZORBACK specification. The generic fit is very close to the $\sqrt{T}$ fit when the temperature of the fuel is heated in isolation from other components. Progressing from 300.5 K to 2,500 K results in a drop from \$5.40 to −\$0.23, and the critical configuration is maintained until 2,337.63 K (2,064.48°C). Therefore, the loss of criticality from Doppler broadening in the fuel with extreme heating may be concurrent with the melting of Zircaloy, which in itself can destroy the critical configuration.

The derivative of the reactivity fits in Figure 6-29 with respect to temperature are shown in Figure 6-30. The temperature feedback coefficient when heating is restricted to the fuel is therefore

$$\frac{\partial \rho}{\partial T} = -\frac{4.7834907 \times 10^{-4}}{\sqrt{T}} \; [K^{-1}] \qquad \textit{Equation 6-6}$$

From a β_{eff} of 0.00543 ± 0.00005, the corresponding fit in dollars is

$$\frac{\partial \rho_{\$}}{\partial T} = -\frac{8.8017527 \times 10^{-2}}{\sqrt{T}} \; [\$/K] \qquad \textit{Equation 6-7}$$

which suggests coefficients of $\mathcal{C}_0 = 0$ and $\mathcal{C}_1 = -8.8017527 \times 10^{-2}$ for use in the kinetics code.

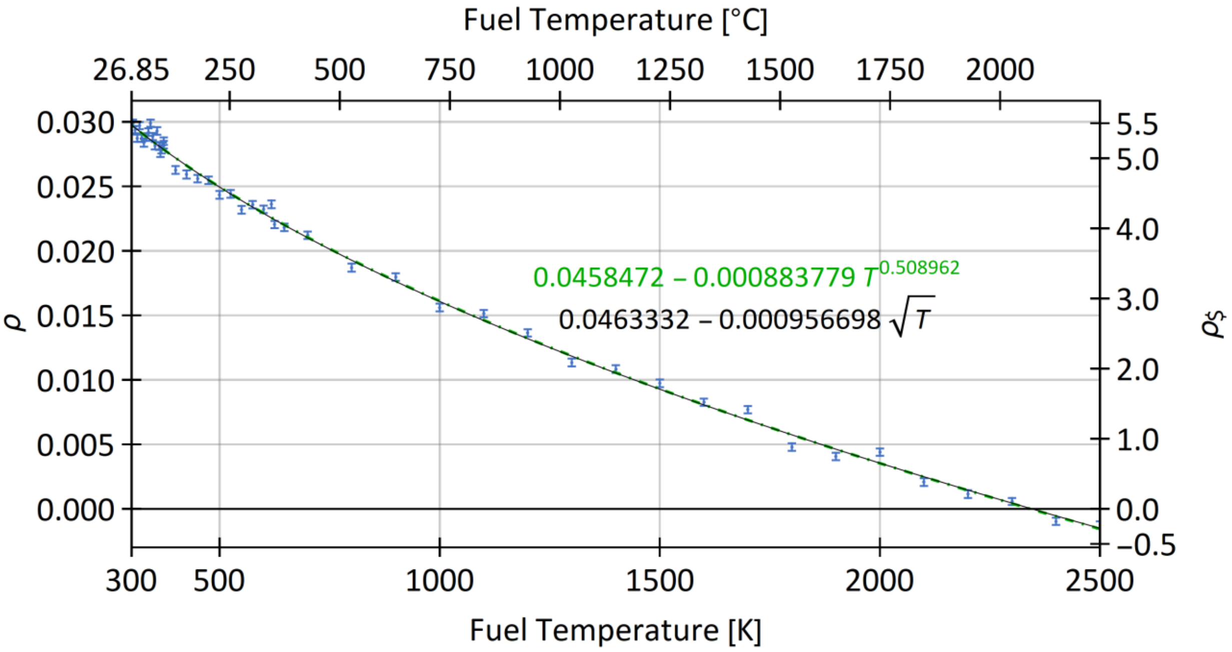

NOTE: The figure shows a generic power law fit (green) and a $\sqrt{T}$ fit (black) for all points as well as the associated equations.

Figure 6-29. Reactivity as a Function of Fuel Temperature When Perturbing the UO_2 in Isolation

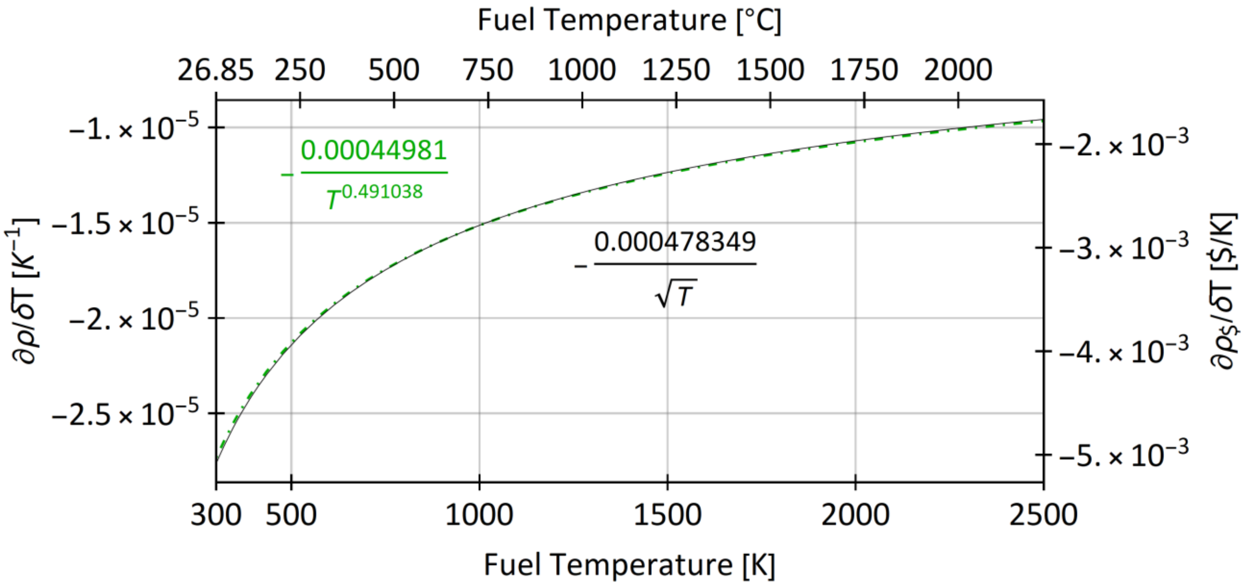

NOTE: The figure shows a generic power law fit (green) and a $1/\sqrt{T}$ fit (black) for all points as well as the associated equations.

Figure 6-30. Temperature Feedback Coefficient as a Function of Fuel Temperature When Perturbing the UO_2 in Isolation

The second iteration of the analysis involved doppler-broadening the Zircaloy clad (which includes ^{90}Zr) and the water infiltrating the clad gap (^{1}H and ^{16}O) along with the fuel. The water density was modeled strictly at 101,325 Pa and allowed to boil off at 100°C, while water elsewhere in the DPC was maintained at 300.5 K. This approach assumes rapid heating from the transient quickly forms a two-phase layer around the fuel that inhibits major heat transfer. Once again, the material geometries were not affected with increasing temperatures. The effect of temperature on material geometries is explored further in the thermal expansion study in Section 6.2.2.9.

The results for reactivity are shown in Figure 6-31 along with three fits: (1) a generic power-law fit for all points in the study, (2) a generic power-law fit for points at 100°C and above, and (3) a $\sqrt{T}$ fit for all points for adaptation to the kinetics input deck. The reactivity results are steady in the liquid phase region, but there is a discontinuity when the gap water enters the vapor form, moving from 0.02822 to 0.02710 and then decreasing afterwards with decreasing vapor density. The reactivity decreases from \$5.67 to −\$0.56, and the critical configuration is maintained until 2,266.41 K (1,993.26°C).

Figure 6-32 shows the derivatives with respect to temperature of the three reactivity fits. The generic fits bound the $\sqrt{T}$ at lower temperatures, but at higher temperatures, the postboil fit serves as a more accurate representation. The $\mathcal{C}_1$ coefficient is $-5.0458373 \times 10^{-4}$ reactivity per √K or $-\$9.3481042 \times 10^{-2}$ per √K (from a β_{eff} of 0.00540± 0.00005), which is slightly more negative than the result from the first iteration. However, given the quality of fit, the results from the UO_2-only analysis will be passed to the kinetics evaluation.

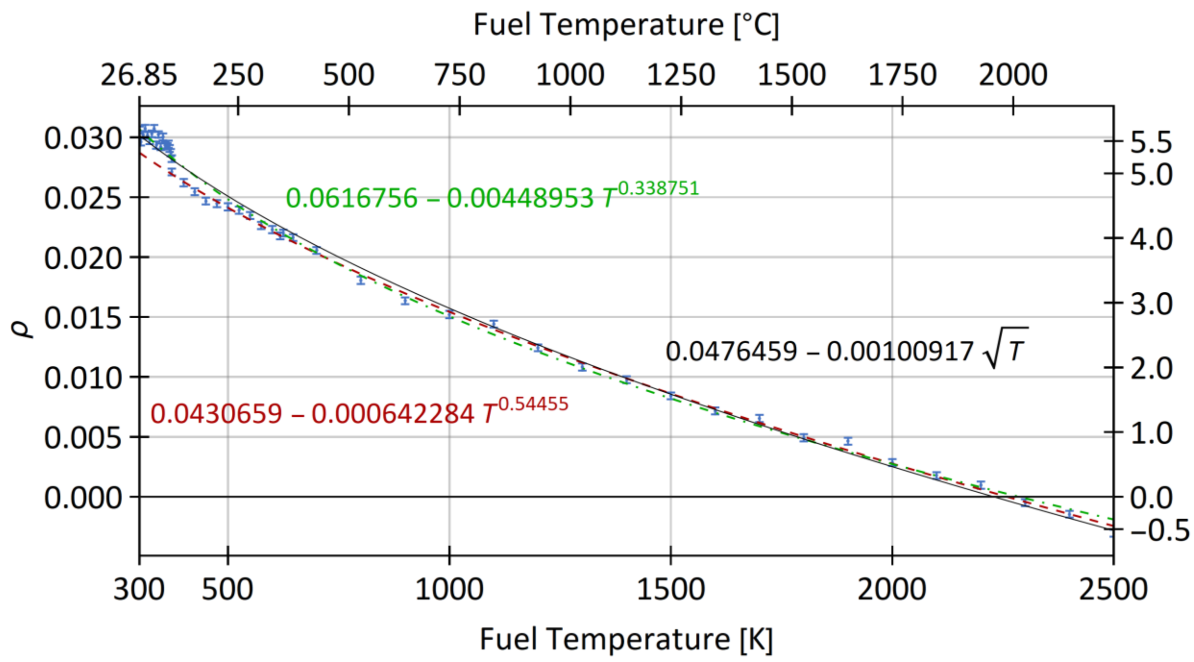

NOTE: The figure shows the power law fits for all points (green) and postboil points (red) along with a $\sqrt{T}$ fit (black) for all points.

Figure 6-31. Reactivity as a Function of Fuel Temperature When Perturbing the UO_2, Gap, and Zircaloy Clad

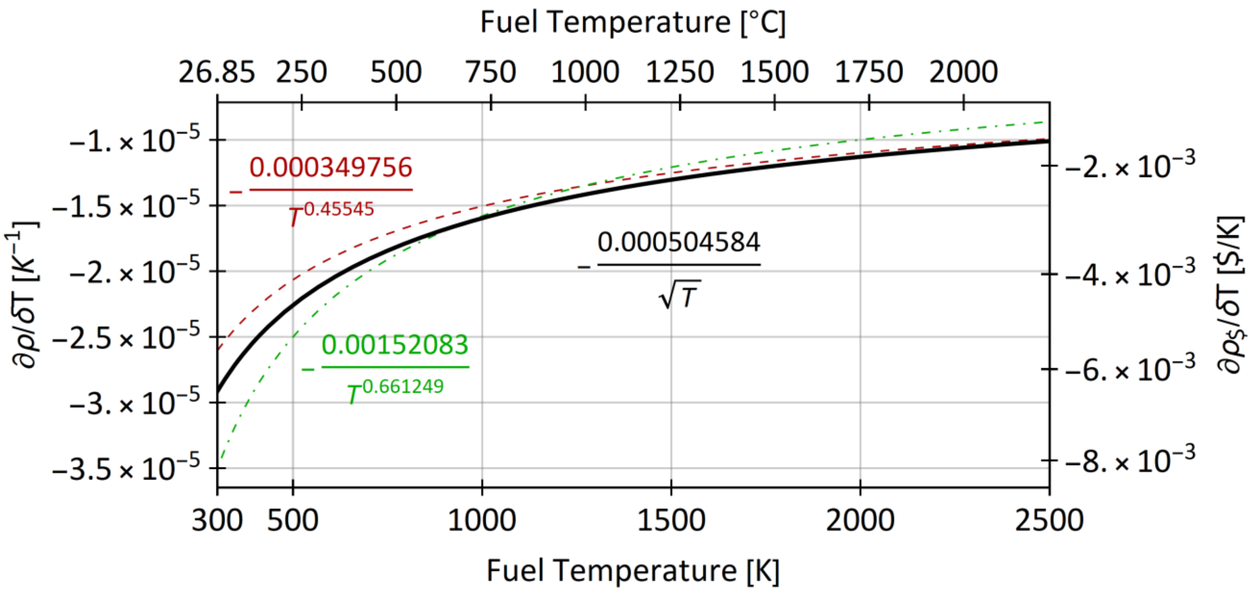

NOTE: The figure shows the generic power law fits for all points (green) and postboil points (red) along with a $1/\sqrt{T}$ fit (black) for all points. The associated equations are also provided using the same color coding.

Figure 6-32. Temperature Feedback Coefficient as a Function of Fuel Temperature When Perturbing the UO_2, Gap, and Zircaloy Clad

6.2.2.7 Temperature Feedback in the Coolant

The analysis for the coolant temperature feedback coefficient was conducted by varying the temperature and density of all water infiltrating the canister, including the fuel rod gaps, the tube/void cavities, the space outside of the basket, and the canister gaps. Any water in the UO_2 fuel matrix was excluded. Doppler broadening via OTFDB is active for the hydrogen (^{1}H) and oxygen (^{16}O) in the water.

The densities for liquid water at 101,325 Pa are used up to the vapor point, terminating at 99.9740°C (373.1243 K). For 100°C and up, in order to maintain the liquid phase, it is assumed that pressure buildup allows for water to remain saturated, and the density of the saturated liquid is used up to the critical point, terminating just below 373.946°C (647.096 K; Figure 6-33). It should be noted that the design pressure for the assemblies is around 15.5 MPa, so higher pressures may compromise the assembly geometry and critical configuration. However, the analysis extends to the critical point to maximize data for fitting.

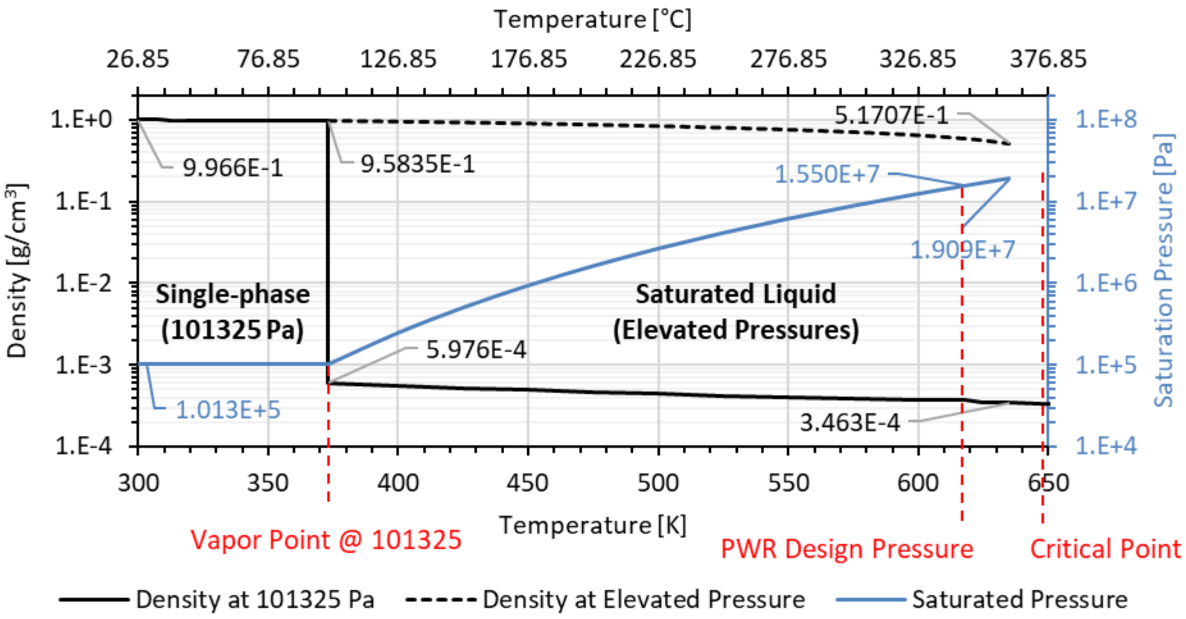

NOTE: The coolant temperature analysis is conducted using the liquid density of water at 101,325 Pa up to the vapor point. Afterwards the densities of saturated liquid at increasing pressures are used until the critical point.

Figure 6-33. Temperature versus Density and Saturation Pressure for Coolant Temperature Analysis

The reactivity effects for the coolant temperature analysis are shown in Figure 6-34, in which the reactivity appears to drop with increasing temperature. Upon closer inspection for the atmospheric region in Figure 6-35, the decrease in reactivity is not monotonic between all data points, as noise from the Monte Carlo error provides extensive overlap. Considering that density does not decrease substantially in this temperature range, this behavior may suggest that interpolations in scattering and absorption cross sections for ^{1}H and ^{16}O are not disparate enough to demonstrate key Doppler broadening effects. Nonetheless, a linear regression of the points is shown in the plot, which implies a coolant temperature feedback coefficient of -4.7×10^{-5} reactivity per K. From the related fit to dollars, given a β_{eff} of 0.00542 ± 0.00097, the feedback coefficient is $-\$8.7 \times 10^{-3}$ per K.

The coolant reactivity results for elevated pressure are shown in Figure 6-36 along with a polynomial fit; the drop in reactivity is monotonic with temperature. This reactivity behavior is mostly influenced by the steady decrease in the density of the saturated liquid as was shown in Figure 6-33. The polynomial fit is fairly representative to 350°C before the reactivity decreases sharply upon reaching a density of 0.33 g/cm^3 near the critical point. The derivative of this polynomial fit is simplified to first order and plotted in Figure 6-37. The reactivity feedback coefficient decreases with temperature, with a coefficient of -3.4×10^{-2} reactivity per K at 100°C (atmospheric) and -7.2×10^{-2} reactivity per K at 344.8°C (15.5 MPa). The corresponding fit to dollars shows feedback coefficients of −\$6.3 per K at 100°C and −\$13.4 per K at 344.8°C. The integrated mean over the saturated region is -5.6×10^{-2} reactivity per K or −\$10.3 per K. It may be more conservative to the kinetics analysis to use the least negative coefficient from the atmospheric region.

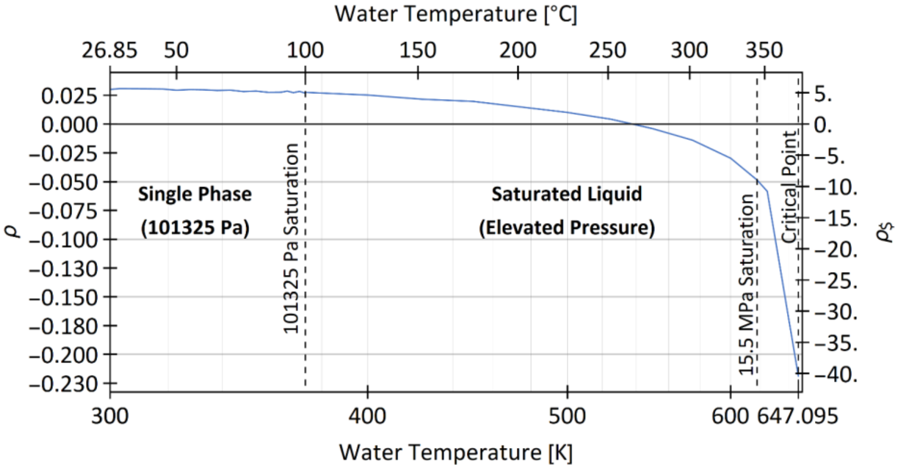

Figure 6-34. Reactivity for the Coolant Temperature Analysis

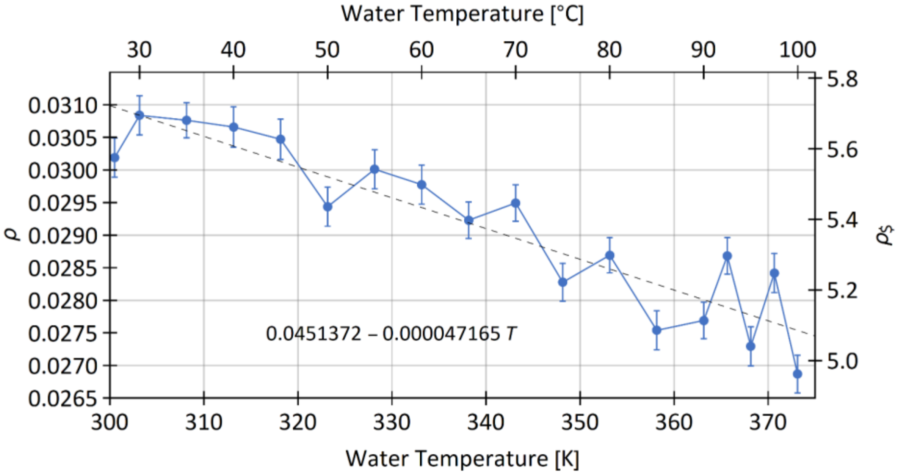

Figure 6-35. Reactivity for the Coolant Temperature Analysis under Atmospheric Conditions Based on a Linear Fit

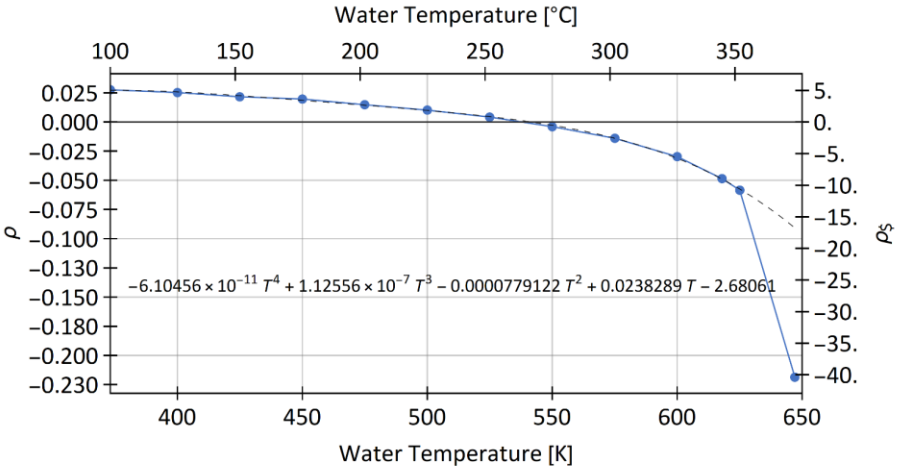

Figure 6-36. Reactivity for the Coolant Temperature Analysis under Elevated Pressure Conditions for Saturated Water Based on a Polynomial Fit

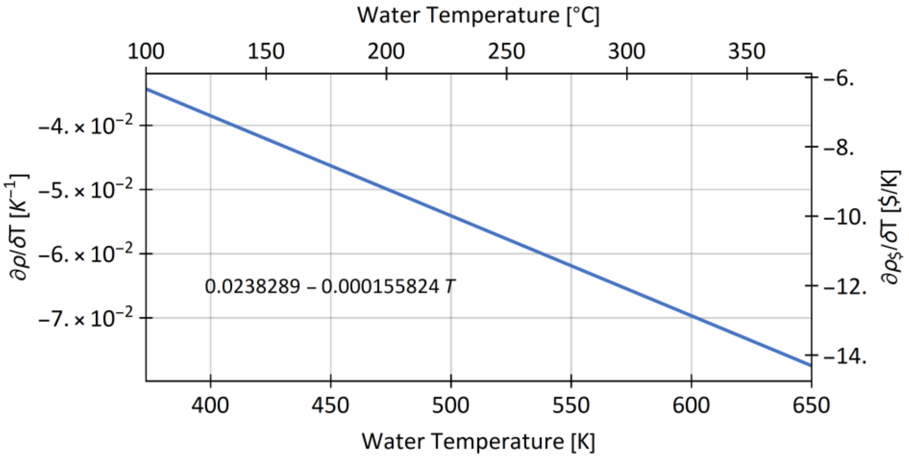

Figure 6-37. Reactivity Feedback Coefficient for the Coolant Temperature Analysis under Elevated Pressure Conditions for Saturated Water Based on a Reduced-Order Fit

6.2.2.8 Feedback from Voiding in the Coolant

The void coefficient is evaluated for saturated water/steam at 99.9740°C at various steam qualities, which is referred to as the voiding. The temperature of the water in the DPC is fixed while the density is modeled as homogenous and a function of quality, as plotted in Figure 6-38. It should be noted, however, that two-phase flow includes considerations of bubbling (dispersed flow) and steam layer formation (separated flow), which are spatially heterogeneous effects that would affect neutron track lengths in a Monte Carlo simulation.

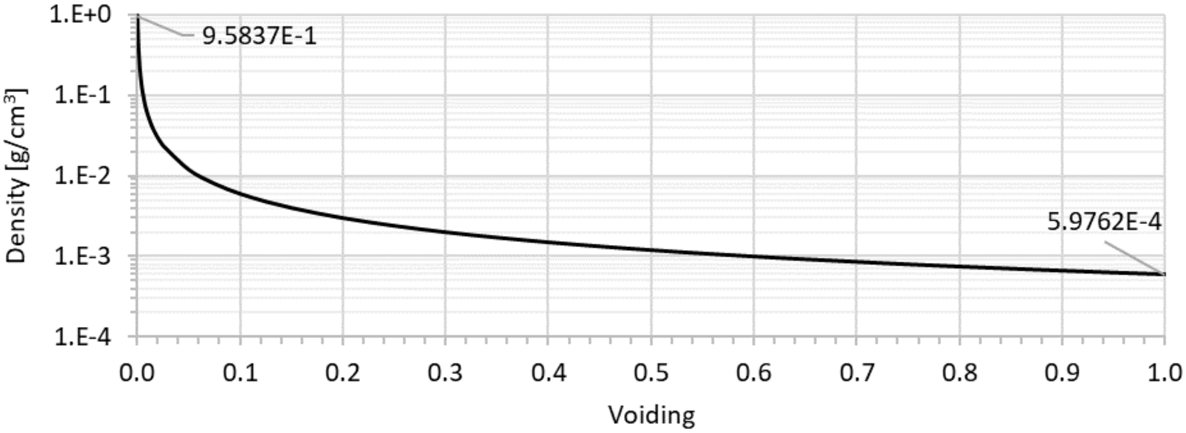

Figure 6-38. Density of 99.9740°C Saturated Water at 101,325 Pa with Increasing Voiding (steam quality)

Figure 6-39 shows the results for reactivity as a function of voiding. In the figure, a hyperbolic cosecant function is used to fit the data over a logarithmic progression in steam quality with a high degree of accuracy. (A related fit for dollars was made using the exponential components of the hyperbolic cosecant explicitly in the regression.) The derivative of this fit is shown in Figure 6-40, in which the integrated mean over the range of steam quality is found to be −2.25387 reactivity per void. The integrated mean of β_{eff} is 0.00571 ± 0.00005, and therefore the integrated average feedback coefficient from the related fit to dollars is −\$394.446 per percent void. This value is highly negative, surpassing the total worth of the absorber plates and the worth from the close contact configuration upon total voiding. The use of this number is a conservative measure for demonstrating the role of liquid water in an undermoderated, thermal system.

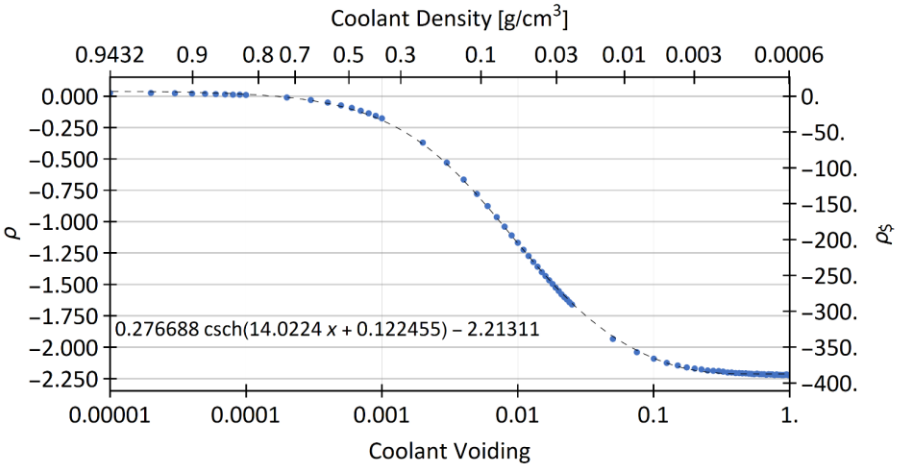

Figure 6-39. Reactivity in the Saturated Water with Increasing Voiding

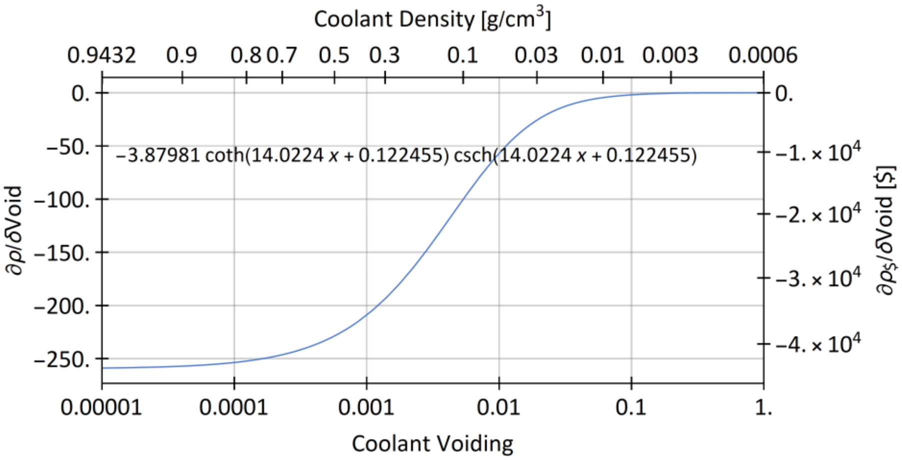

Figure 6-40. Voiding Feedback Coefficient in the Saturated Water as a Function of Steam Quality

6.2.2.9 *Thermal Expansion of the Fuel*

The thermal expansion coefficients are obtained by varying the outer radius of the UO_2 fuel from the engineered specification until it directly presses against the inner wall of the Zircaloy cladding. While SNF has the pellet pressing against the cladding inner wall, maintaining a water-filled gap is important for RAZORBACK execution to accommodate the expansion effect. The total mass of fuel is maintained as constant, so dimensional changes are met with a change in fuel density. When the fuel radius is at its maximal extent, the clad gap is commented from the MCNP input deck and there is no longer interstitial water acting as a moderator between the fuel and cladding. The analysis does not include individual pellet fidelity and therefore does not include pellet dishing or any other off-cylindrical geometry; instead, the simulation represents the fuel as a continuous cylinder. The calculations are performed at 300.5 K to de-couple actual temperature dependence on the expanding geometry, although the template can readily accommodate such coupling in a future test.

Figure 6-41 shows the reactivity in the fuel in terms of the change in radius (cm/cm), while Figure 6-42 shows the effects of the corresponding change in density (g/cm^3). Given the small extent of change, the set of data points is limited, and error from the Monte Carlo simulation is broad. Nonetheless, linear fits to reactivity were made to the radial and density plots, resulting in coefficients of −0.229305 reactivity per cm and 0.00538063 reactivity per g/cm^3, respectively. The integrated delayed neutron fraction for the fuel analysis is 0.00548 ± 0.00006. Therefore, the coefficients from the corresponding fits to dollars are −\$41.821538 per cm and \$0.98133973 per g/cm^3.

A future test can expand the analysis by increasing the fuel radius arbitrarily further while necessarily changing the dimensions of the cladding, thus coupling the effects of the two materials. The analysis can modify the inner radius of the cladding to adjoin the deformed fuel and determine the outer radius by maintaining the original mass of Zircaloy. The analysis can also be coupled with the temperature feedback analysis from Section 6.2.2.6. However, it should be noted that physical limits exist in the form of cladding unzipping, hydride reorientation, fuel warping, and fuel extrusion.

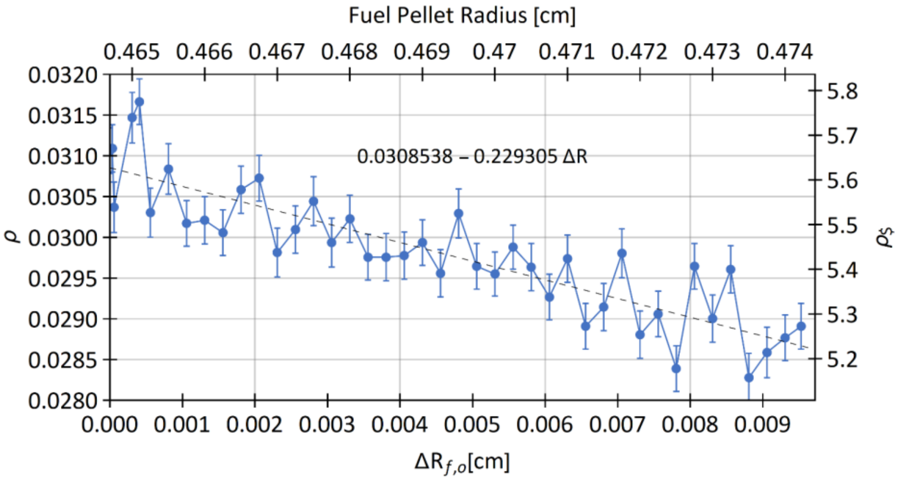

Figure 6-41. Reactivity from Thermal Expansion of the Fuel

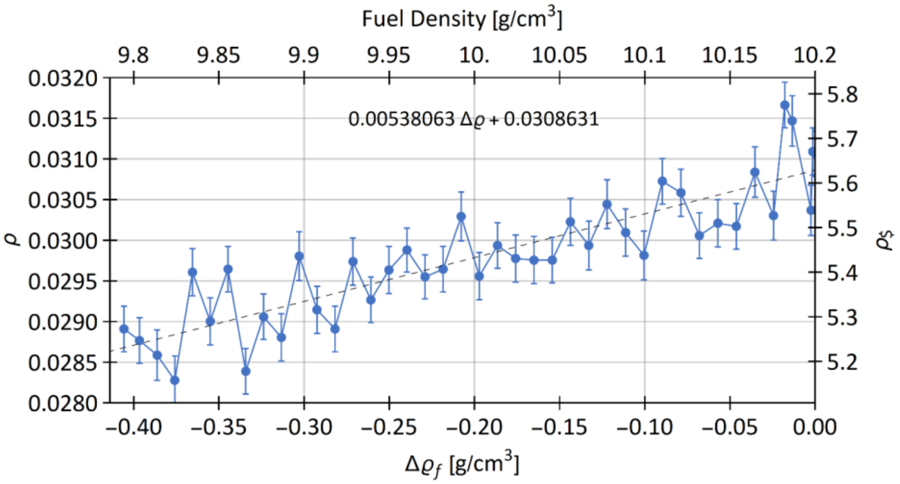

Figure 6-42. Reactivity from the Change in Fuel Density due to Thermal Expansion

6.2.2.10 Thermal Expansion of the Cladding

The thermal expansion analysis was next applied to the Zircaloy cladding, although this time the test probed the change in both the inner radius and outer radius of the clad separately. The mass of Zircaloy (Westinghouse ZIRLO) is kept constant, so dimensional changes are met with changes in clad density. The inner radius of the clad is changed until it adjoins the fuel pellets, at which point the clad gap is commented from the MCNP input deck. The outer radius was modified initially until a commensurate change in density to the inner radius study was achieved, but then additional points were added to probe the effects of severe deformation.

The results for the inner cladding radius are shown in Figure 6-43 in terms of the changes in radius (cm/cm), while Figure 6-44 shows the corresponding changes in density (g/cm^3). A linear fit of the radial and density plots gives reactivity feedback coefficients of 0.198631 reactivity per cm and 0.00193092 reactivity per g/cm^3. The integrated mean of β_{eff} is 0.00551 ± 0.00006. Therefore, the feedback coefficients from corresponding fits to dollars are \$36.070511 per cm and \$0.35064621·cm^3/g.

The results for the outer cladding radius are shown in Figure 6-45 in terms of the changes in radius (cm/cm), while Figure 6-46 shows the corresponding decreases in density (g/cm^3). By expanding the outer radius arbitrarily, the density data conform more to a quadratic, while the dimensional data are essentially linear. In this analysis, the area available to water between fuel rods is decreased as the cladding expands outwardly, so moderator reduction effects are demonstrated. The reactivity feedback coefficient implied by the linear fit to the changes in radius is −0.31039845 reactivity per cm. The integrated mean of β_{eff} is 0.00550 ± 0.00004. Therefore, the feedback coefficient from the corresponding fit to dollars is −\$56.471229 per cm.

The density feedback coefficient is plotted in Figure 6-47. The integrated mean of the feedback function is 0.00460461 reactivity per g/cm^3 for all points in the analysis (i.e., down to a $\Delta\rho$ of −4.17 g/cm^3). When restricting the maximum density change to −1.0 g/cc, the average is 0.00133929 reactivity per g/cm^3. The integrated mean of the related fit for dollars is \$0.837724·cm^3/g for all points and \$0.24366·cm^3/g when restricting the density change to −1.0 g/cc. The result for the inner clad radius study lies between these two boundaries, so that value will be passed to kinetics.

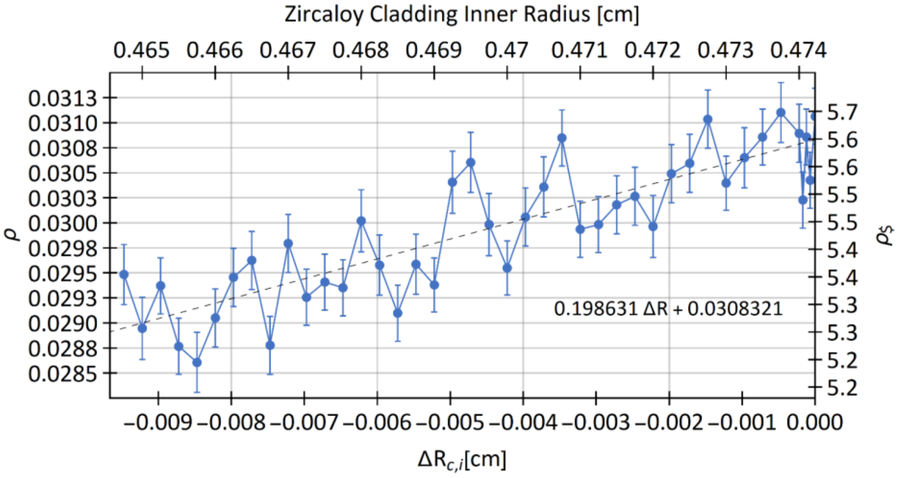

Figure 6-43. Reactivity as the Inner Radius of the Zircaloy Cladding Changes due to Thermal Expansion

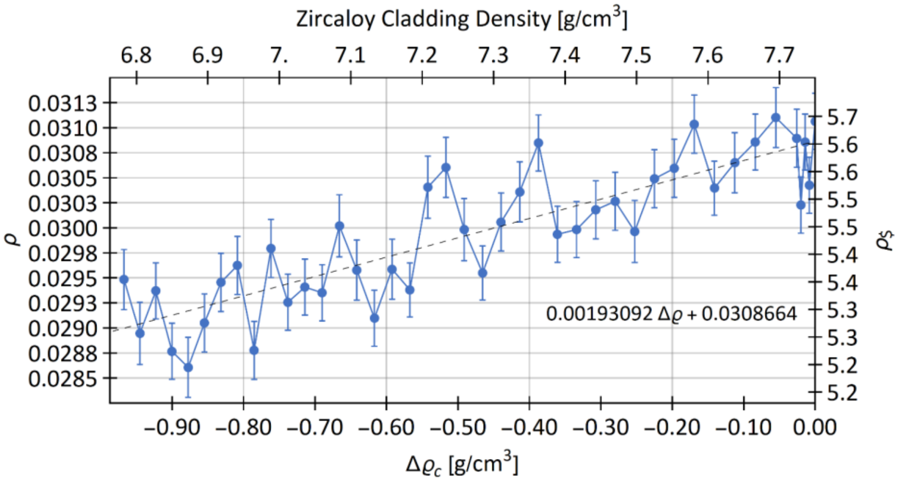

Figure 6-44. Reactivity with Decreasing Zircaloy Density as the Inner Radius Changes due to Thermal Expansion

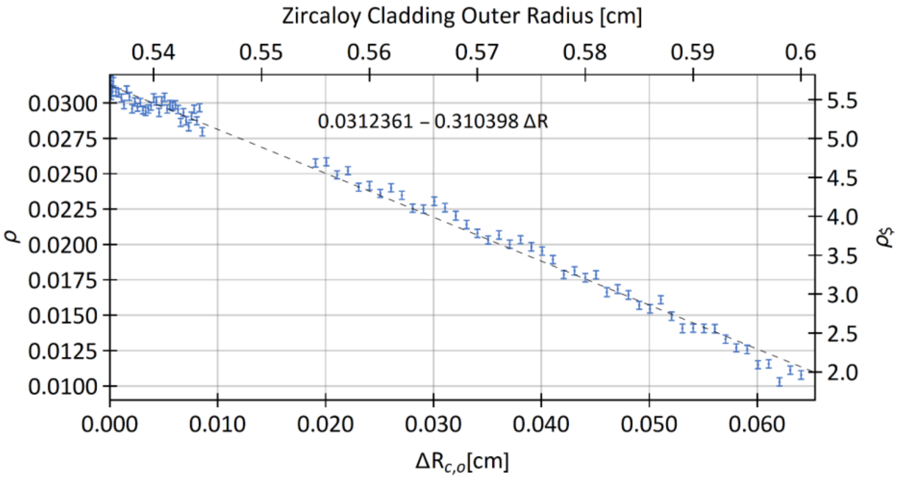

Figure 6-45. Reactivity as the Outer Radius of the Zircaloy Cladding Changes due to Thermal Expansion

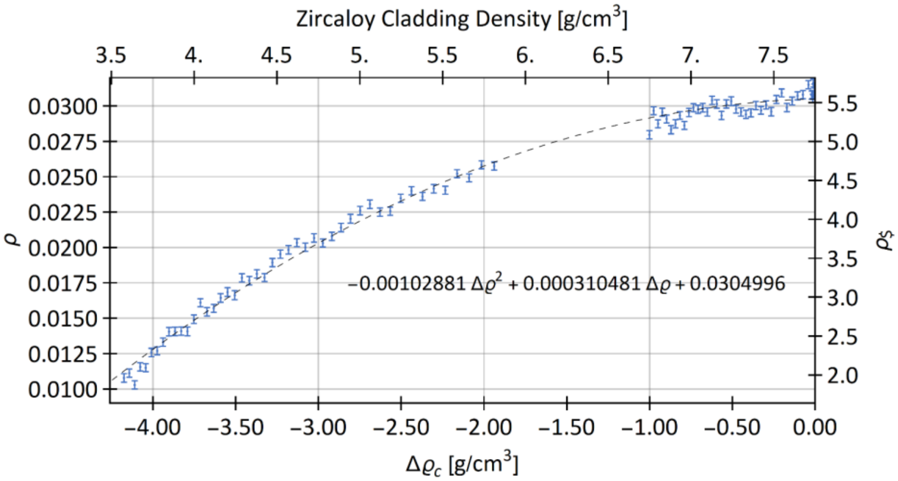

Figure 6-46. Reactivity with Decreasing Zircaloy Density as the Outer Radius Changes due to Thermal Expansion

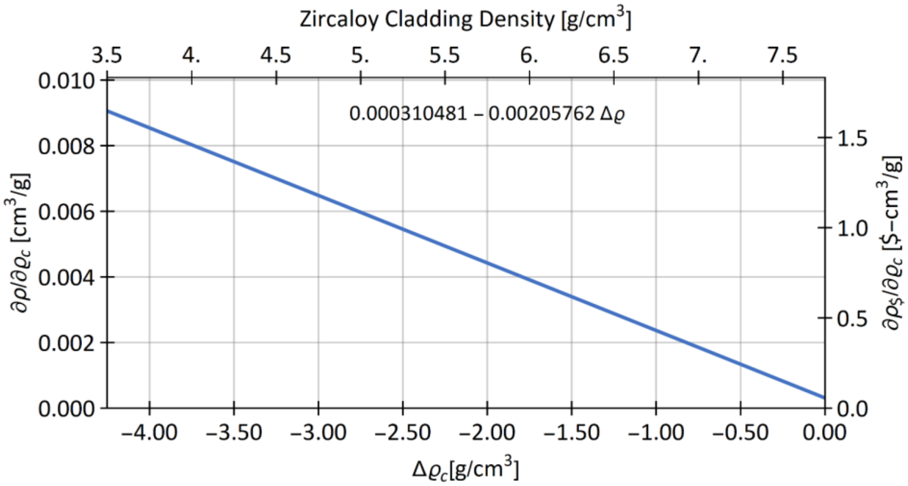

Figure 6-47. Reactivity Feedback Coefficient as a Function of Density as the Outer Radius of the Zircaloy Cladding Changes due to Thermal Expansion

6.2.3 Kinetics Results

6.2.3.1 Application of Neutronics Results

The control rod bank is defined as having a worth of $5.40, which is a representative value obtained from the reactivity feedback studies. The differential reactivity curve from Figure 6-16 is integrated and scaled to the total worth in Figure 6-48. Table 6-6 shows associated control rod bank heights for given reactivity insertions. The control rod withdrawal speed for reactivity insertion is determined using these heights along with the total insertion period.

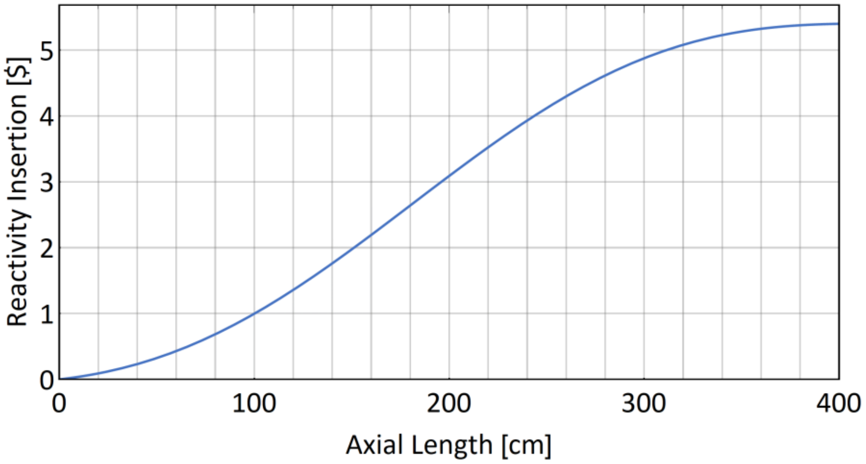

Figure 6-48. Reactivity Insertion as a Function of Axial Height for the Control Rod Bank Used in the Study

Table 6-6. Control Rod Bank Positions per Given Reactivity Insertion

Total Reactivity Insertion ($)	Control Rod Bank Position (cm)
1	100.191
2	151.172
2.67	181.099 (peak differential)
3	195.955
4	243.563
5	311.344
5.40	400 (total worth)

The total neutron generation time (Λ) and delayed neutron fraction (β_{eff}) were obtained from the Phase 1a results as 2.65808E-05 seconds and 0.005443874, respectively. The reactivity feedback coefficients from the MCNP studies are summarized in Table 6-7 below. The fuel temperature feedback is restricted to perturbations of the UO_2 only and not the gap fluid or cladding. The coolant temperature feedback is restricted to the liquid phase at 101,325 Pa. The inner cladding radius study is used to provide the density feedback coefficient for the thermal expansion of Zircaloy, although the outer radius study provided confirmatory bounding results.

Table 6-7. Summary of Reactivity Feedback Coefficients from the Neutronics Studies Shown to Eight Significant Figures

Mechanism	Feedback Coefficient	Units
Fuel temperature	$\left.\frac{\partial \rho_\$}{\partial T}\right\|_F = -\frac{0.088017527}{\sqrt{T}}$	\$ per K
Coolant density	$\frac{\partial \rho_\$}{\partial (\%Void)} = -3.9444568$	\$ per %void
Coolant temperature	$\left.\frac{\partial \rho_\$}{\partial T}\right\|_C = -0.0087093620$	\$ per K
Fuel thermal expansion: outer radius	$\frac{\partial \rho_\$}{\partial r_{f,o}} = -41.821538$	\$ per cm
Fuel thermal expansion: inner radius (N/A)	$\frac{\partial \rho_\$}{\partial r_{f,i}} = 0$	\$ per cm
Fuel thermal expansion: density	$\frac{\partial \rho_\$}{\partial \varrho_f} = 0.98133973$	\$ per (g/cm^3)
Cladding thermal expansion: outer radius	$\frac{\partial \rho_\$}{\partial r_{c,o}} = -56.471229$	\$ per cm
Cladding thermal expansion: inner radius	$\frac{\partial \rho_\$}{\partial r_{c,i}} = 36.070511$	\$ per cm
Cladding thermal expansion: density via inner radius	$\frac{\partial \rho_\$}{\partial \varrho_c} = 0.35064621$	\$ per (g/cm^3)

6.2.3.2 Transient Results

Table 6-8 shows a summary of results for a water-filled gap in a test matrix spanning a total reactivity insertion from $1 to $5 and insertion period from 0.01 to 10 seconds. Results include the peak power, the total integrated energy of the pulse, the maximal and average fuel and coolant temperatures, the time of the power peak, and the maximum reactivity. The results are representative up to the loss of criticality ($\rho<0$) after control rod withdrawal or the simulation termination time, whichever of the two comes first. Due to this convention, the maximum temperatures—in particular the maximum coolant temperatures—may not correspond to the maxima observed up to the end of the simulation due to heat transfer limitations. Tests highlighted in dark red were cut short before the prescribed end time as a result of thermal expansion in the fuel closing the clad gap. These failures do not necessarily imply that the total intended reactivity was not inserted. Averages are based on numerical integrations using the interpolation capabilities of Mathematica. A shorthand for referring to tests will be coordinates of (dollars, period) where the period units are expressed as “s” (second) for convenience.

For insertions of $2 and above for periods of 0.01 to 0.5 seconds, as well as ($5, 1.0 s), the transient does not complete up to a point of subcriticality due to closure of the clad gap from thermal expansion. However, all 0.01-second periods showed that the maximum intended reactivity was inserted regardless. The fuel element radii during the ($2, 0.01 s) test are shown in Figure 6-49, in which the fuel radius is observed to meet that of the gap (inner clad) after 0.07 second near the time of power peaking, which blocks RAZORBACK from obtaining a numerical solution. However, Figure 6-50 shows that the reactivity reaches the $2 peak at the time of insertion and then proceeds to succumb to negative reactivity feedback. To illustrate, Figure 6-51 shows the corresponding reactivity feedback from various mechanisms. Due to a pressure increase in the coolant channel, there is brief positive feedback from the coolant that approaches zero at the insertion period. After the insertion (control rod withdrawal) there is negative feedback in the fuel, most prominently from Doppler Broadening and next from thermal expansion. After some time, thermal expansion in the cladding and coolant feedback become negative and bring reactivity towards subcriticality around the time of power peaking.

Table 6-8. Summary of RAZORBACK Results for Water-Filled Gap with Key at Bottom

Reactivity ($) Time (second)	$1	$2	$3	$4	$5
0.01	P: 8.13E+09 W E: 1.86E+09 J MF: 651.32°C AF: 100.08°C MW: 67.66°C AW: 62.61°C PT: 3.501 s ρ: 1.040	P: 5.85E+11 W E: 5.61E+09 J MF: 1721.62°C AF: 228.90°C MW: 64.96°C AW: 62.54°C PT: 0.074 s ρ: 2.002	P: 1.40E+12 W E: 4.29E+09 J MF: 1359.82°C AF: 159.18°C MW: 64.96°C AW: 62.54°C PT: 0.041 s ρ: 3.005	P: 2.15E+12 W E: 4.12E+09 J MF: 1299.05°C AF: 144.94°C MW: 64.96°C AW: 62.54°C PT: 0.030 s ρ: 4.002	P: 3.00E+12 W E: 4.25E+09 J MF: 1313.62°C AF: 141.15°C MW: 64.96°C AW: 62.54°C PT: 0.024 s ρ: 4.997
0.1	P: 1.45E+09 W E: 1.31E+09 J MF: 484.82°C AF: 270.21°C MW: 67.55°C AW: 63.42°C PT: 0.712 s ρ: 1.000	P: 4.88E+11 W E: 3.87E+09 J MF: 1148.50°C AF: 123.12°C MW: 64.96°C AW: 62.54°C PT: 0.141 s ρ: 2.000	P: 1.63E+11 W E: 4.40E+08 J MF: 218.93°C AF: 70.49°C MW: 64.96°C AW: 62.54°C PT: 0.101 s ρ: 2.938	P: 2.16E+12 W E: 5.35E+09 J MF: 1635.99°C AF: 109.61°C MW: 64.96°C AW: 62.54°C PT: 0.092 s ρ: 3.229	P: 2.11E+12 W E: 4.40E+09 J MF: 1376.01°C AF: 103.39°C MW: 64.96°C AW: 62.54°C PT: 0.077 s ρ: 3.557
0.5	P: 1.40E+09 W E: 1.29E+09 J MF: 473.30°C AF: 237.60°C MW: 67.40°C AW: 63.30°C PT: 1.101 s ρ: 0.999	P: 3.20E+11 W E: 4.62E+09 J MF: 1466.78°C AF: 101.00°C MW: 64.96°C AW: 62.54°C PT: 0.471 s ρ: 1.580	P: 4.50E+11 W E: 5.68E+09 J MF: 1769.47°C AF: 111.63°C MW: 64.96°C AW: 62.54°C PT: 0.381 s ρ: 1.688	P: 3.37E+11 W E: 2.65E+09 J MF: 794.49°C AF: 85.02°C MW: 64.96°C AW: 62.54°C PT: 0.311 s ρ: 1.802	P: 2.17E+11 W E: 1.49E+09 J MF: 454.98°C AF: 77.30°C MW: 64.96°C AW: 62.54°C PT: 0.251 s ρ: 1.936
1	P: 1.39E+09 W E: 1.28E+09 J MF: 474.97°C AF: 209.80°C MW: 67.52°C AW: 63.19°C PT: 1.501 s ρ: 0.998	P: 1.24E+11 W E: 6.18E+09 J MF: 1848.98°C AF: 189.09°C MW: 71.25°C AW: 62.56°C PT: 0.851 s ρ: 1.349	P: 1.77E+11 W E: 7.19E+09 J MF: 1682.98°C AF: 209.76°C MW: 64.97°C AW: 62.54°C PT: 0.681 s ρ: 1.427	P: 2.26E+11 W E: 1.01E+10 J MF: 1705.67°C AF: 204.12°C MW: 64.96°C AW: 62.54°C PT: 0.561 s ρ: 1.499	P: 3.31E+11 W E: 5.17E+09 J MF: 1646.87°C AF: 106.90°C MW: 64.96°C AW: 62.54°C PT: 0.461 s ρ: 1.594
5	P: 5.79E+08 W E: 7.95E+08 J MF: 316.68°C AF: 113.21°C MW: 68.15°C AW: 63.03°C PT: 5.301 s ρ: 0.931	P: 6.62E+09 W E: 2.82E+09 J MF: 927.34°C AF: 150.10°C MW: 68.44°C AW: 62.68°C PT: 3.601 s ρ: 1.031	P: 1.05E+10 W E: 3.23E+09 J MF: 1056.16°C AF: 161.84°C MW: 68.50°C AW: 62.65°C PT: 2.901 s ρ: 1.067	P: 1.61E+10 W E: 3.57E+09 J MF: 1155.22°C AF: 170.91°C MW: 68.13°C AW: 62.63°C PT: 2.301 s ρ: 1.100	P: 2.11E+10 W E: 3.70E+09 J MF: 1291.06°C AF: 178.86°C MW: 71.6°C AW: 62.61°C PT: 1.901 s ρ: 1.151
10	P: 9.88E+07 W E: 2.64E+08 J MF: 140.65°C AF: 78.81°C MW: 68.97°C AW: 63.10°C PT: 10.001 s ρ: 0.686	P: 7.09E+08 W E: 1.32E+09 J MF: 478.73°C AF: 128.14°C MW: 70.60°C AW: 63.22°C PT: 7.401 s ρ: 0.865	P: 2.05E+09 W E: 1.97E+09 J MF: 683.98°C AF: 135.26°C MW: 70.41°C AW: 62.86°C PT: 5.601 s ρ: 0.942	P: 4.12E+09 W E: 2.43E+09 J MF: 812.84°C AF: 141.85°C MW: 68.94°C AW: 62.74°C PT: 4.501 s ρ: 0.991	P: 7.05E+09 W E: 2.87E+09 J MF: 947.29°C AF: 151.55°C MW: 69.06°C AW: 62.68°C PT: 3.501 s ρ: 1.037

NOTE: 🟥 Test failed due to thermal expansion closure, ◻ Test failed from out-of-bounds enthalpy, ⬜ Other error

P = peak power, E = total integrated energy, MF = max. fuel temperature, AF = avg. fuel temperature,
MW = max. coolant temperature, AW = avg. coolant temperature, PT = peak power time, ρ = max. reactivity

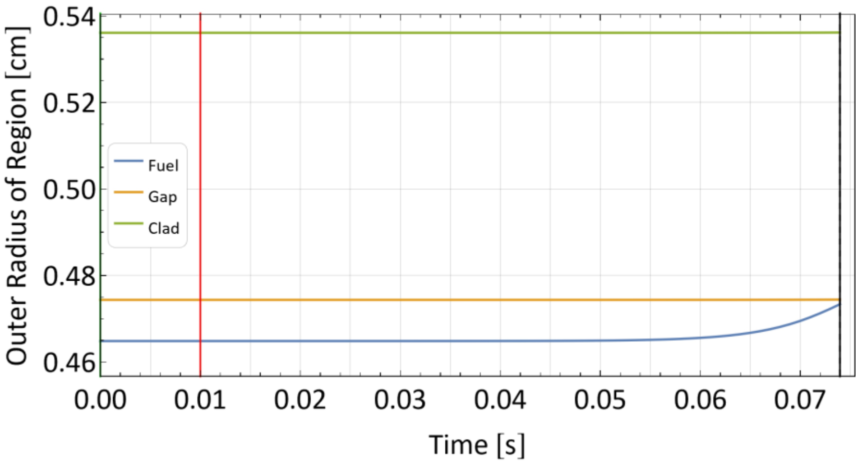

NOTE: The black line is the time of power peaking, while the red line is the reactivity insertion period.

Figure 6-49. Thermal Expansion of the Fuel in the ($2, 0.01 s) Test Results in Failure

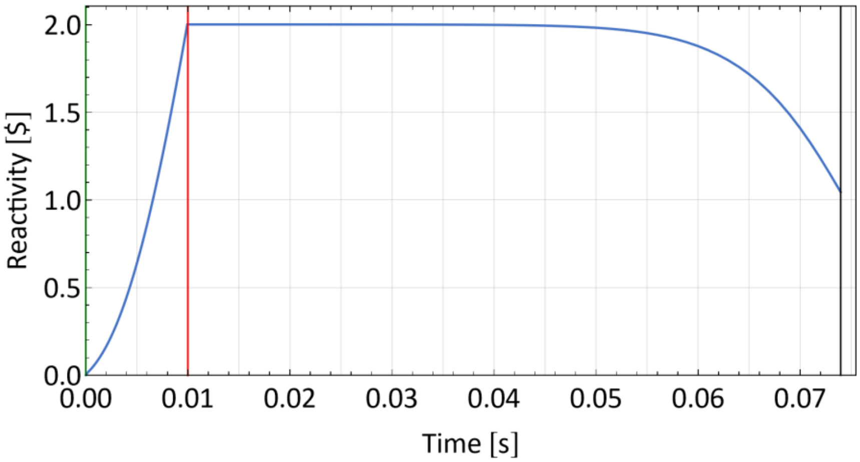

NOTE: The black line is the time of power peaking, while the red line is the reactivity insertion period.

Figure 6-50. System Reactivity in the ($2, 0.01 s) Test, Where the Peak Reactivity Is Achieved before Power Peaking and Failure

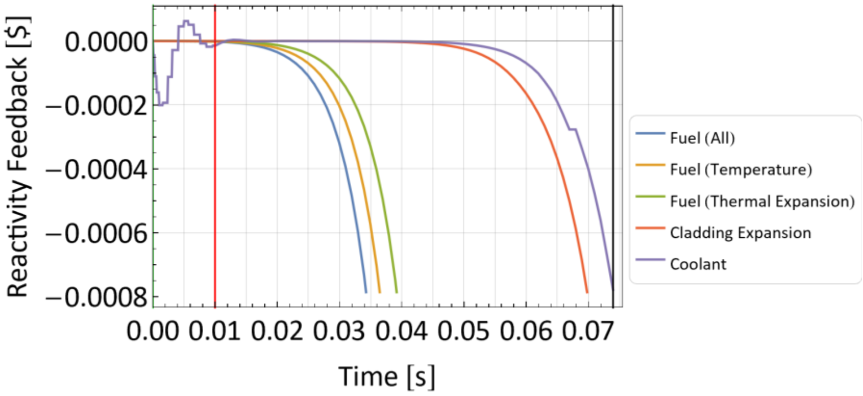

NOTE: The black line is the time of power peaking, while the red line is the reactivity insertion period.

Figure 6-51. Reactivity Feedback in the ($2, 0.01 s) Test

While the $3 and $4 insertions for 1.0 second are preempted due to gap closure, they do reach some maximum reactivity before approaching subcriticality. For the longest periods at 5.0 and 10.0 s, the tests reach maximum reactivities below the intended dollar insertion before negative feedback mechanisms result in subcriticality. These tests exhibit relatively modest power output, especially with small insertions.

The ($3, 1.0 s) and ($4, 1.0 s) tests provided the largest energy releases at 7.19×10^9 and 1.01×10^{10} J, respectively, while the ($1, 10 s) test provided both the lower power of 9.88×10^7 W and lowest energy release of 2.64×10^8 J. The maximum fuel temperature of 1848.98°C, maximum cladding temperature of 386.50°C, and maximum coolant temperature of 71.25°C are all observed in the ($2, 1.0 s) test when restricted to the time of criticality. However, for the whole simulation time (including subcriticality) the maximum coolant temperature of 112.75°C is observed in ($3, 10 s). In that test, the maximum observed fuel temperature was only 733.48°C. Figure 6-52 shows the coolant temperature profile, which reveals that the peak temperatures are observed at the end of the simulation beyond the time subcriticality is achieved. In Figure 6-53, which shows the profile for the cladding surface temperature, the peak temperature profile aligns closely with the one observed at subcriticality. These results indicate that heat transfer occurs over a more prolonged period compared to the time of the transient criticality event, as the cladding temperature reaches a steady state closely after the end of criticality compared to the coolant channel.

The *average* integrated coolant temperature is actually very similar for all tests, although the $1 series has higher values. The highest integrated average coolant temperature over all time is 74.34°C in ($1, 0.5 s).

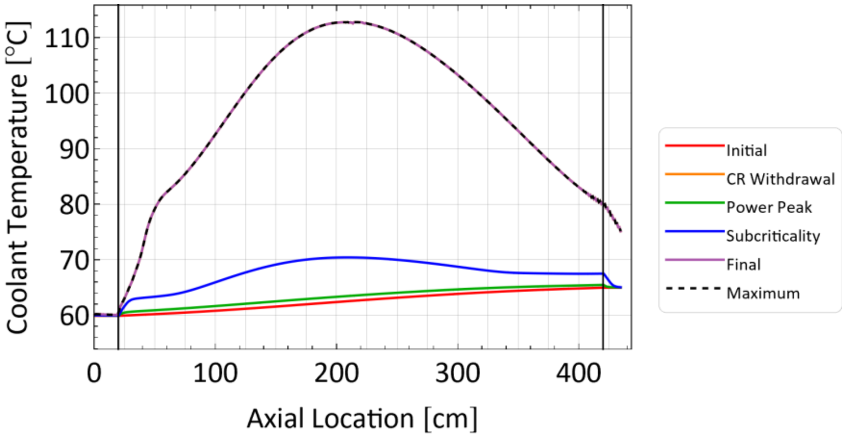

NOTE: The black lines indicate the extent of the fueled region.

Figure 6-52. Coolant Temperature Profile in the ($3, 10 s) Test

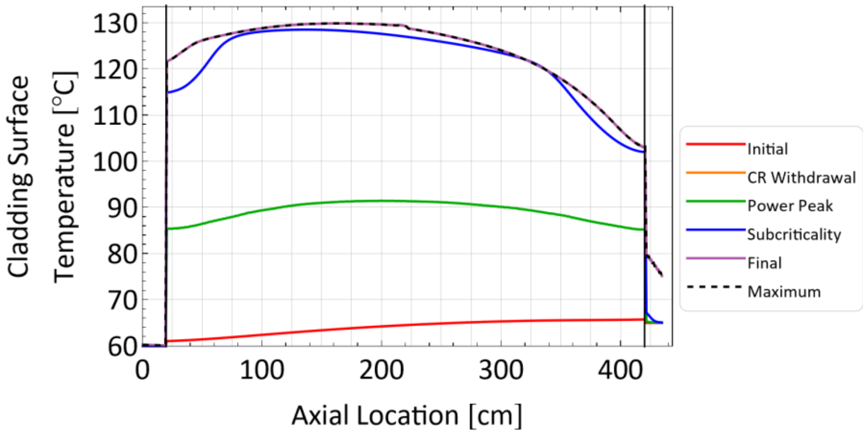

NOTE: The black lines indicate the extent of the fueled region.

Figure 6-53. Cladding Surface Temperature Profile in the ($3, 10 s) Test

The ($2, 5.0 s) test is a low-power-output case in which feedback suppresses the maximum intended insertion. The power profile in Figure 6-54 shows a peak of 6.62 × 10^9 W at 3.6 seconds; the integrated energy up to the time of subcriticality at 4.1 seconds is 2.82 × 10^9 J. Figure 6-55 shows that the peak reactivity of $1.03 is less than the intended $2 insertion and occurs at 3.5 seconds shortly before the peak power and much sooner than the prescribed 5-second period. Figure 6-56 shows that negative feedback from the coolant is most prominent early in the transient and has to deal with the density changes as the temperature increases from the bottom to the top of the fueled region (like the initial behavior in Figure 6-52). The fuel and cladding feedback effects are active later to finally counteract the control rod withdrawal effects. While the fuel does undergo expansion, it does not proceed enough to close the gap. Figure 6-57 shows that the fuel element pressure and fuel temperature begin increasing shortly before the peak power. The pressure peaks at the time of peak thermal expansion, and the peak temperature of 927.34°C is observed at subcriticality (1,002.20°C at the end of the simulation).

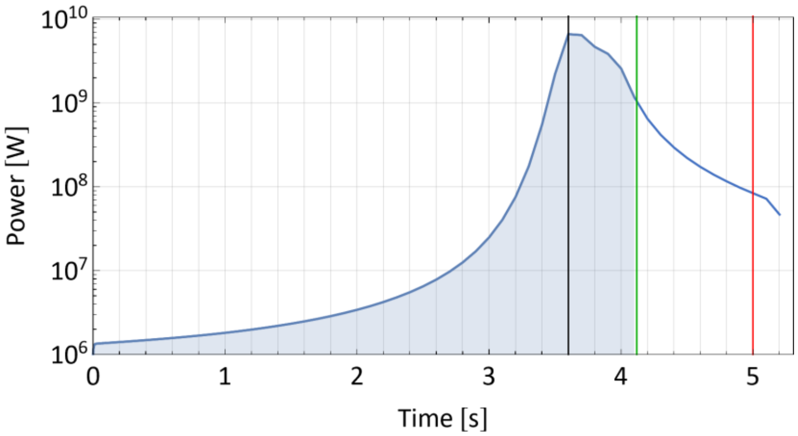

NOTE: The black line indicates the time of peak power, the red line is the insertion period, and the green line is the time of subcriticality.

Figure 6-54. Power Output over Time in the ($2, 5 s) Test

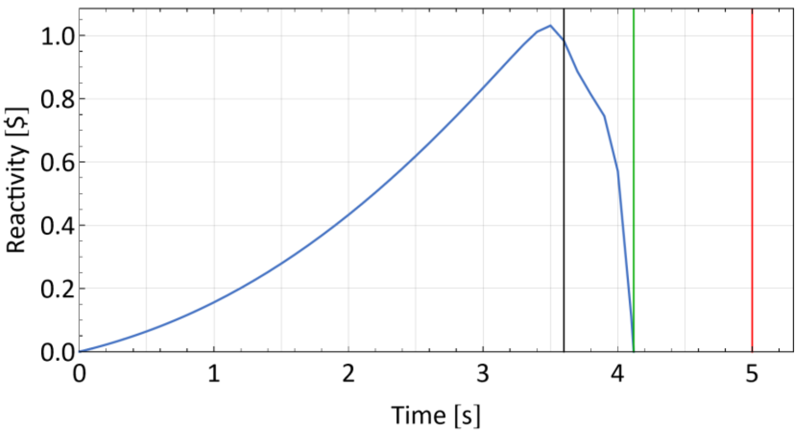

NOTE: The black line indicates the time of peak power, the red line is the insertion period, and the green line is the time of subcriticality.

Figure 6-55. Reactivity over Time in the ($2, 5 s) Test

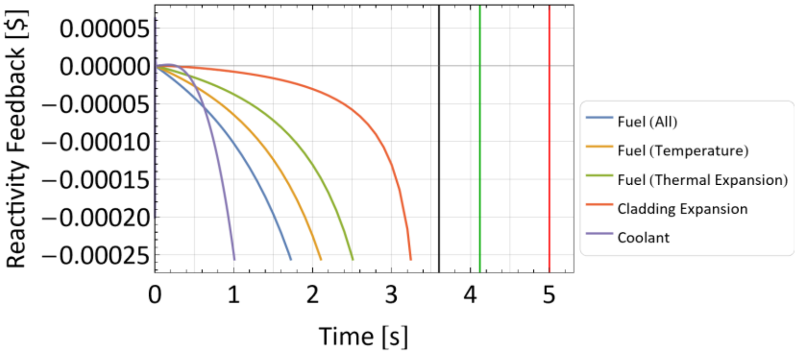

NOTE: The black line indicates the time of peak power, the red line is the insertion period, and the green line is the time of subcriticality.

Figure 6-56. Reactivity Feedback in the ($2, 5 s) Test

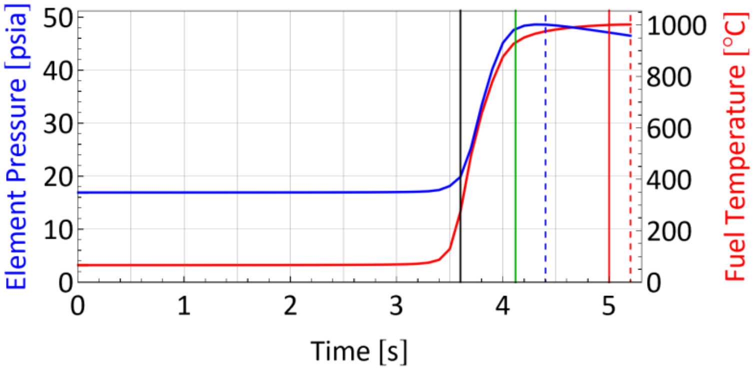

NOTE: The solid black line indicates the time of peak power, the solid red line is the insertion period, and the green line is the time of subcriticality. The dashed blue and red lines are the times of peak fuel expansion and temperature, respectively.

Figure 6-57. Maximal Element Pressures and Fuel Temperatures over Time in the ($2, 5 s) Test

To demonstrate the effects of the gap material on thermal expansion effects, Table 6-9 shows a summary of results for a helium-filled gap in a test matrix spanning a total reactivity insertion from $1 to $5 and insertion period from 0.01 to 10 seconds. Results are comparable except for a few differences. A major observation is that per given test that reaches subcriticality, the time at which subcriticality is achieved occurs sooner. To demonstrate, in a comparison of Figure 6-58 to Figure 6-55, the peak reactivity of $1.03 is achieved at 3.5 seconds like the water-filled results but subcriticality is reached earlier at 3.82 seconds. This observation suggests that combined negative feedback effects become stronger when helium fills the gap. Figure 6-59 shows that per given time, fuel feedback effects are a bit more negative compared to those from Figure 6-56 for the water-filled gap, although the negative effects from cladding expansion are active at later times. Since helium is a low-density gap with different heat transfer characteristics, the pressure and temperature evolution in the element are different, as shown in Figure 6-60. It is shown that peak fuel expansion occurs sooner after subcriticality and maximum fuel temperatures are lower. One interesting effect is that the peak power of 7.69×10^9 W is higher but the energy release of 1.81×10^9 J is lower due to the aforementioned subcriticality times (Figure 6-61). Therefore, given the variation in effects, the choice of gap-filling fluid is highlighted for deeper investigation for future studies.

Table 6-9. Summary of RAZORBACK Results for He-Filled Gap with Key at Bottom

Reactivity ($) Time (second)	$1	$2	$3	$4	$5
0.01	P: 1.69E+09 W E: 9.23E+08 J MF: 373.46°C AF: 189.45°C MW: 68.89°C AW: 62.96°C PT: 0.641 s ρ: 1.001	P: 5.80E+11 W E: 5.15E+09 J MF: 1600.68°C AF: 212.85°C MW: 64.96°C AW: 62.54°C PT: 0.073 s ρ: 2.002	P: 1.53E+12 W E: 4.72E+09 J MF: 1512.10°C AF: 168.34°C MW: 64.96°C AW: 62.54°C PT: 0.041 s ρ: 3.005	P: 2.42E+12 W E: 4.64E+09 J MF: 1479.45°C AF: 154.49°C MW: 64.96°C AW: 62.54°C PT: 0.030 s ρ: 4.002	P: 3.39E+12 W E: 4.79E+09 J MF: 1506.25°C AF: 150.63°C MW: 64.96°C AW: 62.54°C PT: 0.024 s ρ: 4.997
0.1	P: 1.66E+09 W E: 9.16E+08 J MF: 363.50°C AF: 181.51°C MW: 67.01°C AW: 62.94°C PT: 0.721 s ρ: 1.000	P: 5.13E+11 W E: 4.12E+09 J MF: 1219.86°C AF: 127.34°C MW: 64.96°C AW: 62.54°C PT: 0.141 s ρ: 2.000	P: 1.69E+11 W E: 4.48E+08 J MF: 220.88°C AF: 71.11°C MW: 64.96°C AW: 62.54°C PT: 0.101 s ρ: 2.931	P: 1.60E+12 W E: 3.77E+09 J MF: 1220.30°C AF: 97.71°C MW: 64.96°C AW: 62.54°C PT: 0.091 s ρ: 3.218	P: 2.28E+12 W E: 4.76E+09 J MF: 1518.72°C AF: 106.74°C MW: 64.96°°C AW: 62.54°C PT: 0.077 s ρ: 3.545
0.5	P: 1.63E+09 W E: 9.07E+08 J MF: 366.41°C AF: 156.03°C MW: 67.88°C AW: 62.86°C PT: 1.101 s ρ: 0.999	P: 3.18E+11 W E: 4.73E+09 J MF: 1488.18°C AF: 102.42°C MW: 64.96°C AW: 62.54°C PT: 0.471 s ρ: 1.577	P: 2.61E+11 W E: 2.29E+09 J MF: 720.26°C AF: 82.51°C MW: 64.96°C AW: 62.54°C PT: 0.371 s ρ: 1.682	P: 3.54E+11 W E: 2.78E+09 J MF: 828.35°C AF: 86.36°C MW: 64.96°C AW: 62.54°C PT: 0.311 s ρ: 1.796	P: 2.32E+11 W E: 1.57E+09 J MF: 473.96°C AF: 78.32°C MW: 64.96°C AW: 62.54°C PT: 0.251 s ρ: 1.931
1	P: 1.59E+09 W E: 9.05E+08 J MF: 368.89°C AF: 136.51°C MW: 68.86°C AW: 62.79°C PT: 1.501 s ρ: 0.999	P: 1.23E+11 W E: 5.73E+09 J MF: 1748.89°C AF: 148.22°C MW: 69.68°C AW: 62.56°C PT: 0.851 s ρ: 1.346	P: 1.76E+11 W E: 6.86E+09 J MF: 1680.46°C AF: 208.56°C MW: 64.97°C AW: 62.54°C PT: 0.681 s ρ: 1.423	P: 2.28E+11 W E: 9.38E+09 J MF: 1708.35°C AF: 194.85°C MW: 64.97°C AW: 62.54°C PT: 0.561 s ρ: 1.496	P: 3.27E+11 W E: 5.21E+09 J MF: 1620.62°C AF: 107.28°C MW: 64.96°C AW: 62.54°C PT: 0.461 s ρ: 1.590
5	P: 8.58E+08 W E: 7.17E+08 J MF: 300.06°C AF: 94.00°C MW: 67.56°C AW: 62.72°C PT: 5.301 s ρ: 0.944	P: 7.69E+09 W E: 1.81E+09 J MF: 635.91°C AF: 99.31°C MW: 67.58°C AW: 62.61°C PT: 3.601 s ρ: 1.035	P: 1.01E+10 W E: 2.22E+09 J MF: 772.84°C AF: 103.89°C MW: 69.40°C AW: 62.60°C PT: 2.801 s ρ: 1.070	P: 1.70E+10 W E: 2.57E+09 J MF: 835.04°C AF: 107.22°C MW: 65.11°C AW: 62.58°C PT: 2.301 s ρ: 1.101	P: 2.01E+10 W E: 1.92E+09 J MF: 891.43°C AF: 94.12°C MW: 65.02°C AW: 62.54°C PT: 1.901 s ρ: 1.150
10	P: 1.51E+08 W E: 3.41E+08 J MF: 175.35°C AF: 82.65°C MW: 69.66°C AW: 62.98°C PT: 10.001 s ρ: 0.722	P: 1.01E+09 W E: 8.31E+08 J MF: 335.34°C AF: 91.11°C MW: 69.19°C AW: 62.76°C PT: 7.102 s ρ: 0.888	P: 2.53E+09 W E: 1.16E+09 J MF: 440.09°C AF: 93.19°C MW: 68.33°C AW: 62.67°C PT: 5.501 s ρ: 0.954	P: 4.43E+09 W E: 1.48E+09 J MF: 540.57°C AF: 95.97°C MW: 68.98°C AW: 62.63°C PT: 4.501 s ρ: 0.997	P: 8.13E+09 W E: 1.86E+09 J MF: 651.32°C AF: 100.08°C MW: 67.66°C AW: 62.61°C PT: 3.501 s ρ: 1.040

NOTE: 🟥 Test failed due to thermal expansion closure, ▨ Test failed from out-of-bounds enthalpy, ⬜ Other error

P = peak power, E = total integrated energy, MF = max. fuel temperature, AF = avg. fuel temperature,
MW = max. coolant temperature, AW = avg. coolant temperature, PT = peak power time, ρ = max. reactivity

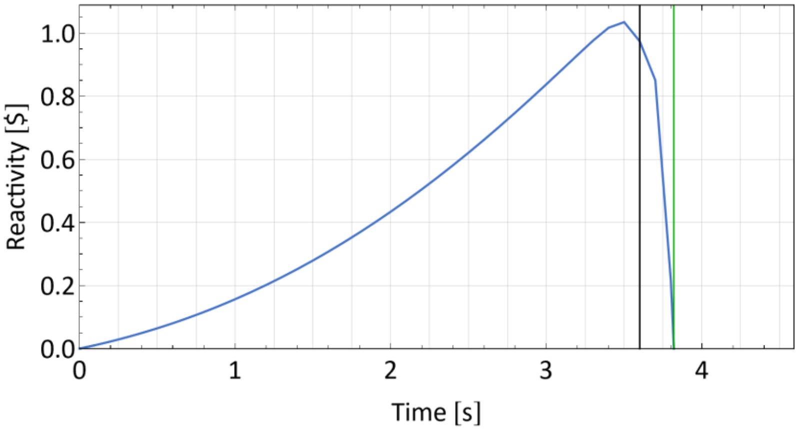

NOTE: The black line indicates the time of peak power, and the green line is the time of subcriticality.

Figure 6-58. Reactivity over Time in the ($2, 5 s) Test with a He-Filled Gap

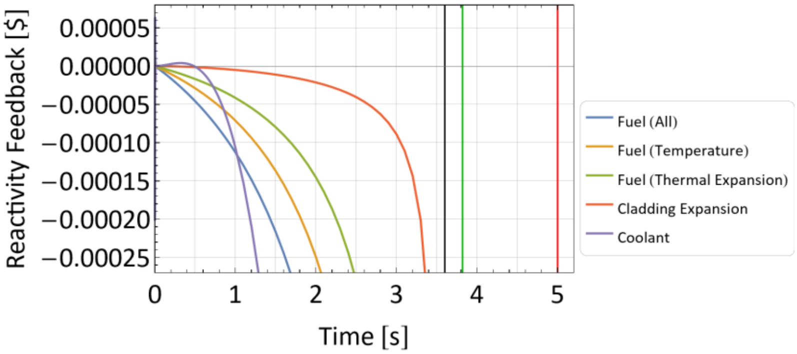

NOTE: The black line indicates the time of peak power, the red line is the insertion period, and the green line is the time of subcriticality.

Figure 6-59. Reactivity Feedback in the ($2, 5 s) Test with a He-Filled Gap

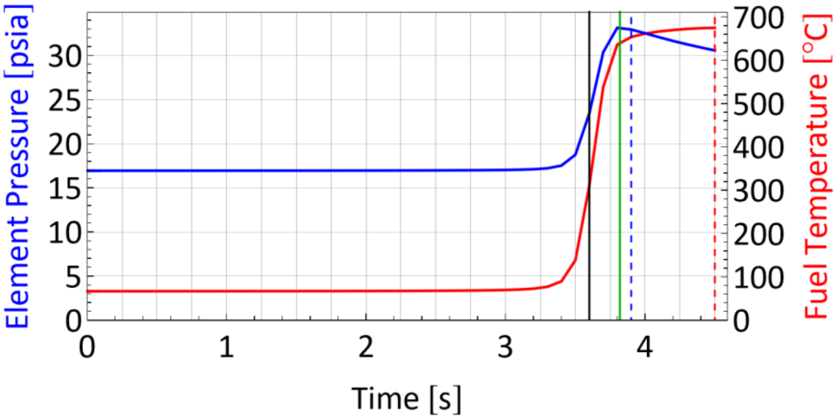

NOTE: The solid black line indicates the time of peak power, the solid red line is the insertion period, and the green line is the time of subcriticality. The dashed blue and red lines are the times of peak fuel expansion and temperature, respectively.

Figure 6-60. Maximal Element Pressures and Fuel Temperatures over Time in the ($2, 5 s) Test with a He-Filled Gap

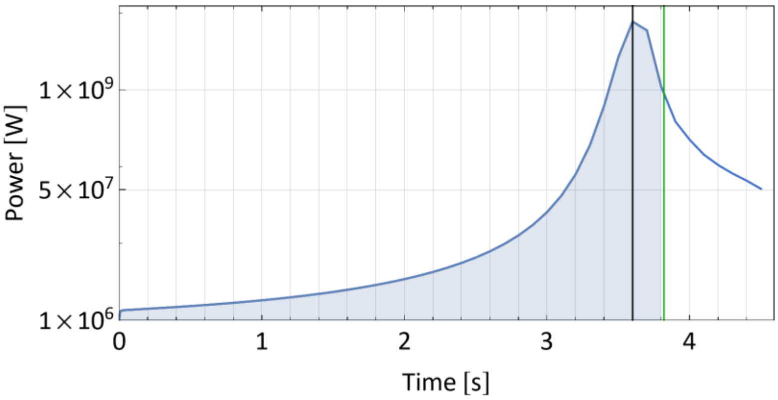

NOTE: The solid black line indicates the time of peak power and the green line is the time of subcriticality.

Figure 6-61. Power Output over Time in the ($2, 5 s) Test with a He-Filled Gap

6.2.4 Discussion

The kinetics study indicated that most parameter sets of reactivity insertion and time result in rapid evolution of certain system properties, such as fuel expansion, rod element pressure, and fuel temperature, that prevent the code from fully evaluating the transient. However, it has been demonstrated that some successful reactivity insertions can be modeled in a transient analysis if it is assumed that the DPC absorber plates can function analogously to reactor control rods and disintegrate catastrophically enough to be removed from the basket in rapid time. These successful reactivity insertions result in rapid releases of energy on the order of 10^8 – 10^9 J, and while it is not yet clear whether these energies would be consequential in-situ, they are worthy of further investigation.

6.2.5 Future Work

The MCNP model can be enhanced by reducing error through an expansion of neutron histories or implementing any of several variance reduction techniques in use by the neutronics community. For the Doppler feedback-related studies in particular, noisy results can possibly be reduced by restricting the broadening effect to key nuclides (i.e., only U and O in the SNF). Replacing water with helium or void in the gap or eliminating the gap altogether may be additional routes for simplifying the analysis and reducing noise in the results. (It should be noted that removing the gap in RAZORBACK would eliminate use of the thermal expansion features if the intention is to have commonality between the neutronics and kinetics analyses.)

The MCNP geometry model can be improved by adding Zircaloy grid spacers in each assembly, modeling the fission gas plenum region in the cladding, and perhaps adding more detail to the basket. Providing axial discretization is an essential priority as it will allow for differential reactivity worth curves to be developed and for the distribution of fission energy to be investigated via a depletion study with CINDER, both of which can be implemented in RAZORBACK. Additionally, if the model accommodates individual rod fidelity (i.e., characteristics such as temperature and density defined on a per-rod basis), the distribution of fission power across the DPC can also be explored in the radial direction.

Both axial and radial enhancement in the DPC model in MCNP may require a departure from the nested geometry structure employed in this study in favor of a more explicit approach. Nonetheless, this accommodation would allow for a study of power-peaking factors in the DPC and for an investigation of varying water levels in the DPC that are more representative of unsaturated alluvium. Indeed, the entire analysis can be repeated for the set of simulations corresponding to the baseline critical water level in void space of the canister. The effects of heterogeneous two-phase flow, cavitation, and condensation on the evolution of criticality can be investigated in a partially full canister with an open breach or closed breach in an alluvial repository.

The RAZORBACK simulation can benefit from employing characteristics more representative of SNF (as opposed to fresh UO_2) to the material properties in the input deck. This approach would include the entire suite of material properties including thermal conductivity, specific heat, thermal expansion, and Young’s modulus. It may be possible to obtain these properties from site measurements of the fuel from Zion and the ongoing investigation of the sister rods study (Saltzstein et al. 2017). The overall study can be enhanced through closer alignment with sister calculations discussed in Section 6.3. Refinements are also needed for characterizing feedback from thermal expansion in the fuel. Such improved characterization may allow the RAZORBACK simulation to avoid thermal expansion of fuel to the point that the gap is closed.

After refinement of the transient criticality investigation, results can be compared to known reactivity-initiated accidents to check for consistency. If the total number of fissions deduced from the energy output are deemed of concern, the next phase of the analysis can apply the transient kinetics results to a solid mechanics study. A primary task would be the application to a simple hoop stress model, in which the system components can be modeled as nested infinite cylinders. A more detailed analysis with a tool such as Zapotec can be done using a highly simplified DPC and barrier system. The source term will be determined by the energy values such as those in Table 6-8 and other conditions supported by results from RAZORBACK.

6.3 Shale Repository

6.3.1 Approach

The following subsections describe the approach taken to model a DPC in a generic saturated shale repository.

6.3.1.1 Introduction

A University of Nevada, Las Vegas independent study (Sanders 2021) was performed to evaluate the behavior of a transient criticality event in a DPC containing PWR SNF. The DPC is assumed to be disposed in a shale saturated geologic repository. The transient criticality event in the DPC is simulated through the rod ejection accident (REA) using the S3K code to evaluate, among other characteristics, the integrity of the fuel and thermodynamic impacts during the power transient. S3K is a transient analysis code developed by Studsvik Scanpower Inc. (Studsvik) with neutronic and thermal-hydraulic analysis capability. The model focuses on providing criticality transient characteristics based on the potential magnitudes and rates of reactivity insertions as well as the reactivity feedback mechanisms.

The following information is generated for the modeled PWR DPC transient criticality scenarios:

- Peak power of criticality transient
- Duration of criticality transient
- Total energy released during criticality transient
- Thermohydraulic characteristics of the system including fuel temperatures, moderator temperatures, and pressure.

University of Nevada, Las Vegas's independent study was performed using the education version of Studsvik's S3K code (license # SSP-U20-1008).

6.3.1.2 Code/Methodology Description

Studsvik's S3K code is a proprietary code which performs transient analysis of the core of commercial PWRs and BWRs. The code applies a time-dependent 3D diffusion theory solution method with six delayed neutron groups, coupled with a thermal-hydraulic channel model. The cross-section input to S3K is provided by CASMO, a lattice fuel 2D multigroup transport-based Method of Characteristics code (Grandi et al. 2011). CASMO produces a 2D transport solution rooted in a heterogenous model geometry, which is used for steady-state neutronic analysis in SIMULATE that, in turn, is used for transient neutronic analysis in S3K.

SIMULATE is a 3D, steady-state, nodal diffusion theory, reactor simulator code. It solves the multigroup nodal diffusion equation, employing a hybrid microscopic-macroscopic, cross-section model that accounts for depletion history effects. SIMULATE output includes steady-state nuclear analysis predictions, such as critical boron concentration, boron worth, reactivity coefficients, control rod worth, shutdown margin, power distributions, and peaking factors.

The thermal hydraulics model of S3K is combination of a conduction model and the hydraulics model (Grandi et al. 2011). The conduction model calculates the heat flux and temperature distribution in the fuel pins, while the hydraulics model calculates flow rate, density, and void fraction of water flowing in the channels.

6.3.1.3 Rod Ejection Accident Analysis

A criticality transient in a disposed DPC can potentially occur due to displacement of neutron absorbers or changes in geometry. To illustrate such a potential event, the REA can be used to simulate the mechanisms initiating a potential criticality transient event in the DPC. A REA is an assumed rupture of the control rod drive mechanism (CRDM), or of the CRDM nozzle. Upon this rupture, the pressure in the reactor coolant system provides an upward force that rapidly ejects the control rods from the core. The ejection of the control rods results in positive reactivity addition, leading to a peaked core power distribution. As the power rapidly rises, fission energy accumulates in the fuel rods faster than it can be transferred into the coolant, raising the fuel temperature. The power rise is mitigated primarily by fuel and moderator temperature.

For 3D REA analysis, the key parameters are as follows (EPRI 2002):

- Ejected control rod worth
- Effective delayed neutron fraction
- Moderator reactivity coefficient
- Doppler coefficient, and
- Core power peaking

The REA can behave differently based on the static worth of the ejected control rod. For example, REA can behave as follows:

- Reactivity insertion close to or greater than effective delayed neutron fraction; this scenario results in a prompt critical scenario. This situation is the condition of interest in this analysis.
- Reactivity insertion much less than the delayed neutron fraction; this scenario is considered subprompt critical.

A higher ejected control rod worth at reduced power can result in prompt critical power excursions.

In a prompt critical scenario, the energy deposition can be defined by the following equation (Hetrick 1993):

$$E_d = \frac{2 * (\rho - \beta) * C_p}{\alpha_D} \qquad \textit{Equation 6-8}$$

where

E_d = energy deposition,

ρ = static ejected control rod worth,

β = delayed neutron fraction,

C_p = fuel heat capacity, and

α_D = Doppler temperature coefficient.

This equation implies that the key parameters affecting the energy deposition during a prompt critical REA are the ejected control rod worth, delayed neutron fraction, fuel heat capacity, and the Doppler temperature coefficient.

For the REA analysis, SIMULATE is used to run the static portion of the calculation. It initializes the cycle-specific model and reactor conditions for the REA simulation performed in S3K. SIMULATE writes an initial condition restart file containing the core model geometry, including control rod positions, reactor operating conditions, and depletion history, to establish the initial core conditions before the start of the REA transient. The restart file contains the explicit neutron library data produced by CASMO necessary for the S3K transient calculations. It automatically accounts for differences between the SIMULATE calculation model and the data necessary for the S3K calculation model to execute properly. Figure 6-62 explains the calculation flowthrough process for calculating the REA scenario for the modeled DPC.

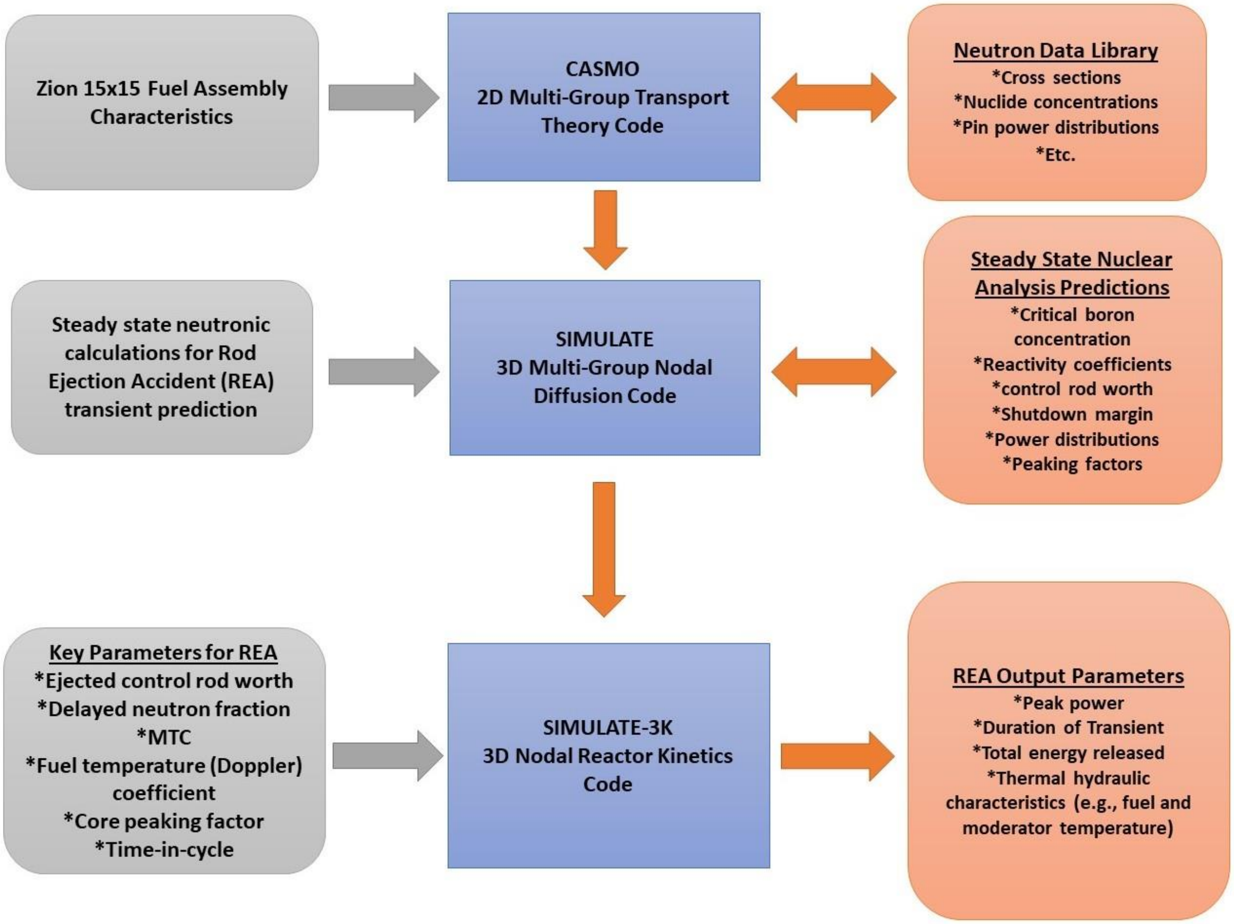

NOTE: 2D = two dimensional
3D = three dimensional
MTC = moderator temperature coefficient
REA = rod ejection accident

Figure 6-62. Calculation Schematic for the REA

6.3.1.4 Design Input

The DPC model used is based on the NAC MAGNASTOR TSC-37 design. The DPC consists of 37 PWR SNF assemblies that have been irradiated in the Zion Nuclear Power Plant. The fuel basket inside the DPC is not included in the calculations. Figure 6-63 displays the layout of the fuel loading (initial enrichment and max burnup) inside the DPC as modeled in S3K.

The depletion characteristics of the Westinghouse 15 × 15 PWR assemblies are shown in Table 6-10. The assembly layout and associated dimensions are shown in Figure 6-64.

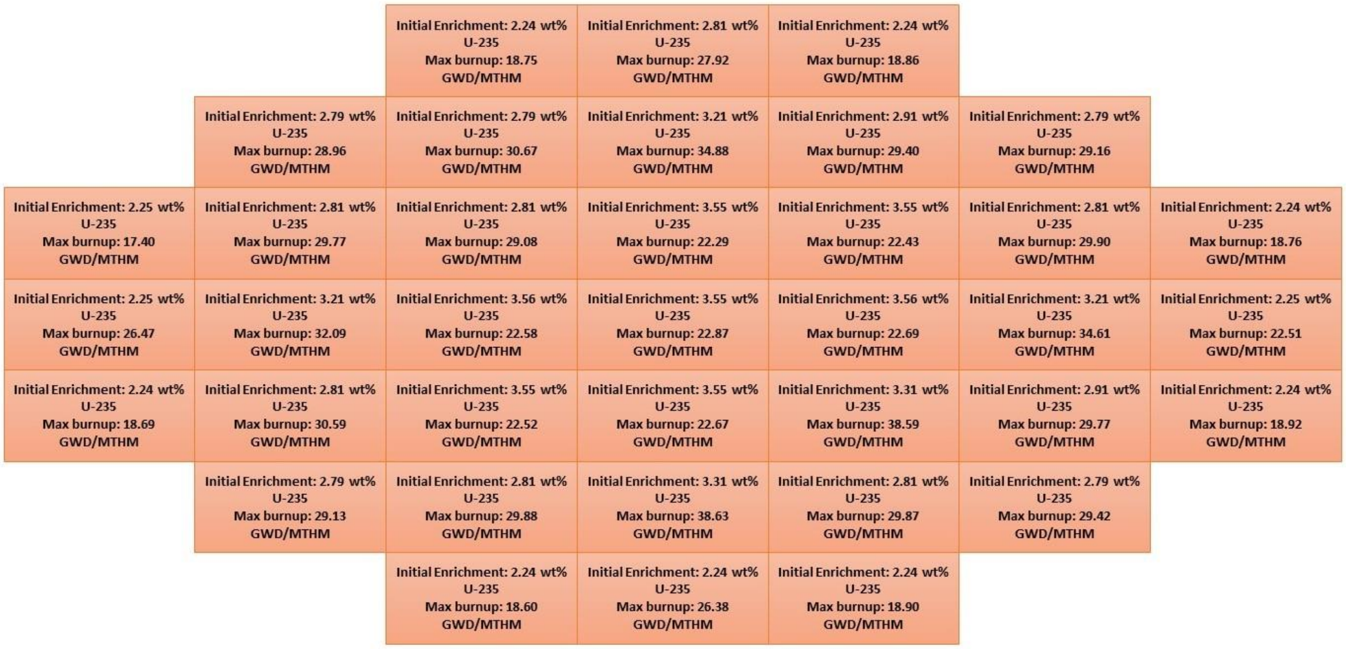

		Initial Enrichment: 2.24 wt% U-235 Max burnup: 18.75 GWD/MTHM	Initial Enrichment: 2.81 wt% U-235 Max burnup: 27.92 GWD/MTHM	Initial Enrichment: 2.24 wt% U-235 Max burnup: 18.86 GWD/MTHM		
	Initial Enrichment: 2.79 wt% U-235 Max burnup: 28.96 GWD/MTHM	Initial Enrichment: 2.79 wt% U-235 Max burnup: 30.67 GWD/MTHM	Initial Enrichment: 3.21 wt% U-235 Max burnup: 34.88 GWD/MTHM	Initial Enrichment: 2.91 wt% U-235 Max burnup: 29.40 GWD/MTHM	Initial Enrichment: 2.79 wt% U-235 Max burnup: 29.16 GWD/MTHM	
Initial Enrichment: 2.25 wt% U-235 Max burnup: 17.40 GWD/MTHM	Initial Enrichment: 2.81 wt% U-235 Max burnup: 29.77 GWD/MTHM	Initial Enrichment: 2.81 wt% U-235 Max burnup: 29.08 GWD/MTHM	Initial Enrichment: 3.55 wt% U-235 Max burnup: 22.29 GWD/MTHM	Initial Enrichment: 3.55 wt% U-235 Max burnup: 22.43 GWD/MTHM	Initial Enrichment: 2.81 wt% U-235 Max burnup: 29.90 GWD/MTHM	Initial Enrichment: 2.24 wt% U-235 Max burnup: 18.76 GWD/MTHM
Initial Enrichment: 2.25 wt% U-235 Max burnup: 26.47 GWD/MTHM	Initial Enrichment: 3.21 wt% U-235 Max burnup: 32.09 GWD/MTHM	Initial Enrichment: 3.56 wt% U-235 Max burnup: 22.58 GWD/MTHM	Initial Enrichment: 3.55 wt% U-235 Max burnup: 22.87 GWD/MTHM	Initial Enrichment: 3.56 wt% U-235 Max burnup: 22.69 GWD/MTHM	Initial Enrichment: 3.21 wt% U-235 Max burnup: 34.61 GWD/MTHM	Initial Enrichment: 2.25 wt% U-235 Max burnup: 22.51 GWD/MTHM
Initial Enrichment: 2.24 wt% U-235 Max burnup: 18.69 GWD/MTHM	Initial Enrichment: 2.81 wt% U-235 Max burnup: 30.59 GWD/MTHM	Initial Enrichment: 3.55 wt% U-235 Max burnup: 22.52 GWD/MTHM	Initial Enrichment: 3.55 wt% U-235 Max burnup: 22.67 GWD/MTHM	Initial Enrichment: 3.31 wt% U-235 Max burnup: 38.59 GWD/MTHM	Initial Enrichment: 2.91 wt% U-235 Max burnup: 29.77 GWD/MTHM	Initial Enrichment: 2.24 wt% U-235 Max burnup: 18.92 GWD/MTHM
	Initial Enrichment: 2.79 wt% U-235 Max burnup: 29.13 GWD/MTHM	Initial Enrichment: 2.81 wt% U-235 Max burnup: 29.88 GWD/MTHM	Initial Enrichment: 3.31 wt% U-235 Max burnup: 38.63 GWD/MTHM	Initial Enrichment: 2.81 wt% U-235 Max burnup: 29.87 GWD/MTHM	Initial Enrichment: 2.79 wt% U-235 Max burnup: 29.42 GWD/MTHM	
		Initial Enrichment: 2.24 wt% U-235 Max burnup: 18.60 GWD/MTHM	Initial Enrichment: 2.24 wt% U-235 Max burnup: 26.38 GWD/MTHM	Initial Enrichment: 2.24 wt% U-235 Max burnup: 18.90 GWD/MTHM		

Figure 6-63. Illustration of DPC Loading with 37 PWR SNF Assemblies

Table 6-10. CASMO Input Depletion Parameters

Parameter/Reactor Type	Westinghouse PWR
Fuel rod mixture	UO_2
Fuel density (g/cm^3)	10.741
Specific Power (MW/MTU)	30
Fuel temperature (K)	1157
Moderator temperature (K)	598.2
Moderator density (g/cm^3)	0.6668
Soluble boron concentration (ppm)	1,000
Burnable absorber exposure	All assembly guide tubes (20) contain Pyrex rods fully inserted throughout irradiation time
Type of absorber	SiO_2-B_2O_3

NOTE: MTU = metric tons of uranium
PWR = pressurized water reactor

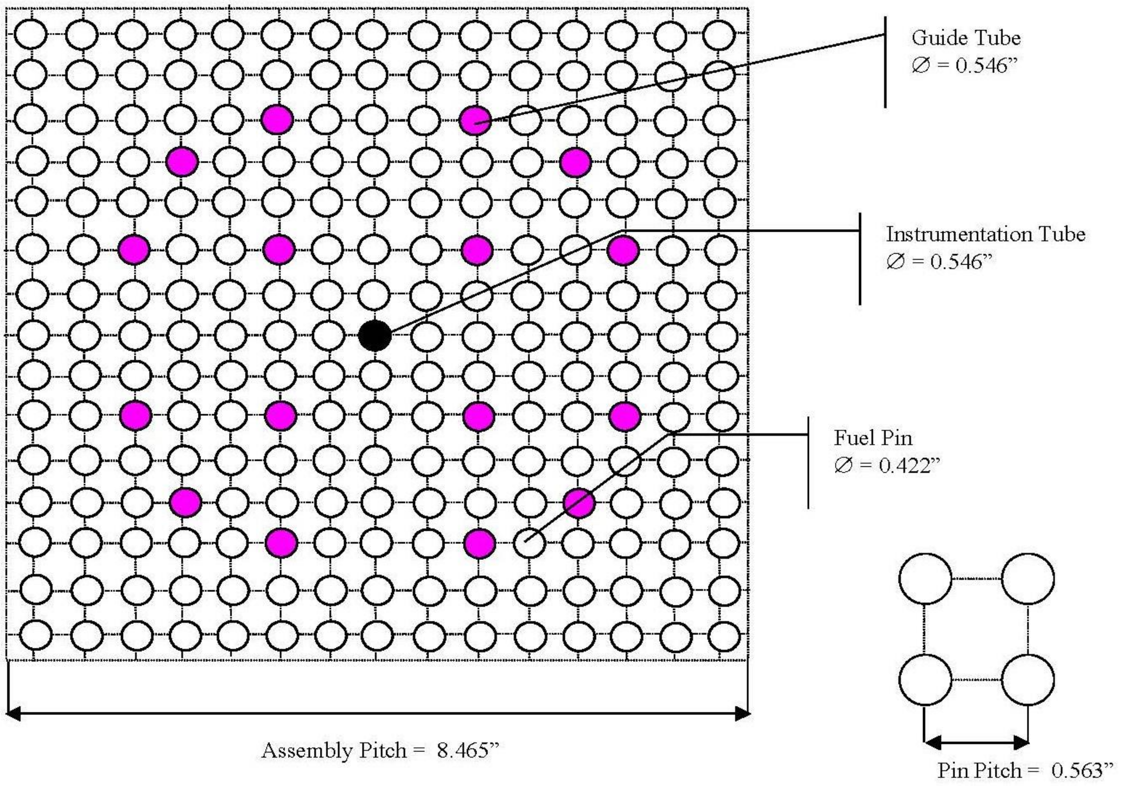

NOTE: 205 Fuel Pins, 20 Guide Tubes, 1 Instrumentation Tube

Figure 6-64. Westinghouse 15 × 15 Fuel Assembly Layout

During the static and transient calculations, the DPC was modeled at a pressure of 725 psi at 0 m/sec flowrate and 0 ppm soluble boron; these conditions are consistent with those for a saturated shale repository. The k_{eff} of the DPC is ~1.1, which is consistent with the calculation performed by ORNL and demonstrates that the selected DPC has significant excess reactivity.

6.3.1.5 Limitations/Assumptions

Since it is not the intended function of S3K to model transient analysis of canisters/out-of-reactor conditions, there are some limitations to the analysis. The following limitations apply:

- The maximum reactivity insertion rate (i.e., control rod withdrawal speed) is limited to 9,999 cm/s, which translates to 0.0365 seconds.
- CASMO/SIMULATE captures decay times on the order of tens of years and not the thousands of years (e.g., 9,000) that the DPC conditions require. This will make the isotopic composition bounding in nature (i.e., higher excess reactivity in the DPC). To capture longer decay times, the fuel is modeled as cold, as the decay heat transfer model/option was turned off in S3K.

It should also be mentioned that S3K starts a transient at critical conditions, independent of the steady-state conditions. Therefore, the transient is initiated by first inserting the control rods to create subcritical conditions (to eliminate delayed-neutron effects) before the initiation of the critical transient.

6.3.2 Results

As previously stated, a prompt critical power excursion can be simulated by ejecting control rods with high worth (i.e., greater than the delayed neutron fraction. Therefore, reactivity insertion worth between approximately $1 to $3 were considered. The S3K model has delayed neutron fraction of 0.00556.

The results of the fuel and moderator temperature coefficient (MTC) calculations are presented below.

6.3.2.1 Fuel Temperature Coefficient

Perturbations were performed to calculate the distributed Doppler coefficient as a function of the fuel average temperature in DPC modeled conditions. The method used calculates the reactivity change associated with a change in fuel temperature having the same spatial distribution as the power divided by the change in the average fuel temperature.

Table 6-11 presents the results from this method of the calculated Doppler coefficients as a function of fuel temperature. The results from the distributed Doppler coefficient reflects the power gradient/peaking in the DPC (which is shown in Table 6-13, Table 6-14, and Table 6-15). The distributed Doppler coefficient is also illustrated in Figure 6-65.

Table 6-11. Distributed Doppler Coefficient in the DPC

Fuel Average Temperature (°C)	Fuel Average Temperature (°F)	Distributed Doppler Coefficient (pcm/°F)
73	164	−3.03
85	185	−2.91
199	390	−2.63
238	460	−2.46
251	484	−2.41
266	511	−2.38
296	564	−2.27
330	626	−2.21
374	705	−2.15
518	965	−2.01
581	1,078	−1.99
643	1,190	−1.89
706	1,303	−1.84
731	1,348	−1.82
831	1,528	−1.73
956	1,753	−1.65
1,237	2,258	−1.51
1,887	3,428	−1.2
2,499	4,530	−1.16

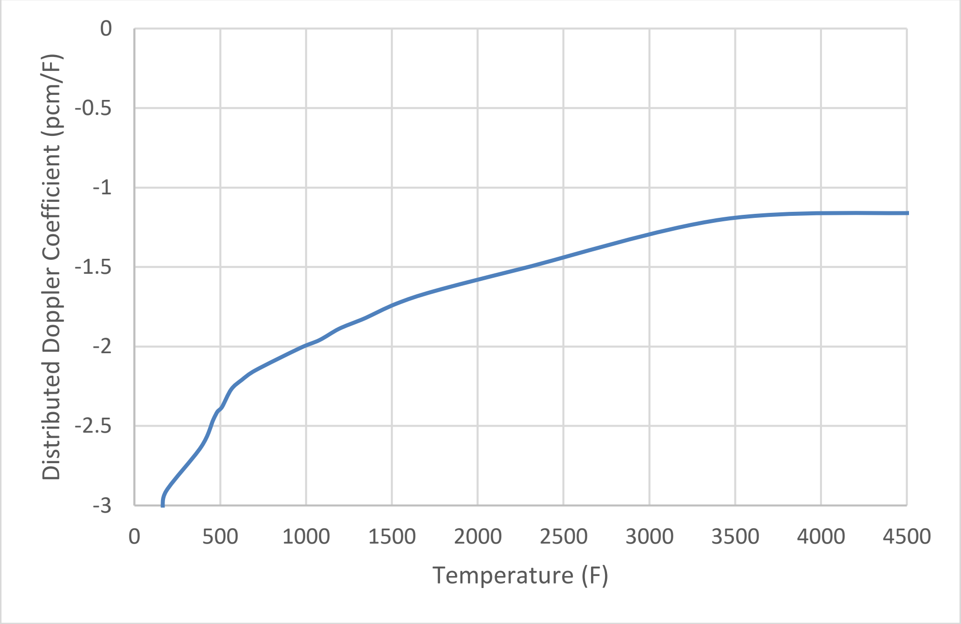

Figure 6-65. Distributed Doppler Coefficient

6.3.2.2 Moderator Temperature Coefficient

MTCs were calculated as a function of the coolant average temperature. As the saturation temperature of the 725 psia pressured DPC is 507°F, data points beyond this value cannot be observed. The results are presented in tabular format in Table 6-12 and illustrated in Figure 6-66.

Table 6-12. Moderator Temperature Coefficients in the DPC

Coolant Average Temperature (°F)	MTC (pcm/°F)
105	–2.74
155	–4.09
205	–5.24
255	–6.18
305	–7.11
355	–8.65
405	–10.74
455	–14.07
505	–19.26

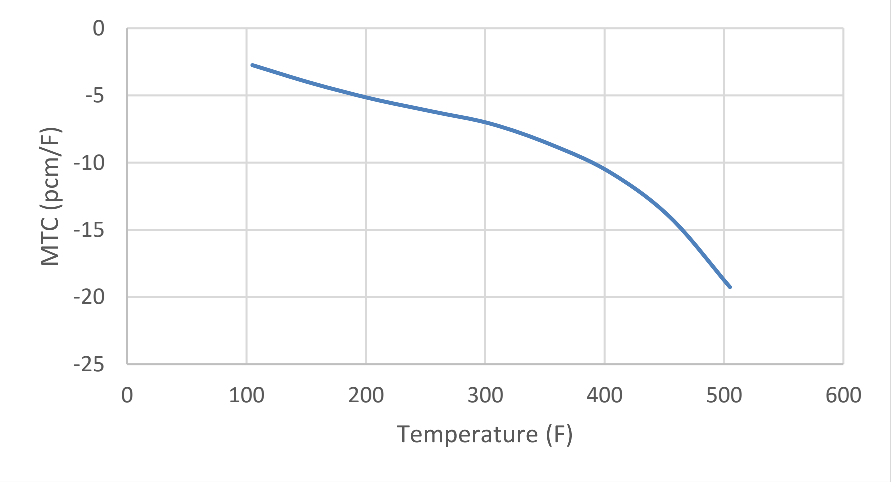

Figure 6-66. Moderator Temperature Coefficient (0 ppm Soluble Boron)

6.3.2.3 REA Results

Presented in Table 6-13, Table 6-14, and Table 6-15 are summaries of the transient criticality scenarios evaluated. The summaries include peak power of criticality transient, total energy released during criticality transient, duration of criticality transient, fuel temperature, moderator temperature, and peaking factors. The reactivity insertion magnitudes are varied between $1.3 and $3.2. Seven different reactivity insertion times are considered ranging from approximately 0.04 to 7 seconds.

Table 6-13 presents the reactivity insertion amount at $1.30 as a function of reactivity insertion time. The results indicate that the slowest insertion time considered (~7 seconds) does not fully complete the transient before all of the reactivity worth has been inserted (i.e., the control rods have not been fully withdrawn during the transient). The highest peak power occurs during the fastest insertion time (2.21E+03 MW), while the largest amount of energy is released during the 73-millisecond insertion time (1.25E+03 MJ). At the beginning of the transient, the core average moderator temperature is 450 K. The maximum average moderator temperature reached during the transient for all insertion times considered is approximately 471 K, indicating an increase of 21 K. It should be noted that the maximum moderator temperature occurs when the transient has reached near pretransient power levels, which is much past the end of the transient (i.e., when the reaction goes subcritical). The maximum/peak water temperature is not provided by S3K, so it is conservatively estimated by multiplying the peaking factor by the maximum average moderator temperature. The water temperatures indicate that only localized boiling may occur during the transient (the saturation temperature for the DPC is 507 K).

The initial/starting transient average fuel temperature is 452 K and the initial peak/maximum fuel temperature is 537 K. Table 6-13 shows that maximum average fuel temperature reached during the transient for all insertion times considered is approximately 514 K, resulting in an increase of 62 K. The maximum/peak fuel temperature is about 708 K for all insertion times considered, indicating an increase of 171 K. These results demonstrate that the fuel remains intact during the transient as the peak temperature is far from the melting temperature (UO_2 melting temperature is about 3,000 K). While not included in the results in Table 6-13, the surface temperature of the fuel rod indicates that the cladding remains intact as the fuel temperature is comparable to the surface temperature of the fuel rod.

As a slight side note, the core inlet and exit temperatures remain unchanged during the transient confirming that the no-flow conditions in the DPC have been captured.

Table 6-13. Summary of Criticality Transient Results—Reactivity Insertion Amount $1.30

Reactivity Insertion Amount $1.30							
Parameter	**Insertion Time (second)**						
	7.3[a]	**1.825**	**0.9125**	**0.4563**	**0.304**	**0.073**	**0.0365**
Peak Power (MW)	9.70E+02	1.98E+03	2.16E+03	2.19E+03	2.18E+03	2.19E+03	2.21E+03
Total Energy (MJ)	6.12E+02	7.91E+03	8.74E+03	8.85E+03	8.85E+03	1.25E+03	5.20E+02
Maximum Fuel Temperature	423.7°C (696.8 K)	434.0°C (707.1 K)	434.8°C (707.9 K)	434.8°C (707.9 K)	434.8°C (707.9 K)	435.0°C (708.1 K)	435.1°C (708.2 K)
Maximum Average Fuel Temperature	238.9°C (512 K)	241.2°C (514.3 K)	241.7°C (514.8 K)	241.8°C (514.9 K)	241.8°C (514.9 K)	241.7°C (514.8 K)	241.7°C (514.8 K)
Maximum Water Temperature	402.0°C (675.1 K)	403.0°C (676.1 K)	403.1°C (676.2 K)	403.1°C (676.2 K)	403.1°C (676.2 K)	398.4°C (671.5 K)	394.1°C (667.2 K)
Maximum Average Water Temperature	198.0°C (471.1 K)	198.7°C (471.8 K)	198.8°C (471.9 K)	198.8°C (471.9 K)	198.8°C (471.9 K)	195.5°C (468.6 K)	192.5°C (465.6 K)
Transient Time (sec)	4.41	3.01	2.81	2.79	2.75	2.73	2.67
Power Peaking Factor	1.433	1.433	1.433	1.433	1.433	1.433	1.433

NOTE: [a] Insertion time too slow for transient; reactivity insertion ~ $1.2.

Table 6-14 presents the reactivity insertion amount at $1.80 as a function of reactivity insertion time. The results indicate that the two slowest insertion times considered (i.e., ~7 seconds and ~1.8 seconds) do not fully complete the transient before all of the reactivity worth has been inserted (i.e., the control rods have not been fully withdrawn during the transient). Consistent with the results in Table 6-13, the highest peak power occurs during the fastest insertion time (2.38E+04 MW), while the largest amount of energy is released during the 73-millisecond insertion time (4.13E+03 MJ). At the beginning of the transient, the core average moderator temperature is 439 K. The maximum average moderator temperature reached during the transient is approximately 473 K, indicating an increase of 34 K. This temperature increase is a little higher than seen in the results in Table 6-13, which can be attributed to the larger reactivity insertion amount. The maximum/peak water temperature shows that localized boiling may occur during the transient.

The initial transient average fuel temperature is 439 K and the initial peak/maximum fuel temperature reached during the transient is 537 K. The maximum average fuel temperature, displayed in Table 6-14, reached during the transient is approximately 553 K, resulting in a maximum temperature increase of 114 K. The maximum/peak fuel temperature is about 965 K, indicating an increase of 428 K. While these fuel temperatures increase are significantly larger than those observed for the $1.30 transients (Table 6-13), the fuel remains intact during the transient as the peak temperature is far from the melting temperature.

The slowest insertion time produces the longest lasting criticality transient (3.24 seconds), while the faster insertion times proved to have transients complete in less than 1 second.

Table 6-14. Summary of Criticality Transient Results—Reactivity Insertion Amount $1.80

Reactivity Insertion Amount $1.80							
Parameter	**Insertion Time (second)**						
	7.3[a]	**1.825**[b]	**0.9125**	**0.4563**	**0.304**	**0.073**	**0.0365**
Peak Power (MW)	1.98E+03	1.10E+04	1.72E+04	2.11E+04	2.33E+04	2.37E+04	2.38E+04
Total Energy (MJ)	1.39E+03	8.17E+03	1.37E+04	1.74E+04	1.92E+04	4.13E+03	2.21E+03
Maximum Fuel Temperature	593.6°C (866.7 K)	641.6°C (914.7 K)	672.0°C (945.1 K)	686.9°C (960 K)	692.1°C (965.2 K)	692.1°C (965.2 K)	691.8°C (964.9 K)
Maximum Average Fuel Temperature	255.6°C (528.7 K)	264.4°C (537.5 K)	271.3°C (544.4 K)	276.7°C (549.8 K)	279.5°C (552.6 K)	280.4°C (553.5 K)	280.3°C (553.4 K)
Maximum Water Temperature	376.2°C (649.3 K)	409.3°C (682.4 K)	393.4°C (666.5 K)	394.6°C (667.7 K)	409.2°C (682.3 K)	411.8°C (684.9 K)	412.4°C (685.5 K)
Maximum Average Water Temperature	175.3°C (448.4 K)	198.2°C (471.3 K)	187.2°C (460.3 K)	188.0°C (461.1 K)	198.1°C (471.2 K)	199.9°C (473 K)	200.3°C (473.4 K)
Transient Time (sec)	3.24	1.72	1.1	0.72	0.61	0.59	0.59
Power Peaking Factor	1.448	1.448	1.448	1.448	1.448	1.448	1.448

NOTE: [a] Insertion time too slow for transient; reactivity insertion ~$1.3.
[b] Insertion time too slow for transient; reactivity insertion ~$1.6.

The results from the highest reactivity insertion amount, $3.20, are presented in Table 6-15 as a function of reactivity insertion time. The majority of the insertion times considered were not sufficiently quick for the transient to fully complete before all of the reactivity worth has been inserted (i.e., the control rods have not been fully withdrawn during the transient). Consistent with previously presented results (Table 6-13 and Table 6-14), the highest peak power occurs during the fastest insertion time (1.74E+05 MW), while the largest amount of energy is released during the 30-millisecond insertion time (6.45E+04 MJ). At the beginning of the transient, the core average moderator temperature is 477 K. The maximum average moderator temperature reached during the transient for all insertion times considered is approximately 512 K, indicating an increase of 35 K. The maximum/peak water temperature shows that not only localized boiling may occur during the transient, but there is also a potential for global boiling to occur.

The initial transient average fuel temperature is 478 K and the initial peak/maximum fuel temperature is 537 K. The maximum average fuel temperature, displayed in Table 6-15, reached during the transient for all insertion times considered is approximately 757 K, resulting in a maximum temperature increase of 220 K. The maximum/peak fuel temperature reached during the transient is about 1,775 K, indicating an increase of 1,238 K. While these fuel temperature increases are significantly larger than those observed for previous transients (Table 6-13 and Table 6-14), the fuel continues to remain intact during this higher reactivity transient as the peak temperature is far from the melting temperature.

Table 6-15. Summary of Criticality Transient Results—Reactivity Insertion Amount $3.20

Reactivity Insertion Amount $3.20							
Parameter	**Insertion Time (second)**						
	7.3[a]	**1.825[b]**	**0.9125[c]**	**0.4563[d]**	**0.304[e]**	**0.073**	**0.0365**
Peak Power (MW)	5.80E+03	3.20E+04	7.58E+04	1.12E+05	1.31E+05	1.74E+05	1.74E+05
Total Energy (MJ)	4.99E+03	2.61E+04	4.33E+04	5.86E+04	6.45E+04	1.59E+04	8.08E+03
Maximum Fuel Temperature	968.8°C (1,241.9 K)	1,089.8°C (1,362.9 K)	1,209.5°C (1,482.6 K)	1,339.9°C (1,613 K)	1,417.4°C (1,690.5 K)	1,502.2°C (1,775.3 K)	1,500.9°C (1,774 K)
Maximum Average Fuel Temperature	317.5°C (590.6 K)	344.5°C (617.6 K)	369.4°C (642.5 K)	417.4°C (690.5 K)	437.6°C (710.7 K)	484.7°C (757.8 K)	484.6°C (757.7 K)
Maximum Water Temperature	459.1°C (732.2 K)	468.0°C (741.1 K)	468.8°C (741.9 K)	474.8°C (747.9 K)	478.0°C (751.1 K)	473.7°C (746.8 K)	474.5°C (747.6 K)
Maximum Average Water Temperature	226.0°C (499.1 K)	232.1°C (505.2 K)	232.6°C (505.7 K)	236.7°C (509.8 K)	238.9°C (512 K)	236.0°C (509.1 K)	236.5°C (509.6 K)
Transient Time (sec)	1.6	0.91	0.11	0.08	0.07	0.06	0.06
Power Peaking Factor	1.467	1.467	1.467	1.467	1.467	1.467	1.467

NOTE: [a] Insertion time too slow for transient; reactivity insertion ~$1.5.

[b] Insertion time too slow for transient; reactivity insertion ~$2.0.

[c] Insertion time too slow for transient; reactivity insertion ~$2.6.

[d] Insertion time too slow for transient; reactivity insertion ~$2.7.

[e] Insertion time too slow for transient; reactivity insertion ~$2.9.

It can also be seen that the transient duration is shorter than previous results have indicated for all insertion times. The slowest insertion time still produces the longest lasting criticality transient (1.6 seconds), while the faster insertion times have very short transient completion times of about 0.06 seconds.

Figure 6-67 compares the transient peak power between the three different reactivity insertions for the fastest reactivity insertion rate considered (~0.04 seconds). In the figure, the highest reactivity insertion worth reaches the highest power. Its peak is the tallest and its width the smallest compared to the other reactivity insertions presented. Furthermore, the highest reactivity insertion transient begins to decrease at a faster rate in power after the completion of the peak transient (i.e., once k_{eff} reaches ~0.999). Additionally, all three transients reach pretransient power levels (which is about 5 W) after approximately 1,000 seconds, as shown in Figure 6-68.

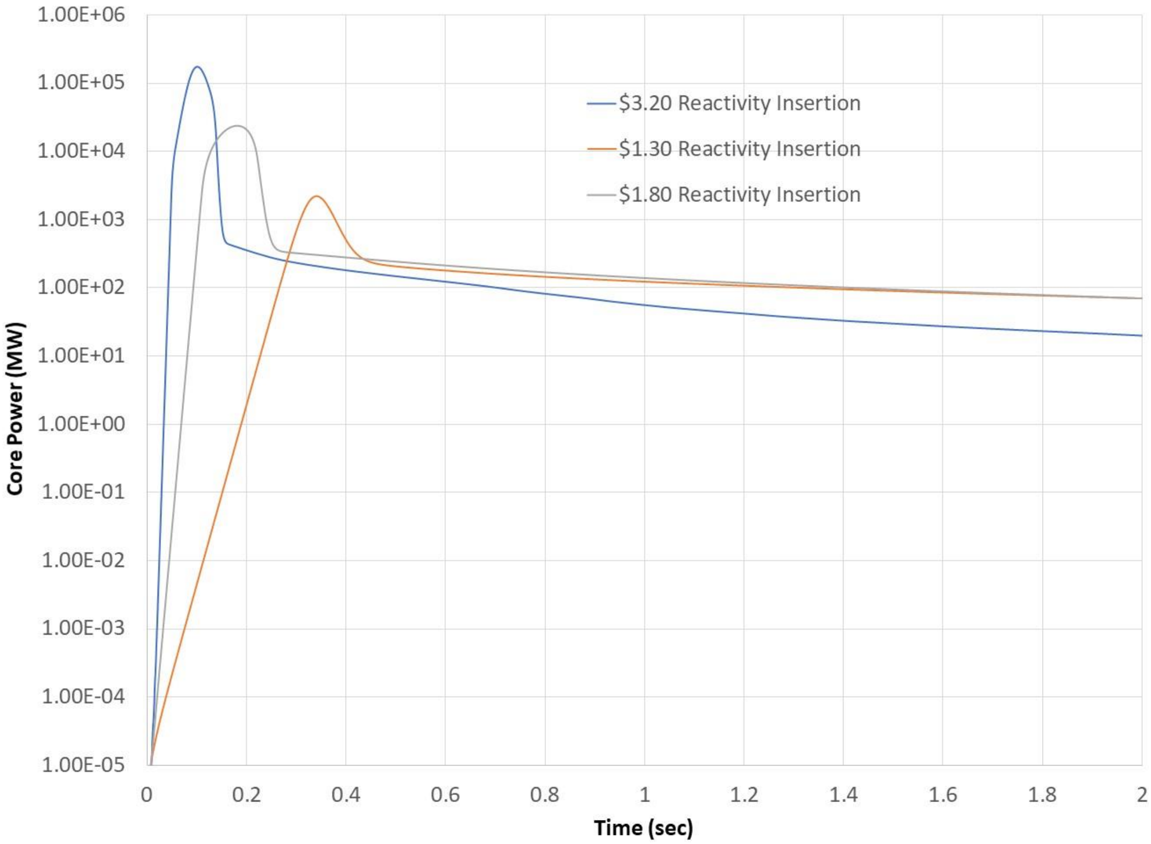

NOTE: Reactivity Insertion Rate ~0.4 seconds.

Figure 6-67. Transient Power versus Time

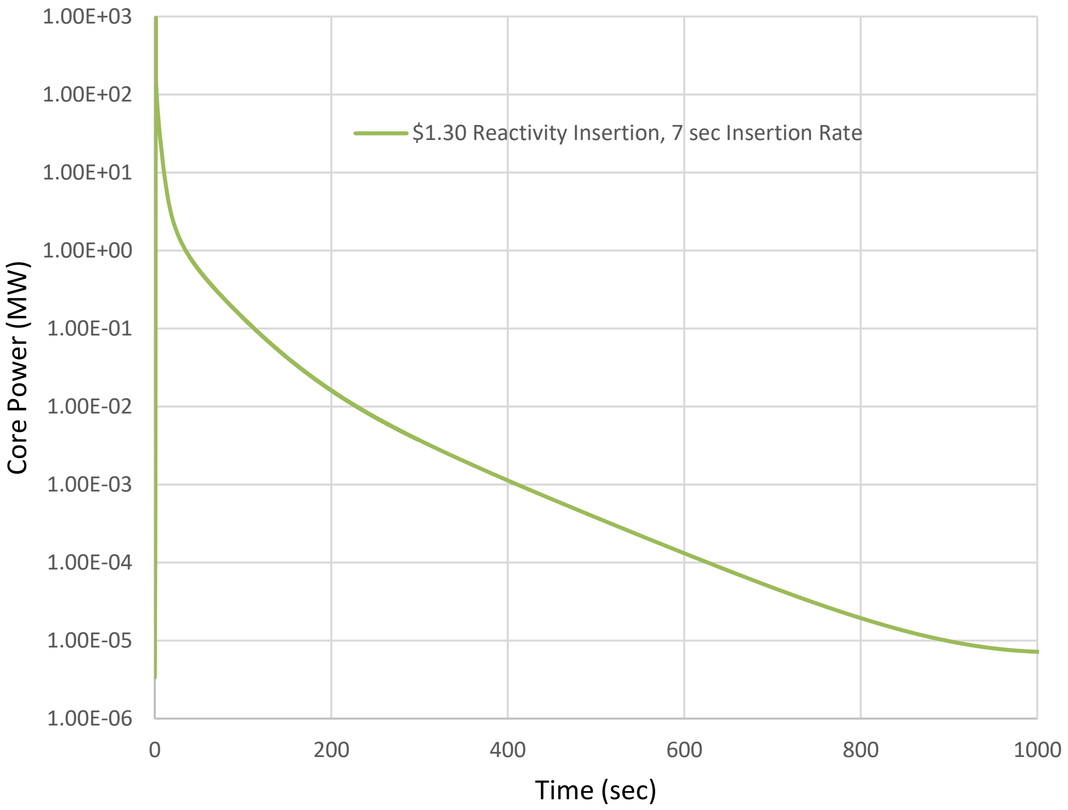

Figure 6-68. Transient Power versus Time—Full Transients

Figure 6-69 represents the average moderator temperature for the $1.80 transient as a function of time. As seen in the figure, the maximum temperature is reached towards the very end of the transient, as opposed to during the peak power.

Figure 6-70 compares the average and maximum fuel temperature during the transient for the $1.80 reactivity worth (~0.04-second reactivity insertion rate). Both the average and peak fuel temperatures reach their highest value after the time of the peak power (Figure 6-67). Included in Figure 6-70 are the inlet and exit temperatures, both of which remain constant throughout the entire transient, indicating that there is no flow/movement throughout the DPC model.

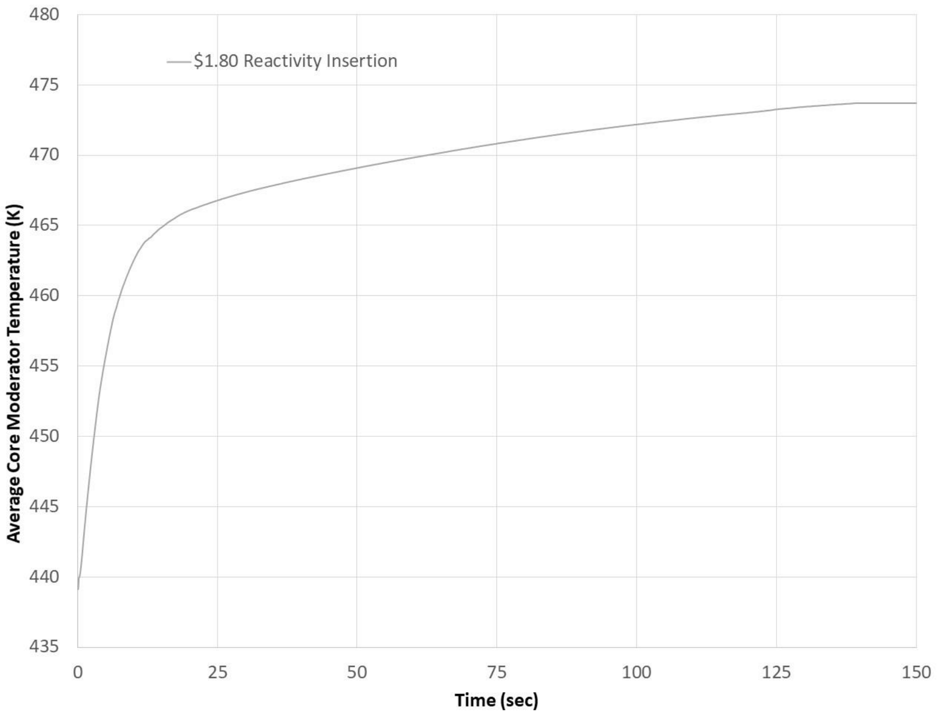

NOTE: Reactivity Insertion Time ~0.04 seconds.

Figure 6-69. Transient Moderator Temperature versus Time

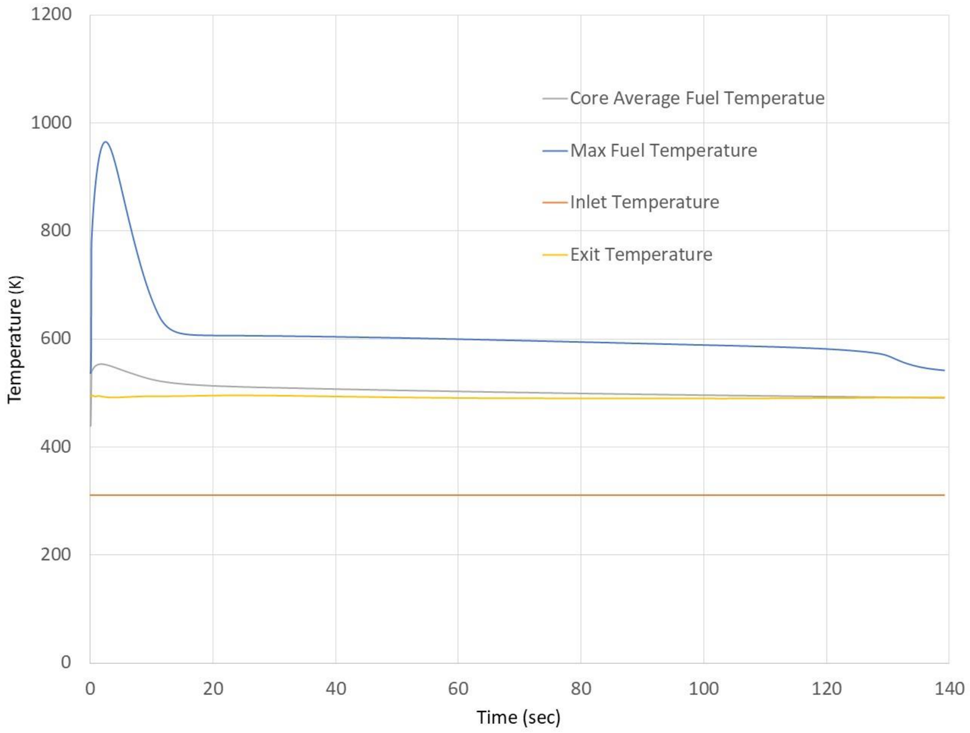

NOTE: $1.80 Reactivity Insertion, ~0.04-Second Reactivity Insertion Rate

Figure 6-70. Fuel Temperature versus Time

6.3.3 Conclusions

The following conclusions can be gleaned based on criticality transients simulating reactivity insertions up to $3.20 in the DPC using the reactor core transient analysis code S3K.

- **Fuel Temperature**—The maximum/peak fuel temperature observed was 1,775 K at a reactivity insertion of $3.20 (Table 6-6). This value is well below the melting temperature of UO_2 fuel of approximately 3,000 K. Therefore, it can be concluded that the fuel will remain intact in the DPC in the event of a potential criticality transient accident.

  Further studies are recommended at higher reactivity insertion values as the DPC (with 37 PWR SNF assemblies) has a k_{eff} ~1.1, indicating that there is more excess reactivity for higher insertion magnitudes. Additionally, a PWR model to evaluate more transient behaviors based on boron dilution phenomena is recommended, as a second modeling approach to qualify the produced results presented herein. Furthermore, the development of a BWR model is recommended to investigate criticality transient behaviors in a low reactivity environment.

- **Moderator Temperature**—The observed average moderator temperatures are slightly below the boiling point while the estimated maximum/localized moderator temperatures are above the boiling point. This observation indicates that there is a potential for localized boiling in the DPC during a criticality transient.

The criticality transients starting/initial moderator temperatures are conservatively higher than what is representative of the DPC. It is recommended that the moderator temperature be reduced in future criticality transient studies to evaluate if localized boiling is actually likely to occur. In addition, two-phase considerations for moderator feedback could be evaluated.

- **Peak Power**—The highest peak power was consistently noted for the fastest insertion rates. The highest noticed peak power is 1.7E+05 MW (Table 6-6, $3.20 reactivity insertion).

  The S3K code is limited to an insertion rate of 0.0365 seconds. Further studies may be warranted at higher reactivity insertion values at the limiting insertion rate.

- **Total Energy Released**—The maximum total energy released observed is 6.45E+04 MJ, which occurred at $3.20 reactivity insertion and at 0.3-second insertion time.
- **Feedback Mechanisms**—This study indicates that moderator and fuel temperature reactivity feedback is dominant during the criticality transient.

  Further refinement of the existing models would allow evaluating reactivity insertion magnitudes and rates, localized reactivity insertions, heat transfer, refined doppler feedback based on fuel temperature profile (mainly for rapid transients).

- **Peaking Factors**—This study shows that there is significant power peaking in the DPC due to the loading patten of the PWR SNF.

  It is recommended, as future work, to survey DPCs to determine peaking factors based on as-loaded conditions. These peaking factors could be important for selecting bounding DPCs for which there could be high disparity in power and heat generation profiles. This issue is important for both steady-state and transient criticality.

Additional recommended future studies include the following:

- **Decay Time**—SIMULATE/S3K is limited in the length of cooling/decay time, changing the fuel composition through isotopic manipulation to more accurately represent fuel composition/isotopic concentrations at 9,000 + years decay time. This could be bounded by evaluating (1) only uranium isotopes presence (^{235}U) and zero out plutonium (^{239}Pu) influence, and (2) only plutonium (^{239}Pu).
- **Generation of Cross-Section Library for Various DPC Models/Content**—This study will allow the investigation of the impact of reactor depletion considerations on transient characteristics. DPCs would be selected based on integral burnable absorbers and/or burnable poison rods design/content to ensure a wide variety of reactor depletion histories.
- **Potential Spectrum Hardening due to Nonpure Water**—Evaluate potential hardening of the spectrum by considering nonpure water, which could become contaminated through dissolved particulates over time in the DPC. This phenomenon would be evaluated for both steady-state and transient criticality behavior. This consideration may also be important because it may result in an initial positive MTC; similar to that of a PWR reactor at the beginning of cycle due to the high soluble boron concentration.

This page is intentionally left blank.

7. FURTHER WORK

The analyses described above represent the first time some of the FEPs associated with postclosure criticality events were incorporated into PA models, facilitating a comparison of the dose to a member of the public when an in-package postclosure criticality event occurs to the dose to a member of the public when no postclosure criticality event occurs. Further work is needed to address questions that arose while these analyses were being performed and to advance this effort. This further work can be categorized as being focused on neutronics; identifying additional FEPs that should be included in the model of postclosure criticality events and incorporating their effects into appropriate codes to include those FEPs; and examining repository-wide sensitivities and variabilities (e.g., spatial and temporal variability in criticality occurrence):

- **Advance neutronics-based work**
  - Improve and finalize the methodology for coupling neutronics calculations and repository-scale calculations with respect to the "steady-state" power, the length of the criticality event, and the associated inventory changes
  - Survey DPCs to determine peaking factors based on as-loaded conditions
  - Estimate powers for each DPC currently characterized in the UNF-ST&DARDS database
  - Continue RELAP model verification
  - Leverage the two-phase capabilities of RELAP to explore more reactive DPCs
  - Generate cross-section library for various DPCs
  - Develop a BWR model
  - Evaluate reactivity at a variety of times greater than 9,000 years
  - Evaluate reactivity with water more representative of repository conditions (i.e., not pure)

- **Identify additional FEPs to include in the model of postclosure criticality events and incorporate their effects into appropriate codes**
  - Steady-state criticality events
    - Include more radionuclides in the radionuclide transport and dose calculations
    - Enable temperature-dependent mineral alteration in the host rock (i.e., not just the backfill) with accompanying changes in transport properties (e.g., sorption coefficients)
    - Enable temperature-dependent radionuclide solubilities
    - Examine extent of reactivity reduction associated with nonuniform pin-pitch reduction due to corrosion of grid spacers
    - Examine effects on backfill and host rock (e.g., fracturing) of gas generation from radiolysis, from higher corrosion rates, and from gaseous fission products
    - Examine thermal fatigue of waste package materials resulting from intermittent criticality
    - Examine effects of criticality in one waste package on adjacent waste packages
    - Examine thermally induced stress changes in backfill
    - Examine potential for fully degraded in-package configuration to lead to permanent criticality termination

    - Examine the role of subcritical heating as criticality is approached
    - Examine consequences of bentonite sealing a canister crack
  - Transient criticality events
    - Calculate damage to fuel, engineered barriers, and natural barriers from rapid energy production.
    - Further refine transient neutronics calculations
    - Examine the role of subcritical heating as criticality is approached
    - Examine thermal fatigue of materials resulting from intermittent criticality
    - Examine effects of criticality in one waste package on adjacent waste packages

- **Investigate repository-wide sensitivities and variabilities**
  - Vary how many waste packages experience criticality events, when they experience criticality events, and their location in the repository
  - Examine effects of varying hydrostatic head
  - Increase the model domain lower boundary to see if the nonuniform heat distribution is an artifact of the size of the domain

8. SUMMARY AND CONCLUSIONS

A study has been initiated to examine the potential consequences, with respect to long-term repository performance, of criticality events that might occur during the postclosure period in a hypothetical repository containing DPCs. The first phase (a scoping phase) consisted of developing an approach to creating the modeling tools and techniques that may eventually be needed to either include or exclude criticality from a PA as appropriate; this scoping phase is documented in Price et al. (2019a). In the second phase, that modeling approach was implemented and future work was identified, as documented in Price et al. (2019b). This report gives the results of a repository-scale PA examining the potential consequences of postclosure criticality events, as well as the information, modeling tools, and techniques needed to incorporate the effects of postclosure criticality events in the PA.

A set of FEPs was evaluated to identify those that could affect the probability and consequences of in-package postclosure criticality as well as FEPs that could be affected by postclosure criticality, or both. (Alsaed and Price 2020). FEPs that are relevant to repository performance in the absence of a postclosure criticality event, as well as FEPs that are relevant to repository performance with the occurrence both of a steady-state, postclosure, criticality event and a transient postclosure criticality event were discussed.

As described in Section 3, a model of a hypothetical saturated repository in shale was created in PFLOTRAN, the software used to model repository performance. The hypothetical repository contained 4,200 waste packages containing SNF from a PWR, all with the same inventory. In the model, the waste packages are emplaced in long tunnels and surrounded by bentonite backfill, a low permeability material designed to delay water movement and radionuclide transport. PFLOTRAN was modified to include both the temperature dependence of thermal conductivity and the anisotropic behavior of thermal conductivity. A well that provides 2 liters per day of drinking water to a member of the public is placed 5 km downstream from the repository.

The PFLOTRAN model developed for the hypothetical shale repository was modified to account for the occurrence of a postclosure steady state criticality. The first modification was to simulate the occurrence of a steady-state criticality event in a DPC disposed of in a repository. This required a loose coupling between neutronics, in-canister TH processes, and rates of conductive heat transfer through the backfill and repository host rock. Another modification was to create and implement a model for the time- and temperature-dependent transformation of smectite to illite and the subsequent change in permeability. In addition, an anisotropic and temperature-dependent model of thermal conductivity was developed and implemented in PFLOTRAN. Finally, a grid spacer vitality model was developed and implemented to simulate the time- and temperature-dependent general corrosion of the grid spacers, the collapse of which would lead to permanent termination of criticality. This model was not used in the simulations described here; rather, it was assumed that the criticality event lasted 10,000 years. The study team will implement this model after developing a tighter coupling between neutronics, TH processes, the length of time of a criticality event lasts, and the subsequent changes in radionuclide inventory. Finally, the radionuclides that might need to be included in radionuclide transport calculations and in dose calculations were identified, although only a subset of those was included in the results presented in Section 5.

For the hypothetical, saturated, shale repository, the PFLOTRAN model described above was implemented for both a repository that remained subcritical and a repository that experienced steady-state criticality events. Transport of several radionuclides was modeled and ^{129}I was the only radionuclide that reached the well used by a member of the public in 1,000,000 years. A comparison of the doses received by a member of the public from ^{129}I shows very little difference between the doses, less than 1%. Thus, in this hypothetical repository system and given the FEPs included in the simulation, the occurrence of a

10,000-year-long, steady-state criticality event does not affect repository performance. Transport calculations for ^{237}Np indicate that this radionuclide remains in the vicinity of the repository over 1,000,000 years and cannot result in a dose to a member of the public. Further, transport of two short-lived fission products produced by the steady-state criticality event (^{90}Sr and ^{137}Cs) does not result in a dose to the member of the public because the products decay before reaching the sand aquifer that is the source of water for the member of the public.

For the hypothetical, unsaturated, alluvial repository, the initial PFLOTRAN model development and implementation indicated the need for improvements before the model could be used to calculate dose to a member of the public for the hypothetical unsaturated alluvial repository with and without the occurrence of a steady-state criticality event. These model improvements were only recently completed. Nevertheless, some conclusions can be drawn from the simulations run thus far. First, the power that can be generated by a steady-state criticality event is limited by the infiltration rate: higher infiltration rates allow for the criticality event to generate more power. Second, at the reference infiltration rate (2 mm/yr), the power that can be generated is between 50 W and 200 W; even at an infiltration rate associated with pluvial conditions (10 mm/yr), the power that can be generated is between 300 W and 400 W.

Progress was made on modeling the transient criticality and its effects on repository performance. For the hypothetical unsaturated repository, a model of the canister under repository-relevant conditions was created and a series of steady-state criticality calculation was run in MCNP to characterize multiple reactivity feedback mechanisms and derive feedback coefficients. These feedback coefficients were then used in the kinetics analysis using RAZORBACK to characterize the expected transient pulse. Multiple simulations were run, each with a different reactivity and insertion time. For each simulation, peak power, total integrated energy, maximum fuel temperature, average fuel temperature, maximum coolant temperature, average coolant temperature, time of peak power, and actual reactivity insertion were calculated. Results indicate that, based on catastrophic failure of the B_4C basket plates, rapid releases of energy on the order of 10^8–10^9 J are possible; future work will refine the kinetics calculations and examine the mechanical consequences of rapid releases of energy of this magnitude with a solid mechanics study. For the hypothetical saturated repository, the transient criticality event was simulated assuming a REA and using the S3K code, a proprietary code that performs transient analysis of the core of commercial PWRs and BWRs. As for the unsaturated hypothetical repository, multiple simulations were conducted, each with a different reactivity and insertion time; for each simulation peak power, total energy, maximum fuel temperature, maximum average fuel temperature, maximum water temperature, maximum average water temperature, transient time, radial peaking factor, and axial peaking factor were calculated. Results indicate that rapid releases of energy on the order of 10^8–10^{11} J are possible and that water could boil, but that temperatures remain well below the melting temperature of UO_2.

Further work has been identified, categorized as being focused on neutronics; identifying additional FEPs to include in the model of postclosure criticality and incorporating their effects into appropriate codes; and examining repository-wide sensitivities and variabilities.

9. REFERENCES

10 CFR 63. *Disposal of High-Level Radioactive Wastes in a Geologic Repository at Yucca Mountain, Nevada.*

10 CFR 71. *Packaging and Transportation of Radioactive Material*.

10 CFR 72. *Licensing Requirements for the Independent Storage of Spent Nuclear Fuel, High-level Radioactive Waste, and Reactor-related Greater than Class C Waste*.

40 CFR 197. *Public Health and Environmental Radiation Protection Standards for Yucca Mountain, Nevada.*

73 FR 61256. *Public Health and Environmental Radiation Protection Standards for Yucca Mountain, Nevada.*

Alsaed, A.A. and L.L. Price. 2020. *Features, Events, and Processes Relevant to DPC Criticality Analysis*. SAND2020-9165. Albuquerque, NM: Sandia National Laboratories.

Banerjee, K. 2021. "Zion TSC-37 k_{eff} values," email message to A. Alsaed, February 10, 2021.

Bell, I.H., J. Wronski, S. Quoilin, and V. Lemort. 2014. Pure and Pseudo-pure Fluid Thermophysical Property Evaluation and the Open-Source Thermophysical Property Library CoolProp. *Industrial & Engineering Chemistry Research* 53 (6): 2498–2508. doi: 10.1021/ie4033999.

Birch, A.F. and H. Clark. 1940. The thermal conductivity of rocks and its dependence upon temperature and composition. *American Journal of Science* 238 (8), 529–558.

Blesch, C.J., F.A. Kulacki, and R.N. Christensen. 1983. *Application of integral methods to prediction of heat transfer from a nuclear waste repository*. No. ONWI-495. Columbus, OH: Ohio State Univ. Research Foundation.

BNL (Brookhaven National Laboratory). n.d. *National Nuclear Data Center (NNDC)*. www.nndc.bnl.gov.

Brady, P.V. and B.D. Hanson. 2020. *An Updated Analysis of Clad Degradation*. SAND2020-13018R. Albuquerque, NM: Sandia National Laboratories.

Briggs, J.B., L. Scott, and A. Nouri. 2003. The International Criticality Safety Benchmark Evaluation Project. *Nucl. Sci. Eng.* 145 (1): 1–10.

Cheng, P., and C.T. Hsu. 1999. The effective stagnant thermal conductivity of porous media with periodic structures. *Journal of Porous Media 2* (1): 19–38. doi: 10.1615/JPorMedia.v2.i1.20.

Clarity, J.B., K. Banerjee, H.K. Liljenfeldt, and W.J. Marshall. 2017. As-Loaded Criticality Margin Assessment of Dual-Purpose Canisters Using UNF-ST&DARDS. *Nuclear Technology* 199:245–275. https://doi.org/10.1080/00295450.2017.1361250.

Croff, A.G. 1983. ORIGEN2: A Versatile Computer Code for Calculating the Nuclide Compositions and Characteristics of Nuclear Materials. *Nuclear Technology* 62 (3): 335–352. doi: dx.doi.org/10.13182/NT83-1.

Cuadros, J., and J. Linares. 1996. Experimental kinetic study of the smectite-to-illite transformation. *Geochimica et Cosmochimica Acta* 60 (3): 439–453.

Cullen, D.E. and C.R. Weisbin. 1976. Exact Doppler Broadening of Tabulated Cross Sections. *Nucl. Sci. Eng.* 60 (3): 199–229.

DOE (US Department of Energy). 2003. *Disposal Criticality Analysis Methodology Topical Report*. YMP/TR-004Q, Revision 2, Las Vegas, NV: Office of Civilian Radioactive Waste Management.

DOE. 2008a. *Yucca Mountain Repository License Application*. DOE/RW-0573, Rev. 0. Las Vegas, NV: US Department of Energy, Office of Civilian Radioactive Waste Management.

DOE. 2008b. *Yucca Mountain Repository License Application*. DOE/RW-0573, Rev. 1. Las Vegas, NV: US Department of Energy, Office of Civilian Radioactive Waste Management.

DOE. 2008c. *Features, Events, and Processes for the Total System Performance Assessment: Analyses.* ANL-WIS-MD-000027 REV 00. Las Vegas, Nevada: Office of Civilian Radioactive Waste Management.

DOE. 2010. *Total System Performance Assessment Model/Analysis for the License Application*. MDL-WIS-000005 REV01. Las Vegas, NM: Office of Civilian Radioactive Waste Management.

Dulla, S., E.H. Mund, and P. Ravetto. 2008. The quasi-static method revisited. *Progress in Nuclear Energy* 50 (8): 908–920. doi: 10.1016/j.pnucene.2008.04.009.

EPRI (Electric Power Research Institute). 2002. *Three-Dimensional Rod Ejection Accident Peak Fuel Enthalpy Analysis Methodology.* Technical Report 1003385. Palo Alto, CA: Electric Power Research Institute.

Evans, T.M., A.S. Stafford, R. Slaybaugh, and K.T. Clarno. 2010. Denovo: A New Three-Dimensional Parallel Discrete Ordinates Code in SCALE. *Nuclear Technology* 171 (2): 171–200. doi: 10.13182/NT171-171.

Flynn, D.R., and T.W. Watson. 1969. *Measurements of the Thermal Conductivity of Soils to High Temperatures.* Final Report No. SC-CR-69-3059. Washington, DC: National Bureau of Standards.

Freeze, G., P. Mariner, J. Blink, F. Caporuscio, J. Houseworth, and J. Cunnane. 2011. *Disposal System Features, Events, and Processes (FEPs): FY11 Progress Report*. FCRD-USED-2011-000254, SAND2011-6059P, Albuquerque, NM: Sandia National Laboratories.

Gauld, I.C. 2011. *ORIGEN: Depletion Module to Calculate Neutron Activation, Actinide Transmutation, Fission Product Generation, and Radiation Source Terms.* Oak Ridge, TN: Oak Ridge National Laboratory.

Gómez Romera, J.J., C.F. Cohen, Vitalij, A. Spontarelli, C. Brachem. 2021. IAPWS Version 1.5.2. Released May 9, 2021. Accessed June 28, 2021. http://doi.org/10.5281/zenodo.4744318.

Grandi, G.M., K.S. Smith, J.D. Rhodes, III. 2011. *SIMULATE-3K Models and Methodology*. SSP9813r7. Studsvik Scandpower, Inc. (proprietary document).

Hammond, G.E., and P.C. Lichtner, and R.T. Mills. 2014. Evaluating the performance of parallel subsurface simulators: An illustrative example with PFLOTRAN. *Water Resources Research* 50:208–228. doi: 10.1002/2012WR013483.

Hands, B.A. and V.D. Arp. 1981. A correlation of thermal conductivity data for helium. *Cryogenics* 21 (12): 697–703. doi: 10.1016/0011-2275(81)90211-3.

Hardin, E. and E. Kalinina. 2016. *Cost Estimation Inputs for Spent Nuclear Fuel Geologic Disposal Concepts*. SAND2016-0235. Albuquerque, NM: Sandia National Laboratories.

Hardin, E., L. Price, E. Kalinina, T. Hadgu, A. Ilgen, C. Bryan, J. Scaglione, K. Banerjee, J. Clarity, R. Jubin, V. Sobes, R. Howard, J. Carter, T. Severynse, and F. Perry. 2015. *Summary of Investigations on Technical Feasibility of Direct Disposal of Dual-Purpose Canisters*. FCRD-UFD-2015-000129, Rev. 0; SAND2015-8712R. Albuquerque, NM: Sandia National Laboratories. doi: 10.2172/1504860.

Hetrick, D.L. 1993. *Dynamics of Nuclear Reactors*. La Grange, IL: American Nuclear Society.

Hou, J., Ivanov, K.N., Boyarinov, V.F., and P.A. Fomichenko. 2017. OECD/NEA benchmark for time-dependent neutron transport calculations without spatial homogenization. *Nuclear Engineering and Design* 317:177–189. https://doi.org/10.1016/j.nucengdes.2017.02.008.

Huang, W.L., J.M. Longo, and D.R. Pevear. 1993. An experimentally derived kinetic model for smectite-to-illite conversion and its use as a geothermometer. *Clays and Clay Minerals* 41 (2): 162–177.

Humphries, L.L., V.G. Figueroa, M.F. Young, D. Louie, and J.T. Reynolds. 2015. *MELCOR Computer Code Manuals*. SAND2015-6692R. Albuquerque, NM: Sandia National Laboratories. https://doi.org/10.2172/1433918.

IAEA (International Atomic Energy Agency). 2003. *“Reference Biospheres” for solid radioactive waste disposal: Report of BIOMASS Theme 1 of the BIOsphere Modelling and ASSessment (BIOMASS) Programme*. IAEA-BIOMASSS-6. Vienna, Austria: International Atomic Energy Agency.

ICRP (International Commission on Radiological Protection) 2012. *Compendium of Dose Coefficients Based on ICRP Publication 60*. ICRP Publication 119. Ann. ICRP 41 Suppl.

Jo, Y., B. Cho, and N.Z. Cho. 2016. Nuclear Reactor Transient Analysis by Continuous-Energy Monte Carlo Calculation Based on Predictor-Corrector Quasi-Static Method. *Nuclear Science and Engineering* 183 (2): 229–246. doi: https://doi.org/10.13182/NSE15-100.

Karnland, O., and M. Birgersson. 2006. *Montmorillonite stability: With special respect to KBS-3 conditions*. TR-06-11. Stockholm, Sweden: Svensk Kärnbränslehantering AB (Swedish Nuclear Fuel and Waste Management Co).

Kochunas, B., B. Collins, D. Jabaay, T.J. Downar, and W.R. Martin. 2013. Overview of Development and Design of MPACT: Michigan Parallel Characteristics Transport Code. In *Proceedings of the 2013 International Conference on Mathematics and Computational Methods Applied to Nuclear Science and Engineering – M&C 2013*. Sun Valley, ID: American Nuclear Society.

Kuhlman, K., M. Mills, R. Jayne, E. Matteo, C. Herrick, M. Nemer, J. Heath, Y. Xiong, C. Choens, P. Stauffer, H. Boukhalfa, E. Guiltinan, T. Rahn, D. Weaver, B. Dozier, S. Otto, J. Rutqvist, Y. Wu, M. Hu, S. Uhlemann, J. Wang. 2020. *FY20 Update on Brine Availability Test in Salt.* M2SF-20SN010303032; SAND2020-9034R. Albuquerque, NM: Sandia National Laboratories.

Lichtner, P.C., G.E. Hammond, C. Lu, S. Karra, G. Bisht, B. Andre, R.T. Mills, J. Kumar, and J.M. Frederick. 2020a. *PFLOTRAN User Manual.* http://documentation.plotran.org.

Lichtner, P.C., G.E. Hammond, C. Lu, S. Karra, G. Bisht, B. Andre, R.T. Mills, J. Kumar, and J.M. Frederick. 2020b. *PFLOTRAN Webpage*. http://www.pflotran.org.

Mariner, P.E., E.R. Stein, J.M Frederick, S.D. Sevougian, and G.E. Hammond. 2017. *Advances in Geologic Disposal System Modeling and Shale Reference Case*. SFWD-SFWST-2017-000044; SAND2017-10304R. Albuquerque, NM: Sandia National Laboratories.

Mariner, P.E., E.R. Stein, J.M. Frederick, S.D. Sevougian, G.E. Hammond, and D.G. Fascitelli. 2016. *Advances in Geologic Disposal System Modeling and Application to Crystalline Rock.* FCRD-UFD-2016-000440; SAND2016-9610R. Albuquerque, NM: Sandia National Laboratories.

Mariner, P.E., E.R. Stein, S.D. Sevougian, L.J. Cunningham, J.M Frederick, G.E. Hammond, T.S. Lowry, S. Jordan, and E. Basurto. 2018. *Advances in Geologic Disposal Safety Assessment and an Unsaturated Alluvium Reference Case*. SFWD-SFWST-2018-000509; SAND2018-11858R. Albuquerque, NM: Sandia National Laboratories.

Martin, W. 2012. *Implementation of On-the-Fly Doppler Broadening in MCNP5 for Multiphysics Simulation of Nuclear Reactors*. Final Report for Project 10-897 DE-AC07-05ID14517. Ann Arbor, MI: Battelle Energy Alliance, LLC.

Munro, R.G. 2002. *Elastic Moduli Data for Polycrystalline Ceramics*. NISTIR 6853. Gaithersburg, MD: National Institute of Standards and Technology.

NAC International. 2010. *MAGNASTOR Final Safety Analysis Report*. Docket No. 72-1031, Revision 10B. Norcross, GA: NAC International.

NEA Working Group on Fuel Safety. 2016. *Reactivity-Initiated Accident Fuel-Code Benchmark—Phase II Volume 2: Task No. 1 Specifications*. NEA/CSNI/R(2016)6/VOL2. Paris, France: OECD Nuclear Energy Agency.

Nole, M., R.C. Leone, H.D. Park, M. Paul, A. Salazar, G.E. Hammond, and P.C. Lichtner. 2021. *PFLOTRAN Development FY2021*. M3SF-21SN010304072; SAND2021-8709R. Albuquerque, NM: Sandia National Laboratories.

Nuclear Waste Policy Act of 1982. 42 U.S.C. 10101 et seq.

Ortiz-Vega, D.O. 2013. A new wide range equation of state for helium-4. PhD dissertation, Texas A&M University.

Ott, K.O. and R. J. Neuhold. 1985. *Introductory Nuclear Reactor Dynamics*. La Grange Park, IL: American Nuclear Society.

Painter, S.L. 2011. Three-phase numerical model of water migration in partially frozen geological media: model formulation, validation, and applications. *Computational Geosciences* 15 (1): 69–85.

Pandya, T.M., S.R. Johnson, T.M. Evans, G.G. Davidson, S.P. Hamilton, and A.T. Godfrey. 2016. Implementation, Capabilities, and Benchmarking of Shift, a Massively Parallel Monte Carlo Radiation Transport Code. *Journal of Computational Physics* 308:239–272.

Powers, J.M. 2004. On the necessity of positive semi-definite conductivity and Onsager reciprocity in modeling heat conduction in anisotropic media. *J. Heat Transfer* 126 (5): 670–675.

Price, L.L., A.A. Alsaed, P.V. Brady, M.B. Gross, E.L Hardin, M. Nole, J.L. Prouty, K. Banerjee, and G.G. Davidson. 2019a. *Postclosure Criticality Consequence Analysis – Scoping Phase.* M3SF-19SN010305061; SAND2019-4644R. Albuquerque, NM: Sandia National Laboratories.

Price, L.L., A.A. Alsaed, A. Barela, P.V. Brady, F. Gelbard, M.B. Gross, M. Nole, J.L. Prouty, K. Banerjee, S. Bhatt, G. G. Davidson, Z. Fang, R. Howard, S.R. Johnson, S.L. Painter, M. Swinney, E. Gonzalez. 2019b. *Preliminary Analysis of Postclosure DPC Criticality Consequences*. M2SF-20SN010305061; SAND2020-4106. Albuquerque, NM: Sandia National Laboratories.

Salazar, A. 2018. Criticality in the Far-Field of a Granitic Repository for Used Nuclear Fuel. PhD dissertation, University of California Berkeley.

Saltzstein, S.J., K.B. Sorenson, B.D. Hanson, R.W. Shimskey, N.A. Klymyshyn, R.A. Webster, P.J. Jensen, P.J. MacFarlan, M. Billone, J. Scaglione, R. Montgomery, and B. Bevard. 2017. *EPRI/DOE High-Burnup Fuel Sister Rod Test Plan Simplification and Visualization*. SAND-2017-10310R. Albuquerque, NM: Sandia National Laboratories.

Sanders, C.E. 2021. *Independent Study to Evaluate Criticality Transients in a DPC Using SIMULATE-3K.* CS-UNLV-2021. Las Vegas, NV: University of Nevada, Las Vegas.

Sevougian, S.D., E.R. Stein, T. LaForce, F.V. Perry, T.S. Lowry, L. Cunningham, M. Nole, C.B. Haukwa, K.W. Chang, and P.E. Mariner. 2019. *GDSA Repository Systems Analysis Progress Report*. M2SF-19SNO10304051; SAND2019-5189R. Albuquerque, NM: Sandia National Laboratories.

Shen, Q., Y. Wang, D. Jabaay, B. Kochunas, and T. Downar. 2018. Transient analysis of C5G7-TD benchmark with MPACT. *Annals of Nuclear Energy* 125:107–120.

Somerton, W.H., J.A. Keese, and S.L. Chu. 1974. Thermal behavior of unconsolidated oil sands. *Society of Petroleum Engineers Journal* 14 (05): 513–521.

Spriggs, G., J. Campbell, and V. Piksaikin. 1998. *An eight-group delayed neutron model based on a consistent set of half-lives*. LA-UR-98-1619. Los Alamos, NM: Los Alamos National Laboratory.

Studsvik AB. n.d. SIMULATE-3K. *Studsvik.* https://www.studsvik.com/what-we-do/products/simulate3-k/.

Talley, D.G. 2017a. *RAZORBACK – A Research Reactor Transient Analysis Code, Version 1.0. Volume 3: Verification and Validation Report*. SAND2017-3372. Albuquerque, NM: Sandia National Laboratories.

Talley, D.G. 2017b. *RAZORBACK – A Research Reactor Transient Analysis Code, Version 1.0. Volume 1: User's Manual*. SAND2017-10561. Albuquerque, NM: Sandia National Laboratories.

Talley, D.G. 2018. *RAZORBACK – A Research Reactor Transient Analysis Code, Version 1.0. Volume 2: Software Design and Development Report*. SAND2018-4507. Albuquerque, NM: Sandia National Laboratories.

The RELAP5-3D Code Development Team. 2018. *RELAP5-3D Code Manual Volume I: Code Structure, System Models, and Solution Methods.* Idaho Falls, ID: Idaho National Laboratory.

TRW Environmental Safety Systems. 1996. *Spent Nuclear Fuel Effective Thermal Conductivity Report*. BBA000000-01717-5705-00010 REV00. Las Vegas, NV: US Department of Energy, Yucca Mountain Site Characterization Project Office. https://www.osti.gov/servlets/purl/778872.

UNSCEAR (United Nations Scientific Committee on the Effects of Atomic Radiation). 2000. *Sources and Effects of Ionizing Radiation: United Nations Scientific Committee on the Effects of Atomic Radiation; UNSCEAR 2000 Report to the General Assembly, with scientific annexes*. New York, NY: United Nations.

Wagner, J. C. and C.V. Parks. 2003. *Recommendation on the Credit for Cooling Time in PWR Burnup Credit Analysis.* Oak Ridge, TN: Oak Ridge National Laboratory.

Wagner, W., J.R. Cooper, A. Dittmann, J. Kijima, H. Kretzschmar, A. Kruse, R. Mareš, K. Oguchi, H. Sato, I. Stöcker, O. Šifner, Y. Takaishi, I. Tanishita, J. Trübenbach, and T. Willkommen. 2000. The IAPWS Industrial Formulation 1997 for the Thermodynamic Properties of Water and Steam. ASME. *J. Eng. Gas Turbines Power* 122 (1): 150–184. https://doi.org/10.1115/1.483186.

Weast, R.C., and M.J. Astle. 1979. *CRC Handbook of Chemistry and Physics*. Boca Raton, FL: CRC Press.

Weck, P.F., E. Kim, V. Tikare, and J.A. Mitchell. 2015. Mechanical properties of zirconium alloys and zirconium hydrides predicted from density functional perturbation theory. *Dalton Transactions* 44 (43): 18769–18779.

YMP (Yucca Mountain Project). 2003. *Disposal Criticality Analysis Methodology Topical Report.* YMP/TR-004Q, Rev. 2. Las Vegas, NV: Yucca Mountain Site Characterization Office.

Appendix A

Simplified Transient Criticality Analysis

This page is intentionally left blank.

A-1.1 Purpose

The purpose of this appendix is to present a simplified analysis that provides perspective on the maximum peak power, maximum energy release, peak fuel temperature, and peak water temperature due to a relatively rapid reactivity insertion in a DPC. The analysis does not evaluate the mechanism of the reactivity insertion to determine the magnitude and rate, but rather assumes values and rates that could be commensurate with a reactivity insertion due to geometry change induced by a seismic event or rapid settling of corrosion products. The analysis conservatively assumes instantaneous reactivity insertion to bound peak fuel temperature and allow for complete heat transfer to the water to bound peak water temperature. The impact of a slower reactivity insertion rate on peak fuel and moderator temperatures is also evaluated.

A-1.2 Analysis Approach and Methodology

The key parameters in evaluating the consequences of potential criticality excursions are (1) power, which is proportional to the neutron flux; (2) reaction period, which dictates the power as a function of time; and (3) duration. These three parameters (i.e., power, period, duration) are a direct function of changes to system reactivity. Reactivity change for a system is defined as follows:

$$\Delta\rho = \rho_{final} - \rho_{initial} = \frac{1.0}{k_{eff-initial}} - \frac{1.0}{k_{eff-final}}$$ *Equation A-1*

The reactivity for a system is quantified in dollars ($) by the ratio of the reactivity change to the delayed neutron fraction (β_{eff}):

$$\Delta\rho(\$) = \frac{\Delta\rho}{B_{eff}}$$ *Equation A-2*

The relationship between the change in reactivity in a system and the delayed neutron fraction directly impacts the criticality excursion kinetics including peak power, reaction period, reaction rate, and heat generation rate. The rate at which the reaction rate and power increase during a criticality excursion is a direct function of the magnitude of the reactivity insertion and system characteristics. The relationship between reactivity (ρ), reaction period (T), delayed neutron fraction (β_i) for each of the delayed neutron groups (n), associated decay constants for each group (λ_i), prompt neutron lifetime (l), and criticality state (k_{eff}), can be described as follows:

$$\rho = \frac{l}{k_{eff} \cdot T} + \sum_{i=1}^{n} \frac{\beta_i}{1 + \lambda_i \cdot T}$$ *Equation A-3*

For small reactivity insertions (i.e., $\Delta\rho < \beta_{eff}$), the reaction rate would rise at a relatively slow rate (minutes to hours) and would be considered a stable period. For relatively large reaction insertions (i.e., $\Delta\rho > \beta_{eff}$), which is the primary focus of this analysis, the reaction rate would rise at a high rate (microseconds to millisecond), the reaction period would be a direct function of the prompt neutron lifetime (l) and approximated as follows:

$$T = \frac{l}{r} \qquad \text{Equation A-4}$$

The power and energy release due to a criticality excursion is a function of fission reaction rate (*RR*) during the excursion, which is a function of the flux (ϕ) and macroscopic fission cross section (Σ_f), simply expressed as follows:

$$RR = f \times S_f \qquad \text{Equation A-5}$$

As discussed above, the reaction period (T), which is a function of the reactivity change magnitude and rate, dictates the rate of power increase by increasing the neutron flux. Based on a given reaction period (T), the neutron flux at time t would be as follows:

$$f(t) = f_o e^{t/T} \qquad \text{Equation A-6}$$

Similarly, the power (P) at time t would be as follows:

$$P(t) = P_o e^{t/T} \qquad \text{Equation A-7}$$

The analysis documented in this appendix solves these equations iteratively using an initial assumed reactivity insertion rate and magnitude with evolving system kinetics parameters based on the analysis considerations discussed in Section A-1.3 and parameters presented in Section A-1.4.

A-1.3 Analysis Considerations

Because of the nature of a rapid transient criticality event, it is assumed that delayed neutrons do not influence the system kinetics. Additionally, because the analysis is simplified to a single node, an explicit solution of neutron diffusion would not be meaningful to represent a DPC with vastly different assembly neutronic characteristics and loading considerations. In order to analyze the kinetics of the systems and extrapolate the results of the analysis to the entire DPC, the fuel temperature coefficient (FTC), MTC), radial peaking factor, and axial peaking factor are taken from relevant literature and S3K analyses. Because the DPC contains depleted SNF and is assumed to contain little or no neutron absorbers (which is an initial condition for initiating a criticality transient), the kinetic characteristics of the representative DPC would resemble those of a typical PWR at the end-of-cycle (EOC). The S3K parameters were generated for the representative DPC discussed in Section 6.3.

The analysis evaluates the power excursion due to a reactivity insertion magnitude and rate with parametric reactivity feedback for the FTC and MTC. The parametric considerations evaluate a range that covers effective and ineffective heat transfer from the fuel to the moderator based on heat conduction. Because of the rapid nature of the transient, it is assumed that convective heat transfer would not contribute significantly to the initial development of the transient. Note that for longer transients associated with lower reactivity insertion rates, the role of convective heat transfer would be more significant. Radiative heat transfer, which may be of importance if conduction is limited due to the potential formation of a steam layer around the cladding, is not considered because the rate is expected to be insignificant due to the nature of the materials (i.e., radiative heat transfer to water) coupled with the rapid transient. Additionally, these considerations are addressed by the parametric evaluation.

Moderator temperature rise due to neutron moderation is ignored since it is a small fraction of the total energy released during fission and because the analysis provides for a parametric evaluation that bounds such effects.

Heat transfer through the cladding is also ignored (i.e., cladding is assumed to have the same thermal characteristics as the fuel). Because the simplified analyses do not aim at predicting actual values, but rather bounds for the fuel and moderator, the parametric analyses represent the effect of cladding on heat transfer. Note that for depleted SNF, the fuel characteristics, gap condition and cladding heat transfer considerations (conduction and emissivity rates) vary considerably.

A-1.4 Analysis Parameters

The list of key kinetics and heat transfer parameters considered in the analysis are provided in Table A-1.

Table A-1. Key Kinetics and Heat Transfer Parameters Used in the Simplified Analysis

Parameter	Value	Basis
Prompt neutron lifetime	1E-04 seconds	Typical value for LEU thermal reactors.
Delayed neutron fraction	0.005	Typical value for thermal reactors with LEU fuel at EOC.
Water heat capacity	4,186 J/(kg·°C)	These values vary with temperature and pressure (where applicable). Because this analysis aims at providing bounds (not predicted values), the variability is captured in the parametric evaluations.
Fuel heat capacity	350 J/(kg·°C)	
Water thermal conductivity	6.5E-03 W/(cm·°C)	

NOTE: EOC = end-of-cycle
LEU = low-enriched uranium

The DPC-specific fuel and MTCs considered in the simplified analysis are shown in Figure A-1 and Figure A-2. A conservative combined radial and axial peaking factor of 2.0 is assumed based on the S3K analysis in Section 6.3. In order to apply the analysis to other DPCs, either a library of parameters could be developed and documented in a lookup table, or a set of bounding (or conservative) parameters could be selected to bound (or represent) the population of DPCs.

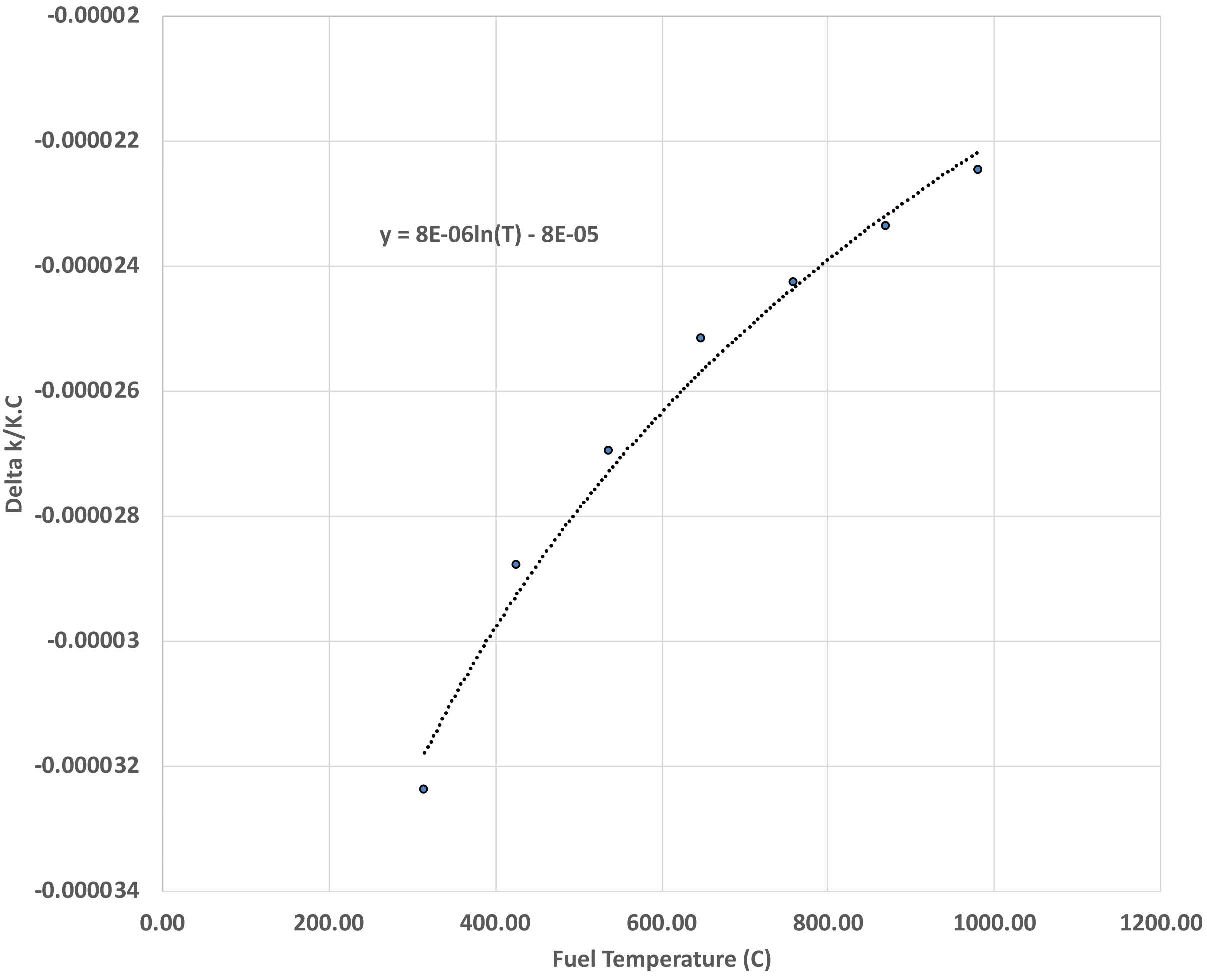

Figure A-1. Fuel Temperature Coefficient

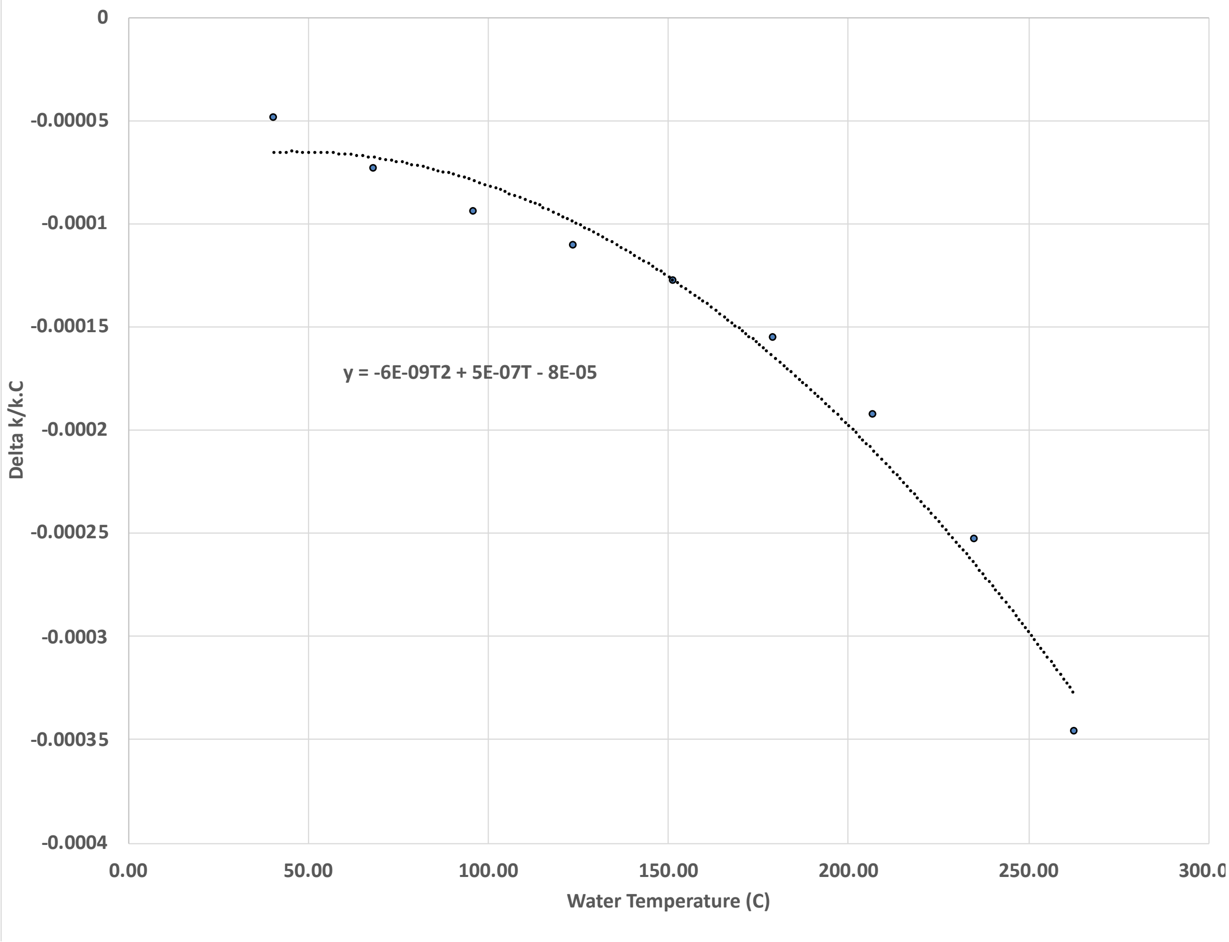

Figure A-2. Moderator Temperature Coefficient

Table A-2 provides the DPC and fuel parameters as well as other information relied upon in the analysis.

Table A-2. Fuel and DPC Parameters Used in the Analysis

Parameter	Value
Fuel Segment Volume	1.00 cm^3
Pellet radius+Gap	0.47 cm
Fuel cross-sectional area	0.71 cm^2
Fuel length	1.41 cm
Cladding radius	0.54 cm
Pin cross-sectional area	0.90 cm^2
Pin volume	1.28 cm^3
Cladding thickness	0.06 cm
Cladding volume	0.09 cm^3
Cladding mass	0.57 g
Cladding surface area	4.76 cm^2
Fuel pitch	1.43 cm
Unit cross-sectional area	2.04 cm^3
Unit volume	2.89 cm^3
Radial fuel surface area	4.21 cm^2
Radial cladding surface area	4.76 cm^3
Water volume	1.61 cm^3
Fuel density	10.20 g/cm^3
Water density	1.00 g/cm^3
Fuel mass	10.20 g
Water mass	1.61 g
Equivalent water radius	0.81 cm
Equivalent water thickness	0.27 cm
Water surface area	4.76 cm^2
Total Fuel Height	365.76 cm
Number of rods per assembly	208 rods
Number of assemblies per DPC	37 assemblies
Initial DPC Power	1.00E+00 W
Total number of segments in DPC	1.99E+06 segments
Initial power in peak cm^3	8.04E-07 W
Initial water and fuel temperatures	50°C
UO_2 mass in DPC	16.65 MT
Water mass in DPC	6.0 MT

A-1.5 Analysis Results

The results of the analysis can be bounded by considerations that maximize peak power and peak fuel temperature. Peak power can be achieved by the highest possible insertion magnitude (i.e., shortest reactor period) and slowest and lowest negative reactivity feedback, which would be associated by the fastest insertion rate and slowest heat transfer to the moderator. Table A-3 provides the bounding results for a set of reactivity insertion magnitudes assuming instantaneous insertion (i.e., bounding insertion rate). The DPC is assumed to be at a steady-state power of 1 W with fuel and moderator temperatures at 50°C prior to the initiation of the transient. Note that the FTC becomes relatively less effective at higher temperatures as shown in Figure A-1 (i.e., lower negative reactivity per degree rise in the fuel). Therefore, the same transient (i.e., reactivity magnitude and insertion rate) would provide more limiting results (e.g., higher peak fuel temperature) if the same transient were to initiate at a higher initial fuel temperature.

Table A-3. Results for a Range of Instantaneous Reactivity Insertions

Reactivity Insertion Magnitude ($)	Peak Power (W)	Peak Fuel Temperature (°C)	Total Energy Release (J)	Eventual Average Water Temperature Rise (°C)
1	5.01E+08	341	1.06E+9	35
2	1.11E+09	697	2.35E+09	77
3	1.76E+09	1,080	3.74E+09	123
4	2.52E+09	1,530 (potential cladding damage)	5.36E+09	177 (potential for bulk boiling)
5	3.19E+09	1,940 (potential fuel damage)	6.86E+09	226 (expected boiling)

Based on the parametric evaluation using this simplified approach, it can be concluded that a reactivity insertion that is lower than $3 would not result in exceeding fuel or cladding temperatures that could cause cladding or fuel damage and would not produce sufficient total energy to cause boiling throughout the DPC regardless of the rate of insertion.

Slowing down the rate of reactivity insertion to 10 seconds, which could be more commensurate with potential reactivity insertion processes, would produce the results presented in Table A-4. Note that ignoring delayed neutrons may impact the reaction period for lower reactivity insertions.

Table A-4. Results for a Range of Reactivity Insertions during a Ten-Second Interval

Reactivity Insertion Magnitude ($)	Peak Power (W)	Peak Fuel Temperature (°C)	Total Energy Release (J)	Eventual Average Water Temperature Rise (°C)
2	9.10E+08	485	1.07+09	56
3	1.44E+09	739	2.69E+09	89

Considerations that maximize total energy release and moderator temperature were found consistent with those for peak power and peak fuel temperature. Many parametric evaluations for various reactivity insertion magnitudes and rates coupled with assumptions that maximize heat transfer to the water did not result in a transient that produced more energy. This is reasonable based on the following considerations:

- The MTC is a factor of 5 to 10 (depending on temperature) higher per degree increase in moderator temperature than the FTC per degree increase in fuel temperature.
- The water heat capacity is approximately a factor of 10 higher than UO_2.
- The mass of UO_2 is approximately a factor of 6 higher than the mass of water per unit cell.

Therefore, there is stronger negative reactivity feedback from the moderator per unit energy (i.e., FTC per joule is less than MTC per joule). Assumptions that increase heat transfer effectiveness to the moderator would result in a transient that produces lower peak power and lower total heat generation during the initial spike. However, the peak moderator temperature could be higher for relatively slower transients, which rely more on the “local” MTC as the primary negative reactivity feedback over the FTC.

A-1.6 Analysis Conclusions

It is not feasible for a simplified model to predict transient parameters for a given reactivity insertion magnitude and rate due to the complexity of the neutronic, kinetic, and heat transfer parameters that are highly dependent on the fuel and loading characteristics as well as the location of the reactivity insertion. Additionally, due to the rapid rate of the transient, minor changes to heat transfer consideration (e.g., fuel–cladding gap, formation of steam layer around cladding) significantly affect the results. The FTC could also be highly dependent on how the effective fuel temperature is determined during rapid transients. Fuel density, cladding density, and moderator two-phase considerations would also have significant effects on the kinetics and heat transfer modeling. Prediction of values is better suited for complex spatial- and time-dependent coupled neutronics and thermal hydraulics codes. The simple analysis in this Appendix provided perspective on bounding consideration such that if the maximum reactivity insertion magnitude is less than \$2, then the potential thermal effects on the fuel as well as the thermal and mechanical effects on the moderator would likely be insignificant. For relatively slower transients, reactivity insertions up to \$4 would likely not results in fuel impacts or sufficient energy generation to result in global boing and pressurization. However, it is important to evaluate localized effects (e.g., local boiling and steam generation) for these relatively slower transients because of the stronger reliance on the “local” MTC relative to the FTC.

Appendix B

Evaluation of Thermal Characteristic Curve Functionality in PFLOTRAN

This page is intentionally left blank.

B-1. Purpose

The purpose of this appendix is to evaluate the new TCC feature in PLFOTRAN described in Section 3.3.

B-2. Basic Functionality

B-2.1 1D Test Problem

A test problem was designed to test the implementation of the basic TCCs and is diagrammed in Figure B-1. It consists of two interacting regions with different material properties extended across ten meters, where Material 1 on the western half has a permeability three orders of magnitude higher than Material 2 on the eastern half. Permeability for either material is isotropic, and the materials differ in porosity, tortuosity, density, and heat capacity. The pore space of either material initially consists of gas at 0°C and 111,325 Pa with a mole fraction of 0.995. The western face of Material 1 bears the liquid phase at 100°C and 111,325 Pa with a gas mole fraction of 10^{-10}.

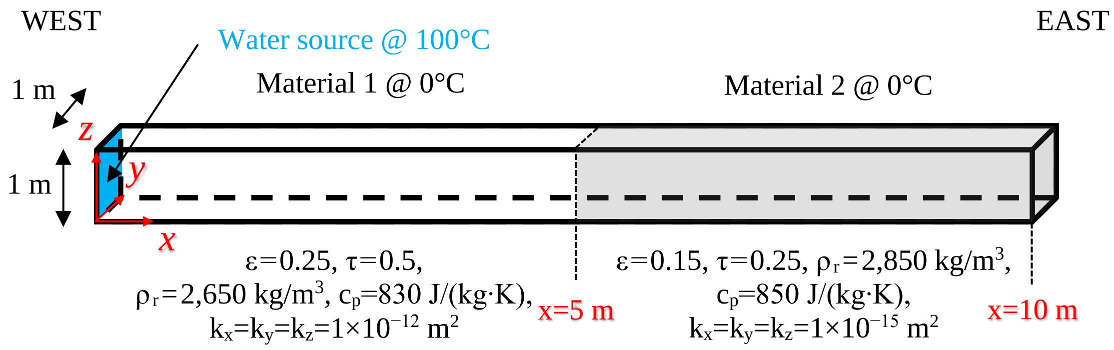

Figure B-1. Test Problem for TCCs with Initial Conditions

The characteristic curve parameters for each material are detailed in Table B-2, where the functions involved are described in detail in Section 3.3.1. Both materials share a common TCC per given calculation based on the parameters in Table B-1. The TCCs are plotted in Figure B-2 for minimal and maximal values of $\kappa_T^D(S_l)$ for unsaturated and saturated cases, respectively. Relative to the default TCC, the power law TCC overestimates the thermal conductivity at temperatures below 26.85°C. This is a consequence of the choice of T_{ref}. Otherwise, at higher temperatures, the power law κ_T will fall below the default thermal conductivity. Since κ_T^{dry} and κ_T^{wet} are universal in this problem setup and $\kappa_T^C = \kappa_T^{dry}$, the cubic polynomial, linear resistivity, and constant TCCs will all underestimate the thermal conductivity relative to the default value. Therefore, for a given heat flux, the change in temperature will be lower for these TCCs compared to the default. It is apparent that saturating the media has the effect of widening the κ_T gap between the power law curve and the linear resistivity/cubic polynomial curves. The latter two remain relatively close to each other.

Table B-1. Values for TCCs used in the Test Problem

Name	Test Inputs
Default	κ_T^{wet} = 7.0 W/(m·K) κ_T^{dry} = 5.5 W/(m·K)
Constant	κ_T^{C} = 5.5 W/(m·K)
Linear Resistivity	κ_T^{wet} = 7.0 W/(m·K) [0°C] κ_T^{dry} = 5.5 W/(m·K) [0°C] $a_1 = 1$ $a_2 = 5.038\times10^{-3}$ °C^{-1} $T_{ref} = 0$°C
Cubic Polynomial	κ_T^{wet} = 7.0 W/(m·K) [0°C] κ_T^{dry} = 5.5 W/(m·K) [0°C] $\beta_1 = -4.53398\times10^{-3}$ °C^{-1} $\beta_2 = +1.41580\times10^{-5}$ °C^{-2} $\beta_3 = -1.94840\times10^{-8}$ °C^{-3} $T_{ref} = 0$°C
Power Law	κ_T^{wet} = 7.0 W/(m·K) [26.85°C] κ_T^{dry} = 5.5 W/(m·K) [26.85°C] $\gamma = -1.18$ $T_{ref} = -273.15$°C

Table B-2. Characteristic Curve Parameters for (M)aterials in the Test Problem

M	Saturation Function	Liquid Permeability	Gas Permeability
1	Van Genuchten S_l^r=0.00, $\alpha=1\times10^{-4}$, m=0.50, $P_{cap}^{max}=1\times10^6$ Pa	Van Genuchten-Mualem S_l^r=0.00, m=0.50	Van Genuchten-Mualem S_l^r=0.00, $S_g^r=10^{-40}$, m=0.50
2	Van Genuchten S_l^r=0.01, $\alpha=2\times10^{-4}$, m=0.55, $P_{cap}^{max}=1\times10^6$ Pa	Van Genuchten-Mualem S_l^r=0.01, m=0.55	Van Genuchten-Mualem S_l^r=0.01, S_g^r=0.01, m=0.55

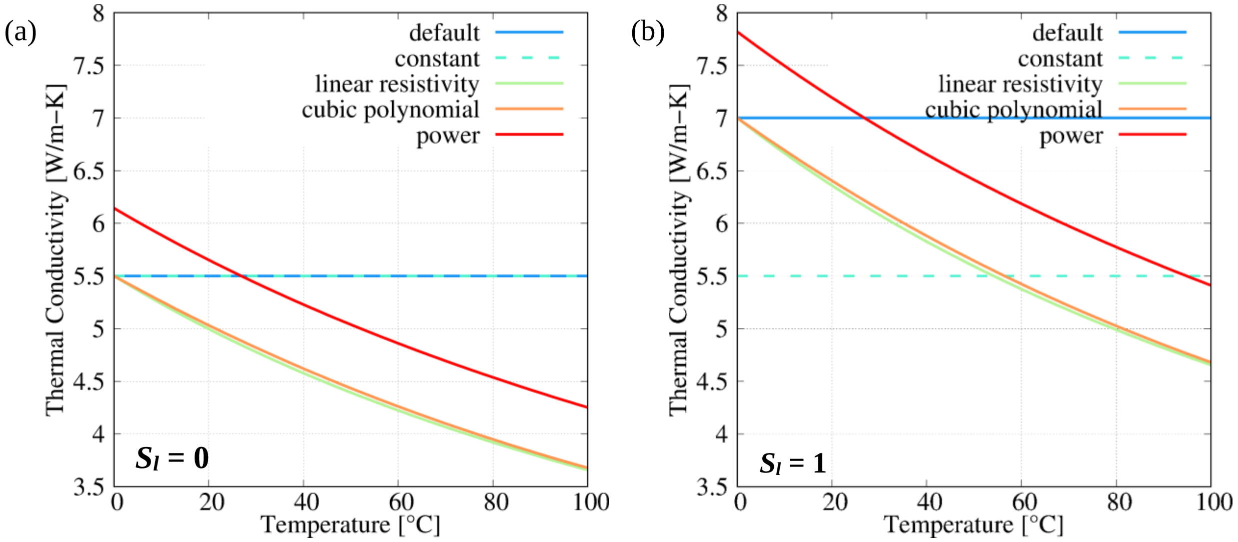

Figure B-2. Thermal Conductivities by Temperature for (a) Unsaturated and (b) Saturated Cases

B-2.2 Results

This test problem was applied to cases employing all five TCCs with the parameters in Table B-1, where κ_T^{dry} and κ_T^{wet} are common among all curves. The constant curve is defined as κ_T^{dry} since the problem begins in a dry state. This assumption was made to relegate difference with the default TCC to the partially saturated regions for purposes of comparison. Results for temperature and saturation were obtained over various time points for a 10-year, subsurface flow calculation in General mode. The problem is considered one dimensional (1D) and results will be presented exclusively over the *x*-axis (Figure B-1) based on a fidelity of 40 grid blocks.

Temperature

The thermal characteristics curves are compared at certain points in time in Figure B-3. For a given point along the *x*-axis at a given time, the default TCC exhibits the highest temperature. This is a direct result of the κ_T parameters selected for each curve, as discussed previously. There is no opportunity for the higher κ_T values of the power law curve to be effective since the region of Material 2 lying below 26.85°C remains largely unsaturated, and the heat flux in the warmer, saturated regions of Material 1 elevates the temperatures in the default curve to the point where higher power law κ_T has a lower impact. The linear resistivity and cubic polynomial results almost overlap due to the similar κ_T behavior observed previously in Figure B-2.

As time proceeds, water is driven from west to east across Material 1 into Material 2. By one month, the temperature profiles assume a downward ramping trend. By six months, the profiles move to a downward linear-to-convex shape since hot water is largely retained in Material 1 and still in the process of permeating Material 2. At this time, temperatures react smoothly to the change in permeability. As more water enters Material 2 and more heat is transferred, the convex profile relaxes at 1 year and eventually at 10 years assumes a more linear shape where temperature behavior behaves most sharply at the eastern boundary. By the end of the problem, the constant TCC assumes higher temperatures than the temperature-dependent curves because heat has been transferred more evenly across the medium and behavior from Figure B-2-a is more dominant.

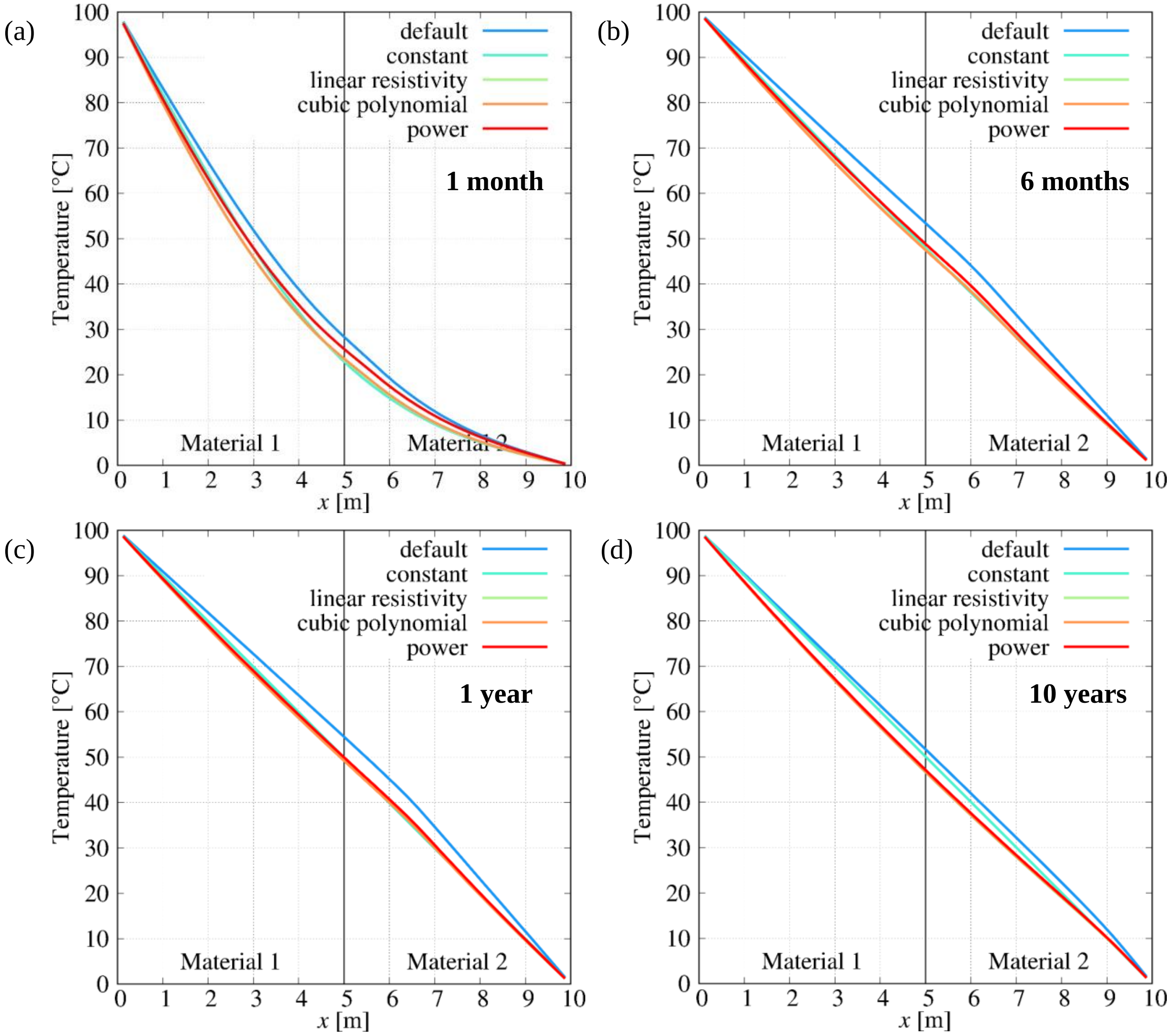

Figure B-3. Temperature over Distance Evaluated at (a) 1 Month, (b) 6 Months, (c) 1 Year, and (d) 10 Years for All Five TCCs

An expanded set of temperature curves for certain points in time is shown in Figure B-4. It is apparent in all TCCs (except constant) that the minimal temperature in Material 1 peaks by *t* = 1 year before heat transfer reduces the minimum further by *t* = 10 years. This transient behavior at 1 year is not reflected in the constant TCC because there is no saturation dependence and the temperature distribution at this time is likely steady. The temperatures for the default TCC in Figure B-4a are clearly most affected by the transition to the less pervious Material 2 at *x* = 5 m. At the opposite extreme, the results for the constant TCC in Figure B-4b almost shows no effects from this material boundary.

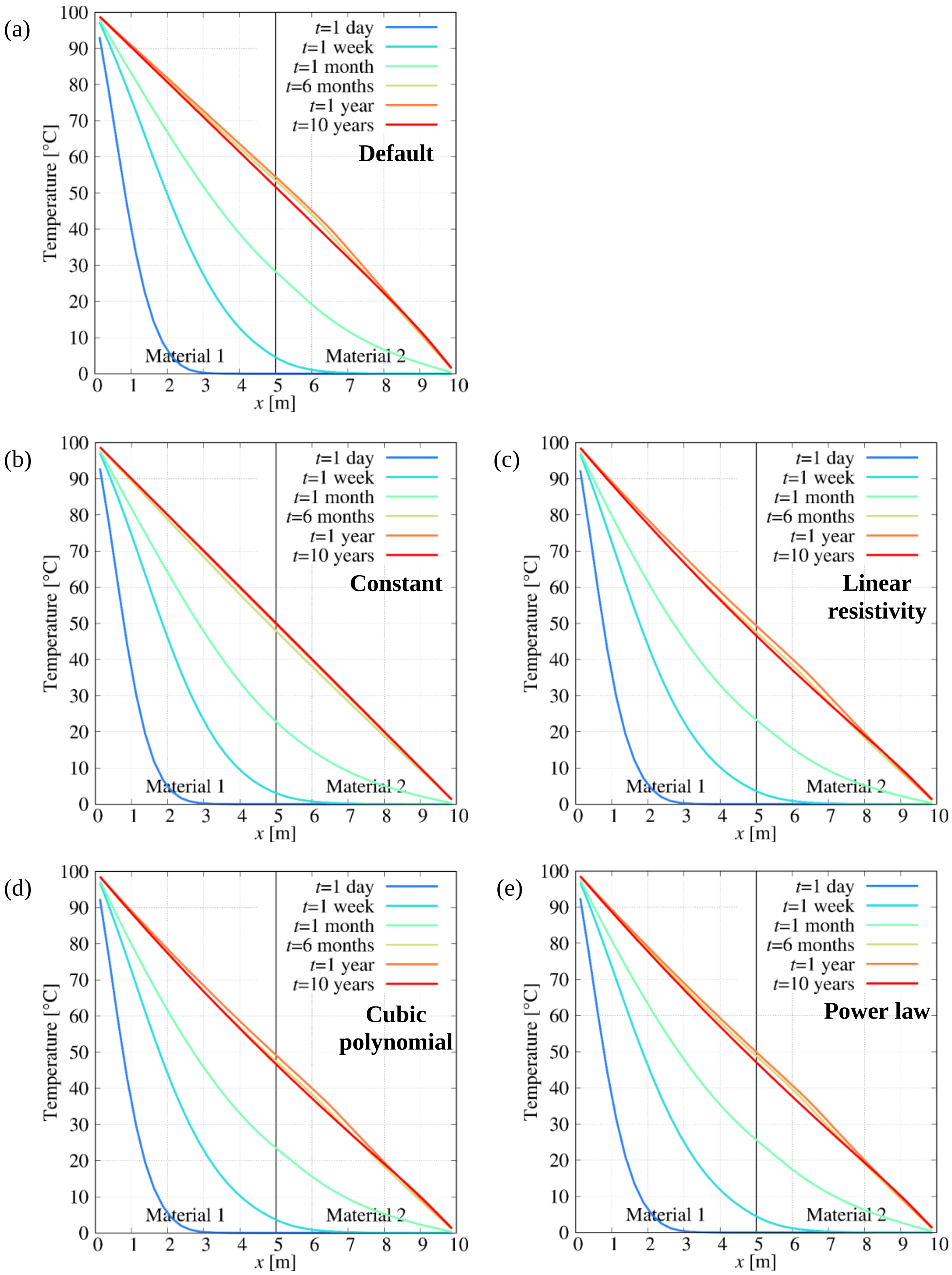

Figure B-4. Temperature over Distance Evaluated at Certain Times for (a) Default, (b) Constant, (c) Linear Resistivity, (d) Cubic Polynomial, and (e) Power Law TCCs

Liquid Saturation

The nuanced differences in temperature behavior among the different TCCs are not as apparent in the results for liquid saturation. The results for all TCCs nearly overlap in Figure B-5 for snapshots at 1 week and 10 years. In Figure B-6, the liquid saturation results for linear resistivity are relatively suppressed at 1 week and elevated at ten years compared to the results for the default TCC, but otherwise align very well. Material 1 becomes completely saturated between 1 week and 1 month and the first 3 meters of the less pervious Material 2 becomes at least 75% saturated by the end of the simulation. Given the strong boundary conditions of the problem setup, the eastern face remains unsaturated in alignment with the temperature remaining near 0°C. Overall, this confirms TCCs have been implemented without affecting other parts of the code.

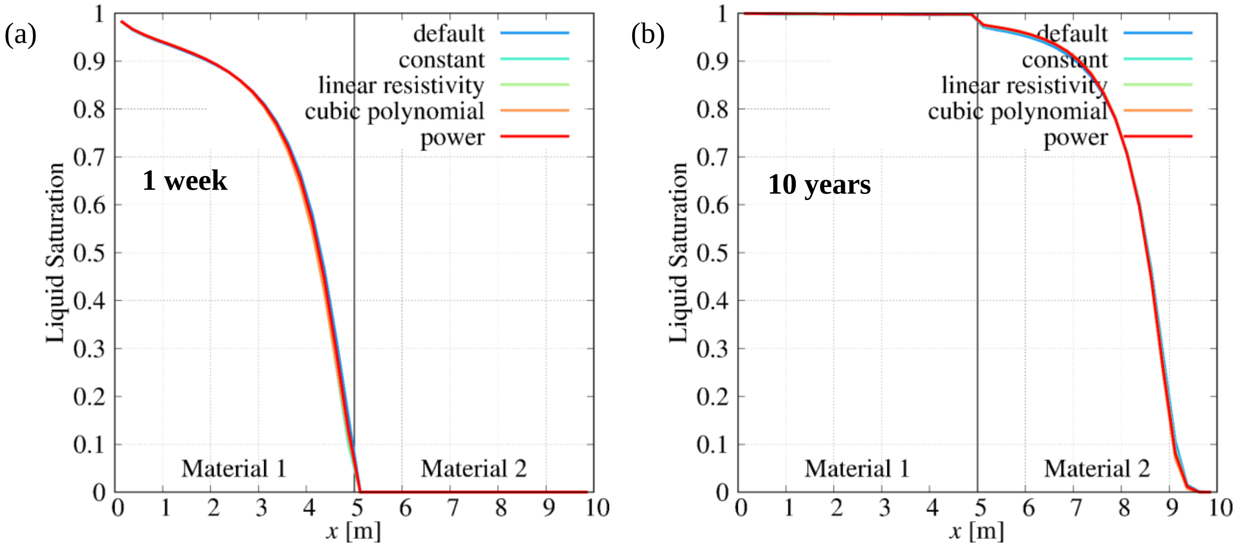

Figure B-5. Liquid Saturation over Distance Evaluated at (a) 1 Week and (b) 10 Years for All Five TCCs

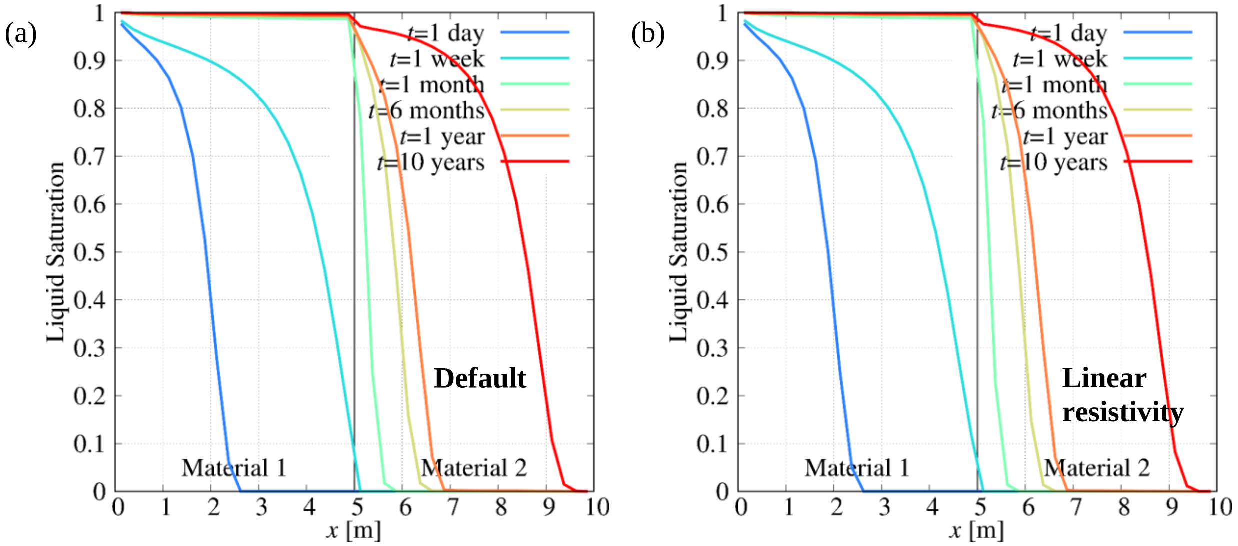

Figure B-6. Liquid Saturation over Distance Evaluated at Certain Times for (a) Default and (b) Linear Resistivity TCCs

B-3. Evaluation of Anisotropic Thermal Conductivity

B-3.1 Test Problems

A 2D test problem was constructed to test the new anisotropy functionality in PFLOTRAN described in Section 3.3.2 and is diagrammed in Figure B-7. It is a block of 10 m^2 area and 1 m depth that is comprised of two materials, with Material 1 on the western half and Material 2 on the eastern half. A 1 m^2 source of water at 100°C is injected at the top of the western face. The system is otherwise dry at 0°C and 111,325 Pa. Given the minimal extent of the *y* component, the problem is effectively treated as 2D in *x* and *z*. The calculation is run with 16 grid cells in the *x* direction and 16 in the *z* direction.

To isolate thermal effects, the nonthermal material properties of the two regions were kept the same, and the saturation characteristic curves are based on M1 in Table B-2. The two materials in this test have the same wet and dry thermal conductivities, heat capacities, and densities. They only differ in their anisotropy ratios, such that Material 1 has strong bias in the *x* direction and weak bias in the *z* direction, whereas Material 2 has strong bias in the *z* direction and weak bias in *x* direction. The off-diagonal components of anisotropy are not relevant, as these components would only be activated in a polyhedral grid (i.e., the unit vectors are always aligned with ±*x*, ±*y*, or ±*z* using cartesian grid blocks). For comparison, the same problem was run with isotropic thermal conductivity.

The off-diagonal components of thermal conductivity were tested using a simple 3D system consisting of a combination of rectangular cuboids and interfacing polyhedra. This special grid option is activated in the code using the *unstructured_polyhedra* grid type. The oblique and cantilever system occupies a portion of a 5 m^3 volume and consists of 15 cells, 24 vertices, and 75 faces. It is initialized with dry conditions at 0°C and 111,325 Pa. The cuboid element at the origin has its 2.5 × 2.5 m *x*–*y* face serve as a source of water at 100°C and 111,325 Pa. The system was evaluated using thermal conductivity modeled as isotropic, anisotropic with a diagonal tensor, and anisotropic with a full tensor. The full tensor of anisotropy ratios was constructed to have a principal direction align closely with one of the cell unit vectors in the polyhedral system. The diagonal tensor uses the diagonal components of the full tensor scaled to unity (Table B-3), which represents a system where thermal conductivity in the *z* direction is lower than the planar thermal conductivity along *xy*. The eigenvalues of the full tensor case (before multiplying by κ_T) are 1.0, 0.673, and 0.319, and the principal directions are [−0.676, −0.676, −0.292], [0.707, −0.707, 0], and [−0.206, −0.206, 0.956].

Temperature-dependent effects are isolated from either test problem by using the default TCC, which still maintains saturation-dependence but emphasizes the thermal anisotropy effects. Since the temperature-dependent TCCs are derived from the default type, the anisotropic functionality can also be specified for those curves, but only in a decoupled manner where the direction dependence is evaluated first and the temperature dependence is evaluated afterwards.

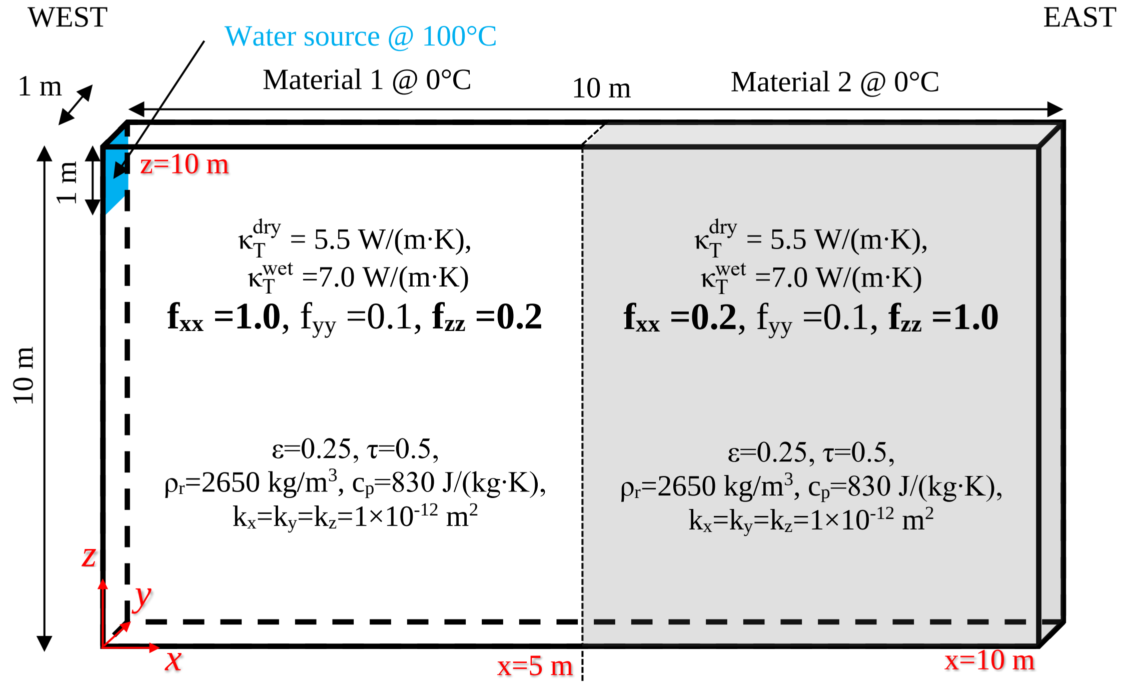

Figure B-7. 2D Test Problem for Thermal Conductivity Anisotropy with Initial Conditions

Table B-3. Test Values for Default TCC in 3D Problem Cases

User Input	Isotropic	Diagonal	Full Tensor
THERMAL_CONDUCTIVITY_DRY (W/[m·K])	5.5	5.5	5.5
THERMAL_CONDUCTIVITY_WET (W/[m·K])	7.0	7.0	7.0
THERMAL_CONDUCTIVITY_X	—	1.000	0.8073
THERMAL_CONDUCTIVITY_Y	—	1.000	0.8073
THERMAL_CONDUCTIVITY_Z	—	0.467	0.3768
THERMAL_CONDUCTIVITY_XY	—	—	0.1345
THERMAL_CONDUCTIVITY_XZ	—	—	0.1345
THERMAL_CONDUCTIVITY_YZ	—	—	0.1345

B-3.2 Results

Temperature—2D

Figure B-8 shows results at one week, where it is clear that in the anisotropic case, the heat flux is unable to raise the temperature in Material 2 as well as it can in the isotropic case. This is a direct result of purposefully employing a low value of κ_{xx} in Material 2. The low value of κ_{zz} in Material 1 is apparent from the 95°C contour reaching lower *z* values. Figure B-9 shows results at one month, where the misaligned anisotropies of the two materials are apparent as most of Material 1 lies above 95°C. However, in the isotropic case, heat is more evenly distributed in Material 1, and the 95°C does not reach across as much of the bottom extent of the region.

Figure B-10 shows results at two months, where the reduced thermal conductivity along *z* in Material 2 is obvious as the temperature front above 95°C extends further into Material 2 at lower *z* values compared to the isotropic case. The 85°C contour is not present in Material 1 for the anisotropic case, but the 60°C contour is observable for the isotropic case. By four months into the simulation, it is shown in Figure B-11 that the bottom of Material 2 is hotter for the anisotropic case compared to the isotropic case due to the insulating effect along *x*. Conversely, the bias towards higher thermal conductivity along *z* in Material 2 produces contours that are more tightly funneled as *x* increases and *z* decreases. In the isotropic case, the contours in Material 2 are more diffused as *x* increases and *z* decreases.

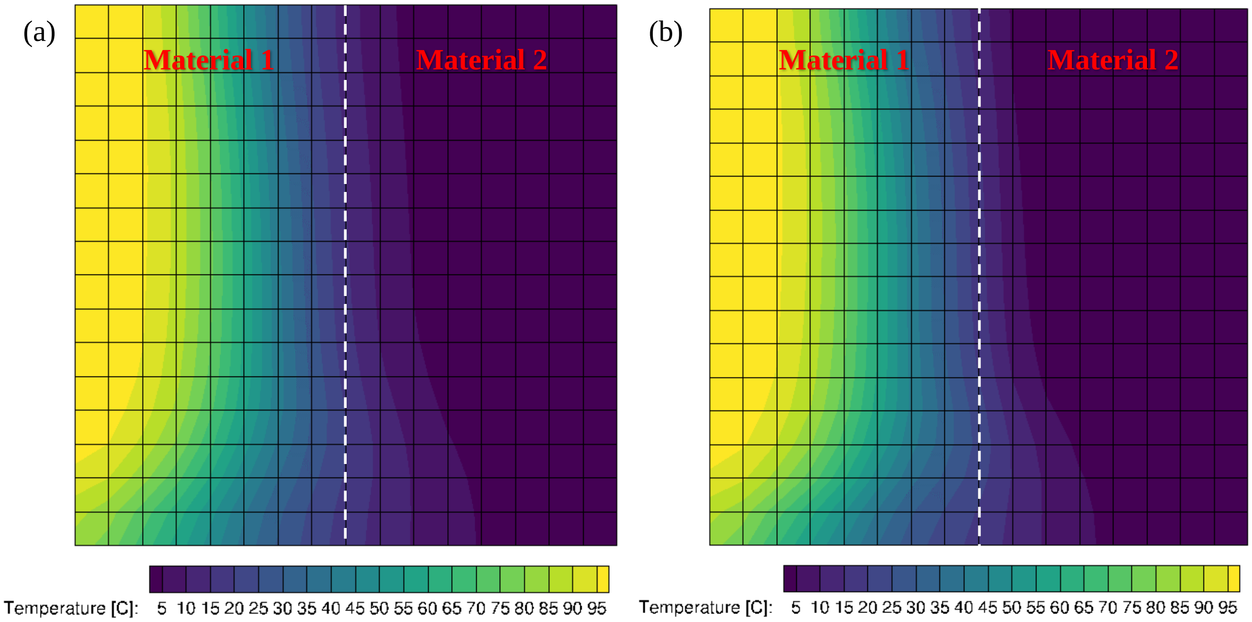

Figure B-8. Temperature at *t* = 7 days for (a) Isotropic and (b) Anisotropic

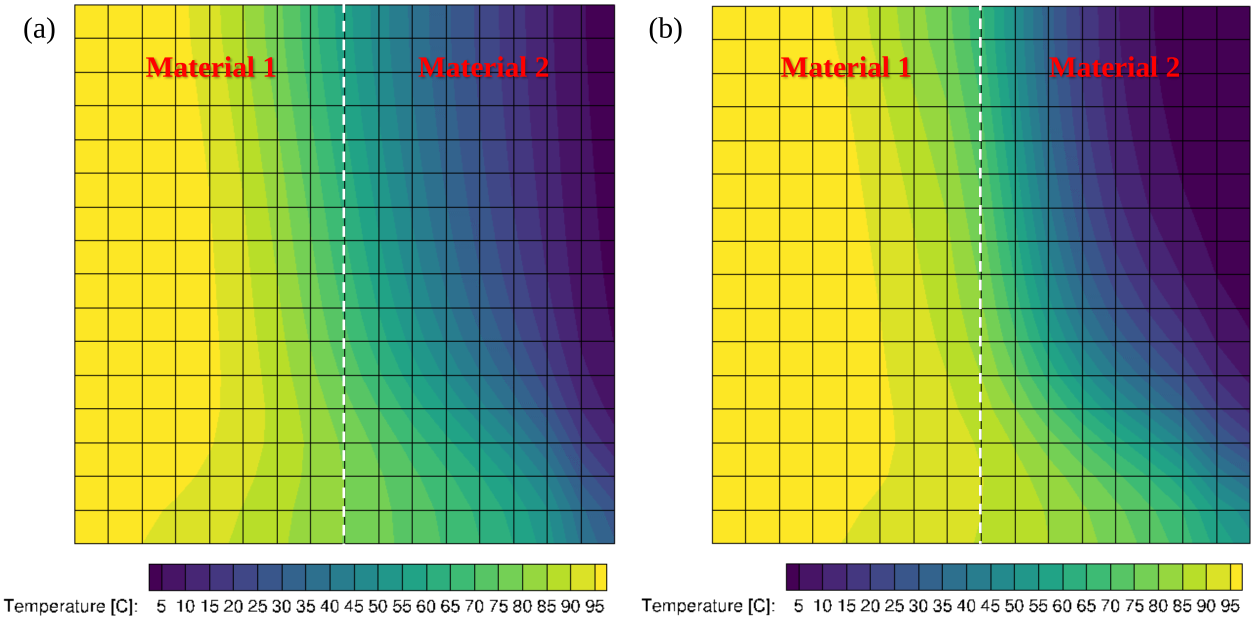

Figure B-9. Temperature at *t* = 30 days for (a) Isotropic and (b) Anisotropic

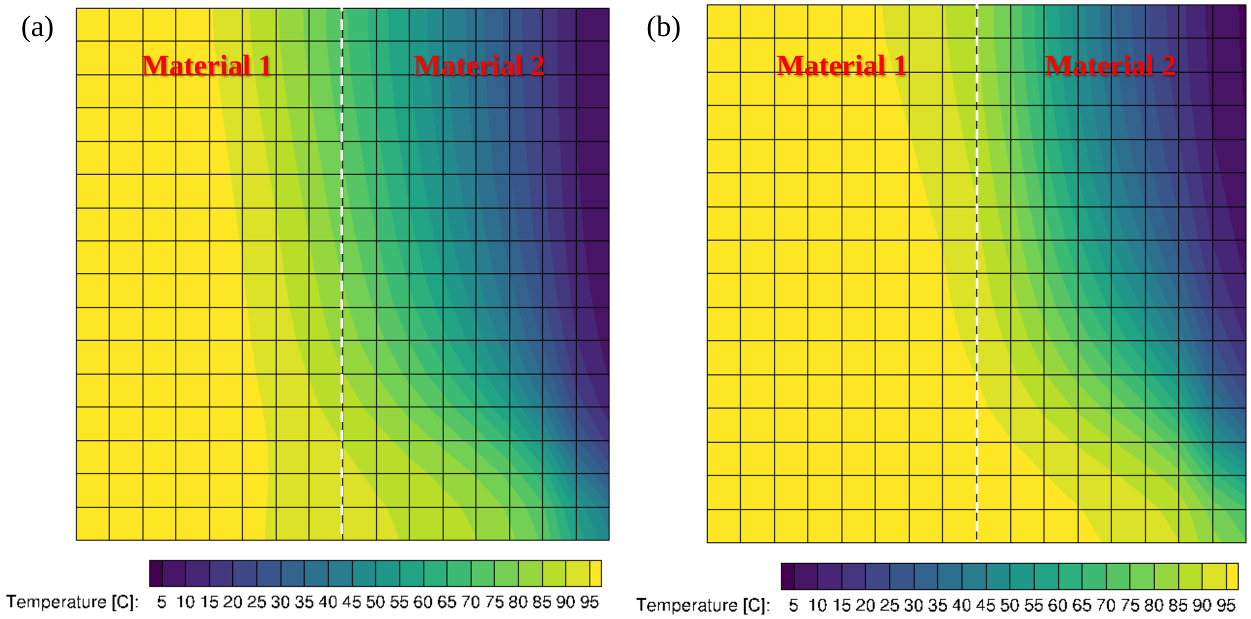

Figure B-10. Temperature at *t* = 60 days for (a) Isotropic and (b) Anisotropic

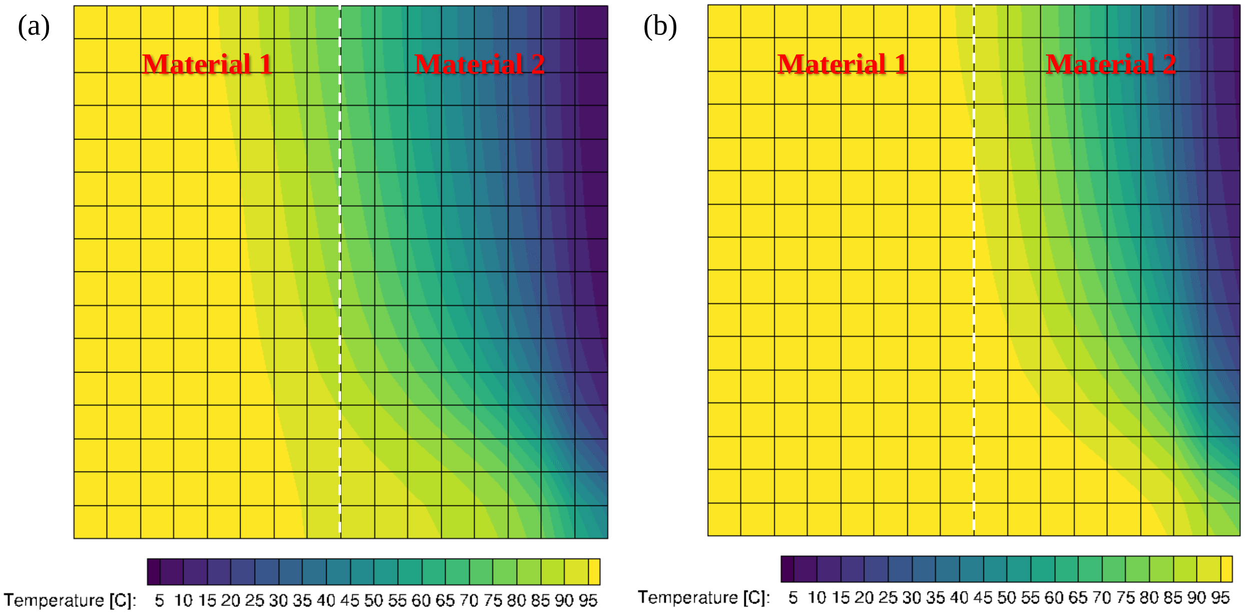

Figure B-11. Temperature at *t*=120 days for (a) Isotropic and (b) Anisotropic

Saturation—2D

In the test problem, both materials shared the same characteristic curves for saturation, so the behavior of liquid saturation as not expected to be substantially different between the anisotropic and isotropic tests. From the 30-day data in Figure B-12, differences between plots (a) and (b) are marginal, where there is a slight depression in the contours of the anisotropic case towards lower *z* values. Otherwise, the results for saturation do not appear to be affected by the new functionality, which is one measure showing that the feature has been implemented correctly.

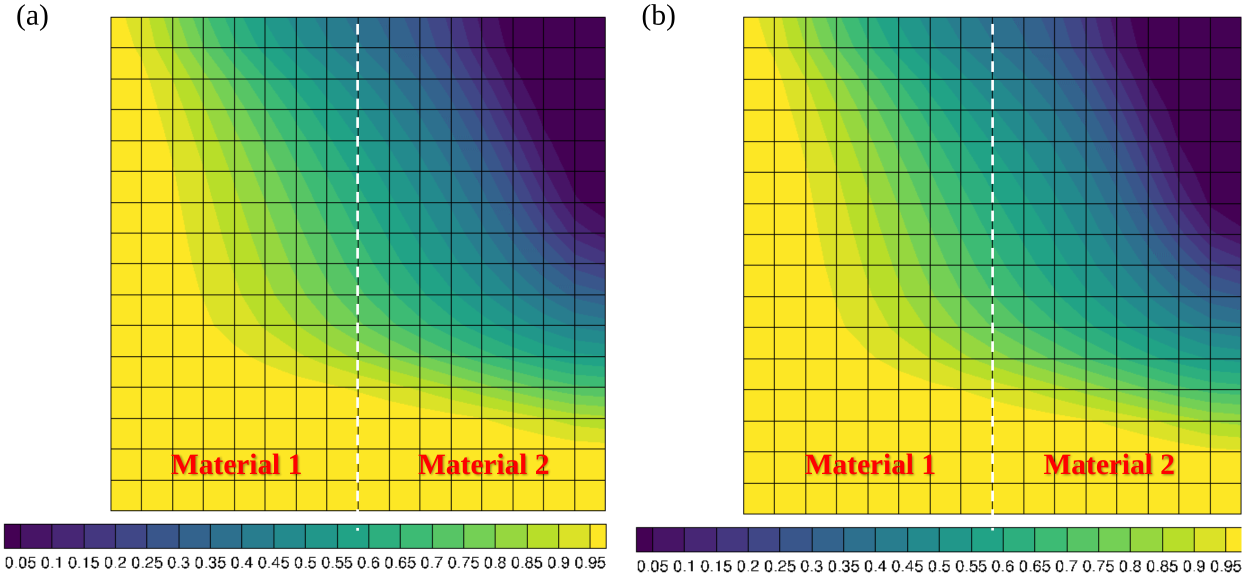

Figure B-12. Liquid Saturation at *t* = 30 days for (a) Isotropic and (b) Anisotropic

Directional Thermal Conductivity—3D

In the 3D test problem, there are 36 unique outward normal unit vectors that are used for evaluating directional thermal conductivity. These include both positive and negative unit vectors along the *y*-axis and a negative unit vector along *z*, which allows for the user-specified anisotropy values in *y* and −*z* to be directly employed for the diagonal tensor, as shown in Figure B-13a. Since the full tensor was constructed to have one principal direction align with a polyhedral unit vector, the maximum value of κ_T^{wet} is only observed along [−0.677, −0.677, −0.290], as shown in Figure B-13b. Otherwise, the scope of possible thermal conductivities is lower compared to the diagonal case, where the thermal conductivity weighted to the total occurrence of unit vectors in the calculation is 3.680 W/(m·K) dry, 4.684 W/(m·K) wet compared to 4.508 W/(m·K) dry, 5.736 W/(m·K) wet. However, this circumstance is tolerated to demonstrate the use of the anisotropy feature by way of ratios unified by the physical bounds of κ_T specified by the user.

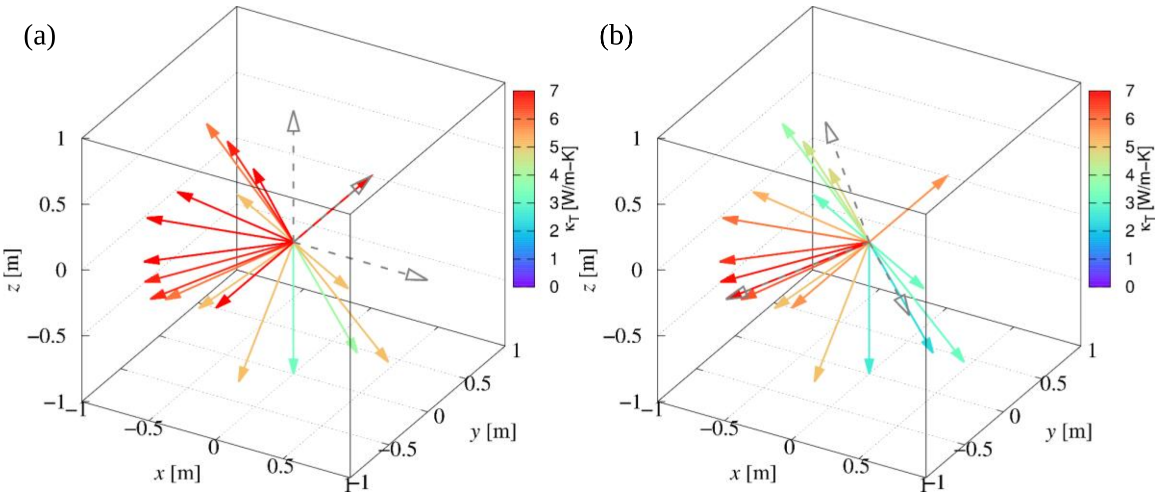

NOTE: Grey, dotted arrows are the principal directions. The wet values overlap the dry values.

Figure B-13. Plot of Unit Vectors Used To Evaluate Directional Thermal Conductivity for (a) Diagonal and (b) Full Tensor Cases

Temperature—3D

The temperature for all three test conditions are plotted with unified contours at instances in time from *t*=1 day in Figure B-14 to *t*=120 days in Figure B-19. The use of isotropic conductivity, given the constraints of the problem setup, allows for the best heat transfer from the water source on the bottom of the lower left block to the upper right edge of the cantilever. At *t*=120 days, the isotropic case shows that the system is isothermal, whereas the anisotropic cases still have temperature distributions. The contours of the diagonal tensor case run parallel to the *x*–*y* plane and clearly demonstrate the weaker conductivity along the *z*-axis. This results in the system being warmer at the bottom compared to the top at *t*=120 days. The isotropic contours aren’t stratified along *x*–*y*; rather, they are angled from the water source towards the opposite extreme of the system as would be expected from the laws of thermodynamics.

Similar *x*–*y* stratification is observed for the full tensor case, although since the system is most conductive within a limited extent of directions, it is clear that some regions off the main cartesian axes remain colder compared to the diagonal case. There is poor thermal conductivity in the lower left of the system and a greater distribution of temperatures per given time compared to the diagonal case. By t=120 days, the full tensor results show that the water source region is still elevated in temperature, while the upper right cantilever region ends up being colder than the coldest regions of the isotropic and diagonal cases. Altogether, the full tensor anisotropic case, despite having cross-talk between the heat flux in x and temperature gradient in z, shows that there are consequences to confining thermal conductivity within a specific range of directions.

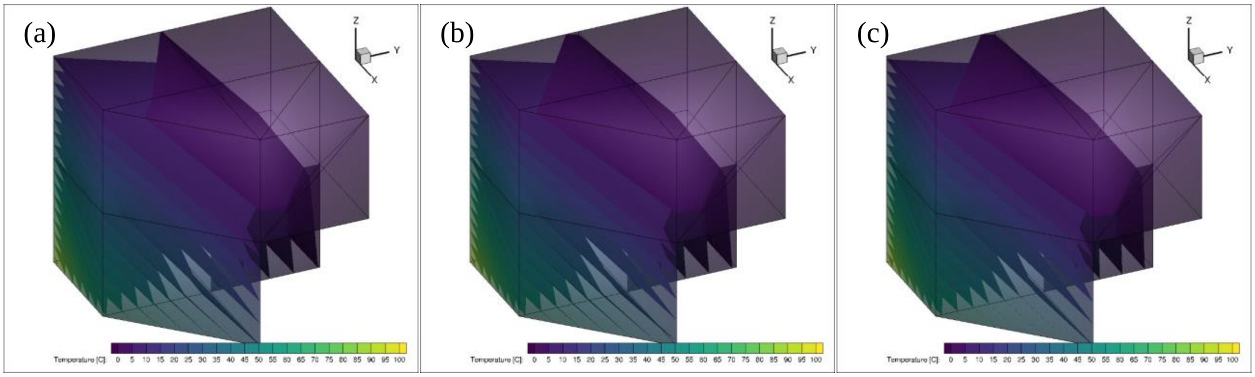

Figure B-14. Temperature Contours from 0°C–100°C at *t* = 1 days for (a) Isotropic, (b) Diagonal, and (c) Full Tensor

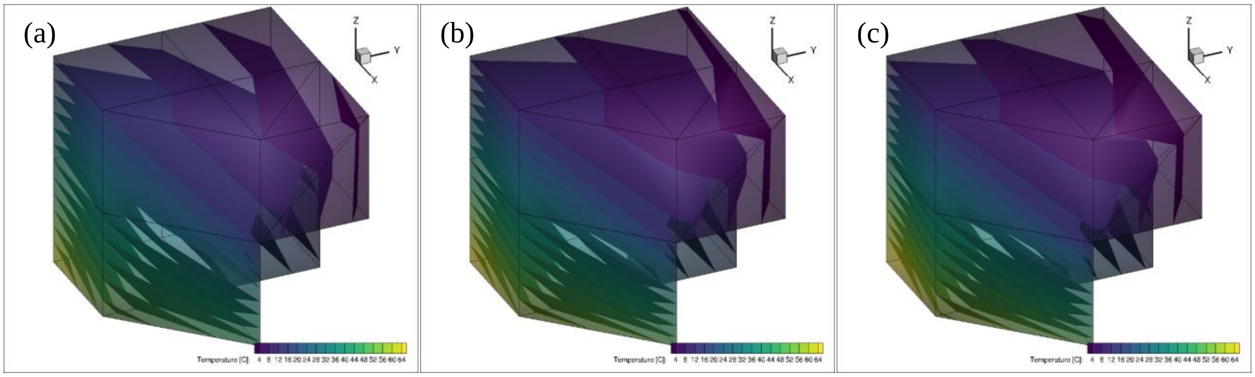

Figure B-15. Temperature Contours from 4°C–64°C at *t* = 7 days for (a) Isotropic, (b) Diagonal, and (c) Full Tensor

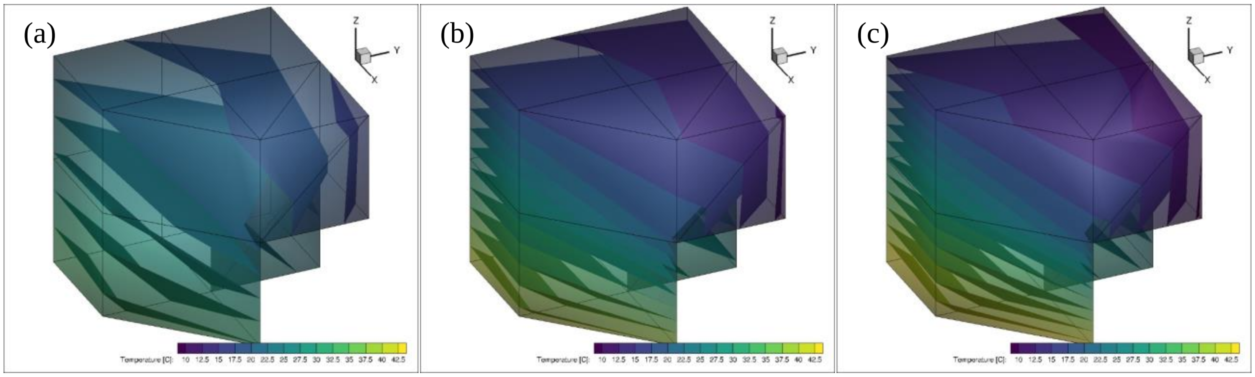

Figure B-16. Temperature Contours from 10°C–42.5°C at *t* = 30 days for (a) Isotropic, (b) Diagonal, and (c) Full Tensor

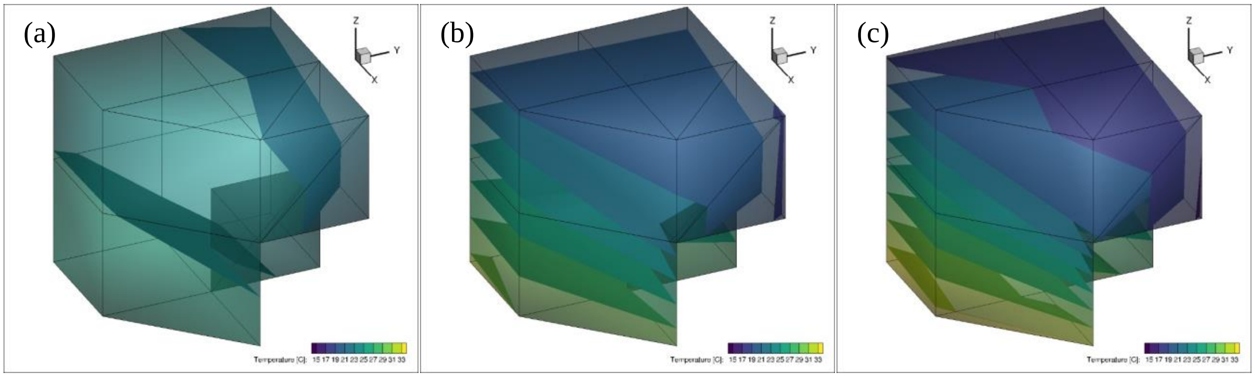

Figure B-17. Temperature Contours from 15°C–33°C at *t* = 60 days for (a) Isotropic, (b) Diagonal, and (c) Full Tensor

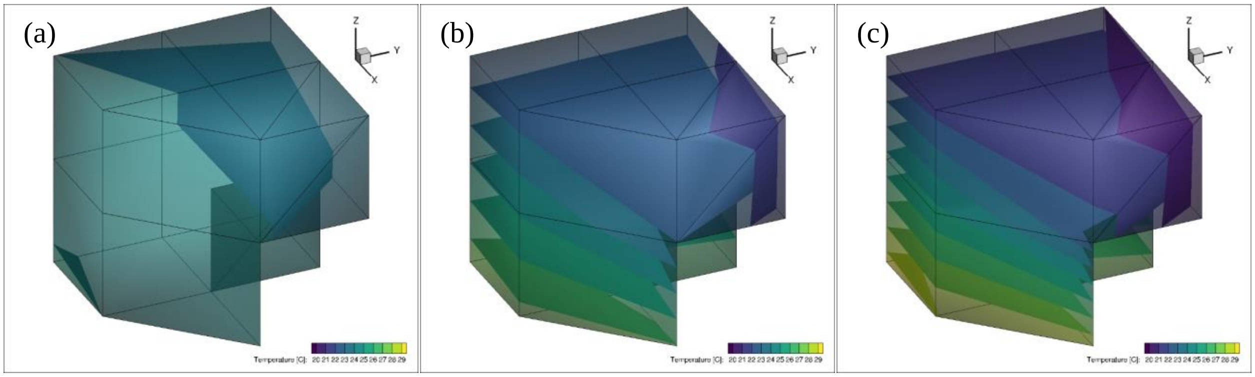

Figure B-18. Temperature Contours from 20°C–29°C at *t* = 90 days for (a) Isotropic, (b) Diagonal, and (c) Full Tensor

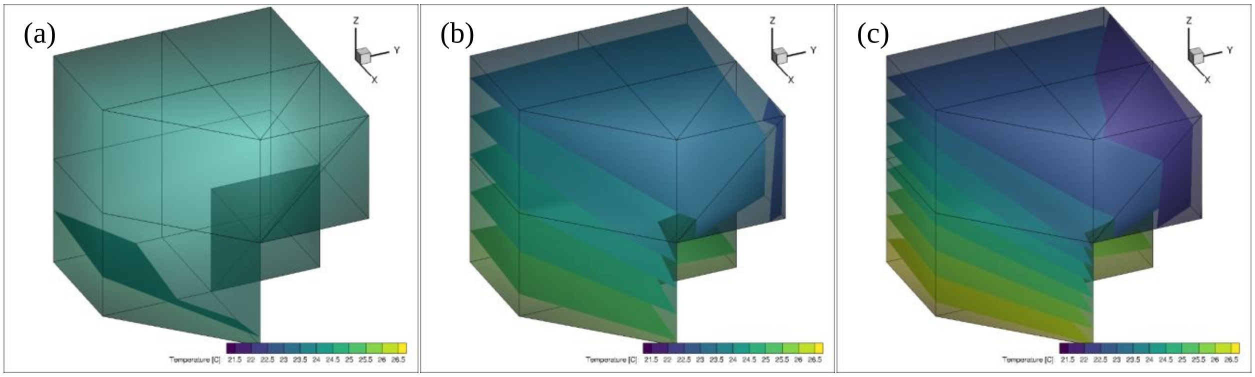

Figure B-19. Temperature contours from 21.5°C–26.5 C at *t* = 120 days for (a) Isotropic, (b) Diagonal, and (c) Full Tensor

This page is intentionally left blank.